Optimisation Studies for a High Gradient Linac for Application in Proton Imaging

ProBE: Proton Boosting Linac for Imaging and Therapy

Sam Pitman

Supervisor: Dr. G.C. Burt

Engineering Department
Lancaster University

This thesis is submitted for the degree of
Doctor of Philosophy

September 2019

I would like to dedicate this thesis in memory of Alan Kinneir who's story is motivation for continued efforts to improve cancer treatments. I would also like to dedicate this thesis in celebration of my Grandmother Nicoletta Berlingieri. She recieved a course of radiation therapy whilst I was writing this thesis, and is a living example of the importance of applying physics knowledge to medicine.

Declaration

Lancaster University
Faculty of Science and Technology
Engineering Department

Signed Declaration on the submission of a thesis.

I declare that this thesis is my own work and has not been submitted in substantially the same form towards the award of a degree or other qualification.
Acknowledgement is made in the text of assistance received and all major sources of information are properly referenced.

Sam Pitman
April 2018

Acknowledgements

I would like to acknowledge those who have helped me in the past 3.5 years, as I could not have completed this work alone. Firstly I must thank my supervisor Dr Graeme Burt for giving me this fantastic opportunity, and for all of his help and encouragement along the way. I must also thank Dr Hywel Owen and Dr Robert Apsimon for all of their input on the ProBE project, and for helping me personally.

I am so thankful to my partner Joe, he has been so understanding and supportive every step of the way and his faith in my completing this has never wavered. I couldn't have done this without you, and hope that one day I can repay the favour.

I am eternally grateful to my parents for supporting me through my school and university education, and for raising me to believe I could achieve anything. I thank my sister Danielle and my best friends Charlotte and Christian for endless phone calls in the low moments, and for reminding me I could do this even when I felt I couldn't. My whole family have been wonderful throughout this process, constantly reminding me of their pride in my achievements, Thank you.

I thank my CERN family, the X-Box team, for their constant humour and good vibes! I have been so lucky to work in such a fantastically close group, you are all amazing and inspire me daily. I send special thanks to Walter Wuensch and Alexej Grudiev for their valuable and fruitful conversations about the RF design of the ProBE prototype structure, it has been an honour to work with you both. I must also thank Anastasiya Solodko, Nuria Catalan Lasheras, and Serge Lebet for their input on the mechanical design of the ProBE cavity, I couldn't have done it without your expertise and I am indebted to you all. My friend Stefano Benedetti whom I also had the pleasure of sharing an office with at CERN. You were always so willing to share information and ideas, and for that I sincerely thank you. Finally I must thank my wonderful friends Carolynne Lord and Jamie Mitchell who were completing their PhD's alongside myself. I can't wait to graduate with you both!

Abstract

Proton beam therapy is an alternative to traditional X-ray radiotherapy utilised especially for paediatric malignancies and radio-resistant tumours; it allows a precise tumour irradiation, but is currently limited by knowledge of the patient density and thus the particle range. Typically X-ray computed tomography (CT) is used for treatment planning but CT scans require conversion from Hounsfield units to estimate the proton stopping power (PSP), which has limited accuracy. Proton CT measures PSP directly and can improve imaging and treatment accuracy. The Christie Hospital will use a 250 MeV cyclotron for proton therapy, but 330 MeV protons are needed to image the largest adult. In this thesis the feasibility of a pulsed linac upgrade to provide 100 MeV acceleration in a cyclinac set up is studied. Space constraints require a compact, high gradient (HG) solution that is reliable and affordable. An overview of accelerator physics and beam dynamics are presented alongside the phenomenology of breakdown in high gradient RF structures. Both a small and large aperture solution are investigated. The small aperture option aims to keep the beam size to a minimum using focussing magnets between cavities and accelerate with a very high gradient. The large aperture solution aims to occupy more of the available space with accelerating structures and less with focussing magnets. This way the optics are simpler and the beam size is larger throughout the linac.

The small aperture optimisation investigated S-, C- and X-band cavities. Firstly with simple pill-box structures then looking at the effect of nose cones on RF efficiency and breakdown limits. Multi-cell structures are then investigated employing side-coupling for standing wave (SW) cavities and various different magnetic coupling slots for backward travelling wave structures (bTW). Limited by 100 MW/m a 15 cm bTW solution was proposed with a calculated gradient of 65 MV/m. Unfortunately to be used with a cyclotron, which typically have large emittance, infeasibly strong magnets would be required.

The large aperture optimisation only considers S- and C-band structures as they exhibit higher shunt impedance with larger apertures than X-band cavities. Side-coupled SW structures and magnetically coupled bTW structures are re-optimised for a larger aperture. An S-band side-coupled SW structure is subsequently identified as being the optimum for this energy range. A full 11-cell structure design with input coupler and end cells is presented calculated to reach 54 MV/m.

A beam dynamics study is also presented considering both the small and large aperture schemes. For the large aperture scheme a particle tracking study is also presented. Mechanical engineering considerations are presented with a novel disk design manufacturing each individual cell from two machined copper disks. Thermal analysis of the temperature distribution inside the cavity is presented alongside heat transfer calculations for the cavity cooling system. Finally the conditioning and high power test of a similar S-band medical structure is presented with comparison made to the prototype structure designed in this study.

Table of contents

List of figures

List of tables

Glossary

ε_0 Permittivity of free space.

σ_c Electrical conductivity.

β_{FE} Field enhancement factor.

β_s Relativistic velocity of the synchronous particle.

β_T Twiss β - betatron amplitude function.

ϕ_{WF} Work function.

A Atomic mass.

ACS Annular Coupled Structure.

ADAM An advanced oncotherapy company.

ADC Analogue to Digital Converter.

ASTRA A Space Charge Tracking Algorithm.

AVF Azimuthally Varying Field.

AVO Advanced oncotherapy.

B Magnetic field.

B_{peak} Peak surface magnetic field.

BDR Breakdown rate.

β Relativistic velocity.

bTW Backwards Travelling Wave.

C Minimum circumference of RF cavity.

c The speed of light in a vacuum.

c_ϵ Specific heat capacity.

C_p Specific heat capacity at constant pressure.

CCC CERN Control Centre.

CCL Coupled Cavity Linac.

CERN Organisation européenne pour la recherche nucléaire.

CFRT ConFormal Radio-Therapy.

CLIC Compact LInear Collider.

CMOS Complimentary metal-oxide-semiconductor.

CST Computer simulation technology.

CT Computed tomography.

CW Continuous Wave.

d Coupling slot depth.

δ Skin depth.

DTL Drift-Tube Linac.

DUT Device Under Test.

E Electric field.

E_0 Axial electric field.

E_{acc} Accelerating gradient.

E_F Fermi Level.

E_k Kilpatrick limit.

E_{peak} Peak surface electric field.

E_r Rest energy.

E_s Energy of the synchronous particle.

ε Geometric emittance.

ES Energy selection.

ESS European Spallation Source.

η Dynamic viscosity.

F Force.

f Frequency.

f_D Darcy friction factor.

FFAG Fixed Field Alternating Gradient.

Δ_H full width half maximum.

g Accelerating gap.

G_c Gap between the nose cones.

Γ Reflection coefficient.

γ_s Lorentz factor of the synchronous particle.

GUI Graphical User Interface.

h Heat transfer coefficient.

H_ϕ Hamiltonian of the system.

HG High Gradient.

HIPA High Intensity 8-sector Ring Cyclotron.

HU Hounsfield Units.

I_{FN} Field emission current.

IARC International Agency for Research on Cancer's.

IDRA Institute for Diagnostics and RAdiotherapy.

IF Intermediate Frequency.

IFIC Institut de Física Corpuscular.

IMPULSE IMaging and Intensity Modulation PULSEd energy booster.

IMRT Intensity-Modulated Radio-Therapy.

INFN Istituto Nazionale di Fisica Nucleare.

J-PARC Japan Proton Accelerator Research Complex.

K K-strength of a quadrupole.

k Coupling factor.

k_B Boltzmann's constant.

κ Thermal Conductivity.

KT Knowledge Transfer.

l Cavity cell length.

L_{cav} Cavity length.

L_D Drift Length.

l_q Length of a quadrupole.

l_{sc} Coupling cell length.

λ Wavelength.

LHC Large Hadron Collider.

LIBO LInear BOoster.

LIGHT Linac for Image Guided Hadron Therapy.

linac Linear accelerator.

LLRF Low Level RF.

LPM Litres per minute.

$\dot{m}$ Mass flow rate.

m_e Mass of an electron.

MAD-X Methodical Accelerator Design.

MRI Magnetic Resonance Imaging.

N_A Avogadro's number.

N_{bd} Number of breakdowns.

N_{cell} Number of accelerating cells.

N_p Number of RF pulses.

NHS National Health Service.

NMR Nuclear Magnetic Resonance.

NORMA NOrmal-conducting Racetrack Medical Accelerator.

Nu Nusselt number.

OAR Organ at risk.

ω angular frequency.

P_d Power dissipated per cycle.

P_{in} Input power.

P_T Travelling wave power.

PAMELA Particle Accelerator for MEdicaL Applications.

pCT proton Computed Tomography.

PEC Perfect electric conductor.

PET Positron Emission Tomography.

φ Phase advance.

PID Proportional Integral Derivative.

PIMS PI-Mode Structure.

PLL Phase Locked Loop.

PMQ Permanent Magnet Quadrupole.

Pr Prandtl number.

PRaVDA Proton Radiotherapy Verification and Dosimetry Applications.

ProBE Proton Boosting Extension for Imaging and Therapy.

PSI Paul Scherrer Institute.

PSP Proton Stopping Power.

$\dot{Q}$ Heat transfer rate.

q Charge of a particle.

Q_0 Internal quality factor.

Q_e External quality factor.

Q_l Loaded quality factor.

r_{ap} Aperture radius.

r_c Cavity radius.

r_e Classical electron radius.

R_{in} Inner nose cone radius.

R_{on} Outer nose cone radius.

R_s Effective shunt impedance.

r_{sc} Coupling cavity radius.

R_{surf} Surface resistance.

Re Reynold's number.

RF Radio Frequency.

RFQ Radio-Frequency Quadrupole.

ρ_r Resistivity.

rms Root mean squared.

RSS Root sum squared.

S Septum thickness.

S_C Modififed Poynting Vector.

S_c Modified Poynting Vector.

SCS Side Coupled Structure.

SCSWS Side-coupled standing wave structure.

SNS Spallation Neutron Source.

SRF Superconducting Radio-Frequency.

SRT Stereotactic Radio-Therapy.

SμS Swiss Muon Source.

SWS Standing-Wave Structure.

T Transit time factor.

t_{fill} filling time.

t_p Pulse length.

TE Transverse Electric.

TEM Transverse Electro Magnetic.

TERA Fondazione per Adroterapia Oncologica.

TM Transverse Magnetic.

TOP-IMPLART Terapia Oncologica con Protoni - Intensity Modulated Proton Linear Accelerator for Radiotherapy.

TULIP TUrning LInac for Proton therapy.

TWS Travelling-Wave Structure.

U Stored energy.

U_d Energy dissipated per cycle.

UHV Ultra-High Vacuum.

v velocity.

V_ϕ Potential energy.

V_0 Voltage across a cavity.

V_c Acceleration voltage (V_0T).

v_g Group velocity.

v_p phase velocity.

VCO Voltage Controlled Oscillator.

VI Virtual Instrument.

Z Atomic number.

Chapter 1

Proton Therapy, Imaging & Accelerators

Cancer has been and will continue to be one of the greatest healthcare challenges of the 21st century. Over 18 million new cancer cases were diagnosed in 2018, alongside 9.6 million cancer deaths, and 43.8 million people reported to be living with cancer according to the International Agency for Research on Cancer's (IARC) GLOBOCAN database. This is predicted to rise to 24.1 million new cancer cases in 2030, with over 13 million cancer deaths [1]. The estimated cancer incidences and deaths from 2018 up to 2040 are shown in figures 1.1 & 1.2. Advancing development of diagnostic methods, such as computer-aided imaging and increased precision in radiation therapy, has seen the cure rates of cancers diagnosed pre-metastasis steadily improve over recent decades [2]. Further improvement of cure rates will be a result of further development of these techniques and also from the rapid transfer of these improved methods into clinical practice. The application of physics to medicine is not a new phenomenon, the first ever Nobel prize in physics was awarded to Wilhelm Conrad Röntgen in 1901 for discovering the X-ray. Figure 1.3 shows the famous image he created of his wife Anna Bertha Ludwig's hand.

Linear accelerators (linacs) have been used in medicine since the 1950s [3], and in 2005 7500 linear electron accelerators were being used for radiotherapy worldwide [4]. Photon radiotherapy was first used to treat cancer and has long been the predominant treatment, but in 1947 Robert Wilson suggested it may be beneficial to use heavy charged particles instead [5]. Proton therapy better spares organs at risk (OARs) from a radiation dose than photon radiotherapy. Sparing OARs also requires accurate imaging techniques. Imaging with protons (pCT) during treatment planning is foreseen to improve the ballistic selectivity of proton beam radiotherapy [6–8], even further beyond that of *photon* radiotherapy presently.

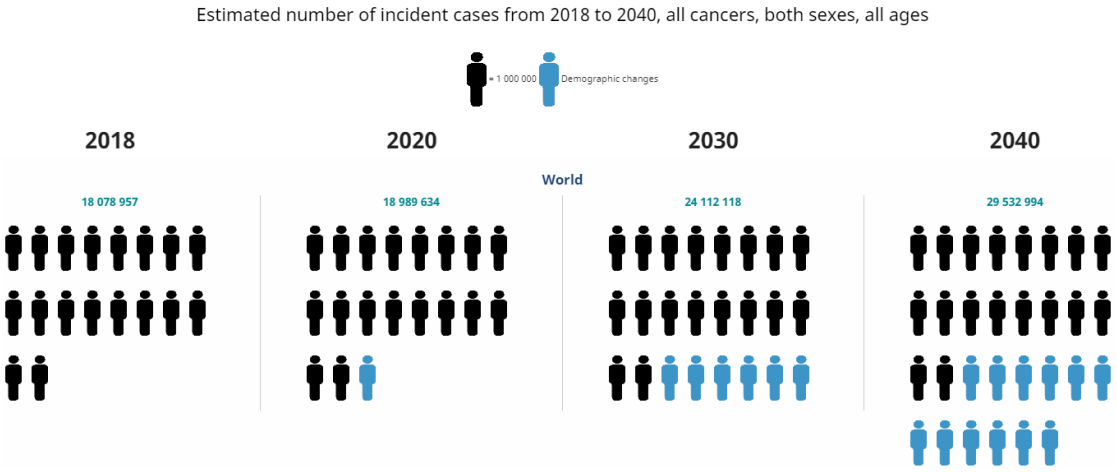

Fig. 1.1 Estimated number of incident cancer cases from 2018 to 2040, all cancers, both sexes, all ages [1].

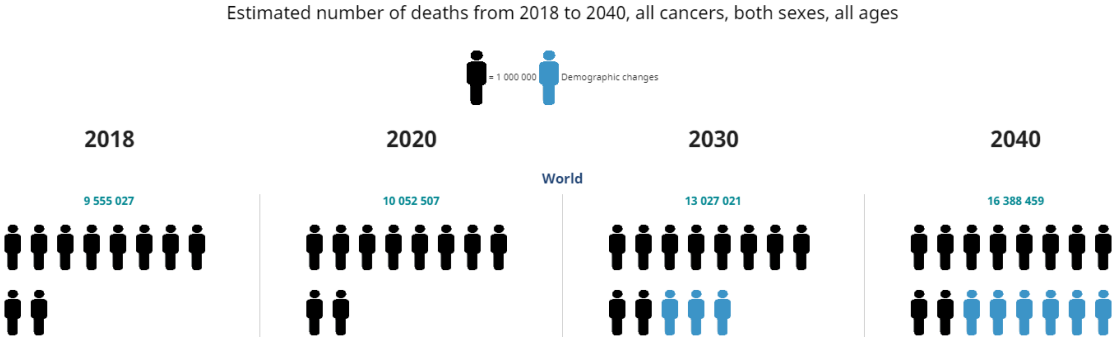

Fig. 1.2 Estimated number of cancer deaths from 2018 to 2040, all cancers, both sexes, all ages [1].

In this work we explore the feasibility of upgrading existing proton therapy centres fitted with 250 MeV cyclotrons with a linear accelerator to provide 350 MeV protons. This is foreseen to improve the accuracy of proton therapy treatments by providing proton imaging, and be far reaching in its accessibility to most existing proton therapy centres.

1.1 Medical Proton Accelerators

Ionising radiation has been used in medicine for over 100 years. Soon after the discovery of radiation and X-rays, high energy photons were being utilised to treat skin diseases and even cancer [10]. As early as 1912 cancer patients were treated using radium-226 as a radiation source [11]. Swiftly after the invention of the Van de Graaff accelerator in 1932 [12], it was utilised in medicine. The large machines were impractical for hospitals not just because of their size, but because of their limited output and high operating costs [13].

Fig. 1.3 Hand mit Ringen (Hand with Rings): a print of one of the first X-rays by Wilhelm Röntgen (1845–1923) of the left hand of his wife Anna Bertha Ludwig. It was presented to Professor Ludwig Zehnder of the Physik Institut, University of Freiburg, on 1 January 1896 [9].

The next advance in medical accelerators was the betatron [14], capable of producing electron beams from 5 to 25 MeV for use in radiotherapy. The betatron's output energy was limited by the strength of the magnetic field possible due to the saturation of iron, and also due to the size of the magnet core. Figure 1.4 shows Kerst working on the first betatron where the magnet weighed 4-tons. Ultimately the betatron was no match for the invention that revolutionised radiotherapy to this day; the linear accelerator or 'linac'.

The linac was first proposed by Widerøe in 1928 [16], so called because the path of the accelerated beam was linear. The small accelerating gradients ($<$10 MeV/m) possible in the early years of linacs meant long accelerators were necessary for significant energy gain, Figure 1.5 is around 2 meters long and yields just 6 MeV energy gain. It is this low gradient and large size that impedes the practicality of such machines in medicine. This is especially true of protons which are heavier and thus require much higher fields (or longer machines) for the same energy gain. A more practical option has been accelerators with a circular path such as cyclotrons and synchrotrons. The latter is known to use linacs as small, low energy transitions between the source and injection.

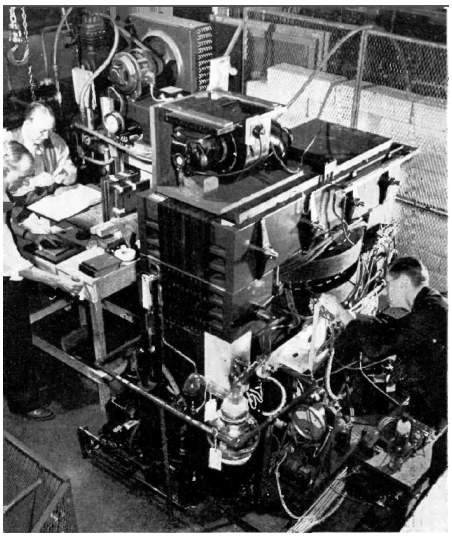

Fig. 1.4 Early betatron at University of Illinois. Kerst is at right, examining the vacuum chamber between the poles of the 4-ton magnet [15].

In recent years, greater understanding of RF cavities has lead to larger accelerating gradients being achieved, which has reduced the size of linacs and made them more useful in medicine. A collaboration between TERA (Fondazione per Adroterapia Oncologica), European Organization for Nuclear Research (CERN), the university and Istituto Nazionale di Fisica Nucleare (INFN) of Milan and the university and INFN of Naples designed a high frequency proton linac for medical applications at 3 GHz. The LInear BOoster (LIBO) structure was designed to reach a gradient of 15.8 MV/m, but after a short conditioning time was able to reach 28.5 MV/m[18]. It has been featured in both the Terapia Oncologica con Protoni - Intensity Modulated Proton Linear Accelerator for Radiotherapy (TOP-IMPLART) project [19], and the Institute for Diagnostics and RAdiotherapy (IDRA) project [20]. The TOP-IMPLART linac is a 150 MeV pulsed proton linear accelerator for proton therapy applications under commissioning at ENEA Frascati. The IDRA (Institute for Diagnostic and RAdiotherapy) is a cyclinac with a 30 MeV commercial cyclotron followed by the LIBO structure accelerating to 210 MeV.

The cyclinac idea was first proposed by U. Amaldi in 1993 [21], where a booster linac is placed at the output of a cyclotron to reach higher energies. This concept is advantageous to hospitals due the simplicity and relative compactness of the cyclotron. Unfortunately the extraction frequency of most cyclotrons is in the MHz range, much lower than the high frequency linac sections which are GHz, and this mismatch is responsible for large beam losses at the start of the linac. Luckily low average currents in the nA range are required for radiotherapy and cyclotrons typically provide μA. Even less current is required for radiography; a few pA are sufficient.

Fig. 1.5 Baby Gordon Isaacs was the first patient to be treated with a linear accelerator at just 2 years old in 1957. His retinoblastoma was cured and he survived into adulthood with normal vision [17].

More recently the TERA foundation with the CERN Compact LInear Collider (CLIC) group designed and built a high gradient medical accelerating cavity for use in the TUrning LInac for Proton therapy (TULIP) *all-linac* project [22] funded by the Knowledge Transfer (KT) group. With a nominal gradient of 50 MV/m, it is the highest gradient proton accelerator demonstrated at this energy level.

1.2 Proton Therapy

Radiotherapy directs ionising radiation at cancerous cells or tumours with the aim of severely damaging the cell's DNA resulting in cell death. The challenge lies in maximising the dose to cancerous cells and minimising the exposure to normal healthy tissue and OARs. Healthy cells that survive DNA damage are at risk of leading to secondary cancers, so minimising dose to healthy tissue is especially important in paediatric cancer patients where cell division is more rapid and life expectancy post treatment is larger. Traditionally radiotherapy has been performed using a photon beam. Complex techniques such as Intensity-Modulated Radio-Therapy (IMRT) [23, 24] and Stereotactic Radio-Therapy (SRT) [25, 26] have improved the accuracy of irradiating only cancerous cells by approaching the target volume from multiple directions overlapping on the tumour (SRT), and employing collimators and degraders to spare healthy tissue. Figure 1.6 illustrates the differences between conventional radiotherapy where the field is limited to a rectangular shape, ConFormal Radio-Therapy (CFRT) where a multi-leaf collimator is employed to produce more complex geometric field shaping around the tumour,

and IMRT where the field is geometrically shaped similar to CFRT but is also intensity modulated pixel by pixel within the shaped field to account for varying tumour depths. Figure 1.7 illustrates the difference between SRT with traditional photon beams (left) and proton therapy (right). SRT approaches the tumour from all available angles around the patient. This results in a lower dose to the healthy tissue and a larger layered dose to the target volume. The region marked in green is the brain stem, and it is desirable to limit the dose to this region as much as possible. Proton beams offer an elegant solution, due to the way that they deposit energy exit dose can be minimised. Thus the proton therapy treatment (right) has no exit dose and has reduced the dose deposited in the brain stem in comparison to SRT.

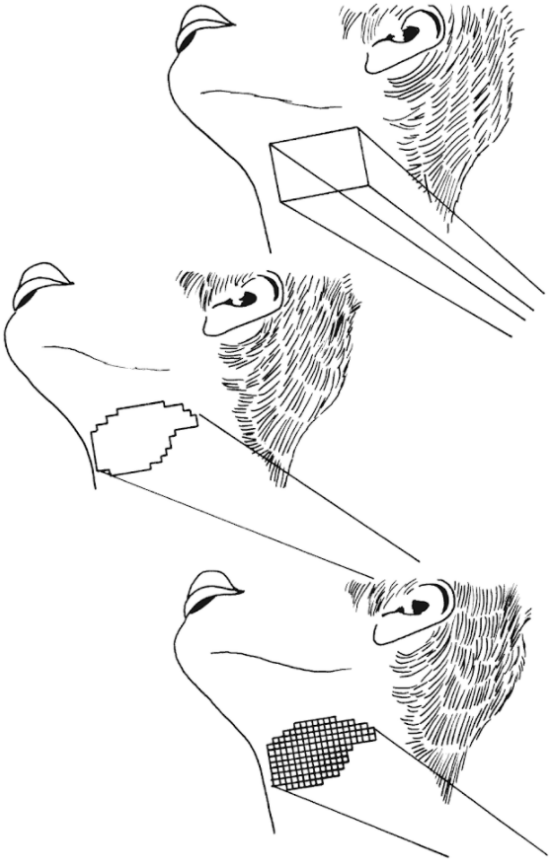

Fig. 1.6 The differences between conventional radiotherapy (top), conformal radiotherapy CFRT (centre) and CFRT with intensity modulation IMRT (bottom) [23].

In 1947 Robert Wilson suggested that with high energy protons, precision irradiation of tumours was possible due to the unique dose deposition of moderately relativistic heavy charged particles [5], described by the Bethe-Bloch equation [28–30]

$$-\left\langle \frac{dE}{dx} \right\rangle = kq^2 \frac{Z}{A} \frac{1}{\beta^2} \left[\frac{1}{2} \ln \frac{2m_e c^2 \beta^2 \gamma^2 T \max}{I^2} - \beta^2 - \frac{\delta(\beta\gamma)}{2} \right] \tag{1.1}$$

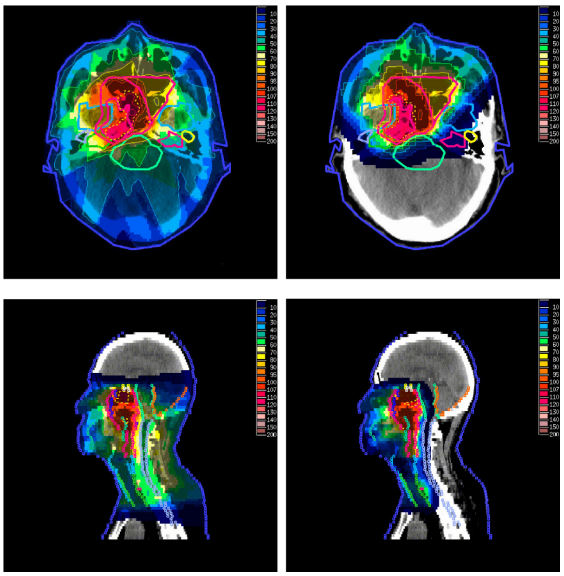

Fig. 1.7 Illustrates the differences between photon radiotherapy (left) where dose is deposited across the entire cross section of the patient and proton therapy (right) where the dose ends half way through, the back of the head, spine and back see no dose [27].

where $-\left\langle \frac{dE}{dx} \right\rangle$ is the stopping power of the material or the energy loss (dE) occurring over distance x. $k = 4\pi N_A r_e^2 m_e c^2$, N_A being Avogadro's number, r_e being the classical electron radius, m_e being the mass of an electron and c being the speed of light. q is the charge of the incident particle, Z and A are the atomic number and atomic mass of the absorber respectively, $I \approx 11.5Z$ eV is the mean ionisation potential, $T_{\max} = 2m_e c^2 \beta^2 \gamma^2 / [1 + 2\gamma m_e / M + (m_e/M)^2]$ is the maximum kinetic energy that may be imparted to a free electron in a single collision and introduces a minor dependence on the incident particle mass M. γ is the Lorentz factor and β is the relativistic velocity of the particle. $\delta(\beta\gamma)$ is a density correction term [31]. Equation 1.1 highlights that the depth at which the Bragg peak occurs depends on the initial energy of the proton beam. Figure 1.8 illustrates the variation in dose deposition with tissue depth. Whereas a traditional photon beam will result in both an entrance and exit dose, a proton beam deposits $\approx 50\%$ of the energy before the Bragg peak, $\approx 50\%$ in the tumour leaving little to no exit dose [32]. This large, precise energy deposit via the Bragg peak requires accurate imaging to ensure it happens inside the tumour margins, this requires a knowledge of the proton stopping power of the tissue between the linac and the tumour. The proton stopping power of tissue is defined as the retarding force acting on the protons which causes them to lose energy. The point at which the Bragg peak occurs depends on not only the depth, but on the density of the tissue in its path.

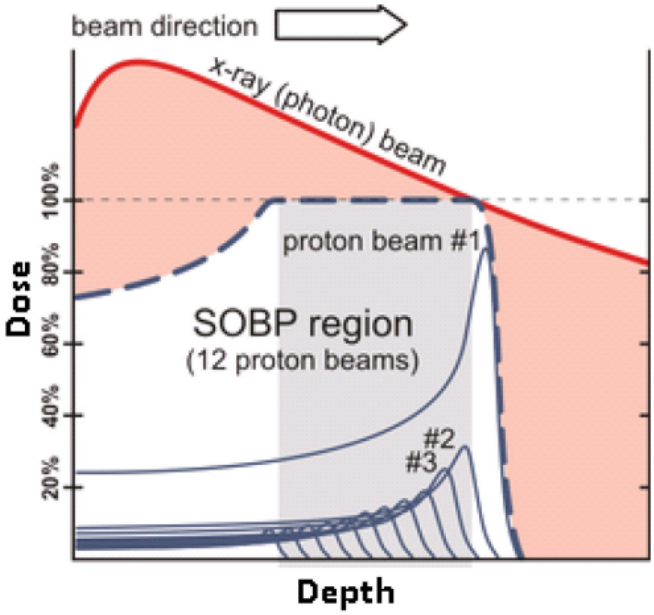

Fig. 1.8 Protons deposit energy in water via the Bragg Peak. Multiple Bragg peaks can be utilised with varying energies, resulting in a cumulative flat top dose called the Spread Out Bragg Peak (SOBP) [33].

1.2.1 The Range Problem

Due to the steep dose fall off distal to the Bragg peak, proton therapy has the potential to deliver higher doses to cancerous tissue while greatly reducing the dose delivered to healthy tissue in comparison to photon radiotherapy this is illustrated in Figure 1.9(a). This steep dose gradient distal to the Bragg peak is not used to spare OARs in practice because of uncertainties around its exact location in the patient. Figure 1.9(b) illustrates the influence of uncertainties on different depth-dose curves. In the case of traditional photon radiotherapy a small uncertainty in the dose delivery makes a small difference to the dose seen by both the tumour and the organ at risk (OAR), in all three curves the peak occurs in the soft tissue. In the case of proton radiotherapy, the same uncertainty can be the difference between the peak dose being deposited entirely in the tumour or entirely in the organ at risk. To benefit from the advantage of the Bragg peak clinicians must know with certainty where it will be deposited.

Several imaging modalities may be used to study the morphology of a tumour, and in both photon and proton radiotherapy a collimator can be used to shape the beam accordingly, and the intensity can be modulated pixel by pixel. To utilise the Bragg peak in proton therapy, the incident kinetic energy must also be modulated thus emphasising the importance of accurate range verification. During treatment planning margins are defined around the target volume to account for uncertainties in the dose deposition, this uncertainty is referred to as the

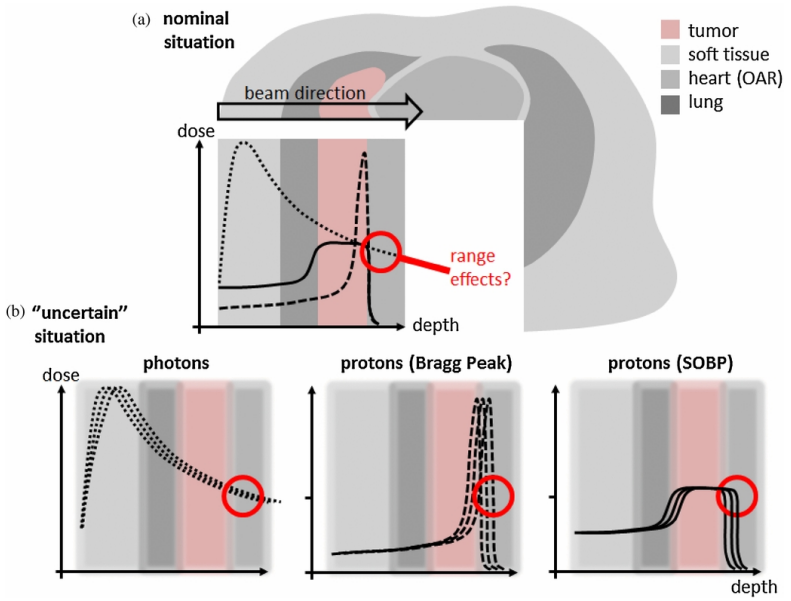

Fig. 1.9 (a) Potential dose benefit of a proton treatment compared to a photon treatment (dotted line: photon depth-dose curve; dashed line: mono-energetic proton depth dose curve known as Bragg Peak; straight line: spread out proton Bragg curve (SOBP) to cover the whole tumour). (b) Influence of uncertainties to these depth-dose curves [34].

range problem. As much as 10 mm inside of the imaged tumour boundary is omitted from the planned treatment target volume to avoid accidentally irradiating healthy tissue or OARs. It has been shown that using pCT to image during treatment planning, this can be reduced to as little as 3 mm [35]. This so-called 'range problem' is yet to be satisfactorily resolved and uncertainties in the energy deposition range of the therapy protons in the patient result in larger than desirable treatment margins [36, 37]. Treatment planning and range calculations are done using both Magnetic Resonance Imaging (MRI) for mapping the location of the tumour, and x-ray computed tomography (CT) which creates images from photon attenuation measured in Hounsfield Units (HU). The HU is a quantity commonly used in CT scanning to express CT numbers in a standardised and convenient form. To calculate the range of the treatment protons in the patient, HU must then be converted to relative Proton Stopping Power (PSP). One source of range uncertainty is the inherent limitations of x-ray CT such as image noise, beam hardening, and reconstruction artefacts in the presence of metal implants such as tooth fillings [38, 39]. The relationship between HU and PSP varies with materials in the body i.e different organs. Furthermore, despite it being known that there is not a simple one-to-one relation between HU and PSP [40], most centres use a single function for the conversion [37]. Algorithms such as the stoichiometric approach produce calibration curves for this conversion from HU to PSP, using data from average, healthy adults [41–43]; which is not patient specific. It has been

shown that this seemingly small inaccuracy results in PSP prediction errors of over 2% [44], and this is widely believed to be a main factor preventing proton therapy reaching its full potential.

1.2.2 Range Verification *in vivo*

There are multiple approaches to managing range uncertainty in proton therapy [45–48], but it will always be deemed necessary to verify proton range *in vivo* be it by directly measuring dose or fluence, or by indirectly measuring secondary emission caused by proton irradiation.

Prompt Gamma Imaging

On their path through the patient, protons undergo nuclear reactions with tissue and some of these interactions produce prompt gammas. After an interaction with a proton, the target nucleus is excited to a higher energy state causing a single photon known as a 'prompt gamma' to be emitted, returning the nucleus to its ground state (see Figure 1.10). The emitted gamma rays can then be detected.

As the protons traverse the patient they lose energy and their reaction cross sections decrease. This means proton interactions occur along the whole penetration path until 2-3 mm before the Bragg peak. Thus the emission of prompt gammas is related to the penetration path of the protons and conclusions can be drawn on the proton range.

The emission of prompt gammas happens during proton therapy whether or not they are being detected. One of the main advantages of this method is real-time verification of dose delivery, and no additional dose is imparted onto the patient. However, this also means prompt gamma imaging can not aid treatment planning efforts. Research into a suitable detector system is ongoing, but so far position verification of the Bragg peak of a 100 MeV proton beam in a phantom has been reported with 1-2 mm accuracy [49].

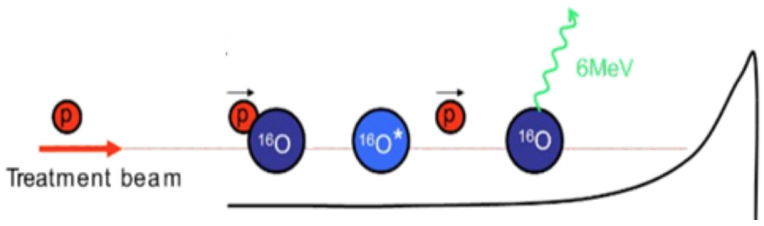

Fig. 1.10 Figure illustrates the concept behind prompt gamma imaging. Protons traverse the tissue and interact with nuclei. The target nucleus is excited to a higher energy state thus it releases a single photon to return to its ground state [50].

Positron Emission Tomography

In the previous example we discussed one outcome of protons' interaction with nuclei - prompt gammas. Another interaction that can occur is the emission of a positron which then annihilates with an electron in surrounding tissue. Coincident gammas are subsequently emitted (see Figure 1.11) and can then be detected with a gamma camera. This is called Positron Emission Tomography (PET).

Similarly to prompt gamma imaging, PET has the advantage of not resulting in any additional radiation dose to the patient. PET imaging can either happen in real time or a certain time after the treatment is completed. It cannot however be used for treatment planning prior to the first treatment.

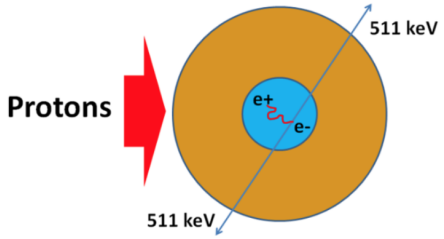

Fig. 1.11 Figure illustrates the concept behind positron emission tomography (PET) protons interact with nuclei in tissue and emitted positrons annihilate with electrons which then emits coincident gammas [51].

Magnetic Resonance Imaging

Nuclear Magnetic Resonance (NMR) Imaging or MRI is commonly used in hospitals to image soft tissue. A strong magnetic field is applied to the patient which excites the protons inside of the body. The excited protons emit an RF signal which is detected using a receiving coil. The rate at which excited protons return to their equilibrium state indicates which type of tissue those protons comprise.

Radiation can cause changes in the constitution of human tissue which can be visible by MRI. This method offers a high spatial resolution and doesn't depart any additional radiation dose. Additionally, MRI scanners already exist in most hospitals and can be used for this type of range verification. Unfortunately it takes days [52] for the cells to actually change enough to be visible, in some cases only after the end of treatment. So although it can verify the range in vivo, it can not be used to directly measure PSP or to adapt therapy during the course of treatment to compensate for observed range errors [52].

Proton Computed Tomography

The only imaging method that directly provides the proton stopping power of the tissue, is pCT [53]. Figure 1.12 illustrates the pCT set up by the Proton

Radiotherapy Verification and Dosimetry Applications (PRaVDA) consortium [54]. Higher energy protons are used for pCT than the 250 MeV used for therapy. At least 330 MeV protons are needed to ensure that when they are sent through the patient and into the detector the Bragg peak occurs in a range telescope behind the patient instead of in the patient. One negative of proton imaging is that the patient will receive a small dose prior to treatment. However, images obtained using protons result in 50-100 times lower image exposure than x-ray radiographs of equal resolution [55].

In pCT a high energy proton beam is sent through two semiconductor detectors which record the x and y positions and direction on entry. After the patient the protons will exit through two more semiconductor detectors again recording the x and y positions and direction on exit. The protons are then bought to a stop in 24 layers of Complimentary metal-oxide-semiconductor (CMOS) sensors separated by absorbers, also referred to as a range telescope, which measures the exit energy. This process is repeated millions of times to collect lots of data, and the paths of the protons are reconstructed in software. The energy lost in the path the protons traversed in the body is thus calculated.

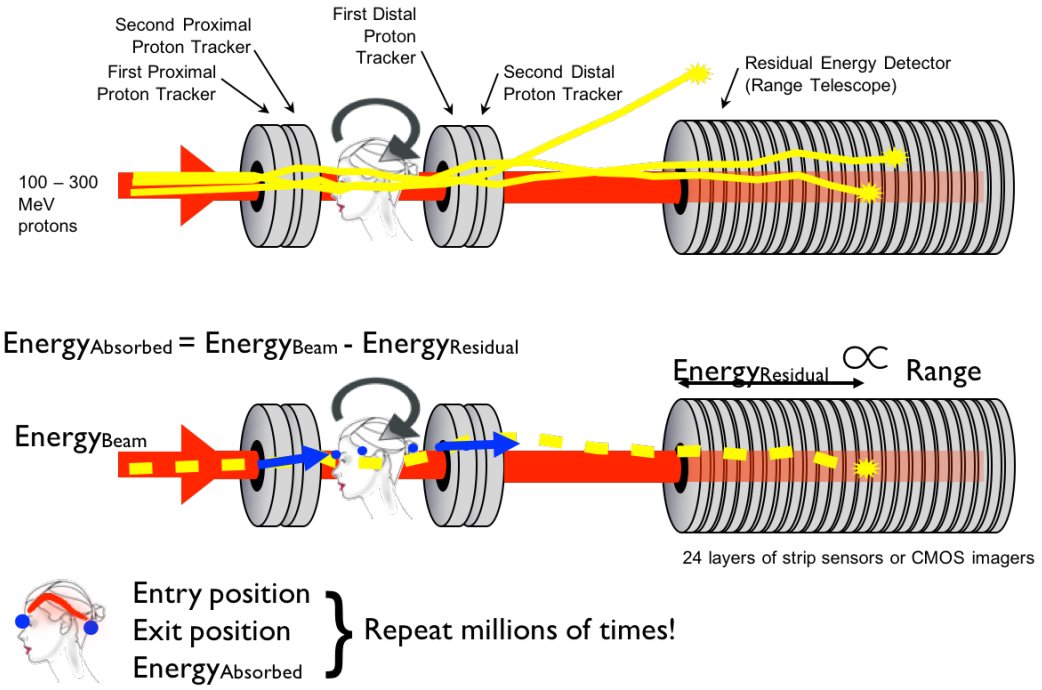

Fig. 1.12 The PRaVDA pCT system concept. The tracker is comprised of the first four units shown here as the two which are placed in front of the object to be imaged and the two after. A range telescope (calorimeter) is placed immediately after the tracker to measure the residual energy of each proton after it has been tracked through the object to be imaged [54].

Despite the advantages of proton radiography it has not been adopted since its conception in 1960s[56] because of source availability and cost. To image full sized adult bodies 330-350 MeV [36] protons are required and this is where the high cost is incurred. There are efforts to provide proton therapy facilities with high energy protons and they are detailed in the next section.

1.3 Producing 350 MeV Protons

In recent years there have been multiple efforts to produce 330 MeV protons for a clinical setting. Figure 1.13 shows the ProTom Radiance 330 proton therapy system. The 330 MeV synchrotron allows for imaging and treatment with the same accelerator [57]. Injection beam line development is still ongoing to achieve the maximum dose rate of 2 Gy per minute per litre, and simulation and existing dose delivery tests suggest it will achieve that [58]. One benefit of this system is its variable extraction meaning no degrader is necessary resulting in a higher quality beam. However it has a large space requirement which some existing centres do not have.

Fig. 1.13 The ProTom Radiance 330 proton therapy system [57].

Although it is common to use cyclotrons as a proton source for 230-250 MeV protons, there are technical complications at higher energies. In the same way that the length of each cell varies in linacs depending on the particle's energy, cyclotrons

must vary either the magnetic field or the frequency. Synchrocyclotrons vary the RF frequency to accommodate the higher energy particles. These tend to have better focussing and can be made compact with high fields. However, one cannot have two separate bunches at different energies in the cyclotron at the same time, as one would not be synchronous. This limits the current that they can provide for a clinical setting. Isochronous cyclotrons vary the field with radius, but at higher energies this makes the beam hard to focus. Azimuthally Varying Field (AVF) cyclotrons vary the field with pole pieces and incorporate edge focussing which is limited at higher energies. At higher energies it is better to use many separate magnets or *'sectors'*, but this prevents the source injecting into the centre of the cyclotron. The Paul Scherrer Institute (PSI) has constructed a 590 MeV High Intensity 8-sector Ring Cyclotron (HIPA) shown in Figure 1.14 which outputs 2.2 mA to feed the Swiss Muon Source (SμS) [59]. It has had issues with RF power leakage into vacuum space [60], but 590 MeV protons are excessive for proton CT and this complication would likely cease with a lower energy output and custom flat top cavity. This was not designed for a medical application and is not an 'all enclosed' solution. The proton beam is pre-accelerated in a Cockcroft-Walton electrostatic column to an energy of 870 keV and this is increased to 72 MeV in the 4-sector Injector 2 cyclotron. Only then is the beam injected into the 8-sector 590 MeV cyclotron. This set up is much too big and complex for a hospital.

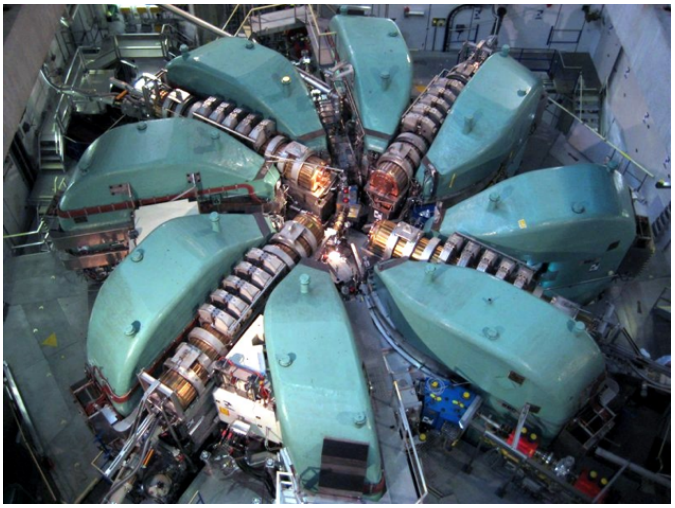

Fig. 1.14 The PSI 590 MeV high intensity 8-sector Ring Cyclotron (HIPA) [59].

There have been attempts to achieve the high current capability of the cyclotron and the variable energy extraction of the synchrotron, both in the UK at the Cockcroft Institute [61], the John Adams Institute [62] and in the USA at Fermilab [63], by developing Fixed Field Alternating Gradient (FFAG) accelerators such as Particle Accelerator for MEdicaL Applications (PAMELA) and NOrmal-conducting

Racetrack Medical Accelerator (NORMA) (Figure 1.15) [64–66]. They are capable of producing 330 MeV protons rapidly with variable energy, but they have a large footprint and they are yet to be demonstrated.

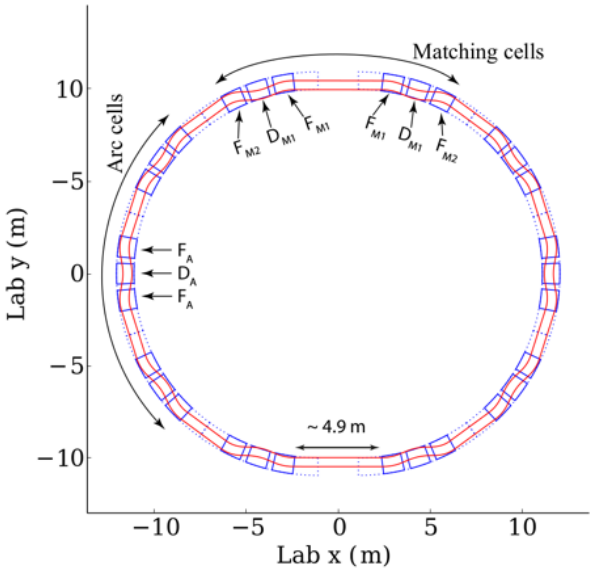

Fig. 1.15 The NORMA NORMAl conducting racetrack medical FFAG [66].

A collaboration between PSI and the TERA proposed the IMaging and Intensity Modulation PULSEd energy booster (IMPULSE) [67] shown in Figure 1.16. This proposes the cyclinac concept to boost protons up to 350 MeV in a linac after a 250 MeV cyclotron used as a source for treatment. The linac proposes four 10 MW power sources to power 7 m of linac with an average gradient of 25 MV/m. More technical information on the RF cavities in these various low-Relativistic velocity (β) systems can be found in Chapter 2.

1.4 The Project: ProBE: Proton Boosting Extension for Imaging and Therapy

Great Britain's first high energy proton therapy facility is being built at the Christie Hospital in Manchester, and artist's impression is shown in Figure 1.17. There is already a low energy (62 MeV) proton facility at Clatterbridge for eye treatments only. The National Health Service (NHS) has to send patients who need proton therapy in the body to other facilities in Europe and the USA for treatment. This method of accessing life saving treatment came at great cost to both the NHS and the families of the patients. Figure 1.19 shows the Varian Probeam cyclotron being delivered to the new building which is now complete, and the facility is due to start

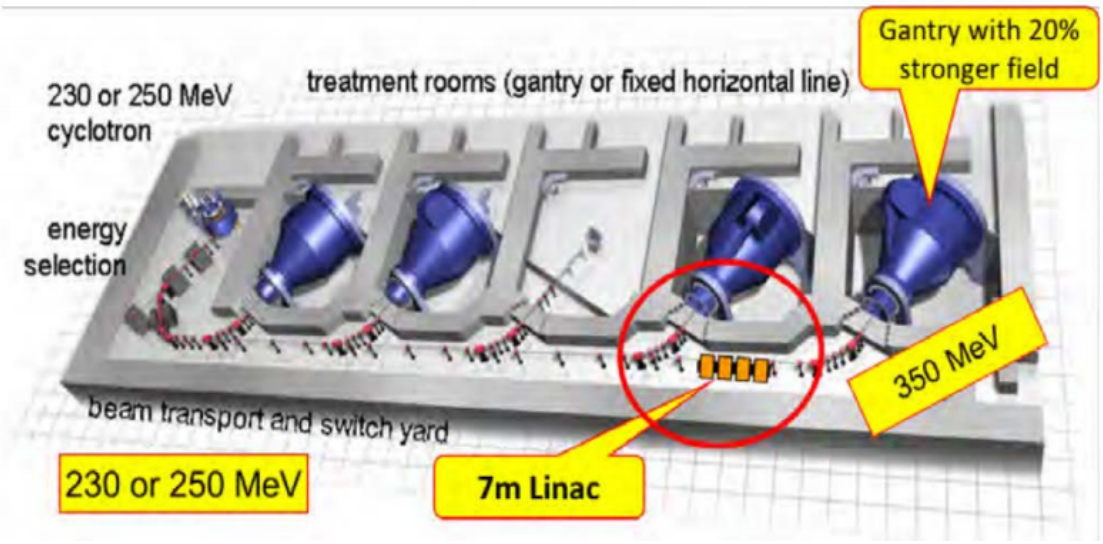

Fig. 1.16 The IMPULSE cyclinac concept proposed by PSI and TERA [67].

treating patients this year. The protons used for treatment will be accelerated in the cyclotron to 253 MeV and transported to one of three treatment gantries shown in Figures 1.18 & 1.20. A fourth treatment room may be constructed but will remain empty initially to allow for a research/medical isotope room.

The ProBE project aims to examine the feasibility of upgrading the Christie proton therapy facility with a proton boosting linac, to accelerate the 250 MeV protons to 350 MeV, the energy required for pCT. Having the capability to image with protons in the same facility as treatment is one solution to the range problem detailed in section 1.2.1, and is expected to reduce patient treatment margins and improve patient outcomes. pCT systems are still in the development phase with research groups working on detector technology[71], image reconstruction[53], and producing a 350 MeV proton beam suitable for pCT. The Christie charity[72] has funded a research space utilising the real treatment beam from the Varian Probeam cyclotron. It is hoped this will facilitate the testing of the ProBE linac with a clinical beam, alongside other experiments such as radio-pharmaceuticals and pCT research which is already funded.

1.4.1 Three Stages:

Linac Development

The first stage of the project is the development of a test cavity. In this work a booster linac is designed to upgrade an existing cyclotron facility to a cyclinac in a compact space thanks to advances in high gradient technology. The RF optimisation of the accelerating cavity is presented in this thesis along with particle tracking results and the mechanical engineering design. The RF cavity design and

Fig. 1.17 Artist's Impression of The Christie Rutherford proton Centre [68].

fabrication was heavily influenced by the results obtained from the CLIC high gradient test programme [**?**] at CERN to ensure the most reliable high gradient operation. A beam dynamics study is also presented determining the best solution for adequate transmission through the linac. When fabrication of the cavity is complete it is foreseen to be conditioned and tested in the CLIC S-band high gradient test facility at CERN known as S-Box.

Linac Testing

Once the cavity testing is complete, the linac testing stage of the project can commence. As is shown in Figure 1.20 the fourth gantry room will be constructed at the same time as the rest of the facility, but patient treatment equipment will not be installed. Instead this room will become a research beam line with a length of around 10 metres. Here it will be possible to test the ProBE cavity with the real clinical beam. There will also be the capability at the Christie to test pCT detectors and conduct radio-biology amongst other research.

Superconducting Gantry

The third stage of the project is concerning beam delivery. Beam rigidity is defined as $R = B\rho = p/q$ where B is the magnetic field, ρ is the gyroradius of the particle due to this field, p is the particle momentum, and q is it's charge. At the high energies necessary for proton imaging, beam rigidity is increased from 2.43 Tm at 250 MeV to 2.84 Tm at 350 MeV. Stronger magnets are necessary to manipulate the beam around the patient in the same amount of space. The fourth treatment room at the Christie hospital is sized for a 250 MeV treatment gantry, so in the

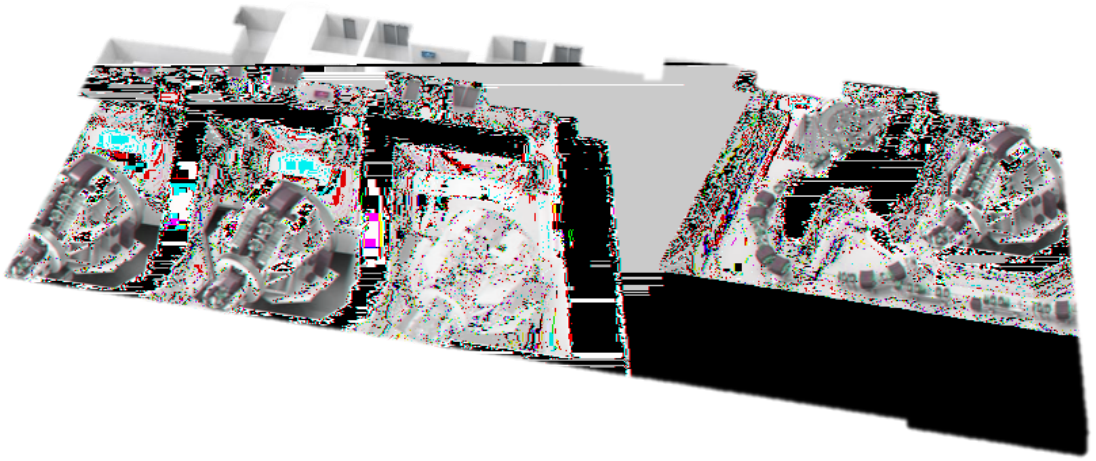

Fig. 1.18 The Varian Probeam multi-room proton therapy system. The fourth treatment room (right) at the Christie will have a superconducting gantry if they upgrade to higher energy protons [69].

same space superconducting magnets will be necessary. A preliminary design shown in Figure 1.21 satisfies the key requirements of the gantry but there are further improvements to be made and research to reduce the size of the achromats is ongoing, alongside beam tracking studies and inclusion of the booster linac into the final gantry design [74].

Fig. 1.19 The Varian Probeam 253 MeV cyclotron being delivered at the Christie [70].

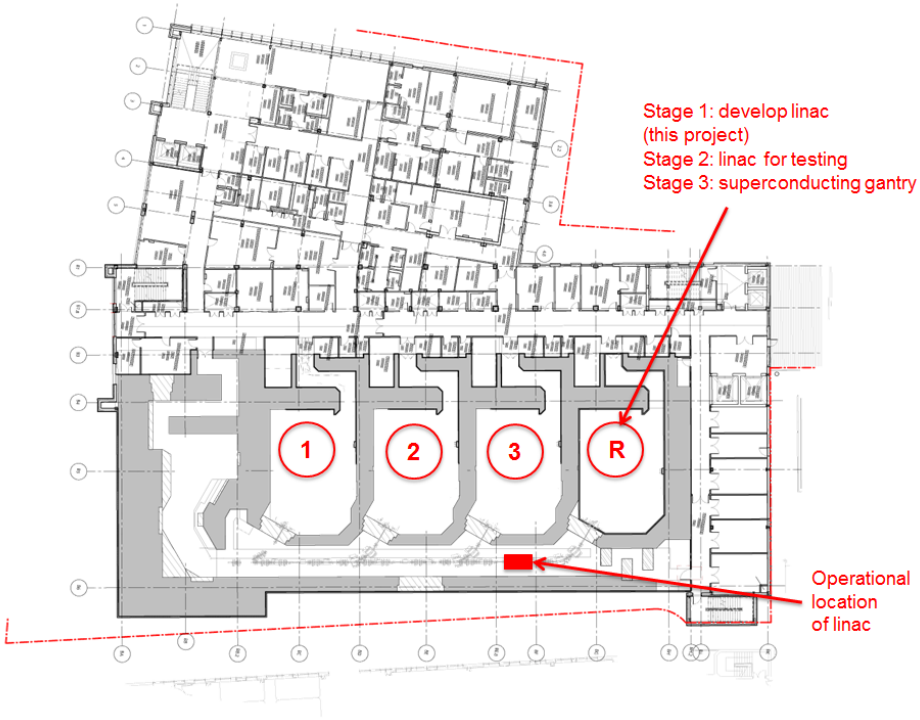

Fig. 1.20 Layout of the proton therapy facility at The Christie Hospital. Four treatment rooms can be seen on the blueprint. Initially the first 3 treatment rooms will be operational using the 253 MeV cyclotron as a proton source for treatment. During this time the fourth room will remain a research room with the clinical beam. The ProBE linac will be developed simultaneously and tested in the research room. Afterwards that the linac will move into the beam line, and the fourth treatment room may be upgraded to a superconducting gantry for pCT [73].

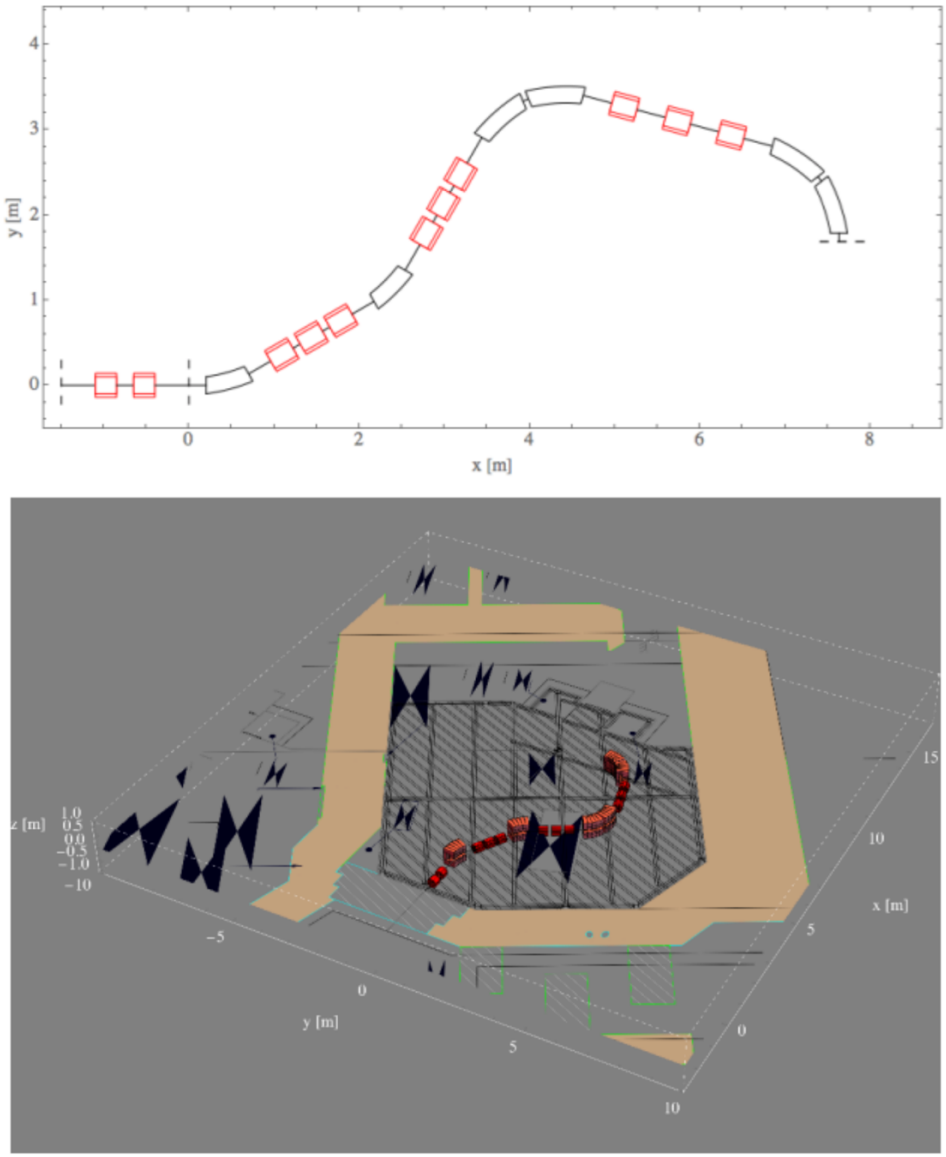

Fig. 1.21 Top:Preliminary layout of the compact pCT gantry design; dipoles shown (curved) in black, quadrupoles shown in red. Bottom: visualisation inside the fourth gantry room at the Christie [74].

Chapter 2

RF Particle Acceleration

In this chapter, the theory of RF particle acceleration is introduced. The theory of RF cavities and the interaction of charged particles is presented, alongside important figures of merit to consider when designing RF cavities. Various RF cavity structures, specifically the current landscape of low/medium-β structures, are described alongside RF breakdown phenomenology and other high gradient (HG) limitations. The Lorentz force law

$$\mathbf{F} = q(\mathbf{E} + v \times \mathbf{B}) \tag{2.1}$$

is the most important equation in accelerator physics. It shows that electromagnetic fields can be used to accelerate and manipulate charged particles. It describes the force (F) of an electromagnetic field on charged particle q [75]. In the presence of an electric field (E), a charged particle q will be accelerated in the direction of motion of that electric field, therefore gaining energy. The force F is perpendicular to both the magnetic field (B) and the particle velocity (v). Hence, the magnetic field component does not increase the energy of the particle but adds a component of motion transverse to the initial direction of motion, bending the particle's trajectory. It is because of this we can use electromagnetic fields to manipulate and accelerate charged particle beams for their desired use.

2.1 RF Cavities

A particle accelerator is made up of one or more RF cavities. An RF cavity is a hollow metallic structure that can be filled with electromagnetic fields, by an external high-frequency power source. The fields that exist inside a cylindrical cavity are given by

$$\left(\nabla^2 - \frac{1}{c}\frac{\delta^2}{\delta t}\right)\begin{Bmatrix}\mathbf{E}\\ \mathbf{B}\end{Bmatrix} = 0. \tag{2.2}$$

Transverse Electro Magnetic (TEM) waves are not possible inside an RF pillbox cavity because to satisfy the boundary conditions either the electric or the magnetic field components must be in the direction of propagation. Assuming the cavity wall is a perfect electric conductor, the boundary condition is

$$E_z|_{R_{cav}} = 0$$

for a Transverse Magnetic (TM) mode, and the magnetic field component is zero in the direction of propagation

$$B_z = 0.$$

For a Transverse Electric (TE) mode, the boundary condition is

$$\frac{\delta B_z}{\delta n}\Big|_{R_{cav}} = 0$$

where $\delta/\delta n$ is normal to a point on the surface and the electric field component is zero in the direction of propagation [76]

$$E_z = 0.$$

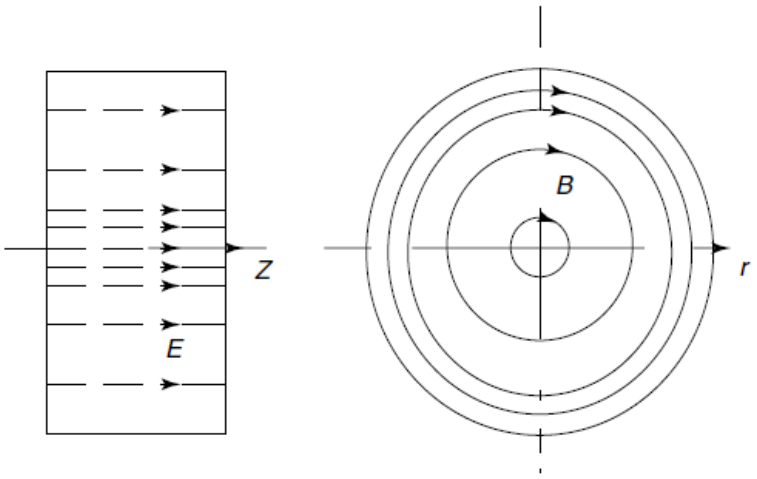

Fig. 2.1 Electric (**E**) and magnetic (**B**) fields for the transverse-magnetic resonant TM_{010} mode in a cylindrical cavity [77].

Figure 2.1 shows the transverse-magnetic resonant mode (TM_{010}) inside of a cylindrical 'pillbox' cavity. The subscripts in TM_{mnp} and TE_{mnp} indicate different mode patterns. In a rectangular cavity, m and n indicate the number of horizontal periods and vertical periods respectively, and p is the number of longitudinal periods in the direction of propagation. In a cylindrical cavity, m is the number of full period variations of that field component in θ. n is the number of zeros of the axial field component in the radial direction in the range $0<r\leq r_c$ where r_c

is the cavity radius and excluding $r = 0$. p once again indicates the number of longitudinal periods in the direction of propagation. The analytical solution for the field components of the TM mode inside a pillbox cavity is given in terms of Bessel functions

$$E_z = E_0 J_m(k_{mn} r)\cos(m\theta)\cos\frac{p\pi z}{l}e^{j\omega t} \tag{2.3a}$$

$$E_r = -\frac{p\pi}{l}\frac{a}{x_{mn}}E_0 J'_m(k_{mn} r)\cos(m\theta)\sin\frac{p\pi z}{l}e^{j\omega t} \tag{2.3b}$$

$$E_\theta = -\frac{p\pi}{l}\frac{ma^2}{x_{mn}^2 r}E_0 J_m(k_{mn} r)\sin(m\theta)\sin\frac{p\pi z}{l}e^{j\omega t} \tag{2.3c}$$

$$B_z = 0 \tag{2.3d}$$

$$B_r = -j\omega\frac{ma^2}{x_{mn}^2 r c^2}E_0 J_m(K_{mn} r)\sin(m\theta)\cos\frac{p\pi z}{l}e^{j\omega t} \tag{2.3e}$$

$$B_\theta = -j\omega\frac{a}{x_{mn} c^2}E_0 J'_m(K_{mn} r)\cos(m\theta)\cos\frac{p\pi z}{l}e^{j\omega t} \tag{2.3f}$$

where E_0 is the electric field on the z-axis which is always the direction of propagation in this work, and l is the length of a one cell pillbox cavity.

The TM_{010} mode is effective in particle acceleration because the particle beam travels along the z-axis in the same direction as the electric field; it should also travel at the correct velocity to ensure the particle only sees the accelerating part of the wave, as is shown in Figure 2.2. If the bunch were to arrive at the wrong phase (ϕ), and see the decelerating part of the wave, it is not accelerated. When synchronising the RF fields and the beam in time, we define a virtual particle called the synchronous particle (ϑ_s). Particles in the bunch that are faster or slower than ϑ_s will see a different accelerating force.

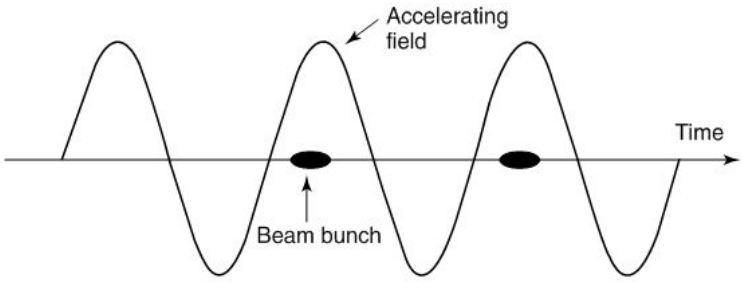

Fig. 2.2 Beam bunches in the positive phase of an RF voltage [77].

2.1.1 Energy gain in an RF gap

In RF cavities the bunch is shielded from the negative phase of the RF voltage in drift tubes. The energy gain occurs in the 'gap' g between the drift tubes,

containing the positive phase. A particle with charge q and velocity v, traversing the gap along the z-axis in Figure 2.3 will experience electric field

$$E_z(r=0,z,t) = E(0,z)\cos[wt(z)+\phi] \tag{2.4}$$

where

$$t(z) = \int_0^z dz v(z)$$

is the time the particle is at position z, and at $t=0$ the phase of the field relative to the crest is ϕ. The energy gain of the particle travelling through the gap is

$$\Delta E = q\int_{-l/2}^{l/2} E(0,z)cos(\omega t(z)+\phi)dz \tag{2.5}$$

This can also be expressed as $\Delta E = qV_0T\cdot cos(\phi)$, where V_0 is the axial voltage across the cavity

$$V_0 = \int_{-l/2}^{l/2} E(0,z)dz \tag{2.6}$$

and T is the *Transit time factor*. The accelerating voltage V_c=V_0T.

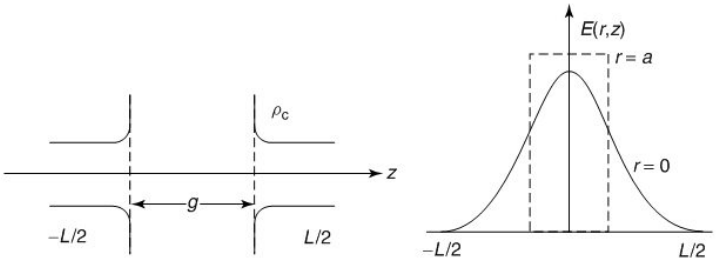

Fig. 2.3 An RF cavity gap geometry and field distribution where L is the cavity length and g is the gap length [77].

2.1.2 Transit Time Factor

The maximum energy gain of a particle traversing an RF gap is

$$\Delta E = eV = e\left|\int_{-l/2}^{l/2} E_z(z,t)e^{i\omega z/c}dz\right| = E_0L_{cav}T \tag{2.7}$$

where T is the transit time factor

$$T = \frac{\left|\int_{-l/2}^{l/2} E_z(z,t)e^{i\omega z/c}dz\right|}{\left|\int_{-l/2}^{l/2} E_z(z,t)dz\right|} = \frac{\sin\left(\pi g/\beta\lambda\right)}{\pi g/\beta\lambda}. \tag{2.8}$$

This factor accounts for the fact that the field is varying with time as the particles traverses it and this has an effect on the total energy gain. Figure 2.4 shows the variation of T with the length of the gap. The length of the gap is shown with respect to the distance the particle travels in one RF wavelength $\beta\lambda$. Where β is the relativistic velocity of the particle

$$\beta = \frac{v}{c} = \sqrt{1 - \frac{1}{\left(1 + \frac{E}{E_r}\right)^2}} \tag{2.9}$$

and λ is the free space wavelength of the RF. In Equation 2.9 E_r is the rest energy of the particle in question. The efficiency of acceleration can be greatly improved by properly optimising the gap length to the distance the particle travels in an RF wavelength.

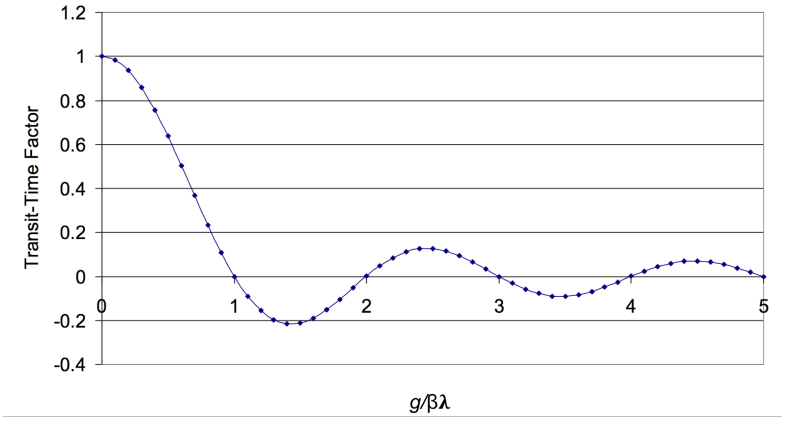

Fig. 2.4 The transit time factor vs the ratio of the length of the gap g to the distance a particle travels in one RF wavelength $\beta\lambda$ [78].

2.2 Introduction to Beam Dynamics

In the previous section the concept of the synchronous particle ϑ_s was introduced. An RF cavity is typically designed around this synchronous particle which is surrounded by all of the other particles in that bunch. Particles in a bunch will naturally disperse from one another so restorative forces are introduced to keep them in close proximity to the synchronous particle. By doing so, one can ensure the particles stay on track thus maximising the output transmission of the linac, for any given application. The study and control of particle trajectories is called beam dynamics, and it must be considered throughout the design of RF cavities to inform design choices such as the cavity length, the number of cavities, and the aperture radius. Particle beams are considered in 6D phase space, where each particle has a

position (x) relative to some point of reference (ϑ_s), and a direction (x') in three planes (x, x', y, y', z, z'). The beam's intended direction of motion is usually defined as the z-direction and a particle's distance from ϑ_s depends on the difference in velocity between it and ϑ_s. Longitudinal beam dynamics is concerned with the variation of particle energies within a bunch, and how the resulting velocity will affect it's energy gain in the next RF cycle. Particles in the bunch may deviate from the synchronous particle perpendicularly to the z-direction in x, and y. Transverse beam dynamics is concerned with this transverse motion, and restorative forces can be applied to focus the beam throughout the course of the linac. This minimises the particles that may be lost on the cavity irises. A basic introduction to both longitudinal and transverse beam dynamics is given in the following sections.

2.2.1 Longitudinal Beam Dynamics

An RF cavity is designed such that the synchronous particle ϑ_s is synchronised to the accelerating field at the synchronous phase ϕ_s. In an electron linac β swiftly reaches 1 within the first one or two RF cycles. After that the particles should see the same phase of the accelerating field in every gap assuming nothing reduces their velocity in the meantime. In lower-β structures there is a wider range of velocities throughout the linac, and longitudinal focussing is employed to ensure the particles have a stable trajectory and the linac has an acceptable output intensity.

In the following section the synchronous particle ϑ_s is referred to as M_1 to be consistent with Figure 2.5. Particles in the bunch with a different velocity to the synchronous particle will arrive in the accelerating gap at a different phase and thus see a different accelerating voltage. For example, synchronous particle M_1 can be seen in Figure 2.5 alongside a particle P with faster velocity, and particle P' with slower velocity. Particle P enters the accelerating gap before the synchronous particle M_1 thus will see a smaller accelerating voltage and will be accelerated less than M_1. The synchronous particle having seen a higher accelerating voltage will then overtake P becoming the faster particle. The two will continue to oscillate around one another remaining in a stable bunch.The same is true for the slower particle P'. It will enter the gap after the synchronous particle and will consequently see a larger accelerating voltage overtake M_1 and become the fast particle in the next gap. These two particles are stable in the bunch despite having different velocities to the synchronous particle because they are on the rising edge of the sinusoidal accelerating voltage. Particles Q and Q' on the other hand are on the falling edge of the wave. Fast particle Q will arrive at the accelerating gap before particle N_1, and will receive a larger accelerating voltage consequently being accelerated further from synchronous particle N_1. Likewise, slow particle Q' will arrive at the accelerating gap after particle N_1 and will see a smaller accelerating voltage, further increasing the gap between it and the synchronous particle. The

two particles Q and Q' are unstable because they continue to get pushed further from the synchronous particle at every accelerating gap. Particles M_1, N_1, M_2, and N_2 will all see the same phase of the accelerating voltage throughout the linac, thus receiving the same acceleration in every gap.

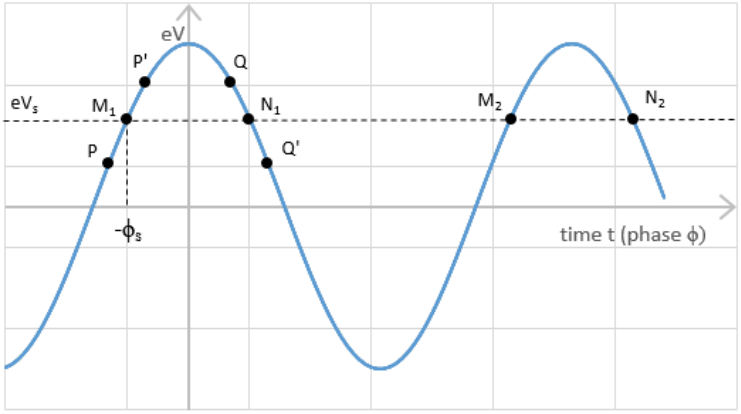

Fig. 2.5 Graphical representation of the phase stability principle whereby the synchronous phase can keep a particle stable in the bunch.

The equation that describes the change in phase ϕ and energy E with respect to the phase ϕ_s and energy E_s of the synchronous particle assuming small continuous acceleration is

$$A\frac{w^2}{2} + B(\sin\phi - \phi\cos\phi_s) = H_\phi \tag{2.10}$$

where

$$A = \frac{2\pi}{\beta_s^3\gamma_s^3\lambda} \tag{2.11}$$

$$w = \frac{E - E_s}{m_0c^2} \tag{2.12}$$

$$B = \frac{qE_0T}{m_0c^2} \tag{2.13}$$

The first term on the left hand side of Equation 2.10 is a kinetic energy term, the second term in a potential energy term V_ϕ, and H_ϕ is a constant of integration that can be identified as the Hamiltonian of the system [77]. There is acceleration for $-\pi/2 \leq \phi_s \leq \pi/2$ and there is both acceleration and a potential well when $-\pi/2 \leq \phi_s/ \leq 0$.The stable phases lie between $\phi_2 < \phi < -\phi_s$ (Figure 2.6) where ϕ_2 is the lower stable phase limit and can be calculated by solving $H_\phi(\phi_2) = H_\phi(-\phi_s)$.

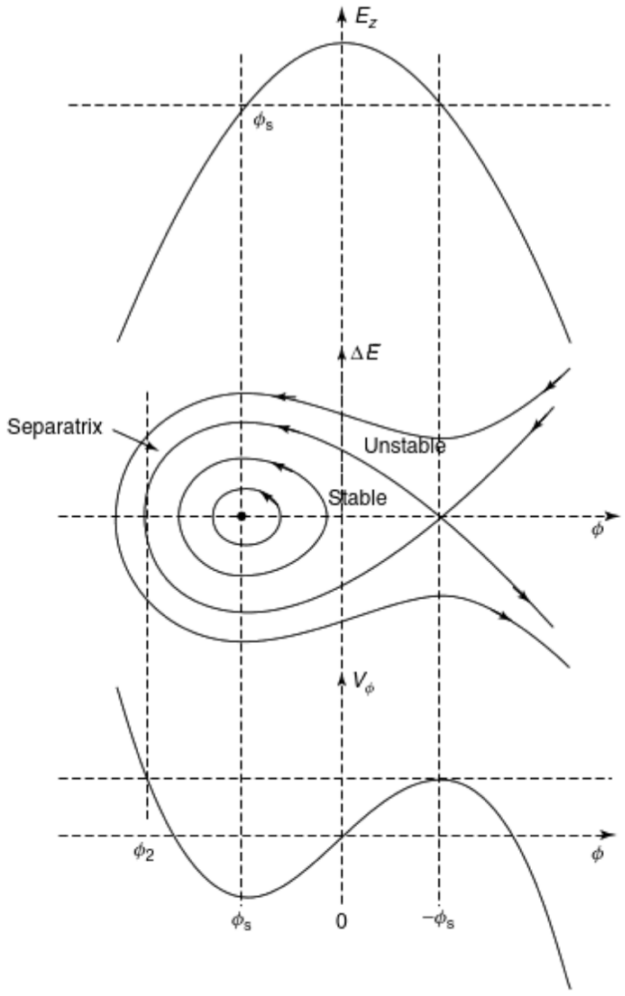

Fig. 2.6 Accelerating field (E_z) as a cosine function of the phase (ϕ)(top). Energy gain (ΔE) as a function of phase for some longitudinal phase space trajectories including the separatrix (centre). The potential energy (V_ϕ) as a function of phase (bottom) [77].

The separatrix defines the area within which particle trajectories are stable and is given by

$$A\frac{w^2}{2} + B(\sin\phi - \phi\cos\phi_s) = -B(\sin\phi_s - \phi_s\cos\phi_s) \tag{2.14}$$

The separatrix shown in Figure 2.6 is defined assuming β_s and γ_s are constant, and is a 'fish' shape. The stable area within it is referred to as the stable 'bucket'. Maximum energy gain happens when $\phi = \phi_s$ and can be calculated as

$$w_{max} = \sqrt{\frac{2qE_0T\gamma_s^3\beta_s^3\lambda}{\pi m_0c^2}}(\phi_s\cos\phi_s - \sin\phi_s) \tag{2.15}$$

and the total width of the stable bucket (Ψ) can be estimated as

$$\Psi = |\phi_s| + |\phi_2| \approx 3 \cdot |\phi_s| \tag{2.16}$$

and is a good approximation up to $\|\phi_s\| \approx 1$. The derivation for Equation 2.16 can be found in [77].

When one takes into account the larger acceleration in a linac cavity the separatrix looks more like a 'golf club' shown in Figure 2.7.

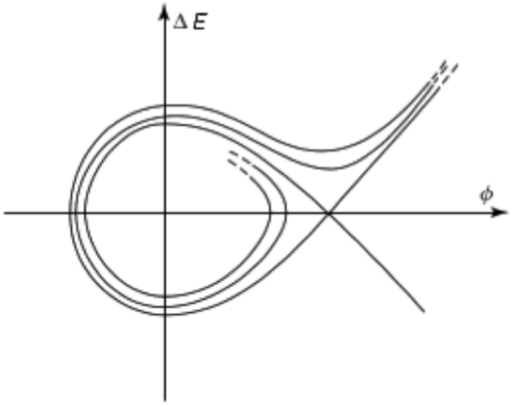

Fig. 2.7 Longitudinal phase space trajectories when acceleration is considered. This separatrix is called a 'golf club' [77].

2.2.2 Transverse Beam Dynamics

When off-axis particles pass through an accelerating gap they experience radial electric and magnetic forces, in addition to the longitudinal electric field by which they are accelerated. This is due to the fact that the electric field is not completely parallel to the axis throughout the length of the cavity. The irises perturb the field and introduce radial forces. Synchronising the synchronous particle with the rising edge of the electric field was shown in the previous section to give longitudinal focussing, but it means the particles see a higher field in the second half of the gap. Rather than the radial forces in and out of the gap cancelling each other out, it results in a net defocussing force. This is especially prominent for lower energy ion linacs. To compensate for this defocussing and to ensure desirable beam parameters at the output, quadrupoles are employed between cavities to focus and defocus the beam.

The beam size through the linac can be described in terms of the displacement of the protons within it. This can be visualised in Figure 2.8 which shows a particle's trajectory through a drift space. The centre beam axis line is drawn, and the distance of the particle from that centre axis upon entrance to the drift space is labelled x_0. The angle of the particle's initial trajectory is labelled x_0' and represents the particle's divergence from its design trajectory.

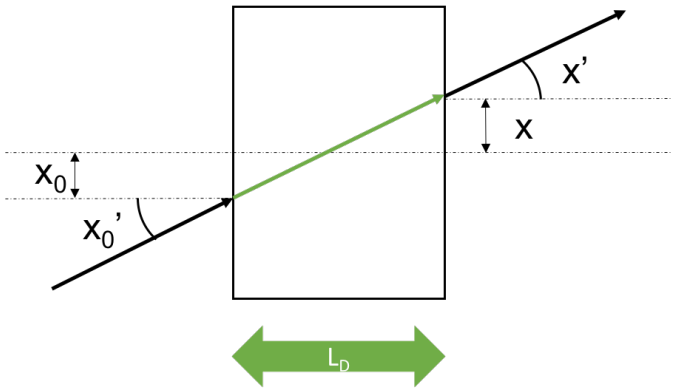

Fig. 2.8 A particle's trajectory through a drift space of length L_D the definitions of x and x' are shown.

The trajectory exiting the drift space is labelled x and x', one can relate the initial parameters x_0 and x_0' to the exit parameters x and x' through a 2×2 *transfer matrix* as

$$\begin{bmatrix} x \\ x' \end{bmatrix} = \begin{bmatrix} a & b \\ c & d \end{bmatrix} \cdot \begin{bmatrix} x_0 \\ x_0' \end{bmatrix} \tag{2.17}$$

where

$$M_O = \begin{bmatrix} a & b \\ c & d \end{bmatrix} = \begin{bmatrix} 1 & L_D \\ 0 & 1 \end{bmatrix} \tag{2.18}$$

is the transfer matrix of the drift length L_D. Each element in an accelerator can be represented as a transfer matrix and one can map the trajectory of the particles by multiplying the transfer matrices of each element together in the correct order. The Twiss transfer matrix for a periodic lattice is

$$M_T \begin{bmatrix} \cos\mu + \alpha_T \sin\mu & \beta_T \sin\mu \\ -\gamma_T \sin\mu & \cos\mu - \alpha_T \sin\mu \end{bmatrix} \tag{2.19}$$

where β_T is the betatron amplitude function relating to the *size* and *shape* of the beam, α_T relates to the beam tilt or the divergence as

$$\alpha_T(s) = -\frac{1}{2}\frac{d\beta_T}{ds} \tag{2.20}$$

where s is defined at the direction of beam propagation, and γ_T is dependent on α_T and β_T as

$$\gamma_T(s) = \frac{1+\alpha_T^2}{\beta_T} \tag{2.21}$$

and finally μ is the phase advance of the betatron oscillation defined as

$$\mu = \int_0^s \frac{1}{\beta_T(s)} ds. \tag{2.22}$$

Equating the machine transfer matrix M and the Twiss transfer matrix M_T links the accelerator parameters with the beam properties.

With linear focussing, the trajectory of each particle lies on an ellipse in phase space. Figure 2.9 shows a beam ellipse in unnormalised phase space, where the x and y-axis are x and x' respectively. Each two dimensional projection of a beam in phase space has an *emittance* ε which is proportional to the area of the ellipse

$$\gamma_T x^2 + 2\alpha_T x x' + \beta_T x'^2 = \varepsilon \tag{2.23}$$

where $\gamma_T \beta_T - \alpha_T^2 = 1$, and the area of an ellipse is $\pi\varepsilon$. The beam distribution in phase space does not generally have a well defined boundary however, so it becomes necessary to define an rms emittance ε_r

$$\gamma_{Tr} x^2 + 2\alpha_{Tr} x x' + \beta_{Tr} x'^2 = \varepsilon_r \tag{2.24}$$

where $\gamma_{Tr}\beta_{Tr} - \alpha_{Tr}^2 = 1$.

Figure 2.9 shows the unnormalised phase space ellipse in the x-direction (although it is also valid for y and z) in terms of the Courant-Snyder (or Twiss) parameters.

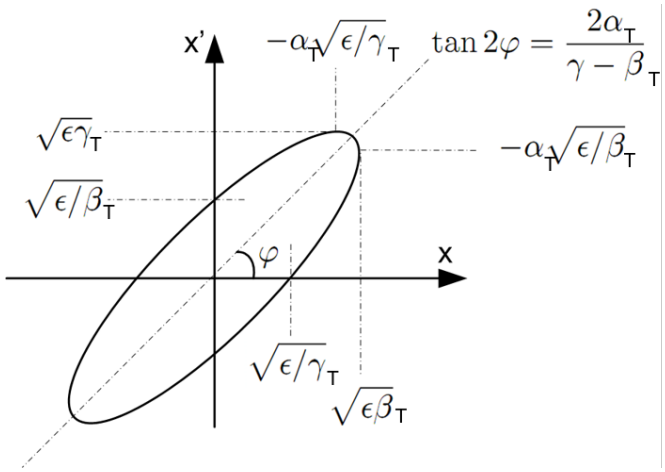

Fig. 2.9 The phase space ellipse in terms of Courant-Snyder or 'Twiss' parameters - adapted from [79].

Quadrupole magnets are used to focus the beam between cavities. A focussing quadrupole focusses the beam in the horizontal plane and a defocussing quadrupole focusses in the vertical plane. A popular arrangement is to have a focussing quadrupole (F) followed by a drift (O) followed by a defocussing quadrupole (D), followed by a drift which in reality focusses the beam in both planes. This is called

a FODO arrangement and cavities can be placed in the drift spaces between the magnets like in Figure 5.4.

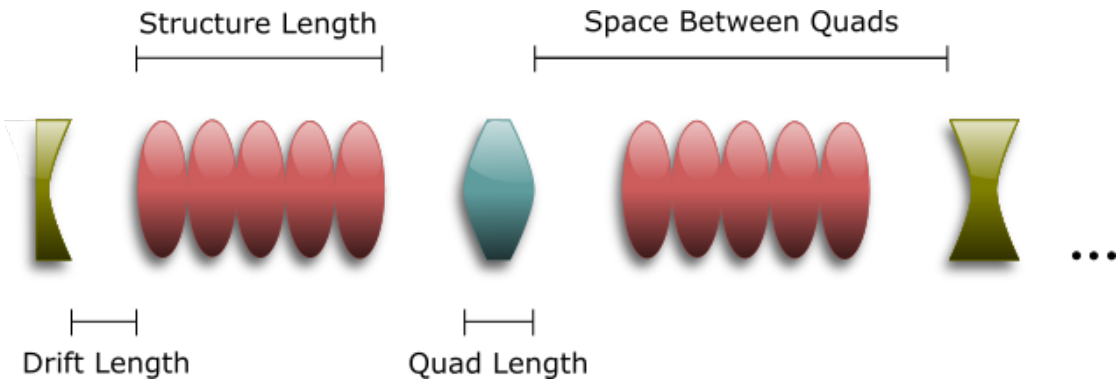

Fig. 2.10 Typical FODO arrangement with focussing quadrupoles (blue) defocussing quadrupoles (green) and RF cavities (red) in the drift spaces between.

The transfer matrix for a focussing quadrupole is

$$M_F = \begin{bmatrix} \cos\sqrt{K}l_q & \frac{\sin(\sqrt{K}l_q)}{\sqrt{K}} \\ -\sqrt{K}\sin(\sqrt{K}l_q) & cos\sqrt{K}l_q \end{bmatrix} \tag{2.25}$$

where l_q is the length of the quadrupole and K is the K-strength of the quadrupole given by

$$K = \frac{e}{pc}\frac{\partial B}{\partial r} = \frac{ec}{\beta_r E}\frac{\partial B}{\partial r} \tag{2.26}$$

and similarly the transfer matrix for a defocussing quadrupole is

$$M_D = \begin{bmatrix} \cos\sqrt{K}l_q & \frac{\sin(\sqrt{K}l_q)}{\sqrt{K}} \\ \sqrt{K}\sin(\sqrt{K}l_q) & cos\sqrt{K}l_q \end{bmatrix} \tag{2.27}$$

These transfer matrices can be significantly simplified by employing the thin lens approximation. In order for the thin lens approximation to be valid $\sqrt{K}l_q << 1$. The transfer matrices for focussing and defocussing quadrupoles become

$$\begin{aligned} M_F &= \begin{bmatrix} 1 & 0 \\ -Kl_q & 1 \end{bmatrix} \\ M_D &= \begin{bmatrix} 1 & 0 \\ Kl_q & 1 \end{bmatrix} \end{aligned} \tag{2.28}$$

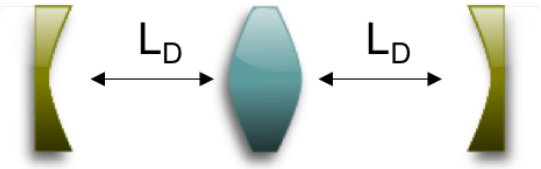

Fig. 2.11 Typical FODO arrangement with focussing quadrupoles (blue) defocussing quadrupoles (green) and drift spacesL_D between.

The FODO cell begins at the centre of the first defocusing quadrupole and ends in the centre of the next focusing quadrupole. At the centre of the quadrupole α_T= 0 and all α_T terms in M_T from Equation 2.19 cancel which simplifies the calculation. Using the thin lens approximation for the quadrupoles, the transfer matrix for periodic FODO cells like in 2.11 can be determined as

$$\begin{aligned} M_{FODO} &= M_D \cdot M \cdot M_F \cdot M_F \cdot M \cdot M_D \\ &= \begin{bmatrix} 1 & 0 \\ \frac{Kl_q}{2} & 1 \end{bmatrix} \begin{bmatrix} 1 & L_D \\ 0 & 1 \end{bmatrix} \begin{bmatrix} 1 & 0 \\ -\frac{Kl_q}{2} & 1 \end{bmatrix} \begin{bmatrix} 1 & 0 \\ -\frac{Kl_q}{2} & 1 \end{bmatrix} \begin{bmatrix} 1 & L_D \\ 0 & 1 \end{bmatrix} \begin{bmatrix} 1 & 0 \\ \frac{Kl_q}{2} & 1 \end{bmatrix} \\ &= \begin{bmatrix} 1 - \frac{Kl_qL_D}{2} & L_D \\ -\frac{K^2L_q^2L_D}{4} & 1 + \frac{Kl_qL_D}{2} \end{bmatrix} \\ &= \begin{bmatrix} 1 - \frac{K^2l_q^2L_D^2}{2} & 2L_D(1 - \frac{Kl_qL_D}{2}) \\ -\frac{K^2L_q^2L_D}{2}(1 + \frac{Kl_qL_D}{2}) & 1 - \frac{K^2l_q^2L_D^2}{2} \end{bmatrix} \end{aligned} \tag{2.29}$$

Equating the Twiss matrix for a periodic lattice M_T from equation 2.19 with $\alpha_T = 0$, with the transfer matrix in equation 2.29 we get

$$\begin{bmatrix} \cos\mu & \beta_T \sin\mu \\ -\frac{\sin\mu}{\beta_T} & \cos\mu \end{bmatrix} = \begin{bmatrix} 1 - \frac{K^2l_q^2L_D^2}{2} & 2L_D(1 - \frac{Kl_qL_D}{2}) \\ -\frac{K^2l_q^2L_D}{2}(1 + \frac{Kl_qL_D}{2}) & 1 - \frac{K^2l_q^2L_D^2}{2} \end{bmatrix} \tag{2.30}$$

equating elements M_{11} from both matrices it follows that,

$$\begin{aligned} \cos\mu = 1 - 2\sin^2\frac{\mu}{2} &= 1 - \frac{K^2l_q^2L_D^2}{2} \\ \sin\frac{\mu}{2} &= \frac{Kl_qL_D}{2} \\ \frac{2\sin\frac{\mu}{2}}{l_qL_D} &= K \end{aligned} \tag{2.31}$$

and

$$\beta_T^2 = \frac{4}{K^2 l_q^2}\left(\frac{1 \pm \frac{K l_q L_D}{2}}{1 \mp \frac{K l_q L_D}{2}}\right) \tag{2.32}$$

The β-function, β_T, is intricately linked to the size of the beam as

$$\sigma = \sqrt{\varepsilon\beta} \tag{2.33}$$

where σ is the beam size and ε is the geometric emittance. The geometric emittance is not Lorentz invariant, and its used for calculating beam size and angular spread. The normalised emittance ε_n

$$\varepsilon_n = \varepsilon_g \beta\gamma \tag{2.34}$$

where β and γ are they relativistic parameters as ε_n is Lorentz invariant.

2.3 RF Breakdown

RF breakdown refers to the occurrence of vacuum arcs in the presence of intense electromagnetic fields. In any high voltage system a failure can occur whereby a high potential difference can result in a conductive path between two points *even if* the material between those two points would not usually conduct. RF breakdown can also be localised it does not necessarily have to occur between two points. High gradient (HG) structures are usually operated under Ultra-High Vacuum (UHV) which minimises the chance of a conductive path between the walls of the structure becoming available. However, in the presence of surface electric fields of hundreds of MV/m which is the case for HG structures, a surge of current can be emitted from the walls resulting in localised heating. The heat can cause neutral evaporation which then forms a plasma resulting in a spike in the vacuum pressure. This occurrence is the main limiting factor on the HG performance of RF linear accelerators.

The undesirable phenomena of plasmas interacting with the incident power inside a resonant cavity can compromise the operation of the accelerator by reflecting the incoming power and introducing non-linearities into the system. Consequently beam kicks can be introduced interfering with the trajectory of the beam, these can be severe enough to lose the beam completely. Furthermore each electric discharge on the surface of a cavity causes surface damage from ion bombardment. Repeated surface damage can detune the structure by deforming the cell wall so severely that it is no longer on resonance, compromising the quality of cell to cell coupling. Surface damage can also encourage further RF breakdowns and cause clusters of breakdowns which may cause damage that can not be recovered through further conditioning. When designing HG structures it is best to minimise breakdown or

try to avoid it completely. This is not trivial as there is no comprehensive model of RF breakdown, and many theories exist to explain it, and predict when it will occur. *The Breakdown Rate*

$$\text{BDR[bpp/m]} = \frac{N_{bd}}{N_p L_{cav}} \tag{2.35}$$

quantifies the number of arcs (N_{bd}) observed during the operation of the cavity and is a valuable figure of merit in HG accelerator design. It is typically given in breakdowns per pulse per meter; as can be seen in Equation (2.35) where N_p is the number of RF pulses sent to the structure during operation, and L_{cav} is the length of the structure in metres.

2.3.1 Field Emission

Surface field emitters are a critical part of the breakdown mechanism. High surface electric fields on the walls of RF cavities modify the potential barrier that prevents free electrons escaping the metal.

Usually conduction electrons existing at the Fermi level (E_F) shown graphically in Figure 2.12, would need to overcome the work function (ϕ_{WF}) of the metal atoms to overcome the potential barrier (Vacuum Level) and leave the metal surface. When an external electric field is applied, it is superimposed with the image potential and the barrier then has a finite width at the Fermi level. The conduction electrons are able to traverse this barrier by quantum tunnelling [80].

The relationship between the applied electric field and the field emitted electron current is described by the Fowler-Nordheim expression

$$\frac{d(log_{10} I_{FN}[\text{A}]/(E_s[\text{V/m}])^2)}{d(1/E_s[\text{V/m}])} = \frac{2.84 \times 10^9 (\phi_{WF}[eV])^{1.5}}{\beta_{FE}} \tag{2.36}$$

where I_{FN} is the field-emission current, E_{peak} is the peak surface electric field, ϕ_{WF} is the work function of the material, and β_{FE} is the field enhancement factor.

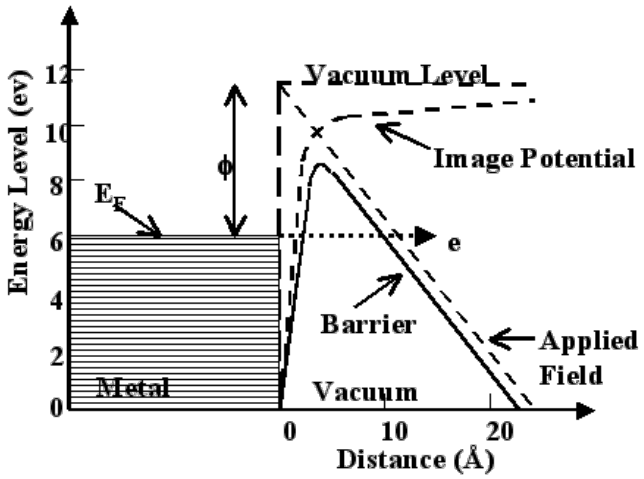

Fig. 2.12 Effective potential barrier seen by the conducting electrons in bulk metal. An applied electric field interacts with the image potential giving the barrier finite width at the Fermi level, and allows electrons to quantum tunnel out of the surface. ϕ in this figure refers to ϕ_{WF} [81].

The field enhancement factor (β_{FE}) is related to the surface quality of the cavity. Tiny scratches and imperfections from the cavity manufacturing process mean small tips remain on the cavity surface, in the presence of an external electric field these become field 'emitters'. They see a much larger electric field than the average surface electric field as can be seen in Figure 2.13, $E_{local} = \beta_{FE} E_0$ because the field is concentrated around the sharp tips. These high fields invoke the field-emission mechanism and the tiny emitters emit dark current which is believed to trigger the breakdown mechanism.

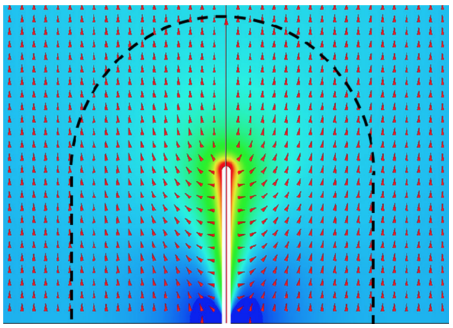

Fig. 2.13 The electric field distribution on a logarithmic scale around a cylindrical emitter [82].

Various cavity manufacturing processes can leave traces and small features that can become field emitters. Naturally emitters can have multiple different geometries, some are shown in Figure 2.14 with their corresponding field enhancement factor.

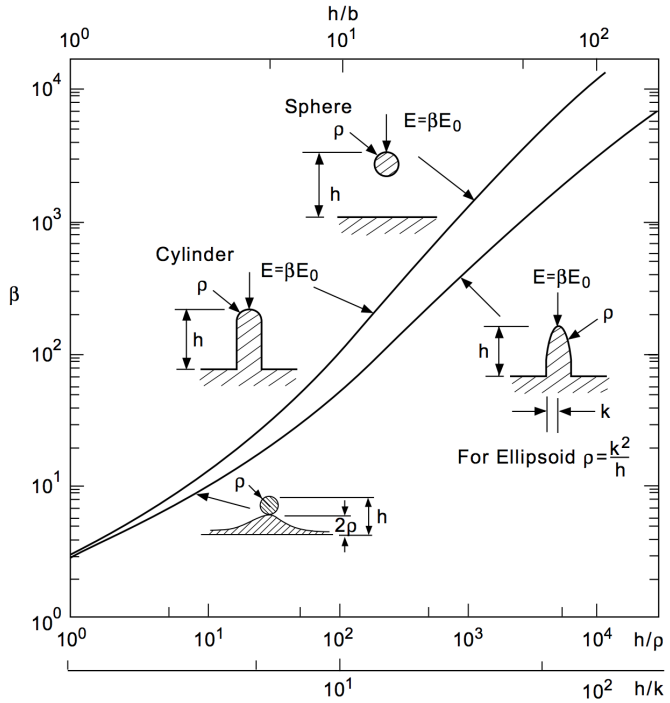

Fig. 2.14 Field enhancement factor β_{FE} for various possible emitter geometries where h is height, ρ is the tip rounding and k is the width [83].

2.3.2 The Defect Model

Surface imperfections can lead to local field enhancement and the formation of field electron emitters. The advances made in surface manufacturing have reduced the number of surface imperfections, not only do we still observe breakdown despite that, but *new* surface imperfections have been observed *after* the application of high fields. It is thought these new imperfections come from existing defects in the crystalline structure of the cavity, as high fields exert tensile stress on the cavity surface and generate new defects. The *stress model* suggests that *any* defect mechanism can trigger RF breakdown, and thus the breakdown rate will be proportional to the number of defects in the crystalline structure of the cavity, not just the size of the surface imperfection. The breakdown rate according to this model is

$$\mathrm{BDR[bpp/m]} \propto e^{\frac{\varepsilon_0 \Delta V}{kT}(E_{max}[\mathrm{MV/m}])^2} \tag{2.37}$$

where ε_0 is the permittivity of free space, ΔV is the defect volume, and k_B is Boltzmann's constant [84]. The model shows good agreement with the BDR dependence on electric field as is shown in Figure 2.15. It does however predict a non-zero BDR at zero field which is not physical, unlike the power law model also shown in Figure 2.15. The power law model is based on experimental data collected from several HG tests of RF cavities of 12 and 30 GHz [82]. It is not based on a theoretical framework like the defect model, but is simply a power fit to the data

$$\mathrm{BDR[bpp/m]} \propto E_{acc}^{30}\mathrm{[MV/m]} \tag{2.38}$$

There is also a BDR dependence on the RF pulse length, as longer pulses present a higher probability of triggering a breakdown

$$\mathrm{BDR[bpp/m]} \propto t_p^5\mathrm{[ns]} \tag{2.39}$$

combining these two power laws gives the following general equation

$$\frac{\mathrm{BDR}}{E_{acc}^{30} t_p^5} = \text{constant.} \tag{2.40}$$

More recently a stochastic model has also been proposed which yields a dependence of BDR on the electric field, it differs from the defect model in that it does not require any prior surface defects which remain post-manufacture. Instead it suggests that the density of dislocations close to but beneath the surface increases under the application of an electric field. At any point in time there is the probability for this population to reach a critical point after which it increases deterministically until a protrusion is formed and arc nucleation occurs. The theoretical fit resulting from this model is shown in Figure 2.16 [85].

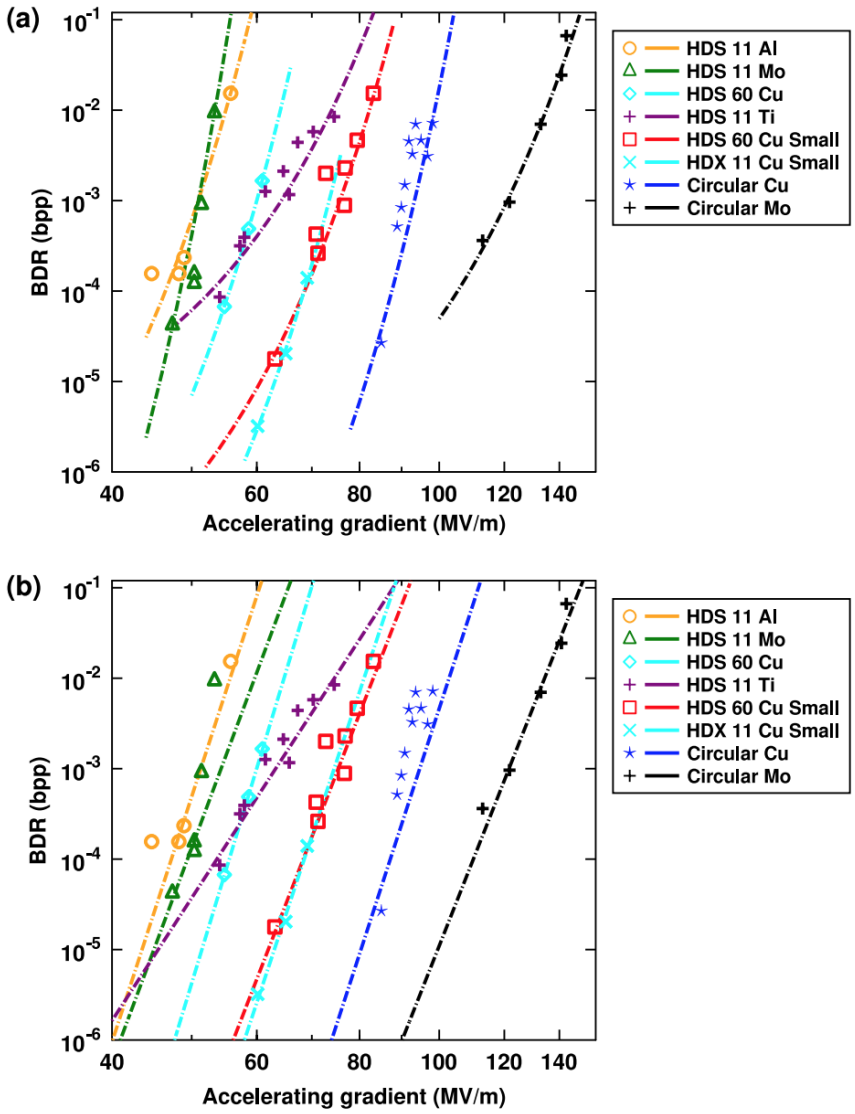

Fig. 2.15 a)Measured BDR versus the accelerating gradient for a selection of HG RF accelerating structures and the defect model fit. b)Fits of power law to the same data [84].

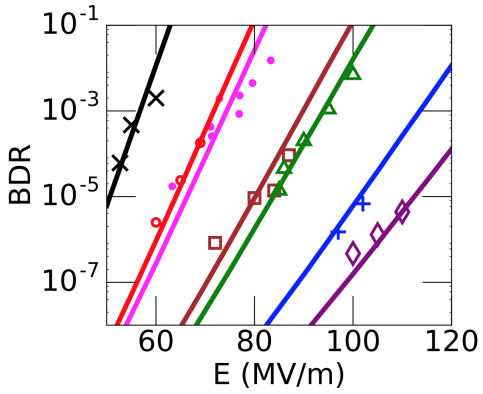

Fig. 2.16 BDR dependence on electric field fitted with theoretical lines based on a stochastic model of breakdown nucleation [85].

2.3.3 The Breakdown Mechanism

Field emission from enhanced electric fields on small protrusions on the cavity wall is widely believed to initiate breakdown. A complete and quantitative description of the vacuum arcing mechanism that follows still eludes researchers, but tests and simulations have provided some insight to this phenomenon. Figure 2.17 illustrates the different stages of a vacuum arc which can be roughly split up into three stages: the onset phase, the burning phase, and the cratering phase.

The Onset Phase

Figure 2.17 a) shows the first nano second of the breakdown mechanism. A small sharp protrusion is shown in the presence of an electric field. Due to field enhancement (see Section 2.3.1) the tip of this protrusion could have electric fields as high as GV/m and as a result emits a significant electron current. This current heats the tip while the electric field is applied, and evaporation of neutral atoms into the vacuum starts.

Figure 2.17 b) shows the evaporated neutrals colliding with the emitted electron current and subsequently being ionised. The ions quickly form an ionised gas above the emitter tip resulting in a sheath potential above the field emitter [86], this further enhances the field on the tip and is followed by the burning phase.

The Burning Phase

The electric field also applies a tensile stress to the surface atoms (see Section 2.3.2) which deforms the tip further as is shown in greater detail in Figure 2.18. Once the tip reaches melting point the top atoms become mobile and the electric field pulls them upwards, further elongating the tip and enhancing the field. The enhanced field results in more field emission and higher temperatures, creating a positive feedback loop eventually resulting in *thermal runaway* [87]. The tip gets thinner and hotter in the electric field and eventually the upper part becomes detached. The detached nano-cluster is charged due to partially charged atoms on the surface, and can be accelerated away by the electric field. Once removed it is believed the process repeats itself until the tip becomes blunt and cools down.

Alternatively the evaporated tip could bombard the surface or form a plasma sheath above the emitter tip (Figure 2.17 c)). Ion bombardment of the surface around the emitter is thought to sputter further ions and neutrals into the plasma [86], however it is shown in [87] that the supply of neutral atoms from the emitter tip is enough to ignite a plasma and that no external source is needed. The expanding plasma increases the size of the surface affected by ion and cluster sputtering. Figure 2.17 d) shows the plasma causing field emission around the

initial breakdown site and ion-electron recombination inside of the plasma resulting in optical emission.

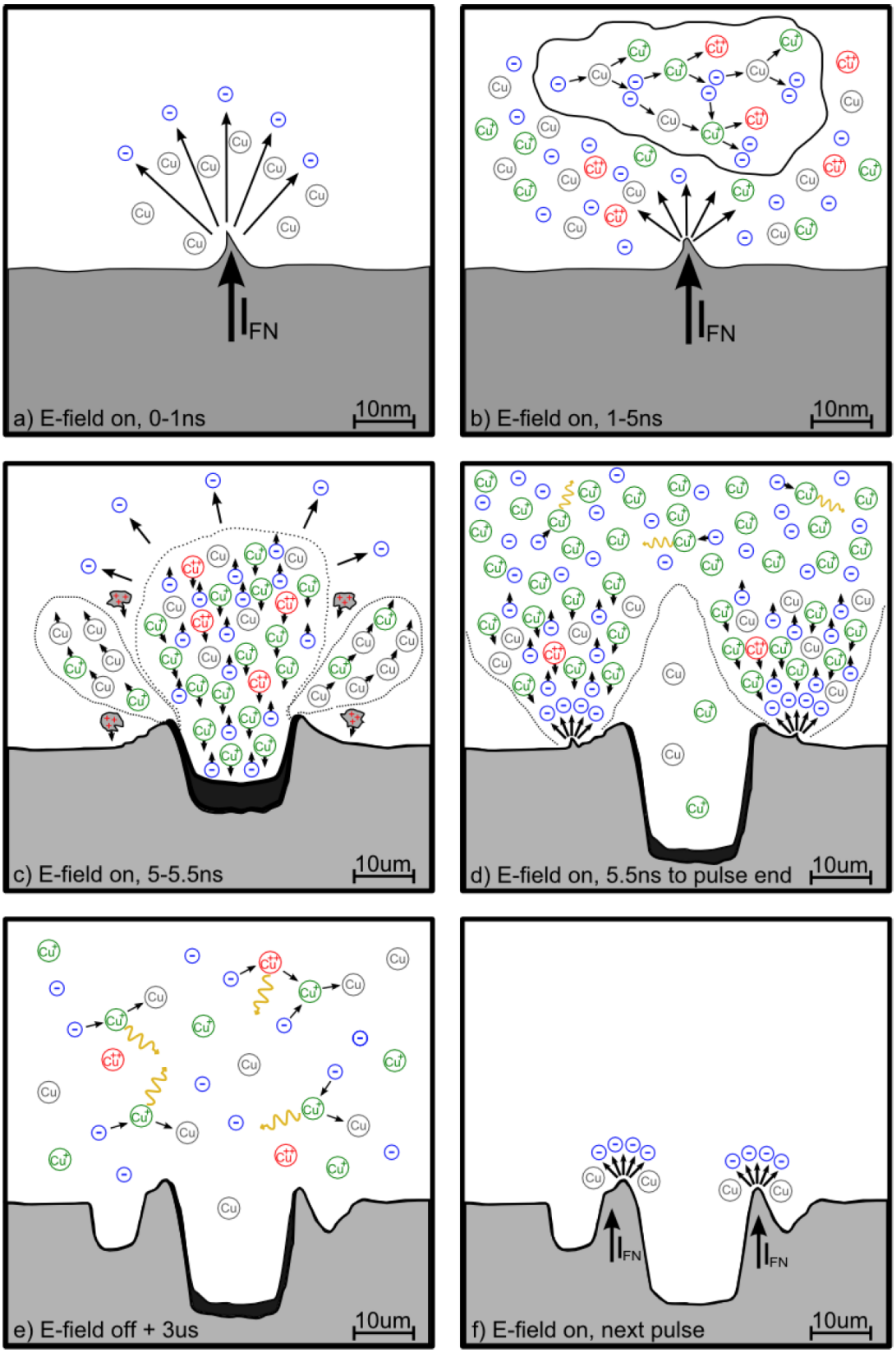

Fig. 2.17 Illustration of the different stages of RF breakdown [86].

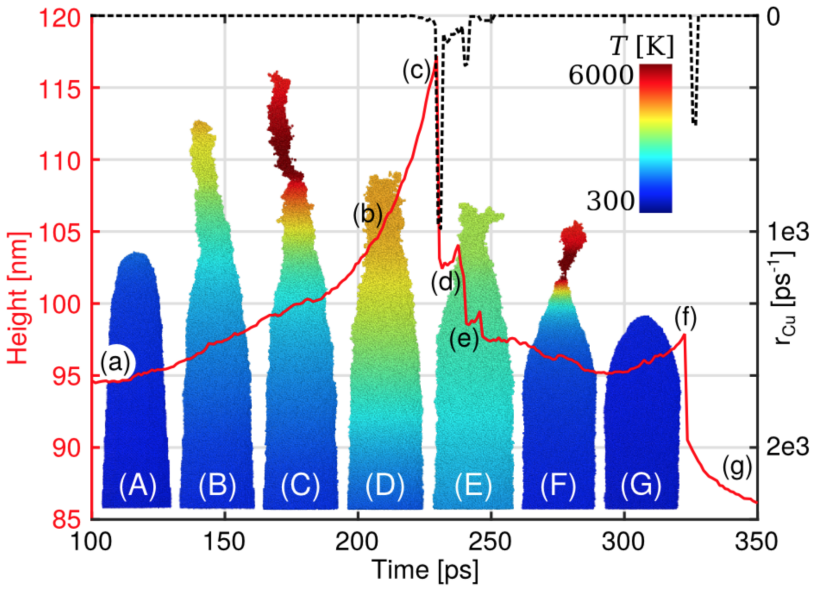

Fig. 2.18 The shape and temperature distribution (colour coding) of a nano-tip during intense electron emission. Tip height (red), and evaporation rate as a function of time (black, inverted) black lower case letters on the height graph demonstrate the time stamp of each frame [87].

The Cratering Phase

Copper ion sputtering on the surface around the emitter creates new field emitters which go on to melt and evaporate in a similar manner to the original emitter tip. Further craters and field emitters are created during this *cratering phase*. The full arc is maintained as long as there is an external power supply feeding the mechanism. Once the electric field is removed the plasma disappears via expansion cooling and by recombination of the ions (Figure 2.17 e)).

When the electric field returns in the next pulse, the surface imperfections caused by the cratering of the previous breakdown may have sufficient β_{FE} to initiate further breakdowns (Figure 2.17f)). This process is understood to continue until the remaining tips are sufficiently blunt as shown in Figure 2.18 g) or the electric field gradient is reduced.

2.3.4 Field Limitations

In order to reduce occurrences of RF breakdown the surface fields on the cavity walls are limited, these limits are largely informed by experimental data. The electric field was originally believed to be responsible for the initiation of RF breakdown through it's influence on field emission. However, the magnetic field is now also believed to play an important role in the BDR, thus it must also be limited for reliable performance.

Kilpatrick Criterion

W.D.Kilpatrick was the first person to provide a quantitative limitation to the peak surface electric field that can exist on a cavity wall without arcing. The *Kilpatrick Criterion* describes a maximum field threshold beyond which the safe operation is not guaranteed. Equation(2.41) was reformulated by T.J.Boyd [88], and was based on experimental data [89].

$$f[MHz] = 1.64(E_k[MV/m])^2 e^{-8.5/(E_k[MV/m])} \tag{2.41}$$

where f is the RF frequency and E_k is the Kilpatrick limit for the electric field. The expression shows that higher fields can be reached with higher frequencies. It does not however depend on pulse length or acknowledge that breakdown is somewhat statistical in nature and breakdowns can indeed occur in the 'safe operation' region it is just unlikely. This threshold became obsolete with advances in vacuum technology and improved surface treatments. Now the limit is used as a figure of merit, a cavity may operate at 2 or 3 times Kilpatricks.

Modified Poynting Vector

Although the Kilpatrick criterion can still be used to inform the design of high gradient cavities, a quantitative theory that can explain and predict RF breakdown is still lacking. The CLIC study at CERN collected high gradient test data with the aim of deriving the high gradient limit due to RF breakdown.

The electric field was originally believed to be solely responsible for the onset of RF breakdown, but the data collected showed a large variation in achievable surface electric field before breakdown, which prompted the idea that it was in fact the power flow rather than the electric field alone limiting high gradient operation. The *power flow model* proposed that the ratio of the input power to the iris circumference was the parameter limiting gradient in travelling wave structures and developed the scaling law [90]:

$$\frac{P_{in} \cdot t_p^{1/3}}{C} < constant \tag{2.42}$$

where P_{in} is the input power to the structure, C is the minimum circumference of the structure or the beam aperture, and t_p is the pulse length. This scaling law fit the data more closely than the peak surface electric field but still had limitations, one being that it does not account for standing wave structures which have no power flow through the beam aperture.

In 2009 a new local field quantity was proposed, the *modified* Poynting vector [82] which describes the power flow density feeding the field emission mechanism:

$$S_c = \left\| \Re\{\overline{S}\} \right\| + \frac{1}{6} \left\| \Im\{\overline{S}\} \right\| \tag{2.43}$$

The real part of the conventional Poynting vector describes the active power flow or the net flux of power that passes through a travelling wave structure. The imaginary part describes the reactive power flow or the cyclic energy transfer between the electric and magnetic field in both travelling and standing wave structures. The $^1/_6$ weighting factor was largely determined by fitting to experimental data and accounts for the phase shift between the active and reactive power flow. Figure 2.19 shows that the reactive power flow is zero when field emission is maximum whereas the active power flow maximum is in phase with the field emission. The weighting factor accounts for the reactive power flow being less efficient in feeding the field emission mechanism.

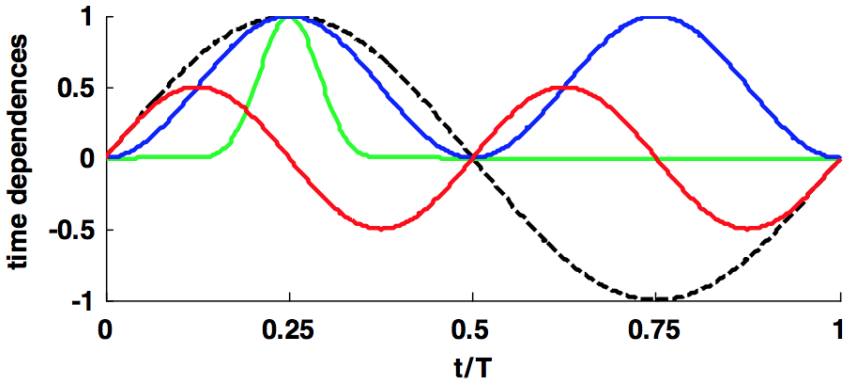

Fig. 2.19 Time dependences of electric field (dashed black line), active power flow (blue), reactive power flow (red), and field emission power flow (green) [82]

Figure 2.20 shows the square root of the scaled modified Poynting vector agrees well with the high-gradient structure data accumulated in the CLIC study. The dependence of the breakdown rate on the accelerating gradient and the pulse length was given in Equation 2.40, and the BDR also scales with S_C:

$$\mathrm{BDR} \propto S_c^{15} \cdot t^5 \tag{2.44}$$

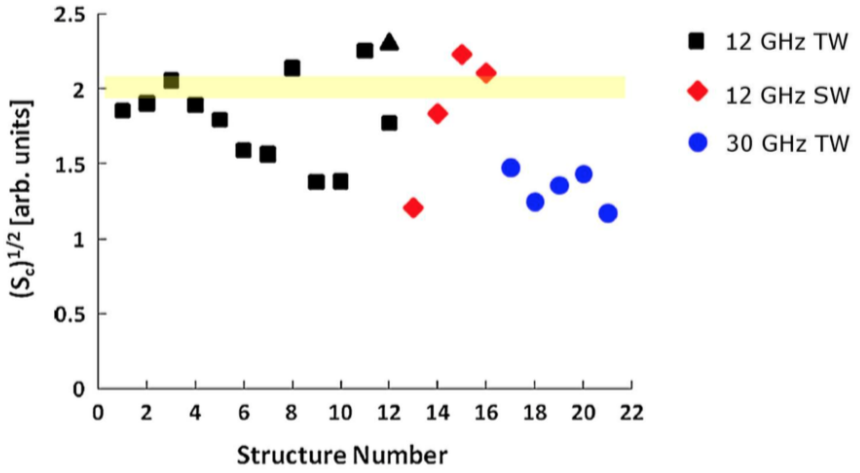

Fig. 2.20 Square root of the scaled modified Poynting vector calculated for the high-gradient performances of several 12 GHz travelling-wave structures (Black), 12 GHz standing-wave structures (Red), and 30 GHz travelling wave structures (Blue) [**?**]. Breakdown rate measurements for the 3 GHz TERA single-cell cavity are found in the yellow band [91].

Pulsed Surface Heating

In an ideal perfect conductor, the fields and currents inside the conductor are zero. As perfect conductors do not exist, RF cavities tend to be made from copper which has a room temperature resistivity of $\rho_r{=}1/\sigma_c{=}\ 1.7{\times}10^{-8}\Omega$m. Copper is a very good, but not perfect conductor so the fields and currents decay exponentially with distance from the surface, this is called the *skin effect*. When RF fields are applied at the surface of a conductor, a current is induced at the surface of the conductor, which then shields the inside of the conductor from any fields or currents. The thin layer containing non-zero fields is called the *skin depth* δ

$$\delta = \sqrt{\frac{2}{\sigma_c \mu_0 \omega}}. \tag{2.45}$$

The surface resistance of an RF structure is $R_{surf}{=}1/\sigma\delta$ this is not the same as DC due to the skin effect. Substituting Equation (2.45) into the expression for R_{surf}, we find that $R_{surf}{=}\sqrt{\mu_0\omega/2\sigma_c}$, and the AC surface resistance is proportional to the square root of frequency. The average power dissipated per cycle is

$$P_d = \frac{R_{surf}}{2} \int H^2 dS \tag{2.46}$$

where dS is an area on the surface of the cavity.

Cavities are typically kept cool with water cooling tubes along the outside surface of the cavity. As the magnetic field is pulsed, a layer δ on the inside of the cavity will heat up, but the temperature drops as it diffuses into the larger

cavity body which is being water cooled. The pulsed fields cause cyclic thermal expansion of the skin depth layer of the cavity, which experiences fatigue as a result. If the temperature differences reaches around 50 K the yield strength of copper is exceeded and micro cracking occurs. Any surface imperfections caused by this cyclic heating can result in field enhancement and field emission. This effect can be minimised by limiting the temperature increase by limiting the peak surface magnetic field. The surface temperature rise ΔT is given by [92]

$$\Delta T = \frac{P_d \sqrt{t_{pulse}}}{2\sqrt{\pi \rho k c_\epsilon}} \tag{2.47}$$

where t_p is the RF pulse length, ρ is the material density, κ is the thermal conductivity, and c_ϵ is the specific heat.

2.4 RF Cavity Figures of Merit

There are certain figures of merit related to the acceleration efficiency of RF cavities, that are extremely helpful in accelerator design. They allow us to compare and contrast different cavity designs, even at different frequencies. They also act as design constraints when optimising a new structure. The main ones are detailed in the following section.

2.4.1 Accelerating Gradient

The accelerating gradient E_{acc} is the most important figure of merit for RF cavities. Cavities are not simply characterised by how much energy they give to the bunch in eV, but in how much energy they can give per unit length. This is usually expressed in terms of the average voltage seen by a bunch traversing the cavity

$$E_{acc} = \frac{|V_c|}{L_{cav}} \tag{2.48}$$

E_{acc} is normally expressed in megavolts per metre [MV/m].

2.4.2 Normalised Electric Field

It is useful look at the ratio between the peak surface electric field (E_{peak}) in a cavity and the accelerating gradient E_{acc}

$$\frac{E_{peak}}{E_{acc}}. \tag{2.49}$$

Normalising it to E_{acc} allows the designer to compare different structures to see which has the best performance. Assuming the peak field is around the beam pipe, the higher the E_{peak} the higher the E_{acc}. However peak fields can increase the

chance of RF breakdown which must be avoided. The peak surface electric field can be limited by optimising the rounding on otherwise sharp edges.

2.4.3 Normalised Magnetic Field

It is also useful to look a the ratio between the peak surface magnetic field (B_{peak}) and E_{acc}

$$\frac{B_{peak}}{E_{acc}}. \tag{2.50}$$

The previous section explained that pulsed magnetic fields can cause cyclic heating and damage the cavity surface. In addition to this the system cooling the cavity during operation has a finite power it can dissipate effectively. For these reasons it is important to limit the B_{peak} and this parameter allows multiple structures to be compared during the design process.

2.4.4 Shunt Impedance

The shunt impedance relates the voltage to the power lost in the cavity. Cavities have finite conductivity and power dissipates through the walls as heat, the shunt impedance relates the accelerating voltage to this lost power. The voltage and therefore energy gain that a particle sees in a cavity varies with time; $\Delta E_{\vartheta_s=0} = qV_0T$, where $\vartheta_s = 0$ denotes the synchronous particle and therefore maximum energy gain. It is useful to apply the transit time factor to define the *effective shunt impedance* of a cavity

$$R_s = \left[\frac{\Delta E_{\vartheta_s=0}}{q}\right]^2 \frac{1}{P_{in}} = \frac{[V_0T]^2}{P_{in}} \tag{2.51}$$

which also shows that to maximise the acceleration voltage V_c for a fixed power P_{in}, the shunt impedance R_s must be maximised. This definition of the shunt impedance is the linac convention. Later in the equivalent circuit section of this chapter the circuit convention is introduced with a factor 2 on the denominator. CST uses the linac definition and that is the definition adopted throughout this thesis. As the shunt impedance increases linearly with length for a given electric field, along with the RF voltage and dissipated power, a more useful figure of merit is the *shunt impedance per unit length*

$$Z = \frac{R_s}{L_{cav}} \tag{2.52}$$

The effective shunt impedance per unit length is usually expressed in $\mathrm{M}\Omega/m$. Maximising the shunt impedance per unit length is equivalent to maximising the energy gain in a given length for a given power loss.

2.4.5 Quality-Factor

The Quality Factor is a useful figure of merit as it represents the maximum energy in the cavity for a given power. The walls of the cavity have finite conductivity σ_c, and thus exhibit lossy behaviour. The internal quality factor (Q_0)

$$Q_0 = 2\pi \frac{U}{U_d} = \frac{\omega U}{P_d} \tag{2.53}$$

and is derived from the equivalent circuit model for a pillbox cavity in Equation 2.62. It is proportional to the ratio of stored energy U

$$U = \frac{1}{2}\mu_0 \int |H|^2 dV \tag{2.54}$$

over the energy dissipated per cycle U_d ω is the angular frequency of the cavity and P_d is the power dissipated in the cavity by electrical resistance. Further power can be lost from the cavity when it is connected to the RF system via waveguide. To account for this we define the loaded quality factor Q_l

$$Q_l = \frac{\omega U}{P_{tot}} = \frac{\omega U}{P_d + P_{ext}} \tag{2.55a}$$

$$\frac{1}{Q_l} = \frac{1}{Q_0} + \frac{1}{Q_{ext}} \tag{2.55b}$$

where P_{tot} is the total power lost and P_{ext} is the external power flow out of the cavity, through the coupling slot and into the waveguide network and Q_e is the external quality factor. Q_l is also related to the full width half maximum (Δ_H) of the resonance peak; $Q_l{=}\omega/\Delta_H$. The coupling factor $\beta_c{=}Q_0/Q_e{=}P_{ext}/P_d$, measures how much power from the waveguide feeding the cavity is being used to power the cavity. Ideally, the coupling slot between the waveguide and the cavity will reflect zero power, this depends on the geometry and location of the slot. The quantity of power reflected by the slot is given by the square of the reflection coefficient Γ

$$\Gamma = \frac{1 - \beta_c}{1 + \beta_c} \tag{2.56}$$

which is only valid on resonance.

2.4.6 Geometric Shunt Impedance

The *Geometric Shunt Impedance* is another valuable figure of merit in RF cavity design as it relates the accelerating voltage V_0 to the stored energy U

$$\frac{R_s}{Q_0} = \frac{|V_0|^2}{2\omega U} \tag{2.57}$$

this value is independent of both frequency and cavity material. It depends only on the cavity geometry, not the losses.

2.4.7 Frequency Scaling

The physical and electromagnetic quantities of RF cavities scale with frequency. Table 2.1 shows the frequency scaling for normal conducting cavities assuming the same cavity length and normal skin effect.

Quantity		f scaling
Cell Radius	r_c	$f^{-}1$
Surface Area	S	$f^{-}1$
Volume	V	$f^{-}2$
Transit-time factor	T	1
Fields	E, B	1
Stored energy	U	$f^{-}2$
Shunt Impedance	Z	$f^{1/2}$
Dissipated power	P_d	$f^{-1/2}$
Quality Factor	Q_0	$f^{-1/2}$

Table 2.1 Table of the main physical and electromagnetic quantities of RF cavities and how they scale with frequency.

2.4.8 Re-entrant Section

Re-entrant sections or *'Nose-cones'* can be added to pillbox cavities to effectively extend the drift tube into the region where the particle bunch was not previously shielded from the RF, reducing the length of the accelerating gap. Nose-cones focus the accelerating field along the beam axis. Referring back to the transit time factor in equations 2.7 and 2.8, one can see that reducing the length of the accelerating gap increases the transit time factor and thus increases the energy gain of the particle for a given axial voltage. Simply reducing the length of the entire cavity would result in high peak magnetic fields and larger RF losses. Shorter cavities would also not be synchronous with the beam.

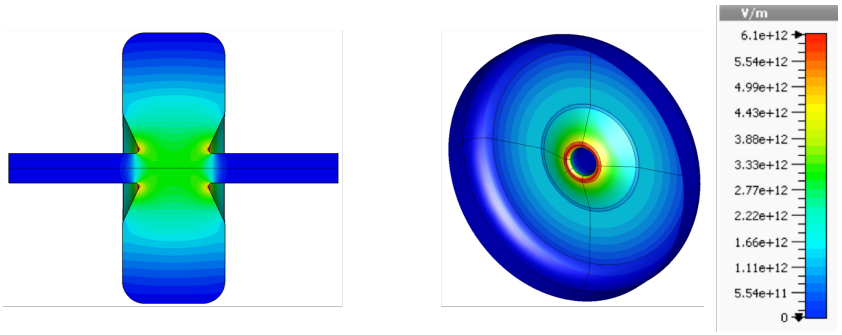

Fig. 2.21 Absolute part of the electric field inside a re-entrant pillbox cavity.

2.4.9 Equivalent Circuits

RF cavities have finite resistance (R), inductance (L), and capacitance (C), and can thus be accurately modelled with simple equivalent circuits. Equivalent circuit models are an invaluable tool in RF cavity design, they can accurately model couplers, cavity coupling, beam loading, and field amplitudes in multi-cell cavities. Figure 2.22 shows an equivalent circuit model of an RF cavity, an RF generator and a particle beam, numerous parameters of the cavity can be calculated using circuit theory.

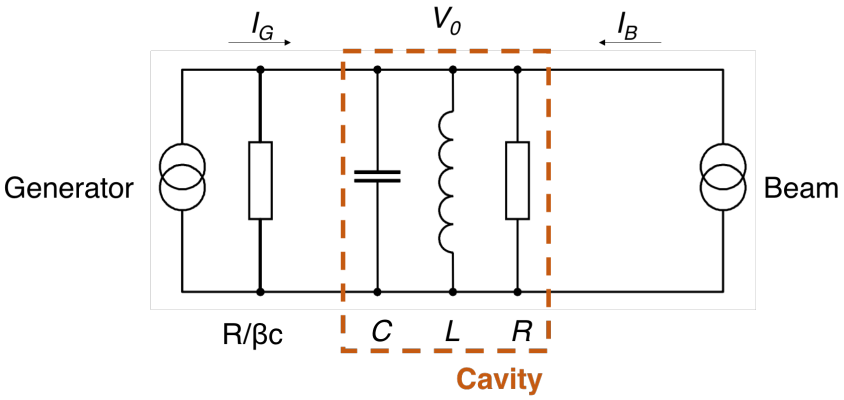

Fig. 2.22 Equivalent circuit model of an RF cavity adapted from [93].

The angular frequency ω is

$$\omega = \frac{1}{\sqrt{LC}} \tag{2.58}$$

to increase the frequency of the cavity, the inductance and/or the capacitance has to be decreased. The power lost in the cavity walls P_d is given by

$$P_d = \frac{V_0^2}{2R} \tag{2.59}$$

using the circuit convention, or by

$$P_d = \frac{V_0^2}{R} \tag{2.60}$$

using the linac convention. The linac definition is used throughout this thesis. The voltage given by the equivalent circuit does not take into account the transit time factor T. The voltage in the cavity $V_c = V_0 T$. The stored energy in the circuit is given by the energy stored in the capacitor. Thus the stored energy in an RF cavity is

$$U = \frac{C V_0^2}{2} \tag{2.61}$$

Q_0 is given by

$$Q_0 = \frac{\omega U}{P_d} = \sqrt{\frac{C}{L}} R \tag{2.62}$$

and $^R/_Q$ is

$$\frac{R}{Q_0} = \frac{V_0^2}{2\omega U} = \frac{1}{\omega C} = \sqrt{\frac{L}{C}} \tag{2.63}$$

I_B is the impedance seen by the beam and the power drawn by the beam $P_B = V_c I_B$. During operation the beam current acts as a load on the generator shown in Figure 2.22 as a resistor parallel to the shunt impedance. If the generator is matched to the unloaded cavity the accelerating voltage will decrease due to beam loading.

2.5 Multi-Gap Structures

Multiple RF cavities can be coupled together to achieve higher accelerating voltages with the same input power. The voltage excited in a single gap structure with shunt impedance R_s, fed by a power supply P_{in} is $V_0 = \sqrt{R_s P_{in}}$. If an additional n cavities are then added to this structure, assuming each have identical R_s (thus power being uniformly distributed throughout all cavities) then the voltage excited in each gap will be $V_0 = \sqrt{R_s P_{in}/n}$. The total voltage excited in the structure will be $V_{ngaps} = \sqrt{n R_s P_{in}}$.

The cavities are coupled together by holes in the end caps, allowing some of the power through to the subsequent cavity. The cells can be coupled together in various ways depending on the position of the holes in the end caps.

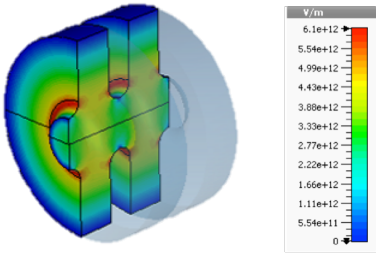

Fig. 2.23 Abs e-field plot of 'electric' or 'capacitive' coupling through the iris of a pillbox cavity [81].

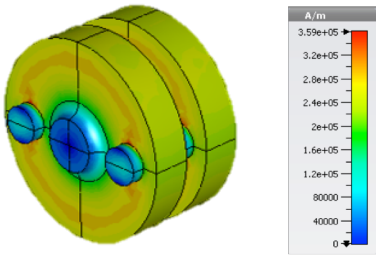

Fig. 2.24 Abs b-field plot of 'magnetic' or 'inductive' coupling through coupling slots in the end cap of the pillbox cavity [81].

Coupling through the beam aperture (the cylindrical pipe concentric to the pillboxes passing through the centre), as seen in Figure 2.23, is 'capacitive' or 'electric' coupling. A large aperture is required which lowers the shunt impedance. The alternative is 'inductive' or 'magnetic' coupling shown in Figure 2.24. Additional coupling slots are added around the beam aperture where the peak magnetic field lies, closer to the cavity walls. This allows for cell to cell coupling but keeping the beam aperture small which has a lesser effect on the shunt impedance. However, there will be peak magnetic fields on the coupling slots which can cause heating and limit the number of cells that can be coupled together. The Coupling factor (k) describes the space between modes, and can be calculated for both electric and magnetic coupling as

$$k = \frac{\omega_\pi - \omega_0}{\omega_{\pi/2}} \tag{2.64}$$

The dispersion curves for electric and magnetic coupling are shown in Figure 2.27 and Figure 2.28 respectively. When the cells are coupled capacitively, the π-mode (the mode where the phase flips by π in each cell) is the highest mode. Alternatively, when the cells are coupled magnetically, the π-mode is the lowest mode. The equivalent circuits for a periodic array of coupled cavities are shown in Figures 2.25 and 2.26 with electric and magnetic coupling respectively. In both cases inductance L_1 and capacitance C_1 in series form a resonator. The electrically coupled circuit has a shunt capacitance C_2 coupling it to the next resonator in the chain. The intercell coupling constant $k{=}2C_1/(C_2 + 2C_1)$ if the shunt capacitance $C_2 \to \infty$ k becomes zero and cells act as independent resonators. The magnetically coupled circuit has a shunt inductance L_2 coupling it to the next resonator in the chain. The intercell coupling constant in this case $k{=}2L_2/(L_1 + 2L_2)$ if the shunt inductance $L_2 \to \infty$ k becomes zero and cells again act as independent resonators.

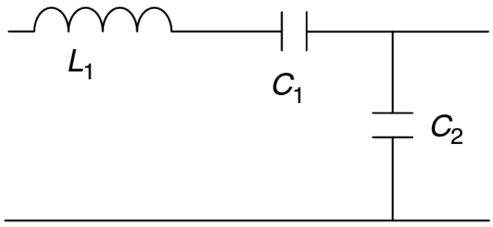

Fig. 2.25 Equivalent circuit for one cell of a periodic array of electrically coupled resonators [77].

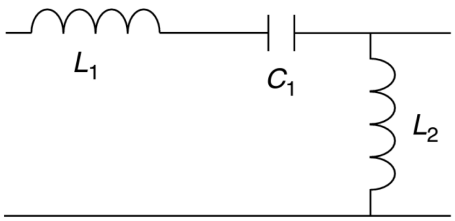

Fig. 2.26 Dispersion for magnetically coupled resonators [77].

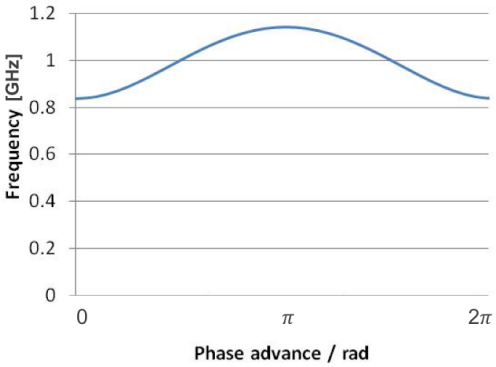

Fig. 2.27 Dispersion for electrically coupled resonators.

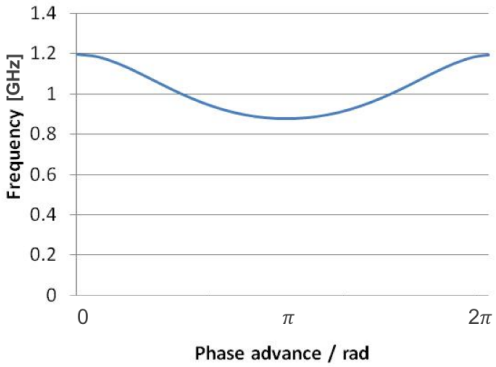

Fig. 2.28 Dispersion for magnetically coupled resonators.

2.5.1 Phase advance

The phase advance (φ) is the phase difference of the accelerating voltage between adjacent coupled cells. The phase change between two gaps when the synchronous particle arrives is given by

$$\phi_n = \phi_{n-1} + \omega \frac{l_{n-1}}{\beta_{n-1} c} + \varphi. \tag{2.65}$$

where ϕ_n is the phase in cell number n. If each cell is powered by a separate power source, the phases can be controlled independently to ensure the particles always see the desired phase. To lower costs, multiple cells are often powered by one source and the RF is coupled between the cells as was described in the previous section. The particles gain energy in each accelerating gap, and β increases as they become more relativistic. The distance (d_β) between cells must then be increased as

$$d_\beta = \frac{\varphi \beta_{n-1} c}{\omega} \tag{2.66}$$

this does not translate to a large d_β for high energy linacs so practically the cell length is usually designed for the average β of the structure, and all of the cells can be kept the same length.

2.5.2 Standing-wave Structures

In a Standing-Wave Structure (SWS), the RF power is coupled in through a waveguide, the wave travels the length of the structure and is reflected back by the cavity walls. The wave continues to bounce back and forth until the field has built up and the structure is full of RF power. A standing-wave field pattern can be thought of as the sum of two waves with the same frequency and amplitude travelling with the same velocity in opposite directions along the same medium. In the field there are nodes - locations with zero displacement - and anti-nodes, locations with maximum displacement. Once filled, the wave does not travel along the structure, it simply oscillates about its nodes. The filling time of a standing-wave structure is t_{fill}=$2Q_l/\omega$.

2.5.3 Travelling-wave Structures

A Travelling-Wave Structure (TWS) is essentially a disk-loaded waveguide. A wave propagating through a homogeneous (same cross-section from start to finish) waveguide under vacuum will always have a phase velocity v_p above the speed of light. The particles being accelerated however are slower than the speed of light, so the phase velocity is slowed down by periodic disks creating multiple cells in the cavity. The disks have holes in the centre to create the beam aperture, the disks with beam holes are sometimes called iris'. In a TWS the RF power is coupled in through a waveguide to the first cell, then it flows through the aperture in the iris to the next cell and so on until the structure is full of RF power. This differs from the SWS as they fill with time, whereas Standing-wave Structures fill spatially. This concept is explained by Figure 2.29. Each cell in a SWS starts at zero field and fills at the same time as its neighbour cells, all cells become full at the same time. In a TWS the first cell will become full before the last cell, perhaps even when the last cell is still at zero field depending on how many cells there are. A TWS fills much faster than a standing wave structure. The field in a travelling wave cavity attenuates throughout the length of the structure as the energy is absorbed by the conductor walls and by the beam. The remaining energy is typically delivered to a resistive load, although it has been proposed that this energy could be recirculated back to the input of the cavity [67]. The filling time of a TWS is determined by the group velocity (v_g) across the full length of the structure as

$$t_{fill} = \int_0^{L_{cav}} \frac{1}{v_g(z)} dz. \tag{2.67}$$

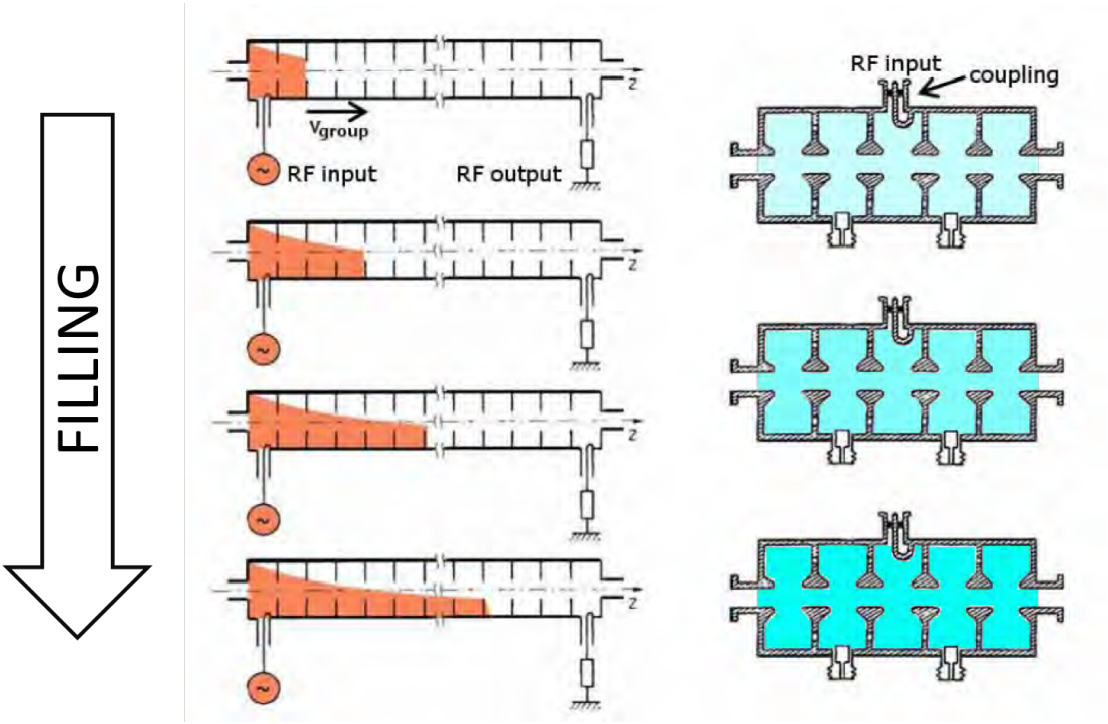

Fig. 2.29 Left: RF power filling of a travelling wave structure; Right: RF power filling of a standing wave structure [94] altered by [67].

2.5.4 Field Profiles

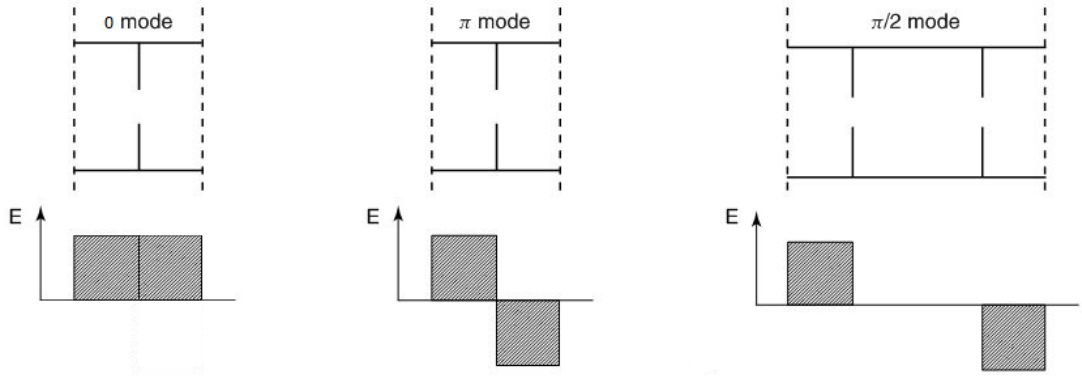

Fig. 2.30 Field profiles of the 0-mode, π-mode and $^{\pi}/_{2}$-mode adjusted from [77].

Figure 2.30 shows some of the field profiles that can exist in multi-cell standing wave cavities. In the π-mode the phase of the RF switches by 180° or π in each cell, hence every cell contributes to the acceleration. This gives it a high shunt impedance and means it can achieve the highest gradients. The 0-mode also has field in every cell but it does not switch so would require long drift tubes to meet the synchronism conditions and the transit time factor which lowers the shunt impedance and thus average accelerating gradient. The field in a $\pi/2$-mode switches every other cell and the cell between is empty. The empty cell does not contribute

to the acceleration of the beam. Figure 2.31 shows the modes within the passband of a 9-cell structure. The frequencies within the passband of a structure can pass through the structure. Frequencies that are outside of the passband are reflected and are therefore outside of the bandwidth of the structure. When there are frequency errors from manufacturing, each mode in the passband contributes a small error term to the excitation of any one particular mode. In a 9-cell standing wave cavity the phase shift per cell ranges from 0 to π in steps of $\pi/8$. In Figure 2.31 mode 1 is the 0-mode, mode 5 is the $\pi/2$-mode and mode 9 is the π-mode. When operating in the $\pi/2$-mode the error terms for the higher frequency modes almost exactly cancel out the errors from the higher frequency modes. Its neighbouring modes are also further apart (in frequency) than the 0 or π-modes making the $\pi/2$ mode the most stable of the three.

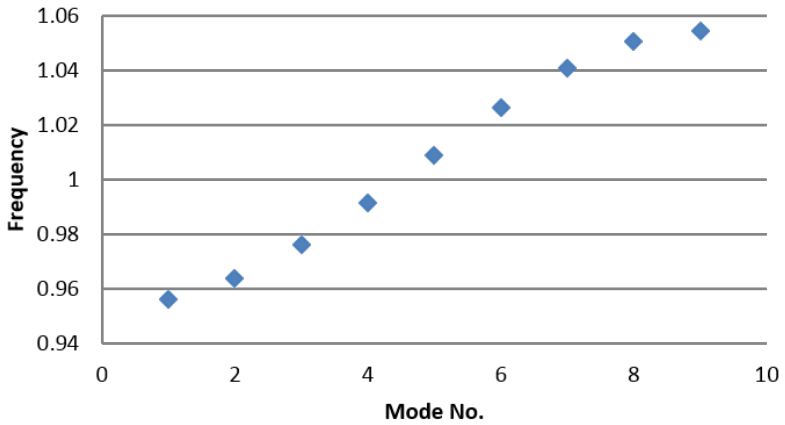

Fig. 2.31 Modes in the passband of a resonant structure [81]

Figure 2.32 shows different cell arrangements to improve the efficiency of the $\pi/2$ mode. One option is a bi-periodic on-axis-coupled structure that reduces the size of the empty cells increasing the accelerating length of the structure. Another option is to take the empty cells off axis in a side-coupled arrangement, this means every cell on the beam axis is an accelerating one containing field, and provides both a high shunt impedance and stability against frequency errors.

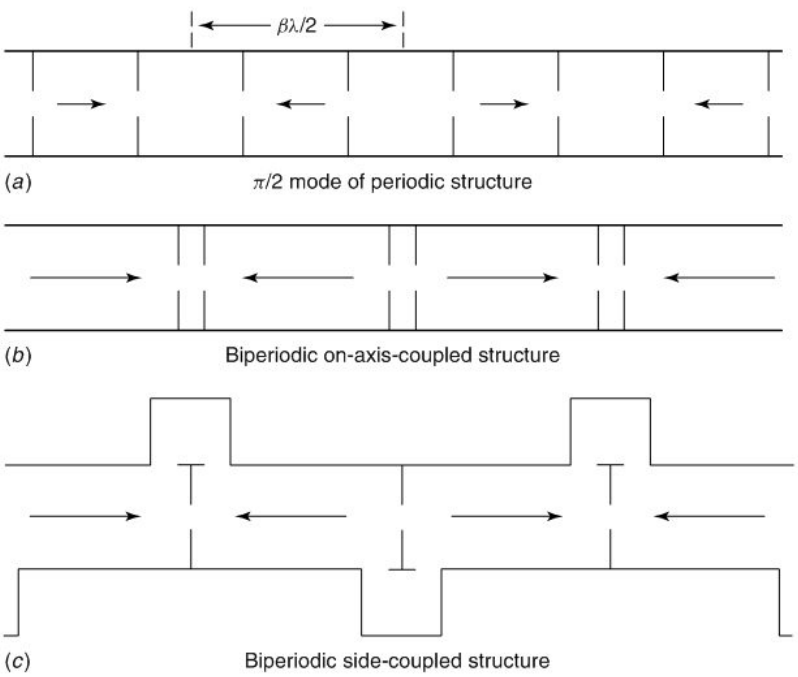

Fig. 2.32 $\pi/2$ mode in a) A periodic structure b) A bi-periodic on-axis coupled-cavity structure and c) A bi-periodic side-coupled cavity [77].

The accelerating mode of a bi-periodic structure was previously described as having field in the accelerating cells and no field in the coupling cells. Another $\pi/2$ mode exists in the pass band this time with field in the coupling cells and no field in the accelerating cells. In order for a bi-periodic structure to benefit from the stability of the $\pi/2$ mode, both of the $\pi/2$ modes have to be the same frequency. Figure 2.33 shows the dispersion curve of a bi-periodic structure where the two $\pi/2$ modes ω_1 and ω_2 have different values, and there is subsequently a discontinuity in the dispersion curve. There is an upper and a lower passband. Once the coupling cells and the accelerating cells are tuned to the same frequency ω_1=ω_2 the discontinuity is removed and the entire curve from the 0-mode to the π-mode looks like a normal dispersion curve. This was shown in Figure 2.31 which has a non-zero slope at the $\pi/2$ mode. Only then will the $\pi/2$ mode be furthest from its neighbours in the passband and thus exhibit enhanced stability over the 0-&π-modes which lie on the plateau close to their nearest neighbour in frequency.

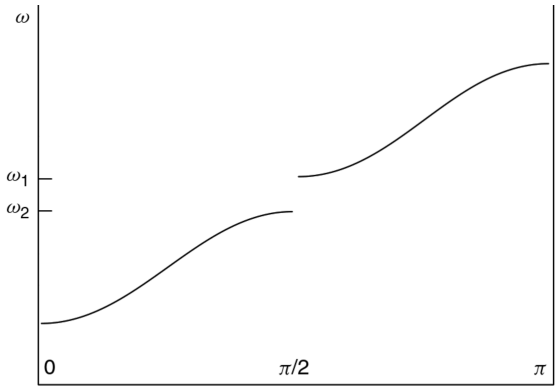

Fig. 2.33 Dispersion curve of a bi-periodic structure [77].

2.6 Medium-β high gradient structures

The aim of this work is to design a compact medical proton linac that provides 100 MeV of acceleration and is shorter than 3 m long which requires a very high gradient. Normal conducting cavities can operate reliably as high as 120 MV/m, with acceptably low breakdown rates as is shown in Figure 2.35. This however applies to electron machines where the particles become fully relativistic within the first cell due to the larger charge-to-mass ratio. Protons have smaller velocities than electrons for a given energy. As β approaches 1, the particles become fully relativistic. Electrons reach 94% the speed of light at 1 MeV but it is much higher for protons, as can be seen in Figure 2.34. This difference stems from the fact that E_r=511 keV/c^2 for electrons and E_r=938 MeV/c^2 for protons but they both have equal charge.

Whereas electron linacs can have identical cell lengths throughout the cavity, low-β linacs have to account for the particles increasing velocity. In the case of disk loaded structures this means more lossy end cells per meter and it becomes more efficient to remove the disks completely. This gives rise to various different linac designs for varying particle velocities.

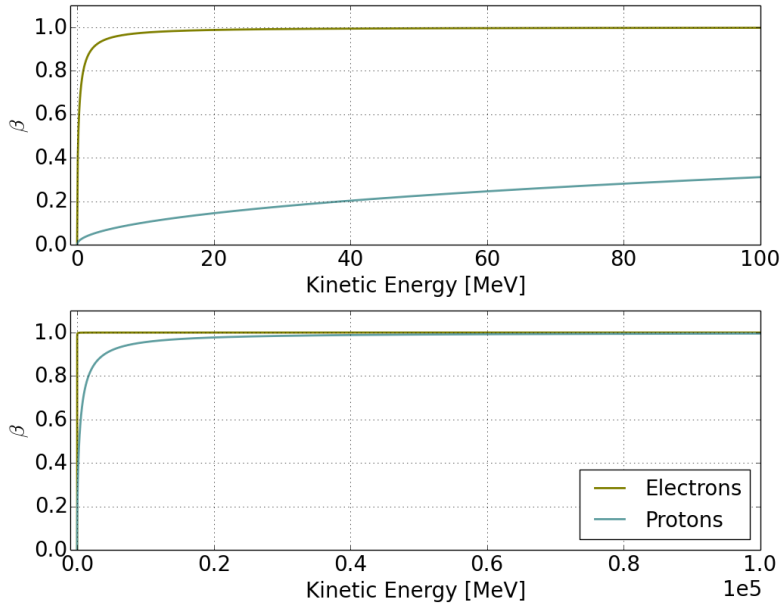

Fig. 2.34 The relativistic β vs Kinetic Energy (MeV)

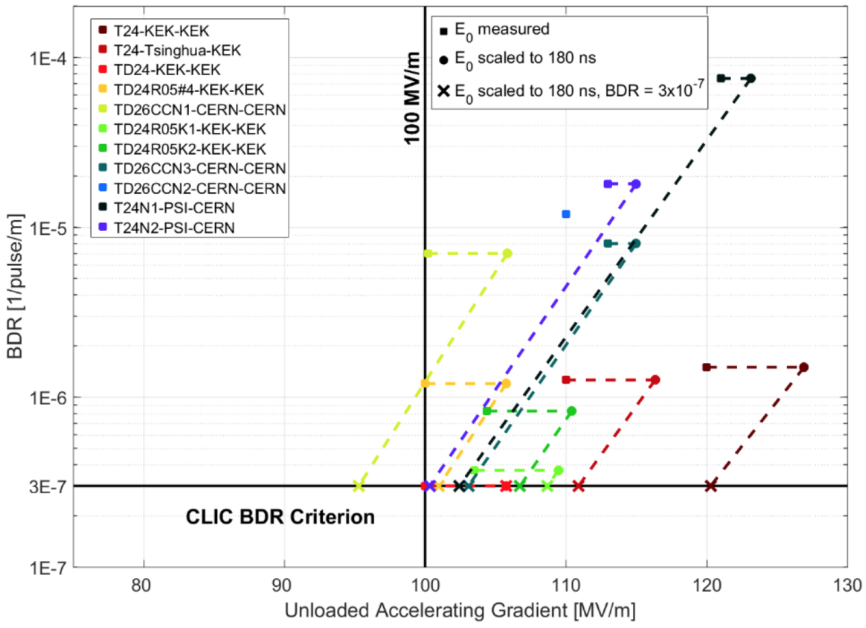

Fig. 2.35 A summary of the achieved performances of the structures tested under the CLIC high gradient test programme. Values are scaled using known scaling laws to the CLIC nominal design parameters [95].

2.6.1 Drift-Tube Linacs

A typical low-β structure is a Drift-Tube Linac (DTL) of which there two types: Alvarez and Widroe. An Alvarez linac is shown in Figure 2.36, it operates in the TM010 0-mode and rather than using lossy end cells, copper tubes around the beam axis shield the beam from the negative phase of the RF, the tubes get progressively longer throughout the structure to remain synchronous with the increasing particle velocity, and the RF frequency stays the same. At low β the beam is more easily defocussed by the RF so low frequencies are preferred as RF defocussing increases with frequency.

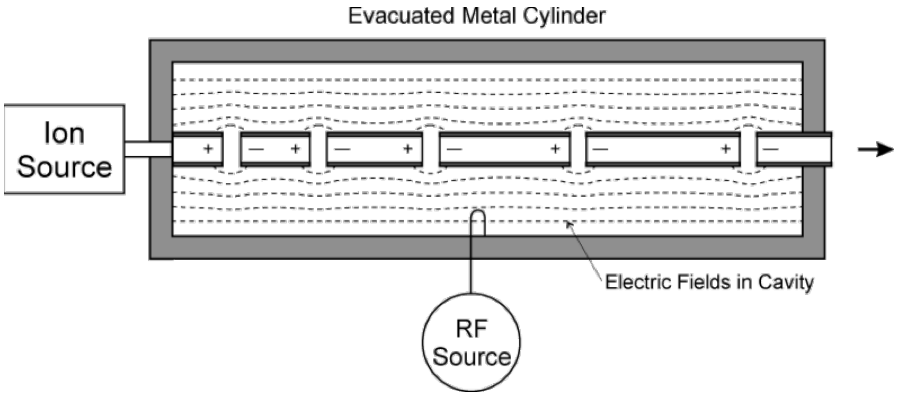

Fig. 2.36 An Alvarez drift-tube linac [96]

Widroe DTLs connect each subsequent drift-tube to the opposite polarity of an RF source as is shown in Figure 2.37. An electric field is created in the gap between the drift-tubes and it alternates every other gap like a π-mode. As the length of the drift-tubes increase with velocity, there is an upper practical limit for these accelerators.

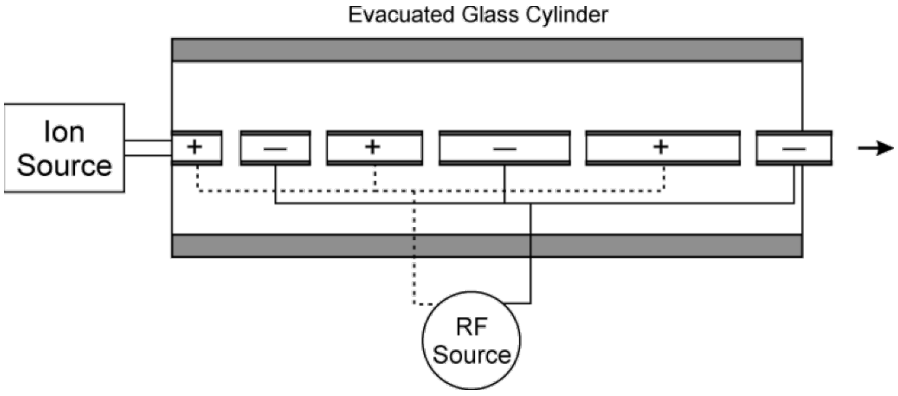

Fig. 2.37 An Widroe drift-tube linac [96]

Figure 2.38 shows H-mode cavities both interdigital and crossbar which operate in the TE11 ad TE21 modes respectively. These are a variation of drift tube linacs

where there is no longitudinal electric field on axis, instead it exists only very close to the ends of the drift-tube in the gap. This results in very high shunt impedance at low energies, but at higher energies the gap gets longer and the voltage decreases lowering the shunt impedance and the efficiency.

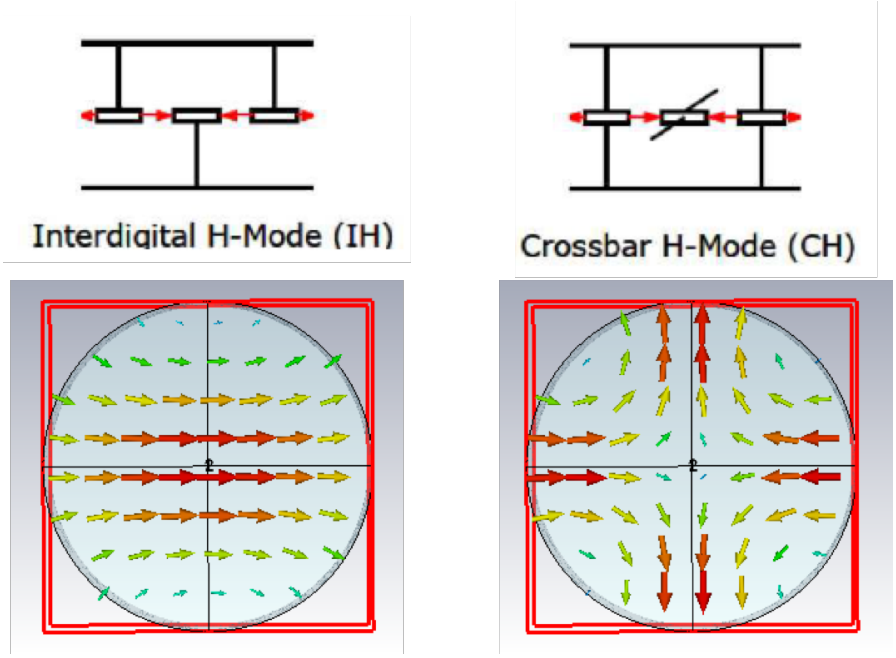

Fig. 2.38 H-Mode cavities. Left shows Interdigital (IH) and right shows Crossbar (CH) [96].

For higher energy proton machines, or medium-β machines, the same voltage will result in less acceleration because of relativity. In this case the cells can remain the same length like in an electron machine, and the particles will oscillate around a stable synchronous phase. This concept is explained further in Section 2.2.1. Furthermore the distance between lossy cell walls in disk loaded structures increases and becomes more efficient at higher β's. Figure 2.39 shows the effective shunt impedance for various structures against the particle energy or β. The previously mentioned H-mode structures have very high shunt impedance at low energies but it drops rapidly and most DTLs become inefficient above around 100 MeV. One can see that at higher energies the disk-loaded coupled-cavity linacs provide higher shunt impedance. The ProBE linac is to be designed for protons starting at 250 MeV, long past the region where DTLs are most efficient and fore this reason DTLs will not be considered. Instead we shall explore existing structures at a more relevant energy range $\beta > 0.5$.

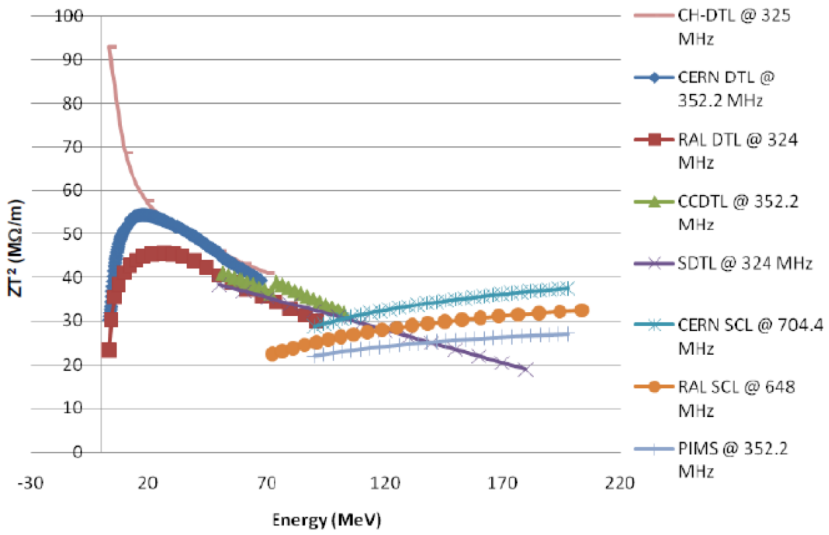

Fig. 2.39 Effective shunt impedance of low-β normal conducting structures [97].

2.6.2 PIMS

PI-Mode Structures (PIMSs) are coupled cavity linacs where the phase flips by π in each cell. They are typically coupled magnetically by slots in the cell walls for normal conducting structures or electrically through the beam aperture in superconducting structures. The cell length remains constant as both the frequency and coupling depend on the length of the cell, hence why PIMSs are typically used for higher velocities where the beam phase slippage is small. They need relatively large coupling for phase stability, so they tend to have large coupling slots which degrades the shunt impedance.

LINAC4 at CERN is a 352 MHz, 160 MeV proton linac built to inject into the PS booster - a part of the network of linacs ultimately feeding the Large Hadron Collider (LHC). The high energy part of this linac has been optimised for medium-β ($\beta > 0.5$) protons from 100-160 MeV. A higher frequency (704 MHz) side-coupled linac operating in the $\pi/2$-mode was also considered for this application and was found to have 20% higher shunt impedance [98] however it would have required a new RF power source at that frequency and more cells which increases manufacturing costs, plus it adds complexity to the tuning process so it was decided in this case to use the PIMS.

Fig. 2.40 PIMS cavity under test in CERN's main workshop [99].

2.6.3 $\pi/2$-mode structures

$\pi/2$-mode structures have the unique benefit of being less sensitive to manufacturing errors due to the mode spacing on that part of the dispersion curve. This allows for reliable operation of longer chains of coupled cells not possible in the π or 0-modes. The acceleration efficiency is typically not as high as a π-mode structure as every other cell has no field during operation (see Figure 2.32(a)), however this can be improved by reducing the length of the empty cell on-axis (see Figure 2.32(b)) or taking the empty cell off axis in a side-coupled configuration (see Figure 2.32(c)).

The Spallation Neutron Source (SNS) at Oak Ridge National Laboratory utilises firstly a Radio-Frequency Quadrupole (RFQ); a type of RF cavity often used at very low energies as it bunches the beam and performs quadrupole focussing. The RFQ accelerates from injection to 2.5 MeV, next a DTL accelerates to 87 MeV, then from 87 MeV to 186 MeV a Side Coupled Structure (SCS) operating in the $\pi/2$-mode is employed [100]. Figure 2.41 shows two segments of the linac joined by a bridge coupler, one can see the main accelerating cells coupled together by side-coupled cells taken off axis. The accelerator operates at 805 MHz and is over 55 m in length and each module is powered by a 5 MW klystron, yielding an average accelerating gradient of 1.78 MV/m. The ProBE linac will require a significantly higher gradient to achieve 100 MeV energy gain in under 3 m.

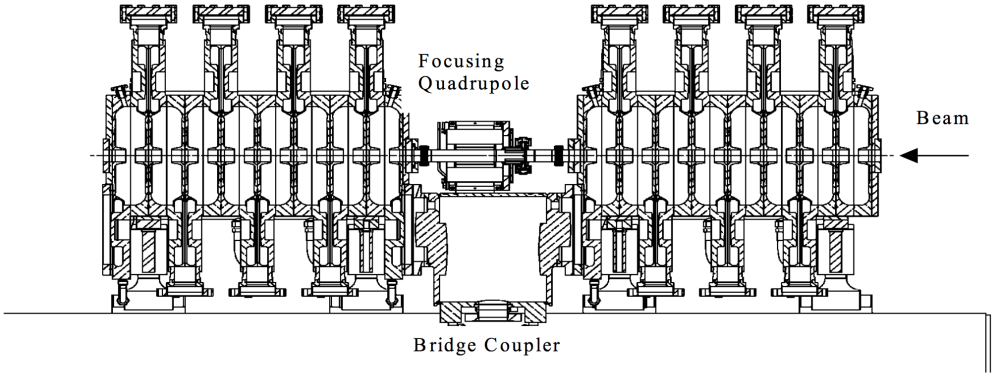

Fig. 2.41 805 MHz SNS side-coupled cavity. Two segments are joined by a bridge coupler [101].

An alternative $\pi/2$-mode structure is an Annular Coupled Structure (ACS) where concentric rings surrounding the accelerating cells couple them together magnetically. The ACS in the Japan Proton Accelerator Research Complex (J-PARC) linac is shown in Figure 2.42. The linac similar to the SNS starts with an RFQ followed by a DTL [102], then at 190 MeV the 925 MHz ACS cavities are introduced to accelerate to 400 MeV. This covers the entire energy range on interest for the ProBE linac but it has an accelerating gradient of only 4.8 MV/m.

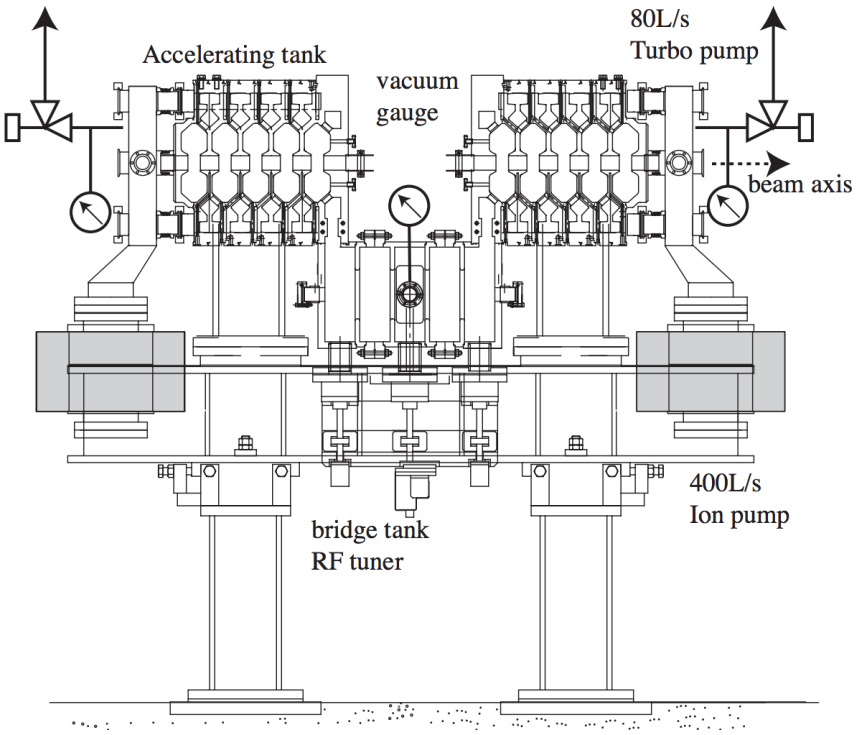

Fig. 2.42 Annular coupled structure at J-PARC [102].

2.6.4 Superconducting Cavities

Superconducting Radio-Frequency (SRF) cavities operating at 2 K have also been used for medium-β applications. After the SCS at SNS there is a β=0.61 805 MHz SRF cavity. It is powered by 805 MHz RF and the cryomodule is shown in Figure 2.43. The efficient superconducting cavity is powered by relatively small 5 MW klystrons and produces a gradient at β=0.61 of 10.5 MV/m [100]. This is still not high enough for the ProBE application.

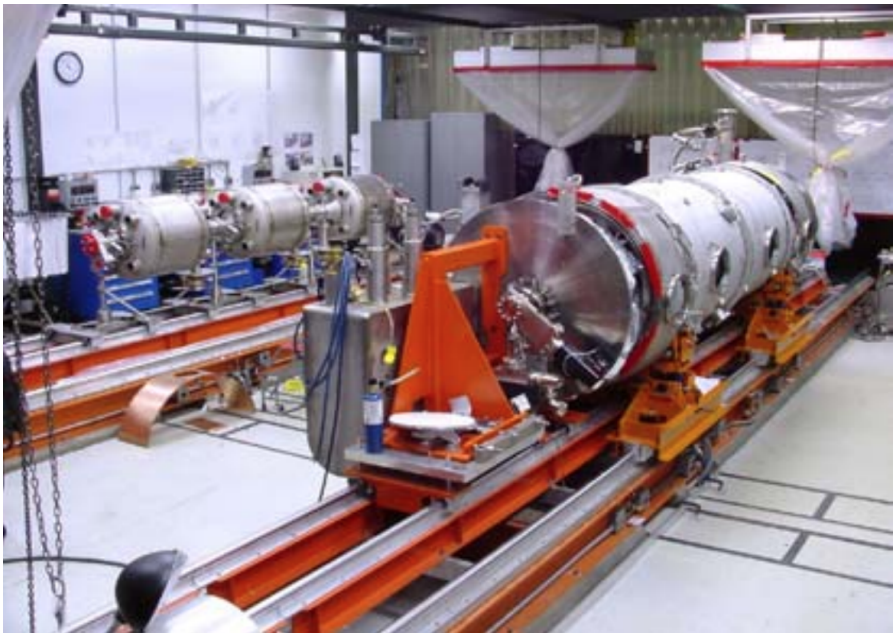

Fig. 2.43 805 MHz medium-β SRF cavity cryomodule at the spallation neutron source [100].

Another example of a medium-β SRF cavity can be found at The European Spallation Source (ESS) and is shown in Figure 2.44. The β=0.67 structure is powered by 1.2 MW peak power at 704 MHz and the nominal gradient is 16.7 MV/m. 4×6-cell cavities are housed in a 6.6 m cryomodule.

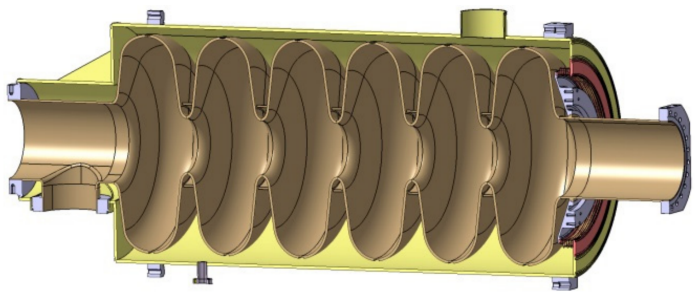

Fig. 2.44 704 MHz medium-β SRF cavity 3D model at the European Spallation Source [103].

The two previous examples were of elliptical SRF cavities, but other types of SRF cavities exist for low, medium, and high beta. Some alternative designs are shown in Figure 2.45. Superconducting technology adds additional complexity to a linac which is to be considered in a hospital environment. Typically SRF cavities are lower gradient than normal conducting cavities as they can quench with temperature increases. Although SRF technology has improved and gradients over 30 MV/m are achievable, the ProBE linac prioritises compactness and simplicity for hospitals and will only investigate normal conducting cavities.

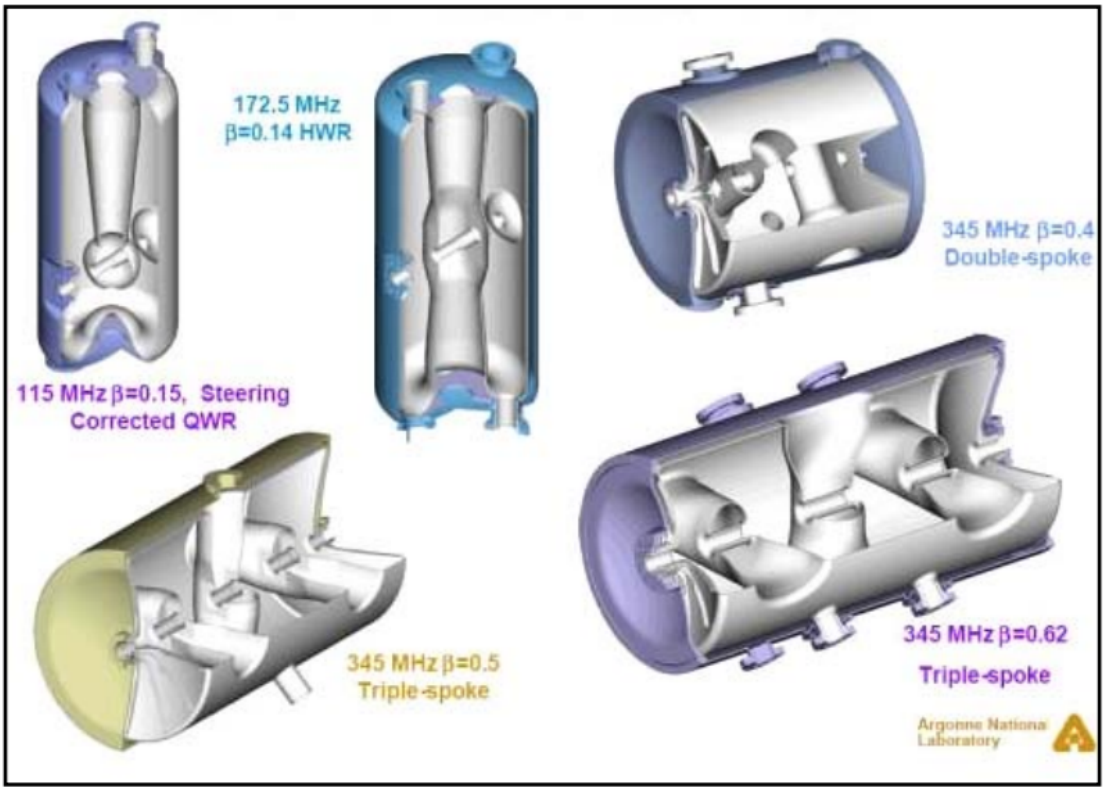

Fig. 2.45 Various low, medium, and high-β SRF cavity designs. [104].

2.6.5 LIBO

The LIBO structure is a 3 GHz a proton accelerator designed as a linac booster for proton therapy [18]. It was designed to be placed after a cyclotron to boost 60 MeV protons to 200 MeV for the treatment of deep-seated tumours. The nominal design gradient was 15.8 MV/m but in high power tests the prototype module was able to reach a gradient of 28.5 MV/m. The LIBO structure is 11 m and produces 33 μA output current. The ProBE linac can tolerate a much lower output current as it is for proton imaging rather than therapy. Re-optimisation of a side-coupled linac such as this to the ProBE specification is feasible and explored in later chapters.

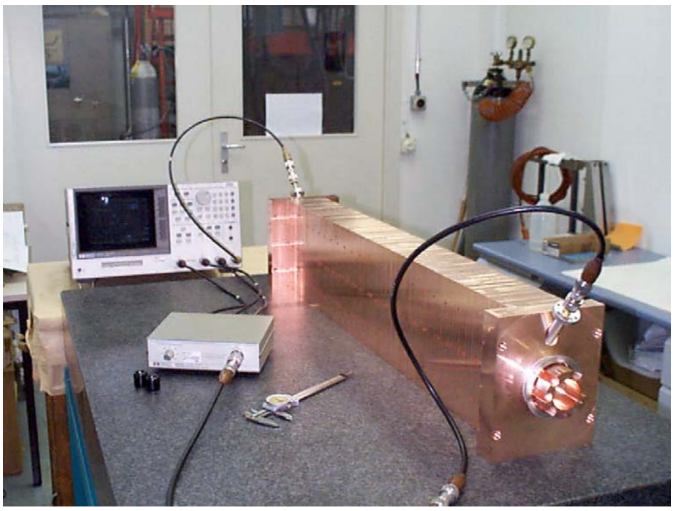

Fig. 2.46 LIBO structure RF measurement set up [18].

2.6.6 bTW & CCL Structures

A high gradient bTW structure was designed at CERN for β=0.38 protons for proton therapy. The bTW structure is so called because it has a negative group velocity, thus the beam traverses the structure in the opposite direction to the RF. The complex magnitude of the electric field distribution inside the cavity is shown in Figure 2.47 [22]. The nominal design gradient was 50 MV/m and this gradient was experimentally verified in the S-Box test bench and is detailed in Chapter 7. This is closer to the sort of gradients that the ProBE linac will require.

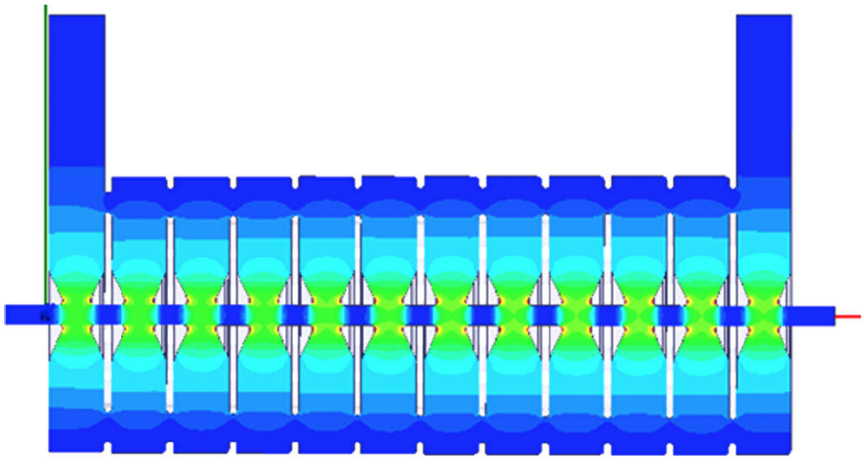

Fig. 2.47 Complex magnitude electric field distribution inside the bTW cavity [22].

When optimising the bTW structure a Coupled Cavity Linac (CCL) was also considered [67] and is shown on the left of Figure 2.48, 'CCL-BL' it was found to have 13% higher shunt impedance than the bTW structure, however adopting

the S_C model it would only reach 30 MV/m due to the sharp nose cones and high peak fields[22]. The structure was re-optimised for high gradient operation and is shown in the centre of Figure 2.48, 'CCL-HG' and still had slightly higher shunt impedance and better RF thermal power dissipation.

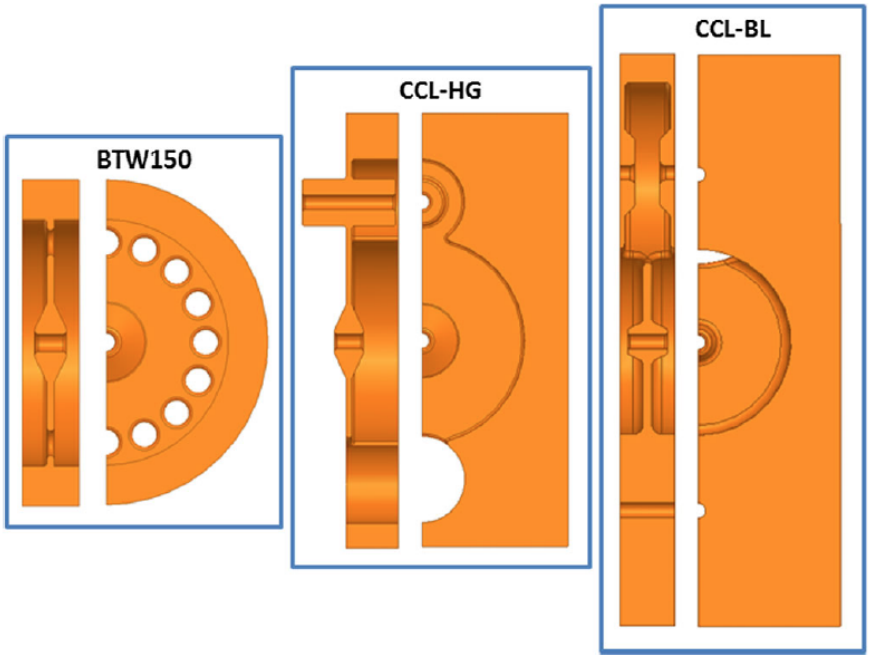

Fig. 2.48 Mechanical view of structures optimised by TERA for β=0.38 [22].

Figure 2.49 shows the effective shunt impedance as a function of the geometric-β for various low-β cavities optimised by the TERA foundation for medical applications. The plot only provides information up to 75 MeV but the plot shows the CCL is the only structure still increasing in effective shunt impedance at the higher energies.

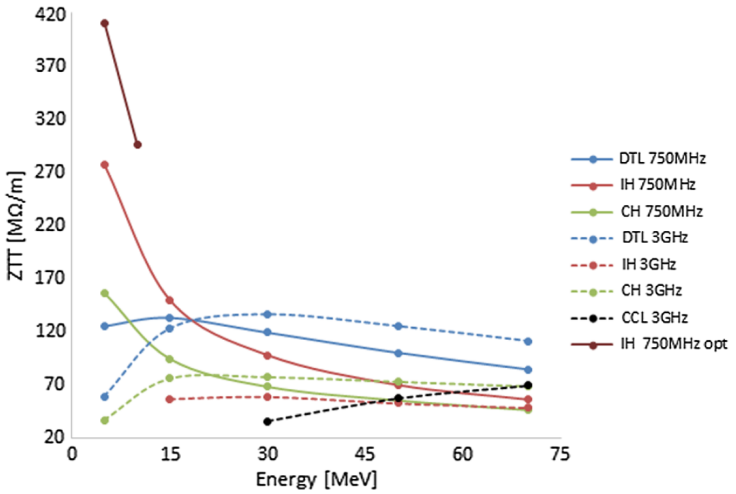

Fig. 2.49 Effective shunt impedance as a function of β for various low-β cavities. [22].

The TERA foundation in collaboration with PSI have also considered a proton booster linac for upgrade of existing facilities with a 250 MeV cyclotron. They propose using a CCL at 3 GHz with an accelerating gradient of 25 MV/m, this would make the linac 7 m long for the 100 MeV energy gain required for proton imaging. This is too long for retrofit directly at the Christie hospital and consequently this study will strive for a higher gradient and a more compact solution.

2.6.7 First negative spatial harmonic structure

RadiaBeam Technologies [105] investigated the feasibility of using the bTW structure described in the previous section but scaled from β=0.38 to accelerate particles with β=0.3. They had found the direct scaling lead to higher peak surface electric fields (>220 MV/m), because the nose cones become very close together. Removing the nose cones dramatically reduces the shunt impedance and thus the achievable gradient. Their solution was to design a similar disk-loaded magnetically coupled structure, but this time synchronous with the first negative spatial harmonic instead of the fundamental as shown on Figure 2.50. Line α_0 shows the v_p of the bTW structure, the tangent to the point on the dispersion curve that intersects with the v_g is line γ_0. The two lines have opposite signs which defines the backward travelling wave mode in the bTW structure. By coupling to the first negative spatial harmonic v_p=α_{-1} has the same sign as v_g=γ_{-1} making it a forward travelling wave structure. The lower gradient of α_{-1} means the cells are spaced further apart, this and further optimisation of the nose cones to take an elliptical shape, has reduced the surface electric field to 200 MV/m at an accelerating gradient of 50 MV/m. This structure has been re-optimised for a lower β than the bTW medical structure. The ProBE application is concerned with higher β protons for imaging.

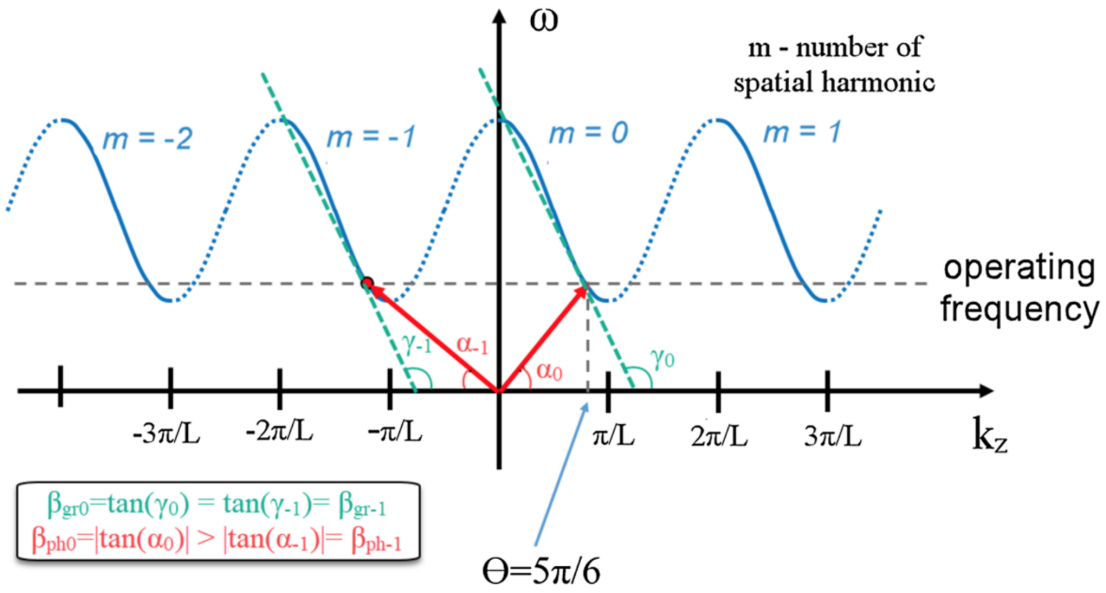

Fig. 2.50 The dispersion curve of a disk-loaded periodic waveguide structure with magnetic coupling. m=0 curve is the fundamental harmonic, m=-1 curve is the first negative harmonic [106].

Chapter 3

Small Aperture High Gradient Cavity Optimisation

3.1 Initial Design Considerations

When embarking on a linac design study one has many options to consider. These initial design choices from requirements, and limitations will dictate many design decisions throughout the optimisation process. As has already been mentioned in section 1.4, the ProBE linac requires a high gradient as the proton therapy beam line is already constructed and has only 3 m available space for an upgrade. Normal conducting RF cavities have exceeded gradients of 120 MV/m [107], whereas superconducting RF cavities are limited by thermal breakdown and exhibit maximum gradients of 30-50 MV/m [108], thus an obvious initial design choice is to use normal conducting RF technology. A vital component of any particle accelerator contributing to the cost, efficiency, and the gradient, is the RF power source. Normal conducting RF cavities dissipate almost as much power, if not more, in the walls of the cavity through ohmic losses, as they transfer to the beam. To compensate for this, and still reach a high gradient considerable RF power is required.

3.1.1 RF Power Source

Initially the decision was taken to use two 50 MW klystrons to power the ProBE linac, as it is a simple and compact option. The alternative may have been to use multiple small klystrons and pulse compress to higher power. RF pulse compression is when a long pulse at a given power is used to fill a cavity, then the phase is flipped and the cavity outputs a higher power at a shorter pulse length. implementing this would take up more physical space and add complications to the low level

RF network feeding the high power system. This is possible, but for a hospital application we would rather avoid it to keep the booster linac as simple and compact as possible. Having acknowledged that, the option to use multiple smaller klystron is always a possibility. However, the starting point of this study was to assume two 50 MW klystrons are powering the ProBE linac. 50 MW klystrons are only commercially available in S-band (3 GHz), C-band (5.7 GHz), and X-band (12 GHz). 50 MW can also be achieved at X-band (9.3 GHz) using a 10 MW klystron with a pulse compressor. Currently the majority of medical accelerators are in the S-band range [109] due the availability of power sources, but high gradient technology has been moving to higher frequencies such as the C-band technology used in the Swiss-FEL [110], and the X-band technology utilised in the CLIC studies [111]. Consequently, this study used the aforementioned frequencies as a starting point for linac design. A standing wave cavity structure at each of these frequencies was simulated in CST microwave studio [112] to determine which could achieve the highest gradient with a fixed input power. The simulations throughout this chapter have been done using the Eigenmode solver in CST. A tetrahedral mesh was used with 40 mesh cells per wavelength, and third order curved elements.

3.1.2 Gradient Limits

The CLIC high gradient test programme has been designing, building and high power testing RF cavities to the highest gradients possible for normal conducting RF cavities for many years [113]. In this work we shall attempt to remain as close as possible to the procedures used in CLIC as it is considered to be the state of the art. With vast data on both 12 GHz and 30 GHz structures they have attempted to shed light on the relatively mysterious phenomenon of RF breakdown. The modified Poynting vector was discussed in section 2.3.4 as a gradient limiting quality. The scaled modified Poynting vector is the S_c calculated for a breakdown rate (BDR) of 10^{-6} breakdowns per pulse per meter (bpp/m), and a pulse length t_p of 200 ns. It can be calculated by applying the experimental approximate scaling law BDR $\propto S_c^{15} \cdot t^5$. S_c should not exceed 4 W/μ m^2 for 10^{-6} bpp/m at 200 ns. This quantity is used to limit peak fields and the gradient is then calculated with the shunt impedance per unit length (Z) and 50 MW of input power per metre linac.

3.2 Single Cell Pillbox Cavities

The starting point for the optimisation study was single cell pillbox simulations with infinite periodic boundary conditions. Although you can not make a cavity like this, it is useful to inform preliminary design decisions. The model overlooks end

cells, a power coupler and cell to cell coupling. The cavity features an asymmetric blend which is shown in Figure 3.1, because typically structures of this kind are manufactured with multiple machined cups stacked upon one another. The machined cups can have blends on one side, but the other side is just the bottom of the next cup, which is a flat surface with no blend.

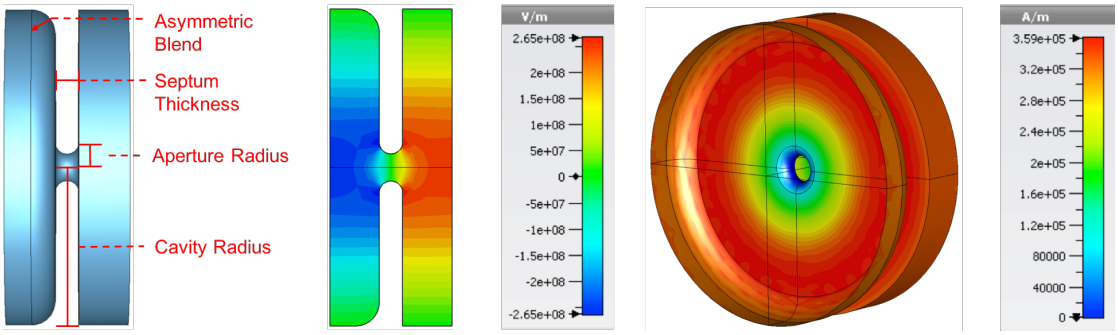

Fig. 3.1 A pillbox cavity vacuum model (left) Electric field profile (centre) and magnetic field profile (right).

Figure 3.1 shows the vacuum model of one cell of the standing wave cavity on the left with some cavity parameters labelled. The centre field map is a cut plane through the centre of the cavity and shows the electric field pattern inside, the phase flips by π from one cell (blue) to the next (red) and a shielded area where there is no field can be seen in the beam aperture between the cells (green). The right hand model is in isometric view and shows the magnetic field pattern on the surface of the cavity, the maximum magnetic field being on the outer wall.

The aperture radius of the pillbox cavity was swept from 0.5 mm to 5 mm to investigate how the main cavity figures of merit vary with the iris aperture. Figure 3.2 shows the peak surface electric field, and the peak surface magnetic field inside the cavity normalised to the accelerating gradient. For the same accelerating gradient, the peak fields increase with frequency and aperture radius. The cavity simulated is almost completely featureless; there are no nose cones or coupling slots to enhance the field. The septum thickness' are scaled with frequency, 1 mm for 12 GHz and 4 mm for 3 GHz. The wavelength at 12 GHz is λ_{12}=25 mm and the wavelength at 3 GHz is λ_3=100 mm, which is why the aperture radii have different effects on the peak fields depending on frequency.

The left hand plot of Figure 3.3 shows the shunt impedance per unit length values for a range of different apertures at the four preliminary frequencies. The shunt impedance includes the transit time factor defined in equations 2.51 & 2.52. The shunt impedance is a measure of the cavity's ability to concentrate the accelerating field around the beam, so it is a desirable figure of merit to maximise. At a 5 mm aperture radius the S-band structure has the highest shunt impedance per unit length, but when you consider a 2 mm aperture radius the S-band structure

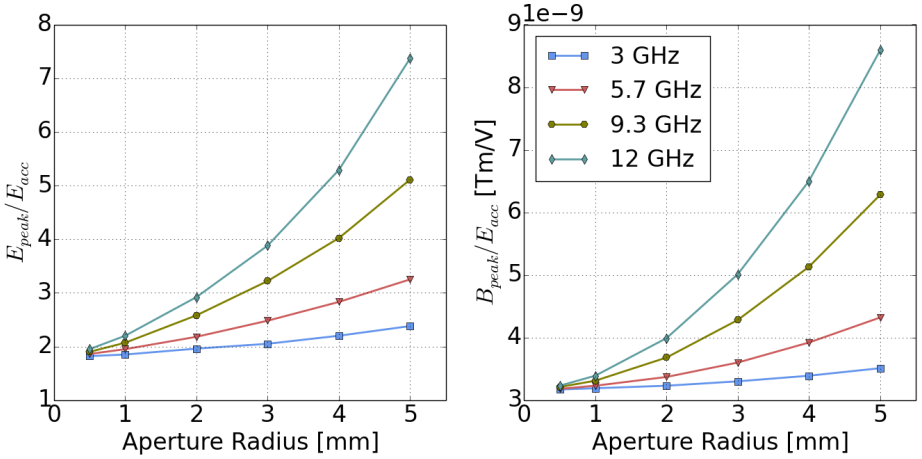

Fig. 3.2 The peak surface electric field (left) and peak surface magnetic field (right) both normalised to the accelerating gradient.

has the lowest shunt impedance. The higher X-band frequencies have higher shunt impedance than the S- & C-band curves at smaller apertures. This is due to the size of the aperture radius relative to the wavelength. Figure 3.4 shows the same shunt impedance plot but this time with the aperture radii normalised to the wavelength. Here one can see the range of apertures investigated are from a much larger range of apertures for X-band than the lower frequencies. A 1 mm aperture radius is small by typical RF cavity standards, a high energy physics machine like the LHC for example has a large beam current and thus needs a large aperture to contain it. However, proton imaging does not require an intense beam to deliver the required dose, a small beam current of pA is sufficient. It is possible that a small aperture X-band structure could provide the high shunt impedance and thus high gradient required for this application.

The plot on the right of Figure 3.3 shows the square root of the modified Poynting vector (S_c) normalised to the accelerating gradient. Unsurprisingly it follows the same pattern as the peak fields, as the Poynting vector is the cross product of the electric and magnetic fields. The power flow model suggests that the modified Poynting vector represents the available power to feed the field-emission mechanism which is believed to trigger RF breakdown [82]. Thus it is a quantity we wish to minimise.

These initial simulations have shown minimising the aperture also minimises the ratio of peak fields to gradient. It has also demonstrated a crossover whereby smaller apertures yield higher shunt impedance at X-band and larger apertures yield higher shunt impedances below 6 GHz. Knowing that proton imaging requires only minuscule beam current we will attempt to take advantage of the high shunt impedance at 12 GHz, with an aperture radius of 1.75 mm.

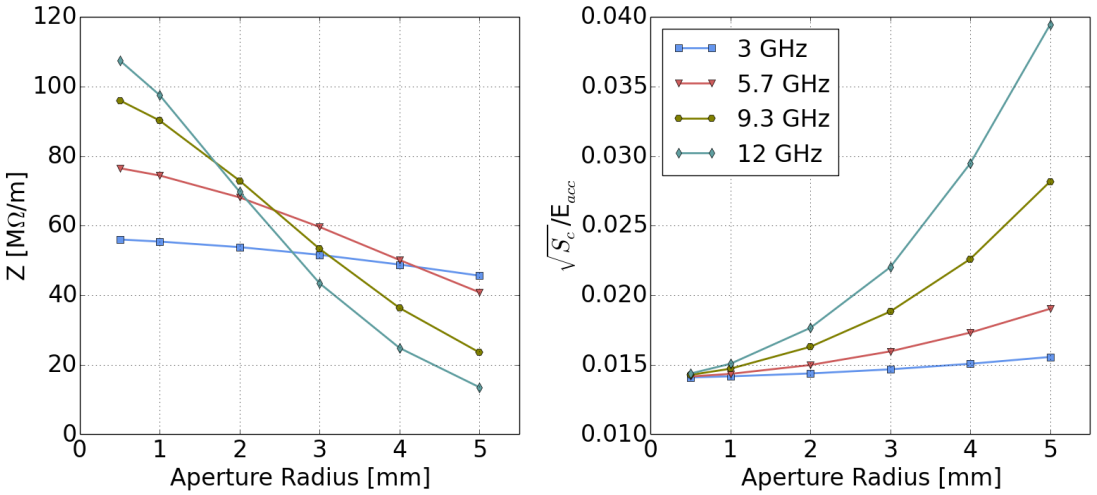

Fig. 3.3 The shunt impedance per unit length and $\sqrt{S_c}$ normalised to E_{acc}.

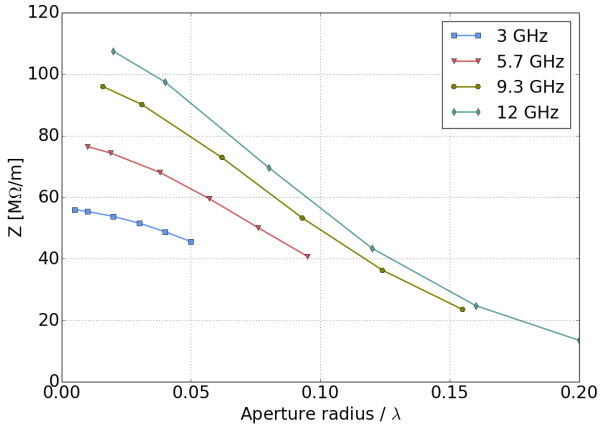

Fig. 3.4 The shunt impedance per unit length and the aperture radius divided by the wavelength of each respective frequency.

3.2.1 Beam Aperture

In this chapter a small aperture radius of 1.75 mm is considered because initial beam dynamics calculations prior to this thesis suggested it would provide sufficient transmission through the structure. Figure 3.3 showed that for apertures below 2 mm X-band structures have the highest shunt impedance per unit length. The aperture is very small and for some applications it would be challenging to get enough transmission through it, but for proton imaging specifically very low beam current is necessary. A beam dynamics study is presented in Chapter 5 which investigates the feasibility of using an aperture radius this small for the ProBE project specifically. The study concluded that an aperture this small was not feasible for the Christie hospital application because the required quadrupole strengths

and matching cell lengths are too high to be practical. However ADAM [114] with AVO [115] are developing a linac only solution for proton therapy called LIGHT [116]. The system does not use a cyclotron as a proton source and thus has no degrader making the beam size smaller right from the source. Next the beam passes through an RFQ which focusses the beam while also accelerating it, minimising the beam size further. A small aperture solution would serve as an upgrade for such a facility. Therefore the minimum aperture scheme is still relevant to the question of whether or not a linac upgrade is feasible for existing proton therapy centres.

3.3 Single Cell Re-entrant Cavities

Re-entrant cavities utilise '*nose cones*' to reach a higher gradient. The smaller the accelerating gap, the higher the effective accelerating voltage because as you reduce the gap the peak fields increase. If the entire gap is simply minimised by moving the cavity walls closer together, high magnetic fields are produced on the walls of the cavity and the beam will no longer be synchronous with the oscillating field, unless the septum was made thicker. Adding a re-entrant section or nose cone allows us to reduce the length of the gap around the beam, but keep it the same in the rest of the cavity to avoid high fields, and maintain synchronism with the beam. The same voltage is between a smaller gap at the aperture this increases the shunt impedance but peak fields are a concern for RF breakdown so there is an optimum.

Figure 3.5 shows a pillbox cavity but with the addition of a re-entrant section. The electric field plot shows the peak fields existing on the nose cones around the aperture. The size of the cones was manipulated until the same maximum gradient was achieved for two limiting factors; the modified Poynting vector and the shunt impedance.

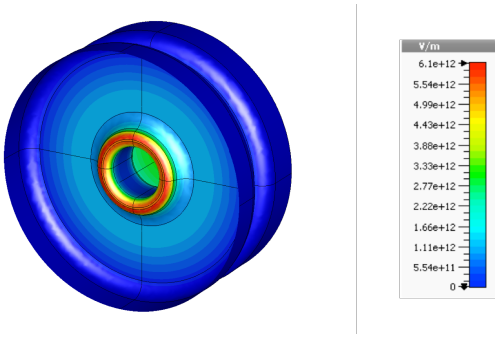

Fig. 3.5 The absolute electric field peaking around the beam aperture for a 12 GHz pillbox cavity with a re-entrant section.

In Figure 3.6 one can observe the reduction in the maximum gradient limited by S_c as one *reduces* the distance between the nose cones. This decreases faster than

the gradient limited by Z with the *increase* of distance between the nose cones. There is an optimum point where the gradient limited by both limits is identical.

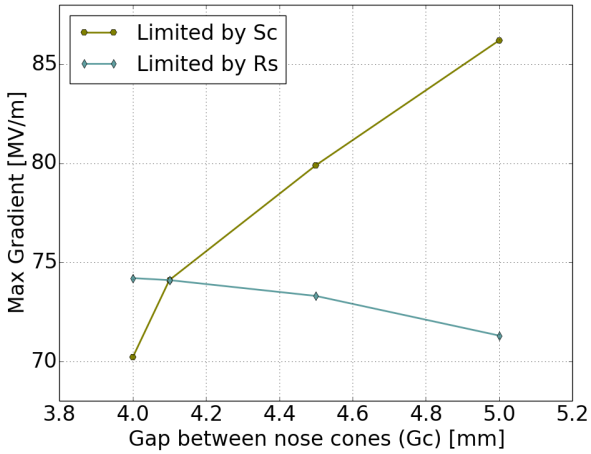

Fig. 3.6 Optimum point between two gradient limits for a 12 GHz structure with a 1.75 mm aperture radius and a 1 mm septum. The peak modified Poynting vector has been limited at 4 W/μm^2 and the input power is 50 MW/m.

Figure 3.7 shows the maximum gradient achievable with 50 MW/m input power calculated with the shunt impedance Z. In the case of the re-entrant cavities their shunt impedance is limited by the peak fields being limited to S_c=4 W/μm^2. The cavity septa are scaled from 1 mm thick for 12 GHz to 4 mm for 3 GHz. The total rise in gradient from the addition of the nose cone reduces as the gradient increases. This is due to the fact that the gradient has been limited by S_c as was shown in Figure 3.6, and higher frequencies have higher peak fields with respect to accelerating gradient than lower frequencies.

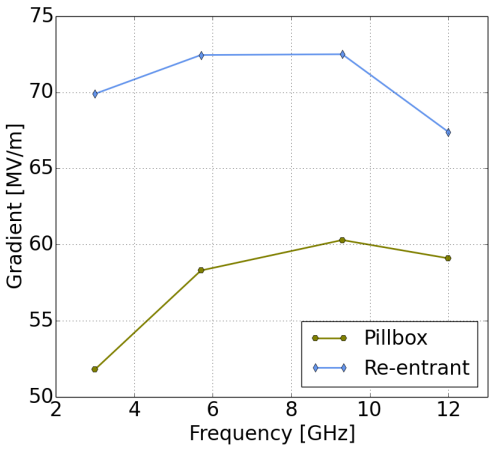

Fig. 3.7 The increase in gradient for a 2 mm radius aperture with the addition of a re-entrant. Gradient limited by 50 MW/m and S_c=4 W/μm^2.

Figure 3.8 shows the maximum gradient calculated with the available shunt impedance and 100 MW/m input power for a range of single cell re-entrant cavities. The septum thickness' are scaled with frequency such that the 12 GHz cavity has a 1 mm septum and the 3 GHz cavity has a 4 mm septum. The plot shows that the shunt impedance behaviour is the same with a re-entrant section as it was with the pillbox cavities presented in Figure 3.3. The higher frequencies have higher shunt impedance at smaller apertures and the lower frequencies have higher shunt impedance at larger apertures.

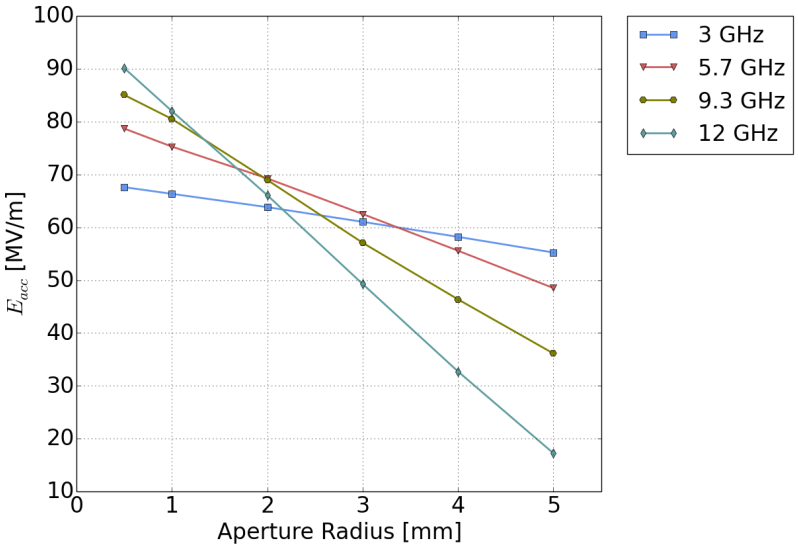

Fig. 3.8 The maximum gradient calculated for a re-entrant pillbox cavity at a range of frequencies and aperture radii. The septum thickness is scaled with frequency the input power is 100 MW/m, and S_c is limited to 4 W/μm^2. Plot courtesy of Graeme Burt.

3.3.1 Nose Cone Optimisation Study

A nose cone optimisation study was performed to investigate the effect of varying the nose cone parameters, shown in Figure 3.9, for different frequency cavities. The plots contain both S- and X-band single cell cavities, 3 and 12 GHz respectively. This is not to compare the frequencies with one another, but to see if the general trends differ between the extremes of the frequencies investigated. Values are normalised to the accelerating gradient achieved with 50 MW input power per metre. The nominal parameters chosen for the study are shown in Table 3.1.

Figure 3.10 shows the effect of varying the distance between the nose cones (G_c) on some chosen important cavity figures of merit. The lower left plot indicates an optimum value of G_c which produces the highest shunt impedance per unit length (Z). As the gap length decreases towards the peak of the curve the peak

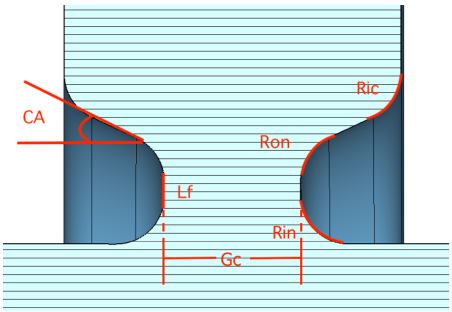

Fig. 3.9 Diagram labelling the parameters on a nose cone geometry.

Nominal nose cone parameters				
	Parameter	X-band	S-band	Units
f	Frequency	12	3	GHz
A	Aperture Radius	2	2	mm
R_{in}	Inner nose radius	0.5	4	mm
R_{on}	Outer nose radius	0.5	4	mm
R_{ic}	Inner corner radius	1	5	mm
G_c	Nose cone gap	6	20	mm
CA	Nose cone angle	65	65	deg
Lf	Nose cone flat	0	0	mm

Table 3.1 The nominal nose cone parameters used in the nose cone optimisation study.

electric field increases - shown in the top left plot - and this raises the shunt impedance. After the peak value the shunt impedance decreases due to the transit time factor. The peak surface magnetic field increases as the gap between the nose cones decreases despite the peak fields increasing. This is due to the nose cone angle remaining constant, thus further reduction of the gap causes the protruding section extend further into the magnetic peak region of the cavity, and enhances the fields.

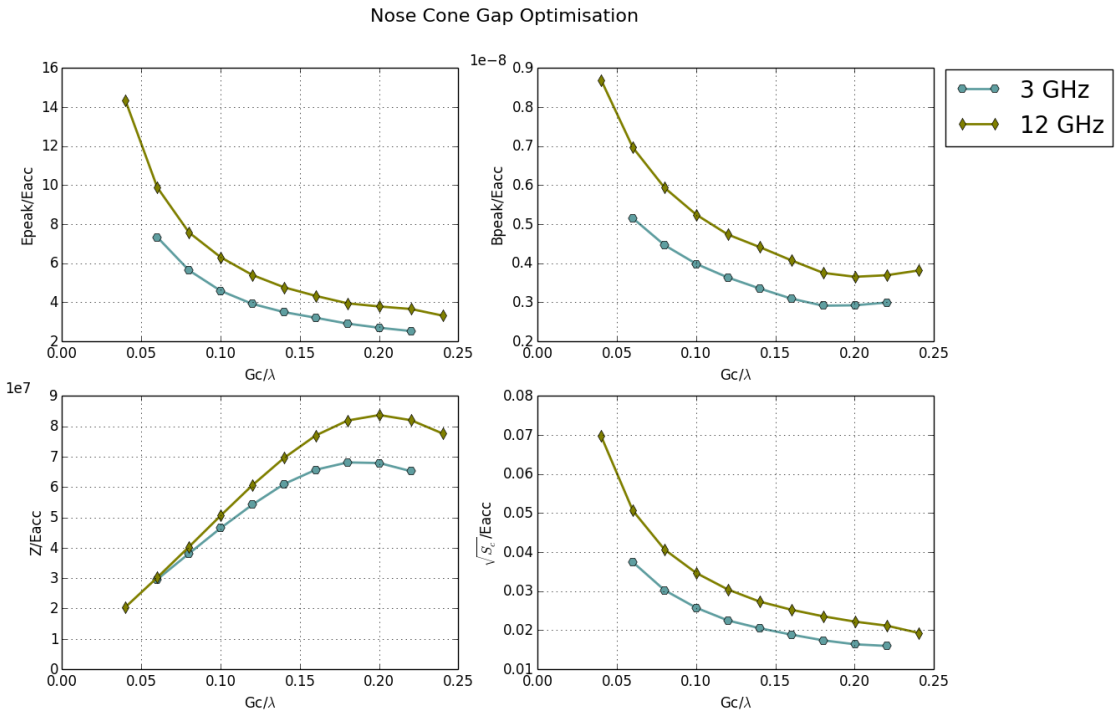

Fig. 3.10 The effect of the gap between the nose cones on shunt impedance and peak fields for both S and X-band.

Figure 3.11 shows the effect of increasing the blend radius on the inner (R_{in}) and outer (R_{on}) edges of the nose cone. In both cases one parameter was kept constant as the other varied. For both frequencies R_{in} has a greater effect on the shunt impedance than R_{on}, and both increase Z as the 'point' of the nose cone sharpens. However both have a similar effect on the peak surface electric field. This is a useful result for optimisation because by reducing R_{on} the peak surface electric field, which is widely regarded as a limiting factor on high gradient operation, is reduced with minimal impact on the shunt impedance. The peak surface magnetic field remains constant which is to be expected given the distance of the nose cones from the magnetic peak region of the cavity. The nose cone radii have no effect on the magnetic peak fields so they have been omitted.

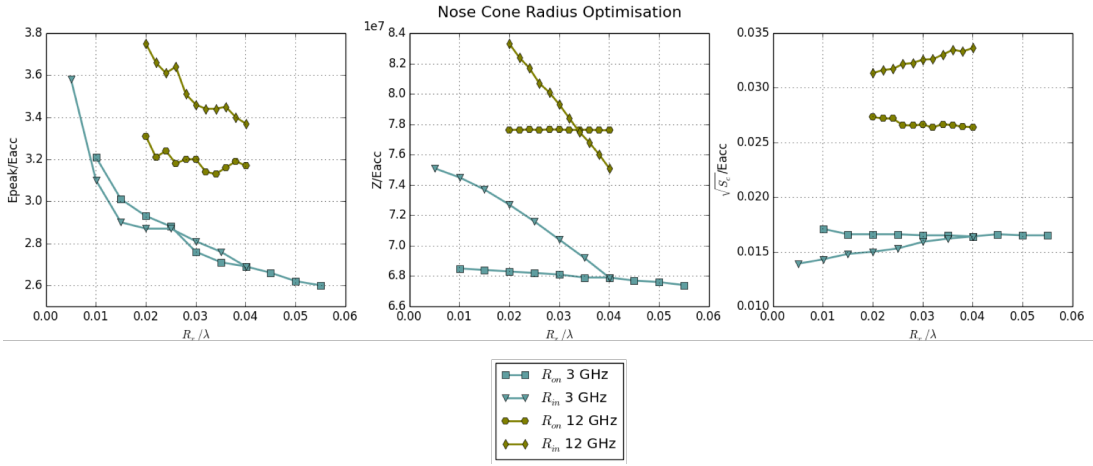

Fig. 3.11 The effect of the nose cone radii on shunt impedance and peak fields for both S and X-band. R_x on the x-axis refers to the radii in the plot legend.

Figure 3.12 shows the effect of varying the nose cone angle on some important figures of merit. The shunt impedance decreases as the nose cone angle increases as does the peak surface electric field this is explained by the width of the base of the cone with respect to the height as was shown in Figure 2.13. As the nose cone angle decreases the field enhancement factor increases. The peak surface magnetic field does not change for S-band but for X-band it reduces slightly. One would expect the magnetic peak to increase as the cone angle pushes the base of the nose cone further into the magnetic peak section of the cavity, but this effect is not seen. The X-band cavity is more sensitive to changes in the nose cone angle than the S-band cavity. This is most visible in the Z plot in the bottom left. Z/E_{acc} stays almost constant for S-band but drops off rapidly after 40°.

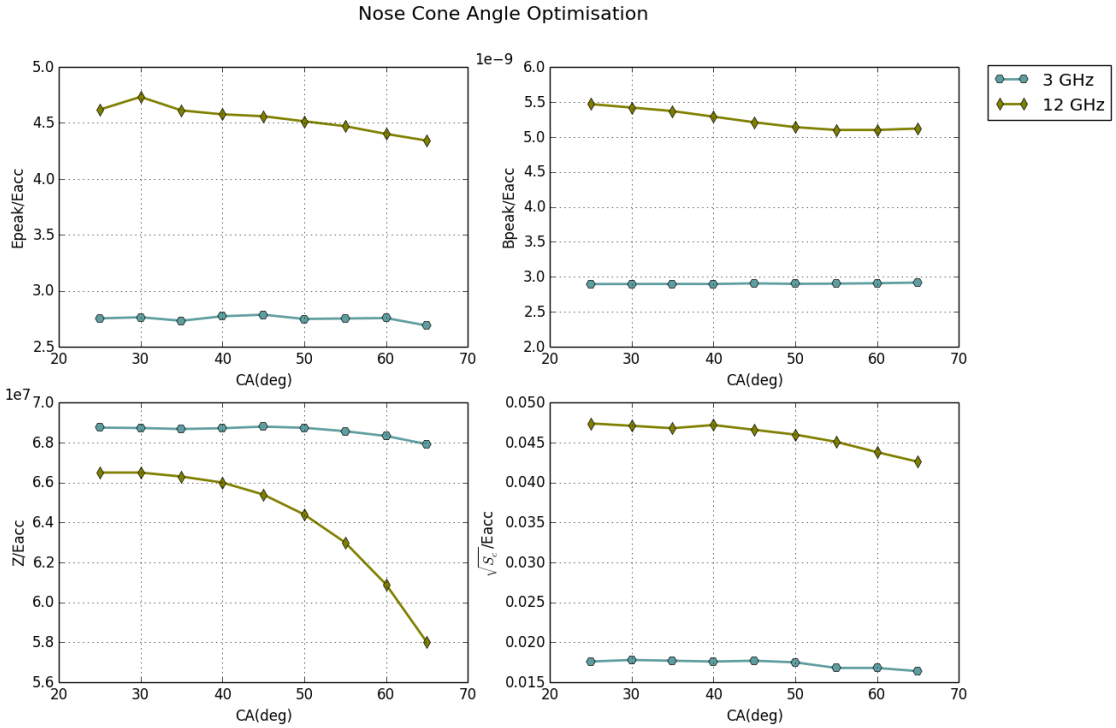

Fig. 3.12 The effect of the nose cone angle on shunt impedance and peak fields for both S and X-band.

Figure 3.13 shows the effect of introducing and increasing the length of the flat section of the nose cone. The trends are similar for both frequencies but are much more pronounced in the lower frequency case, due to a larger range of values being used. The peak surface electric field decreases as the flat 'blunts' the sharp nose cone. In the lower frequency case this is rapid at the start then it saturates as the flat section extends further away from the electric peak region. As expected the peak surface magnetic field increases as the flat raises the radius R_{on} further into the magnetic peak region. The shunt impedance reduces more rapidly than the peak surface electric field, so it is not the most effective parameter in reducing E_{peak} as R_{in} is the most critical parameter for Z. A more effective optimisation would be to reduce R_{on} as that will have a lesser effect on Z for the same reduction in E_{peak} This study was done to investigate the effect of varying the nose cone parameters on the peak fields and shunt impedance, within the range of frequencies we are interested in. It will be referred to throughout this work to inform structure optimisation process. Throughout this thesis, every single structure presented has the nose cones individually optimised for the highest gradient within peak field limits. Every single parameter is optimised in every case, using the lessons learned in this nose cone study about which parameters are more effective for the desired outcome.

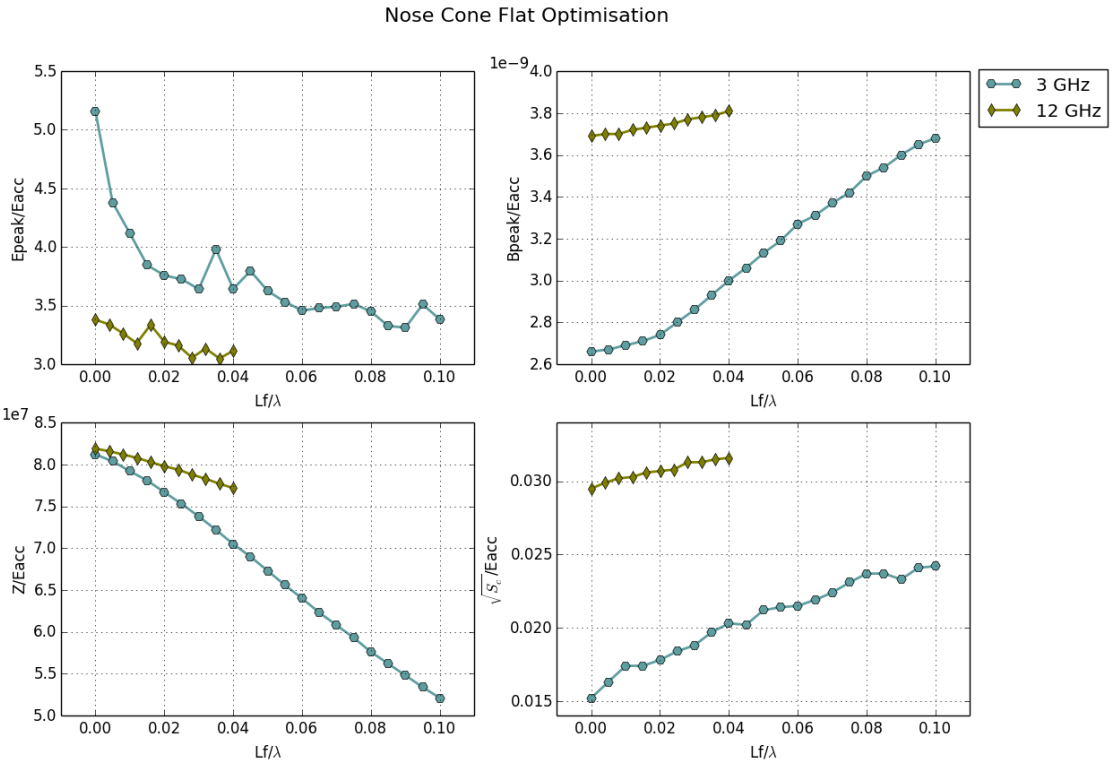

Fig. 3.13 The effect of the flat section of the nose cone on shunt impedance and peak fields for both S and X-band.

3.4 Side-Coupled Standing Wave Structure

3.4.1 k-Factor Study

Only single cell cavities have been considered thus far. In practice it is inefficient to use a single accelerating gap and they are instead coupled together to form multi-cell cavities. When designing multi-cell structures one must consider the coupling between the cells as was mentioned in section 2.5, when discussing the advantageous stability of the $^{\pi}/_{2}$-mode in bi-periodic structures. Multi-cell structures typically have one power coupler, and the power must couple through one cell to the next until the structure is filled (Figure 2.29). If there is insufficient coupling between the drive cell* and its nearest neighbour, the neighbouring cell will likely have a lower field amplitude and potentially a phase error too. We desire uniform field flatness and phase synchronism throughout the cavity for efficient acceleration and thus must consider the amount of coupling between adjacent cells carefully. Increasing the amount of coupling between cells reduces the shunt impedance which is shown in the following section. The coupling slots themselves can induce gradient limiting peak fields so it is desirable to minimise cell to cell coupling. However it is

*The cell in which the power coupler is located

more efficient to couple numerous cells together fed by one power coupler thus one must find an optimum between these considerations. The field amplitude X_{2n} in the n^{th} cell of a bi-periodic resonant cavity can be determined with respect to the field amplitude in the drive cell X_{2m} as

$$X_{2n} \cong (-1)^{n-m} X_{2m} \left[1 - \frac{2(m^2 - n^2)}{k^2 Q_a Q_c}\right] \exp\left[j \frac{4(m^2 - n^2)}{k^2 Q_a} \frac{\delta\omega}{\omega_a}\right] \tag{3.1}$$

where the imaginary term represents the phase shift [77]. The field in the coupling cavity $2n{+}1$ can be calculated as

$$X_{2n+1} \cong (-1)^{n-m} X_{2m} \left[\frac{2n+1}{kQ_a}\right] \exp(j\pi/2) \tag{3.2}$$

In a side-coupled standing wave structure the excited *accelerating* cells on the beam axis are labelled $2n$, and the side-coupled, unexcited *coupling* cells are labelled $2n + 1$, where $n = 0, 1, 2, ...$ Q_a and Q_c are the quality factors for the accelerating and coupling cells respectively. Typically in this sort of structure the *drive* cell, with the power coupler attached, is the centre-most accelerating cell and is labelled $2m$. Thus the end cell is $n = 0$, its nearest neighbour is $n = 1$ and this continues to the centre of the structure where the drive cell is located at $2n = 2m$. Ideally $\omega_a = \omega_c$ for bi-periodic structures. In reality, manufacturing errors and limited tuning can result in a discontinuity in the dispersion curve, the width of this stop-band is represented by $\delta\omega = \omega_c - \omega_a$. In this work $\frac{\delta\omega}{\omega} = 0.0005$. The inter-cell coupling constant k must be chosen such that the end cell had the same field amplitude as the drive cell to ensure adequate coupling. The field flatness target was $\pm 1\%$ and the phase slippage was limited to $\pm 2^\circ$ chosen.

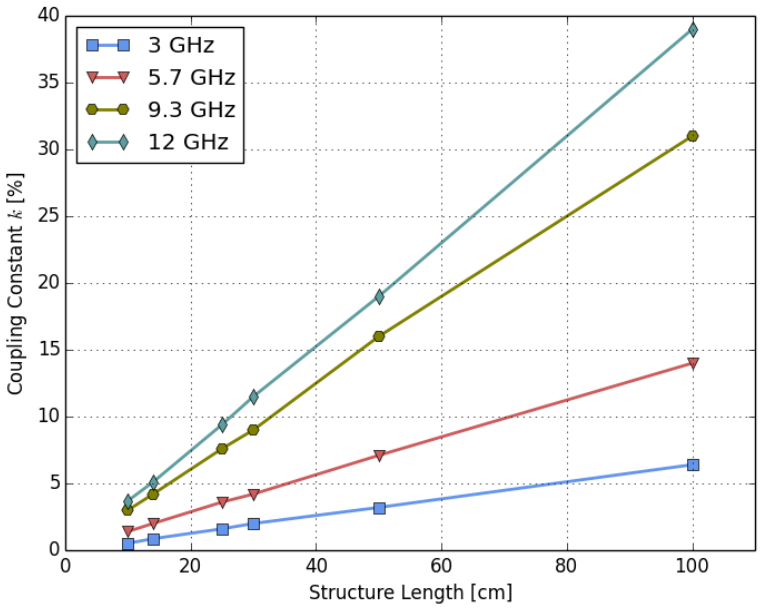

Fig. 3.14 How the coupling requirement to maintain correct phase and field flatness varies with structure length and frequency.

Figure 3.14 shows how the coupling requirement increases with structure length for different frequencies. The coupling requirement increases with frequency which is to be expected given the wavelength λ decreases with frequency, and the length of one cell is a $\lambda/2 \times \beta$ where β is the relativistic velocity of the particle. That means there will be 33 cells in a 3 GHz structure that is 1 meter long, whereas a 12 GHz structure will have 134 cells. Electric coupling through the beam pipe is a possibility for on axis coupled structures, but to get adequate coupling for long structures the aperture would have to opened wide which would degrade the shunt impedance. To keep shunt impedance high it is better to take the coupling cells off axis. Side-coupled standing wave structures couple power from cell to cell magnetically through coupling slots in the outer wall of the cavity. This is shown in Figure 3.15 where one can see the magnetic field distribution of a 12 GHz side-coupled cavity. The slot is simply where the accelerating cell and the coupling cell intersect. As the slot is located within the magnetic peak region of the cavity, there is a high surface magnetic field on the slot.

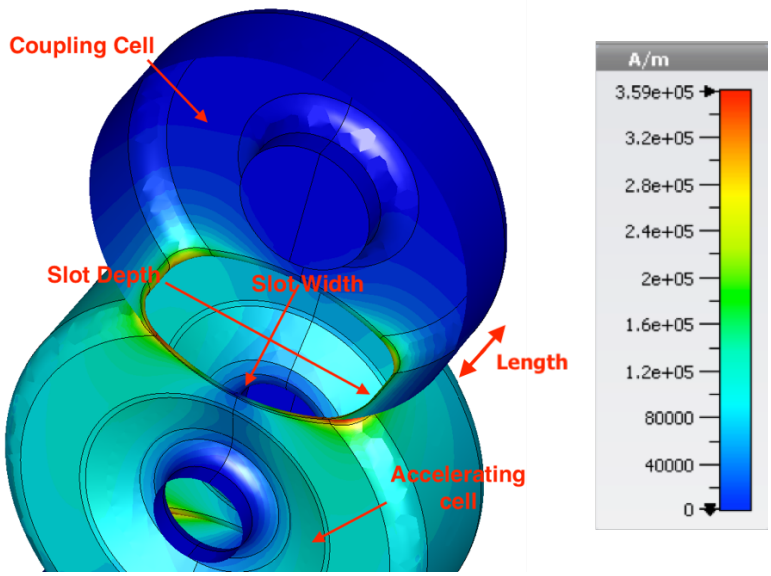

Fig. 3.15 Peak surface magnetic field plot of the side-coupled CST model and the coupling slot geometry.

Coupling is increased by lowering the coupling cell deeper into the accelerating cell. This increases the slot depth labelled in Figure 3.15. The slot width can be increased by increasing the coupling cell length. Traditionally, due to the manufacturing technique side-coupled cells have the same length as the accelerating cell and are offset by half a cell length. In Figure 3.16 one can see the deeper the slot and thus higher the coupling factor, the lower the shunt impedance per unit length. One can increase the coupling factor by a small amount with the coupling cell length without having a dramatic effect on the shunt impedance of the structure.

Initially a 50 cm 12 GHz structure was investigated in CST microwave studio [112]. It contains 67 accelerating cells and required 19% coupling between each cell to maintain field flatness and limit phase slippage. The side-coupled structure is simulated in quadruplets consisting of two accelerating cells and two coupled cells with periodic boundaries. The background material in the simulation environment was set to perfect electrical conductor (PEC) and the vacuum space inside the cavity was built to simplify the meshing by removing completely the copper shell, the vacuum model is displayed in Figure 3.17. In order to increase the coupling as much as possible, the length of the side-coupled cell was maximised until the blend of the coupling slot met the outer radius blend of the accelerating cell. The length of the coupling cell is limited by the meeting of the inner corner blend on the accelerating cell nose cone and the coupling slot blend, indicated in Figure 3.17. In Figure 3.17 the limitation to the depth of the coupling cell is shown. The slot overlapping the inner corner blend is a complex geometry for both simulation and manufacture. A further feature to maximise coupling was removing concentricity

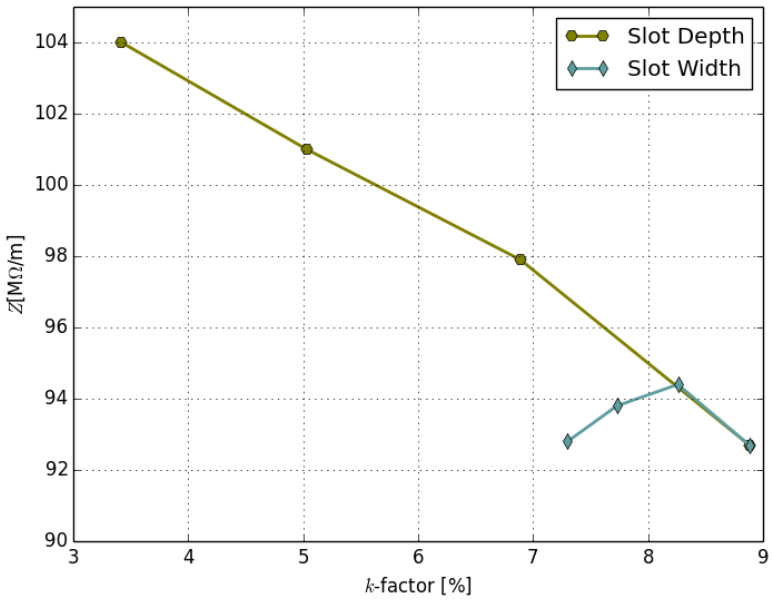

Fig. 3.16 The k-factor can be increased by increasing the length of the coupling slot while having less of an effect on the shunt impedance than increasing the slot depth.

between the coupling cell and its inner capacitive region, shown in Figure 3.17. Raising the inner capacitive region towards the top of the side-coupled cell allowed more space to 'drop' the coupling cell deeper into the accelerating cell. Despite these efforts, the maximum k-factor achieved was 17.6%, just short of the 19% required for a 50 cm structure.

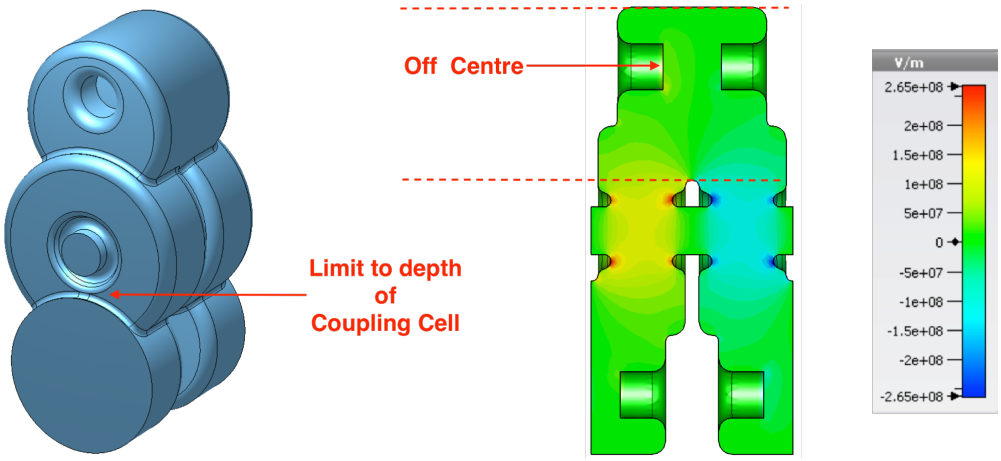

Fig. 3.17 Side-coupled vacuum model and the electric field of the $\pi/2$-mode. This structure had the maximum achieved k-factor at 17.6%.

Since the study presented in this section, a novel side-coupled linac design has been published that offers a soluion to the coupling limitations described. The

3 GHz medical cavity in shown in Figure 3.18. The length of a side-coupled cell is twice that of the accelerating cell [22]. While the ProBE structure has a shunt impedance of 75.5 MΩ/m, the structure in Figure 3.18 has only 60 MΩ/m because the shunt impedance is greatly reduced with the large inter-cell coupling. Thus it isn't advantageous to implement this design in this case, unless one wanted to simplify the machining of the disks and ultimately reduce the cost of manufacture.

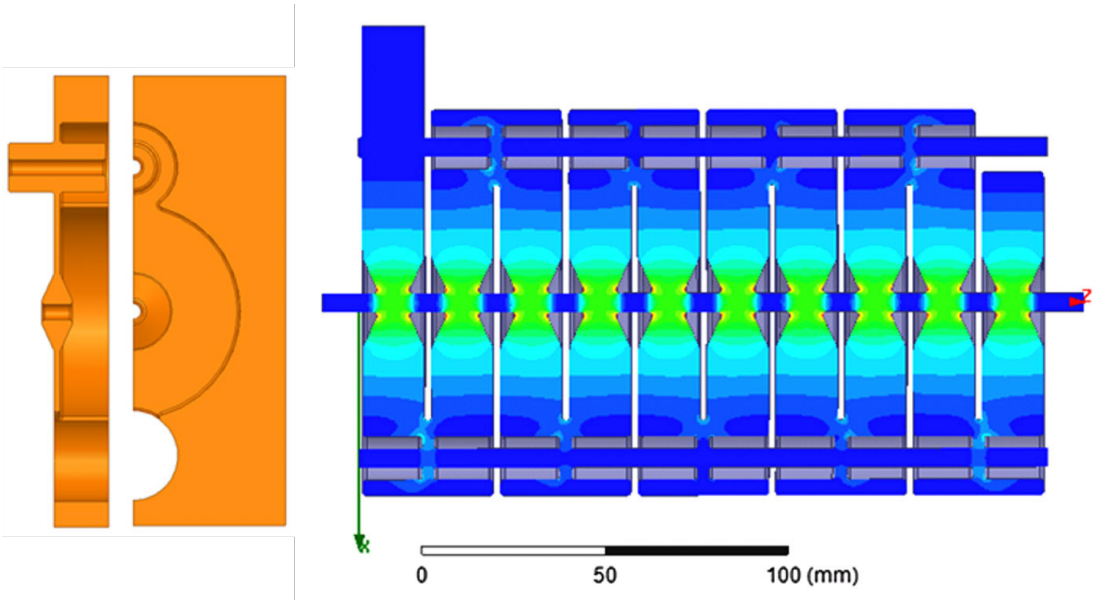

Fig. 3.18 Novel side-coupled cavity design where the inter-cell coupling is maximised. Absolute E-field is shown [22].

3.4.2 12 GHz Multi-cell Structure

As it was not possible to achieve a high enough coupling factor for a 50 cm structure, a structure was optimised for a 12% coupling factor for the possibility of a 30 cm structure. The structure shown in Figure 3.17 could have been 45 cm long in theory however the fields appear to be slightly asymmetric, two of the four peak electric field locations on the nose cone are higher than the other two in each cell. This could introduce beam kicks so the length was limited to 30 cm to avoid this. It also has an aperture radius of 1.75 mm to take advantage of the higher shunt impedance at X-band shown in Figure 3.3. The pillbox cavity alone had a $Z = 80\,\mathrm{M\Omega/m}$ the addition of a nose cone increased this to 110 MΩ/m, then the addition of coupling cells reduced this back down to 81.7 MΩ/m. The pillbox cavity did not see much improvement in shunt impedance through the addition of a nose cone, but the addition of side-coupled cells reduced the shunt impedance and small nose cones were necessary to recover the lost shunt impedance. The values of each structure are summarised in Table 3.2.

Structure	Z [MΩ/m]
Pillbox	80
Pillbox + Re-entrant	110
Pillbox + Re-entrant + 12% coupling	81.7

Table 3.2 Summarises the effect of nose cones and coupling on the effective shunt impedance of a 12 GHz pillbox cavity.

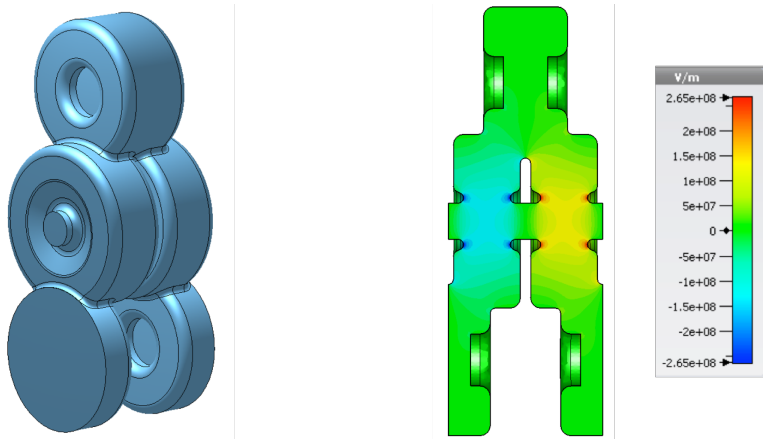

Fig. 3.19 12 GHz X-band side-coupled vacuum quadruplet (left) - electric field E_z (right).

It is assumed the linac will be powered by 50 MW per meter of the machine. Taking into consideration the losses in the power distribution system between the structures and the klystron each 30 cm structure is assumed to have 12.8 MW input power. In simulation the structure shown in Figure 3.19 was calculated to achieve a maximum gradient of 56.1 MV/m limited by input power and shunt impedance. However it is likely the breakdown rate would be too high operating at this gradient because the gradient limited by the maximum S_c of 4 W/μm^2 instead of shunt impedance was slightly lower at 54.2 MV/m. The 12% coupling required for a structure with this many cells meant the modified Poynting vector peaked on the coupling slots as shown in Figure 3.20.

The peak of 4.28 W/μm^2 in Table 3.4 refers to the peak S_c at 56.1 MV/m. A more conservative S_c limit of 4 W/μm^2 was chosen for this optimisation, at that limit the structure would achieve a gradient of 54.2 MV/m for up to a 380 ns flat top pulse length.

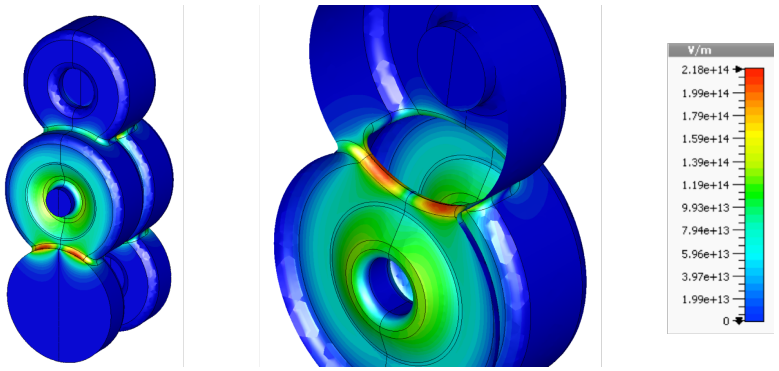

Fig. 3.20 A 12 GHz X-band Side-Coupled Quadruplet. Modified Poynting Vector S_c peaking on the coupling slot.

12 GHz SCSWS Nose Cone			
	Parameter	Value	Units
A	Aperture Radius	1.75	mm
R_{in}	Inner nose radius	0.5	mm
R_{on}	Outer nose radius	0.5	mm
G_c	Nose cone gap	4.5	mm
CA	Nose cone angle	25	deg

Table 3.3 Nose cone parameters for a 12 GHz side-coupled structure. Radii and angle are set to minimum machining limits [117] and the gap is limited by the transit time factor. Parameters are defined in Figure 3.9.

12 GHz SCSWS			
	Parameter	Value	Units
f	Frequency	12	GHz
S	Septum Thickness	1	mm
r_c	Accelerating Cell Radius	8.37	mm
r_{sc}	Coupling Cell Radius	7.29	mm
l	Accelerating Cell Length	7.44	mm
l_{sc}	Coupling Cell Length	8.10	mm
N_{cell}	Number of Accelerating Cells	40	
d	Coupling Slot Depth	2.30	mm
k	Coupling factor	12	%
Q_0	Q-factor	5114	
t_{fill}	Filling time	68	ns
Z	Shunt Impedance	81.7	MΩ/m
E_{acc}	Gradient	56.1	MV/m
E_{peak}/E_{acc}	Normalised Peak Surface E-field	4.16	
H_{peak}/E_{acc}	Normalised Peak Surface H-Field	10.5	A/kV
S_c	Modified Poynting Vector	4.28	W/μm^2

Table 3.4 The parameters for the 12 GHz side-coupled standing wave cavity. Gradient limited by 12.8 MW input power.

Figure 3.21 shows the optimisation of the gap between the nose cones G_c, due to the transit time factor we can see an optimum between 4.5-5 mm. 4.5 mm was chosen as the larger the nose cone, the less electric coupling between the accelerating cells which results in a 7% increase in the coupling factor for the same Z. This is due to the fact that electric and magnetic coupling cancel each other out which is described later in section 3.5. After G_c was optimised the nose cone radii were further optimised to reach the final shunt impedance of 81.7M Ω m.

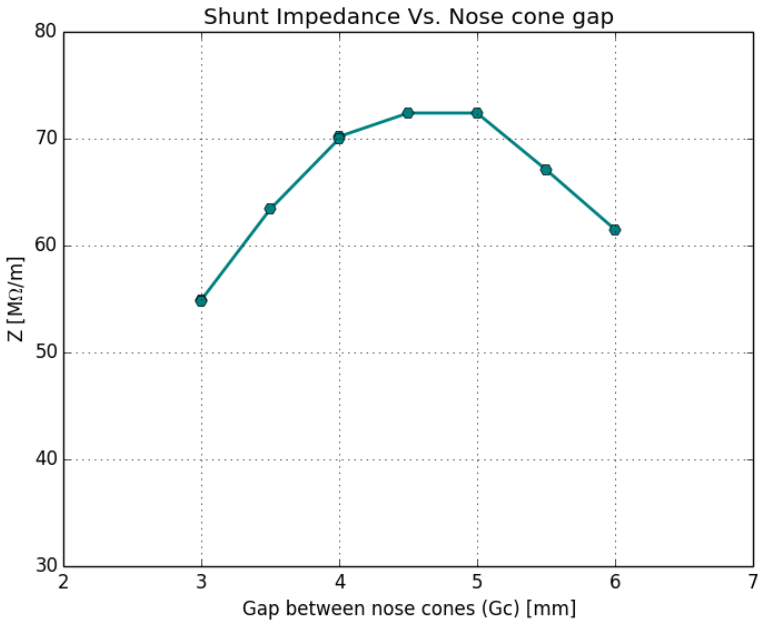

Fig. 3.21 Optimisation of Z using the gap between the nose cones.

3.4.3 3 GHz Multi-cell Structure

The hypothesis at the start of the chapter was that a 12 GHz structure would have a higher shunt impedance with a 1.75 mm radius than a 3 GHz structure. In the following a 3 GHz side-coupled quadruplet was simulated for comparison. The structure, shown in Figure 3.22, was optimised in the same way as the X-band structure with the same gradient limits described in section 3.1.2. Having only 10 accelerating cells in the same 30 cm length, it requires much less cell to cell coupling than the 12 GHz structure; just 2% rather than 12%. The shunt impedance per unit length is 104 MΩ/m which is over 25% higher than the X-band structure. The structure is calculated to reach a gradient of 63.3 MV/m in simulation, limited by input power and shunt impedance. This is shown in Figure 3.23 where G_c=10 mm. The structure would have reached a slightly higher gradient of 64.9 MV/m if there was more available input power and it was limited by just S_c alone. One could

reduce the nose cone radii, R_{in} & R_{on}, to increase the shunt impedance but this would also increase the peak fields.

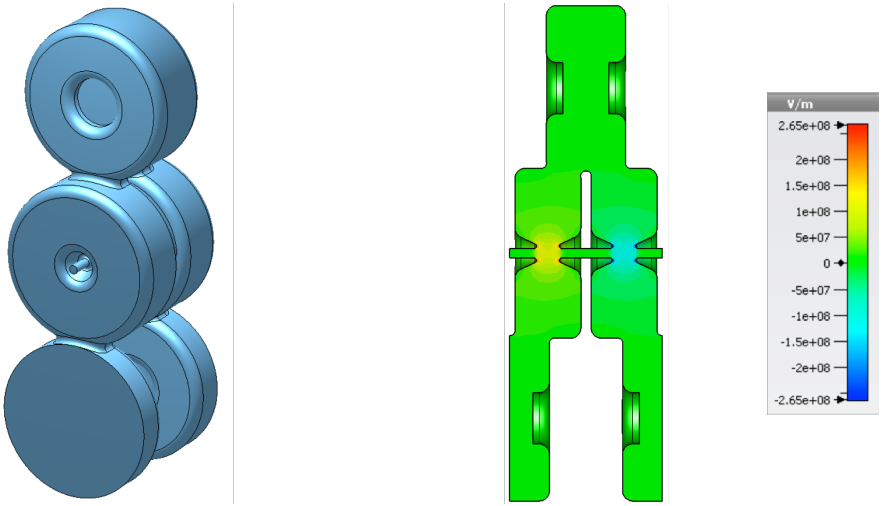

Fig. 3.22 3 GHz S-band side-coupled quadruplet vacuum model (left). Electric field E_z (right).

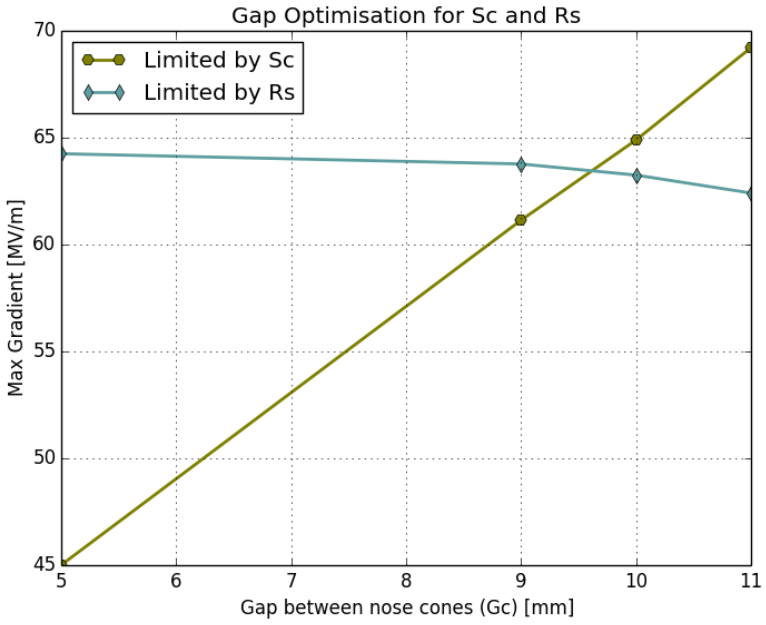

Fig. 3.23 3 GHz S-band Side-coupled quadruplet. Nose cone gap optimisation. Gradient is limited by S_c and shunt impedance with 50 MW/m input power.

3 GHz SCSWS			
	Parameter	Value	Units
f	Frequency	3	GHz
S	Septum Thickness	4	mm
r_c	Accelerating Cell Radius	33.06	mm
r_{sc}	Coupling Cell Radius	32.18	mm
l	Accelerating Cell Length	29.77	mm
l_{sc}	Coupling Cell Length	31	mm
N_{cell}	Number of Accelerating Cells	10	
d	Coupling Slot Depth	1	mm
k	Coupling factor	2.1	%
Q_0	Q-factor	11942	
t_{fill}	Filling time	635	ns
Z	Shunt Impedance	104	MΩ/m
E_{acc}	Gradient	63.3	MV/m
E_{peak}/E_{acc}	Normalised Peak Surface E-field	7.63	
H_{peak}/E_{acc}	Normalised Peak Surface H-Field	4.5	A/kV
S_c	Modified Poynting Vector	3.8	W/μm^2

Table 3.5 The parameters for the 3 GHz side-coupled standing wave cavity. Gradient is limited by 12.8 MW input power.

The S-band structure was calculated to reach a gradient 7.2 MV/m higher than the X-band structure. This is due to the inter-cell coupling. There are *four* times as many cells in an X-band structure than an S-band structure of the same length and it requires 12% coupling between cells whereas the S-band structure only requires 2%. Higher cell to cell coupling degrades the shunt impedance as was presented in Figure 3.16, and this negates the X-band advantage initially envisaged from Figure 3.3. As was explained in Chapter 2 the shunt impedance relates to a cavity's ability to concentrate the available fields around the beam pipe for maximum energy transfer to the beam, hence why smaller apertures exhibit higher shunt impedance, and adding nose cones increases that further. The magnetic coupling utilised in side-coupled cavities creates a hole in the cavity wall, as it is no longer a perfect cavity losses are increased and there is less stored energy available for acceleration.

This effect is shown visible in Figure 3.24 where the quality factor (Q_0) is shown to decrease with an increase in k and the ratio of the shunt impedance from Figure 3.16 to Q_0 or 'R_s *over* Q_0'. R_s/Q_0 is a function only of the cavity geometry, and is decreasing in this case due to the side-coupled cell being lowered

further down the septum of the accelerating cell as increasing the coupling lowers the stored energy.

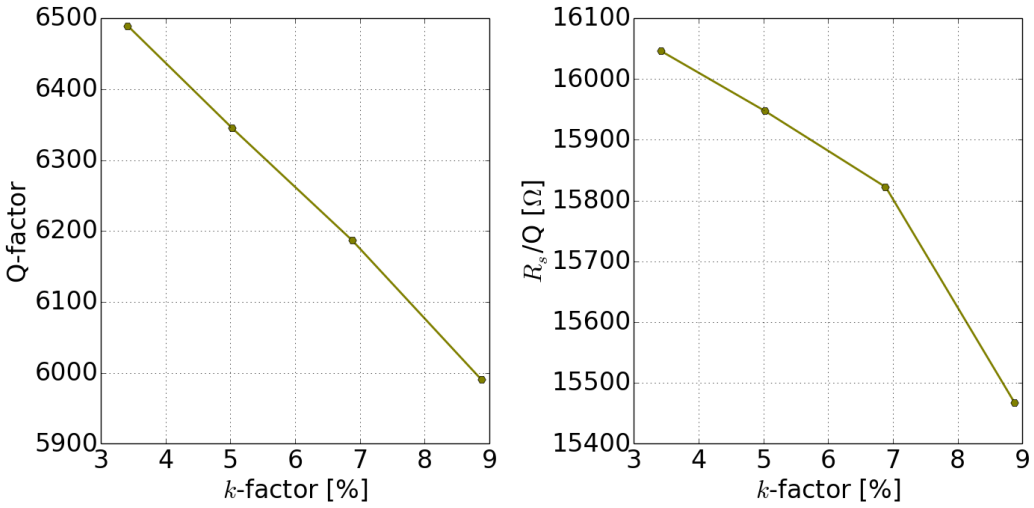

Fig. 3.24 Shunt impedance and unloaded Q-factor reduction with increase in inter-cell coupling for a 9.3 GHz cavity.

The field limiting quantity in this optimisation is S_c, and the S-band and X-band structures have S_c peaks on the nose cones (Figure 3.25) and the coupling slots (Figure 3.20). The peak on the coupling slot is dominated by the magnetic part of the Poynting vector and is a symptom of high inter-cell coupling. The peak on the nose cone is deliberate and contributes to high shunt impedance, as such the peak is more useful in this region of the cavity. Before S_c was proposed as a single field limiting value the peak surface electric field was considered the limit, and the 12 GHz structure has a normalised E_{peak} of 4.16 which corresponds to an E_{peak} of 233 MV/m at it's maximum gradient. X-band standing wave structures have demonstrated acceptable breakdown rates with peak surface electric fields over 300 MV/m [82]. The 3 GHz structure has a much higher normalised E_{peak} of 7.63 nearly double that of the 12 GHz structure. At its maximum gradient that would result in an E_{peak} of 483 MV/m which is extremely high. The magnetic peak field is high on the coupling slots of the 12 GHz structure and to reduce it would mean reducing coupling either by reducing structure length, or the aperture radius. The high electric field on the 3 GHz structure can be reduced with minimal effect on the shunt impedance by increasing the outer nose cone radius as was shown in Figure 3.11 as part of the nose cone optimisation study.

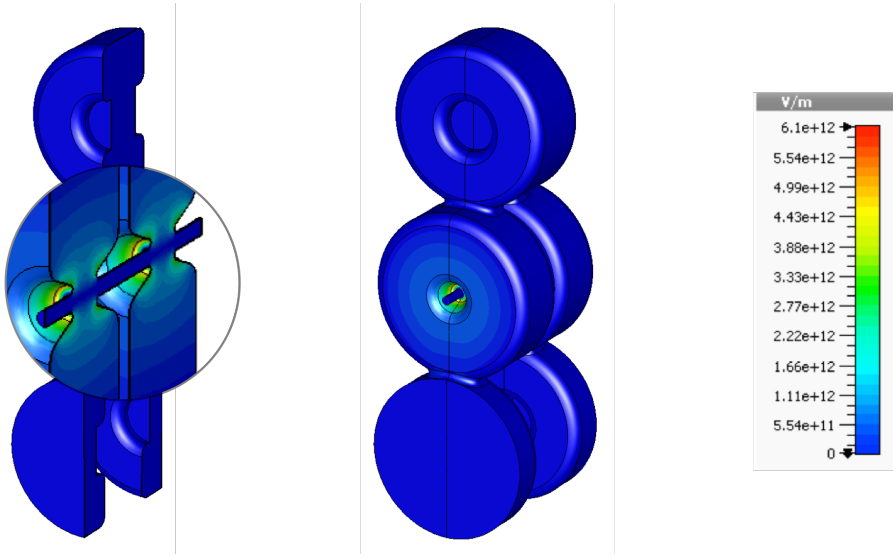

Fig. 3.25 Modified Poynting vector peaks on the nose cone of the 3 GHz side-coupled SW structure as opposed to the coupling slot.

3.4.4 Structure Length

As coupling between cells presented itself as the gradient limiting factor through peak fields and degraded shunt impedance, shorter cavities of 10 cm were also investigated. The same power of 50 MW/m is assumed but split between multiple shorter cavities. Figure 3.26 shows the reduction in gradient for each frequency with the increase in structure length. The effect is increasingly worse as the frequency rises, with 12 GHz seeing an increase in gradient of 12% whereas the 3 GHz only increases by 2%.

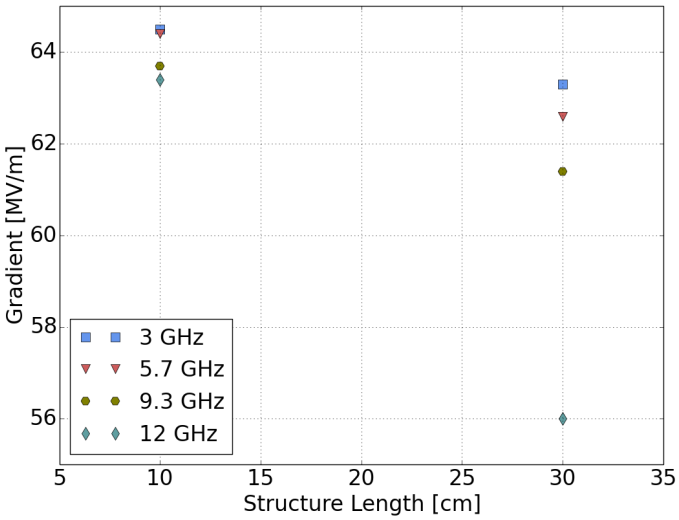

Fig. 3.26 Maximum gradient achieved for side-coupled standing wave structures of different lengths and frequencies. Gradient is limited by 50 MW/m input power and available shunt impedance using $S_c \leq 4\text{W}/\mu\text{m}^2$ as a peak field limit.

Side-coupled standing wave cavities could not benefit from the high shunt impedances demonstrated by X-band pillbox cavities with small apertures. The S- and C-band cavities are able to achieve higher gradients because they require less cell to cell coupling. Making the cavities shorter does not improve things as the power then has to be split between multiple cavities.

3.5 Travelling Wave Structure

Travelling wave structures (TWS) were introduced in section 2.5.3 as structures in which power is coupled into the first cell, and propagates through the structure attenuating in each cell then the power minus the attenuation in the structure is transmitted to a resistive load after the structure. The field amplitude and the power dissipation are affected by the group velocity (v_g) of the structure. Typically TWSs are 'capacitively' or 'electrically' coupled and are forwards travelling wave cavities which means the group velocity propagates from the input to the output. Backwards travelling wave structures have been shown to have optimum performance for lower β cavities [67] and in this case the group velocity propagates from output to input. Power is coupled inductively through coupling slots in the magnetic peak region of the cavity walls. This allows the beam aperture to be kept small to maximise shunt impedance. We are interested in optimising a bTW structure in this study. Figure 3.27 displays the dispersion relation for the 3 single cell structures shown in Figure 3.28. Only the 16 slot structure displays backwards magnetic coupling as

there is more inductive coupling through the coupling slots than capacitive coupling through the beam aperture.

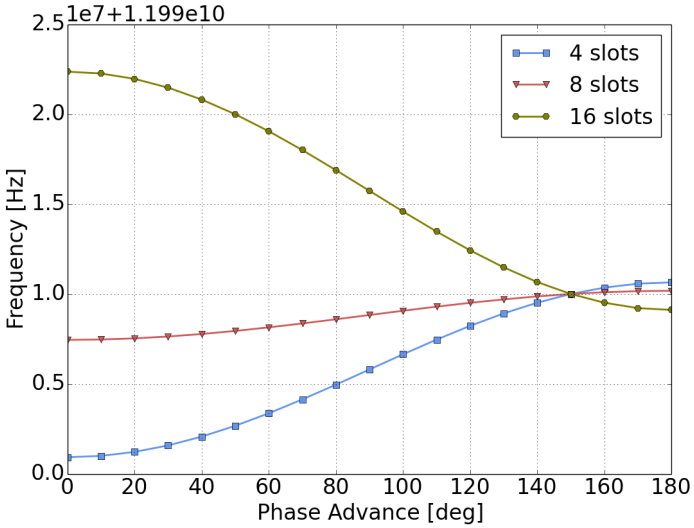

Fig. 3.27 Dispersion diagrams of increasing numbers of circular couplings slots. Only the 16 slot structure exhibits a bTW.

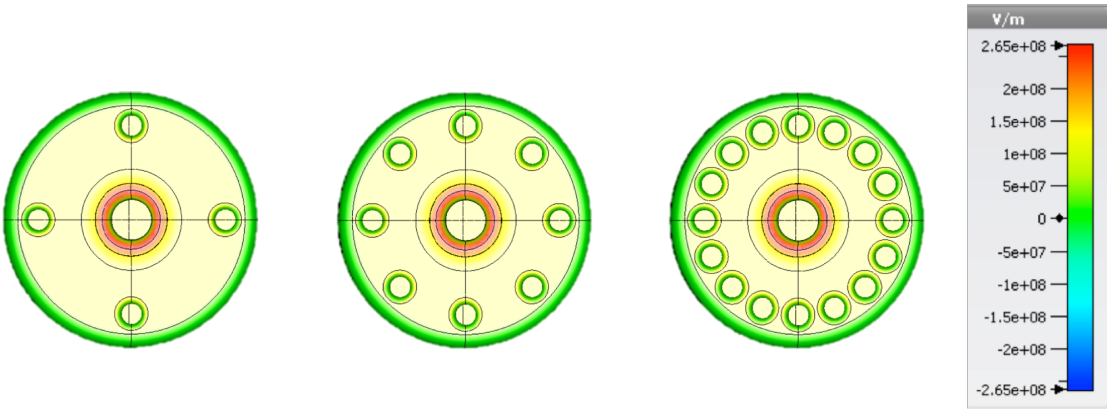

Fig. 3.28 Electric field profiles of circular couplings slots. Various numbers of coupling slots are shown. 4 Slots (left) 8 slots (centre) and 16 slots (right).Only the 16 slot structure exhibits a bTW.

The phase velocity (v_p) of a wave is the velocity with which its phase travels in space. The group velocity (v_g) is the velocity with witch the amplitude-modulation of the wave travels in space. In this case, the group velocity is the velocity with witch the RF travels from the input to the output of a structure. If the group velocity at the beginning of the structure is low, there is high stored energy and high fields because P_T=Uv_g where P_T is the travelling wave power and U is the stored energy and this results in high initial acceleration. If v_g is *too low* at the start however, large ohmic losses in the cavity walls will cause the wave power to decay

rapidly, and therefore not fill the end of the cavity or have very little acceleration at the end. On the other hand if v_g is too high, the stored energy and fields will be too low for high acceleration. Typically travelling wave structures are designed as either constant impedance or constant gradient structures. A constant gradient structure will vary the transverse geometry, the beam aperture or coupling slots, to reduce the group velocity and maintain a constant accelerating field along the structure. A constant impedance structure has uniform cell geometry, thus uniform coupling, throughout the length of the structure, and the power exponentially damps through the structure; every cell has identical parameters including Q_0, v_g, and R_s. The field attenuation per unit length (α_0) also remains constant throughout the structure length, and is given by

$$\alpha_0 = \frac{\omega}{2Q_0 v_g} \tag{3.3}$$

The energy gain over a structure of length L_{cav} depends on the total attenuation parameter τ_0. Maximum energy gain is achieved in a constant impedance structure when $\tau_0 = (e^{\tau_0} - 1)/2$ the solution to which is $\tau_0 \approx 1.26$ [77]. Using this and

$$\tau_0 = \alpha_0 L = \frac{\omega L}{2Q_0 v_g} \tag{3.4}$$

one can calculate the optimum v_g for a given structure length.

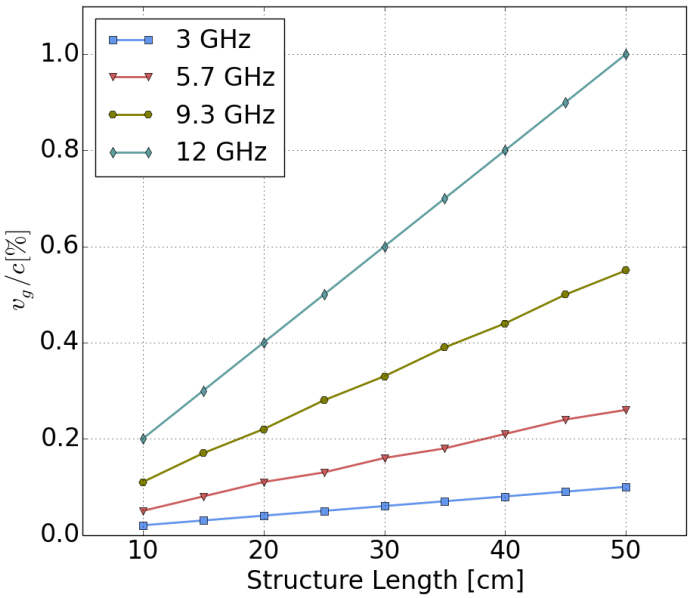

Fig. 3.29 Approximate optimum group velocity for a cell phase advance φ of $2\pi/3$.

Figure 3.29 shows the optimum group velocities for maximum energy gain for 3-12 GHz travelling wave structures of varying lengths. These values were calculated

using the approximate Q-factor values shown in Table 3.6, taken from single cell re-entrant pillbox cavity simulations. A 12 GHz structure has 4 times the number of cells in a given length than a 3 GHz structure but the optimum group velocity increases by 10 times for a 50 cm structure.

Band	Frequency (GHz)	Q
S-band	3	13000
C-band	5.7	9000
X-band	9.3	7000
X-band	12	5000

Table 3.6 Approximate Q-factor values for the selection of frequencies considered in this study.

3.5.1 Coupling Slot Study

Backwards travelling wave structures couple RF power magnetically through coupling slots in the peak magnetic region of the cavity walls. In the case of constant gradient structures, high enough group velocity must be achieved at the start of the structure to account for power losses throughout the length of the structure. Various coupling slot geometries were investigated to maximise v_g, and Z, while minimising gradient-limiting peak fields. 12 GHz single cell cavities were simulated at phase advances of $\varphi = \frac{2\pi}{3}$, $\varphi = \frac{5\pi}{6}$, and $\varphi = \frac{7\pi}{6}$. Figure 3.30 shows some of the many variations of coupling slots investigated.

Shapes include circular, racetrack, dee, and elliptical. The radius of circular slots is varied to vary the group velocity. The angle of racetrack, elliptical and dee slots is varied as is shown in Figure 3.31, which also varies the group velocity as it changes the size of the slot. Another parameter shown in Figure 3.31 is position which is also varied in the study, along with the number of coupling slots.

In Figure 3.32 the variation in group velocity with the different parameters is shown. Achieving high group velocity is limited by the space left between coupling slots. If remaining septum space between slots is too small, the septum could deform and detune or even fail during manufacture. At least 2 mm of copper was left between each coupling slot, while trying to accomplish the maximum coupling between two cells. It is advantageous to not be limited by a relatively low maximum group velocity. The largest group velocity in this study was achieved with 4 racetrack slots, followed by 4 circular slots shown in the bottom right plot of Figure 3.32. By minimising the number of spaces between slots, one can maximise the area occupied by coupling. Group velocity is not the only concern, it is important to recognise the effect the coupling slot parameters have on the main cavity figures of merit, while also acknowledging the group velocity achieved.

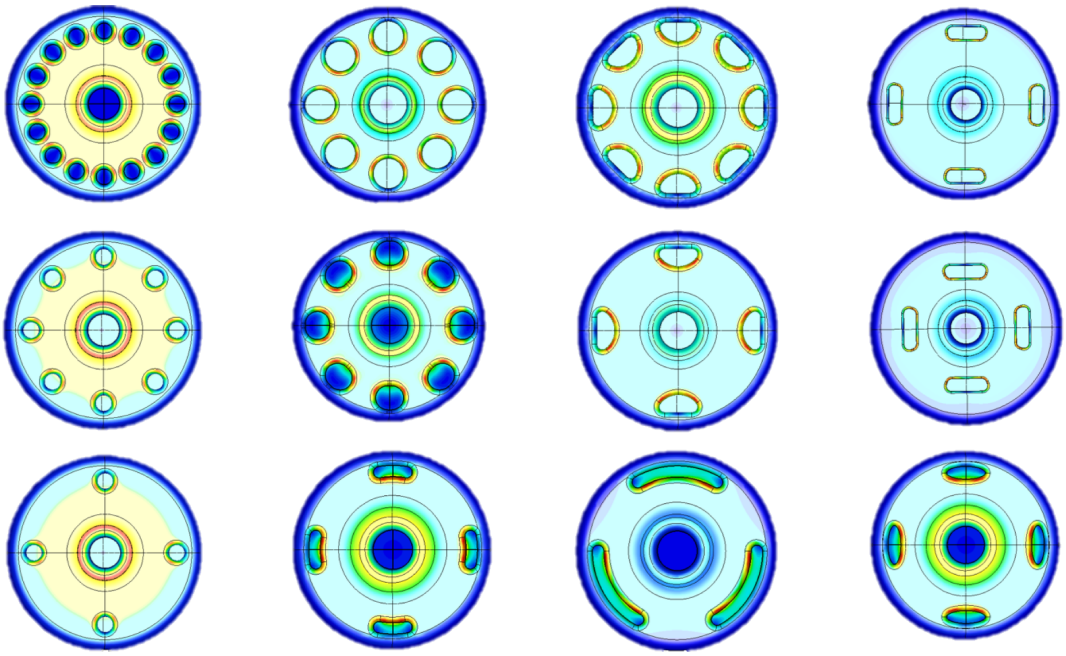

Fig. 3.30 Geometries of the coupling slots studied.

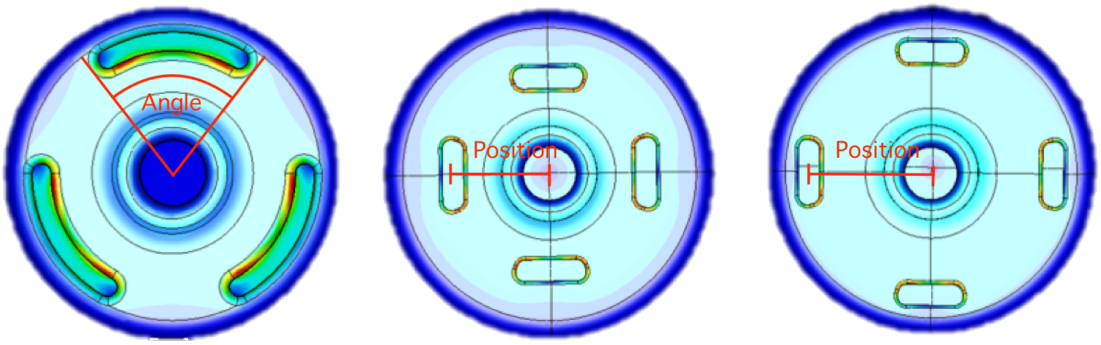

Fig. 3.31 Definitions of 'Angle' and 'Position' in coupling slot optimisation.

Higher group velocity will result in higher peak fields, so only similar v_gs can be fairly compared with one another.

Figure 3.33 shows the variation in shunt impedance and coupling slot parameters. A general trend seen throughout all 4 plots is an increase in group velocity means a decrease in shunt impedance. As was observed with the k-factor with standing wave structures, an increase in coupling between cells decreases the shunt impedance and thus final gradient for a fixed input power. The elliptical slots exhibit lower Z for the same v_g as other slot shapes. The structure with four racetrack slots can achieve a higher shunt impedance for a given v_g than the other slots. Because of the way the 'Dee' shaped slots are parametrised, an increase in 'radius' actually decreases the size of the slot and we can see throughout the variation in v_g the

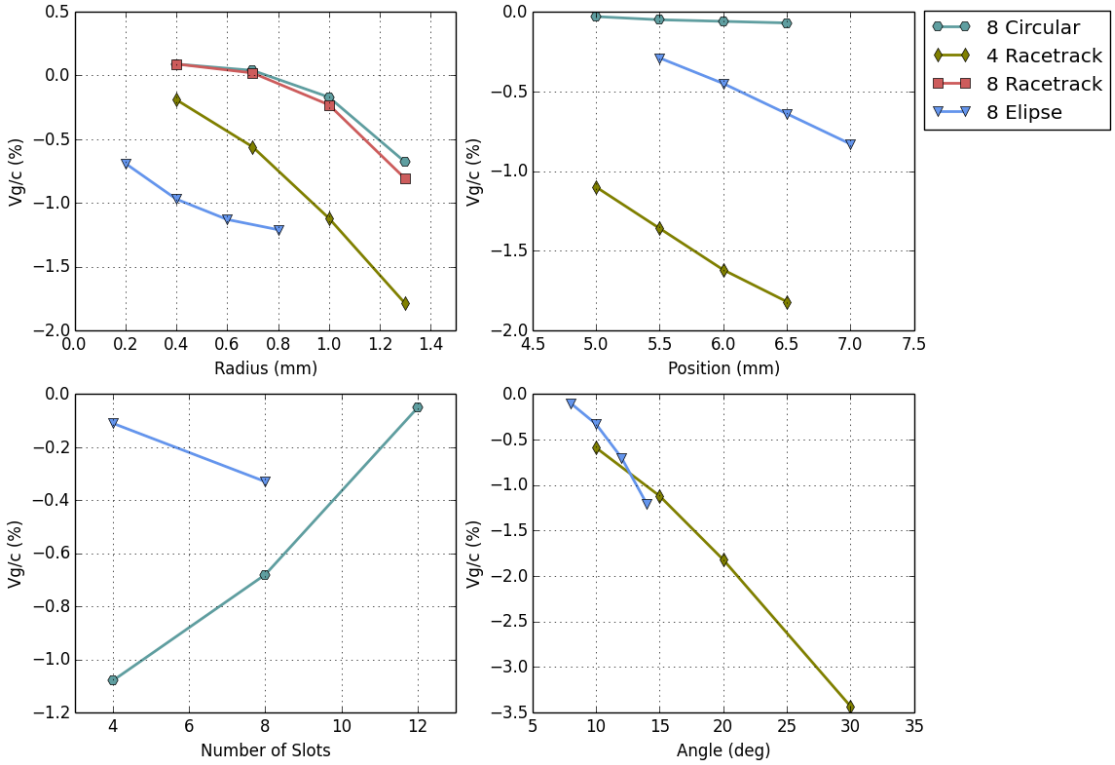

Fig. 3.32 The effect of varying coupling slot parameters on the group velocity of the wave in the structure for $\varphi = \frac{2\pi}{3}$.

shunt impedance stays fairly constant. Interestingly the 8 circular slots and 8 racetrack slots have a very similar response. This is due to the 2 mm between the slots. Racetrack slots with a small angle are essentially circular. A comparison between the two is shown in Figure 3.34.

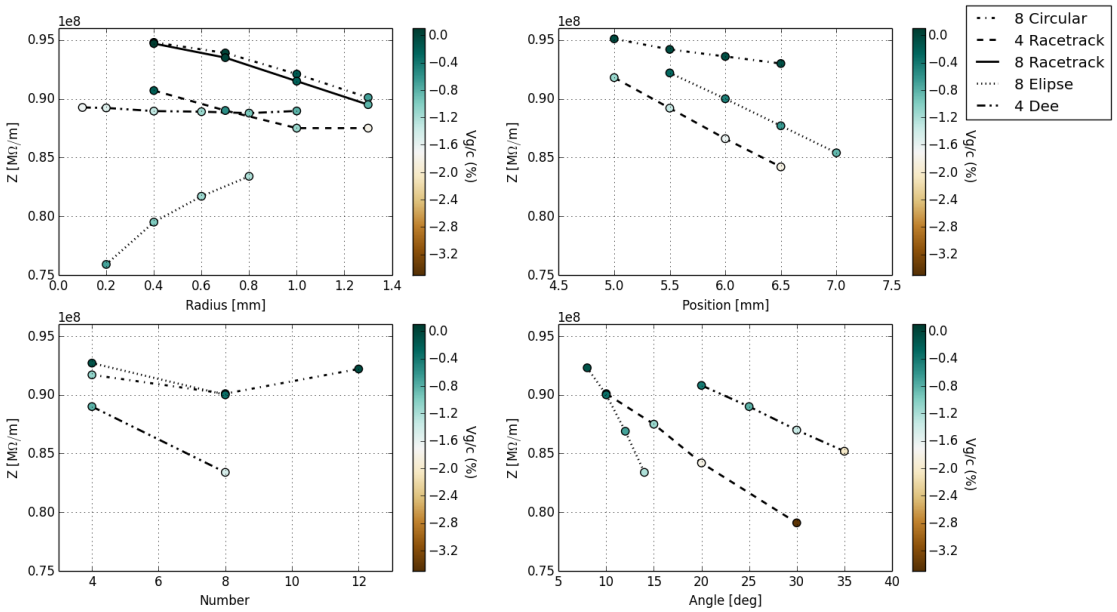

Fig. 3.33 Shunt impedance data with group velocity shown on colour bar for $\varphi = \frac{2\pi}{3}$.

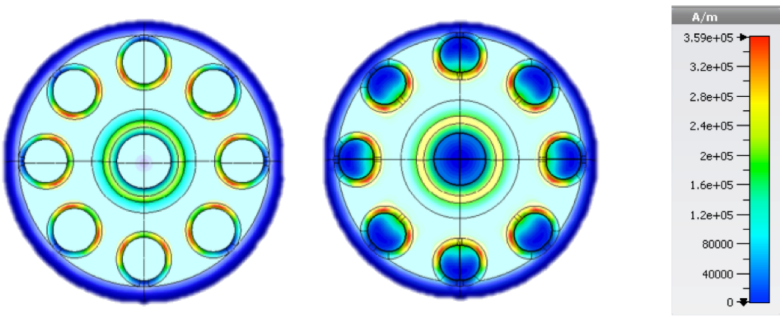

Fig. 3.34 The similarity in geometry between 8 circular slots and 8 racetrack slots.

Figure 3.35 shows the variation in the normalised peak surface magnetic field with coupling slot parameters. As backwards travelling wave structures are coupled magnetically, the higher the v_g the higher the peak magnetic fields. Although the 8 racetrack slot and circular slots lie almost directly on top of each other, it is worth noting that the 8 racetrack slots has slightly higher v_g in each case. It is also apparent that the circular and 8 racetrack slots have a lower peak magnetic field in the lower v_g range than the other geometries for the same v_g. The v_g can also be significantly increased by increasing the number of slots, without a significant increase in the peak surface magnetic field.

Figure 3.36 shows how the coupling slots change the peak modified Poynting vector. S_c peaks on the coupling slots so it is important to minimise this, and the higher the v_g the higher the peak S_c. Additionally, the so far poorly performing elliptical slot exhibits lower peak S_c for higher group velocities than the circular

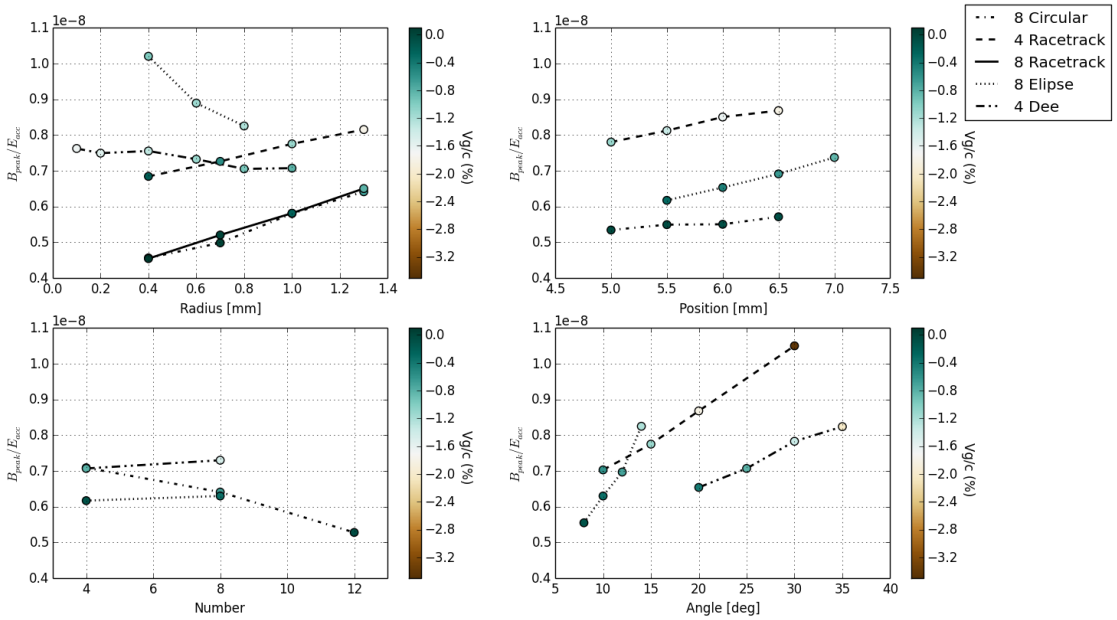

Fig. 3.35 The peak surface magnetic field data with group velocity shown on colour bar for $\varphi = \frac{2\pi}{3}$.

and 8 racetrack slots. Also, like with the magnetic field, the group velocity can be increased by increasing the number of slots without much increasing peak S_c.

Phase Study

A 12 GHz single cell cavity with 'Dee' shaped coupling slots was simulated at phase advances of $\varphi = \frac{2\pi}{3}$, $\varphi = \frac{5\pi}{6}$, and $\varphi = \frac{7\pi}{6}$ to investigate the effect of phase advance on the important cavity figures of merit. Figure 3.37 indicates $\varphi = \frac{2\pi}{3}$ to have the lowest shunt impedance for any investigated group velocity. Also in this plot at $\varphi = \frac{5\pi}{6}$ a slot with an angle of $\psi = 25°$ has a higher shunt impedance for the same group velocity than a slot with $\psi = 30°$, so it may be an advantage to reduce the slot angle and instead increase the thickness of the slot for the same v_g when optimising future structures. $\varphi = \frac{5\pi}{6}$ has the highest shunt impedance, but does not as easily reach as high group velocities as the $\varphi = \frac{2\pi}{3}$ structure.

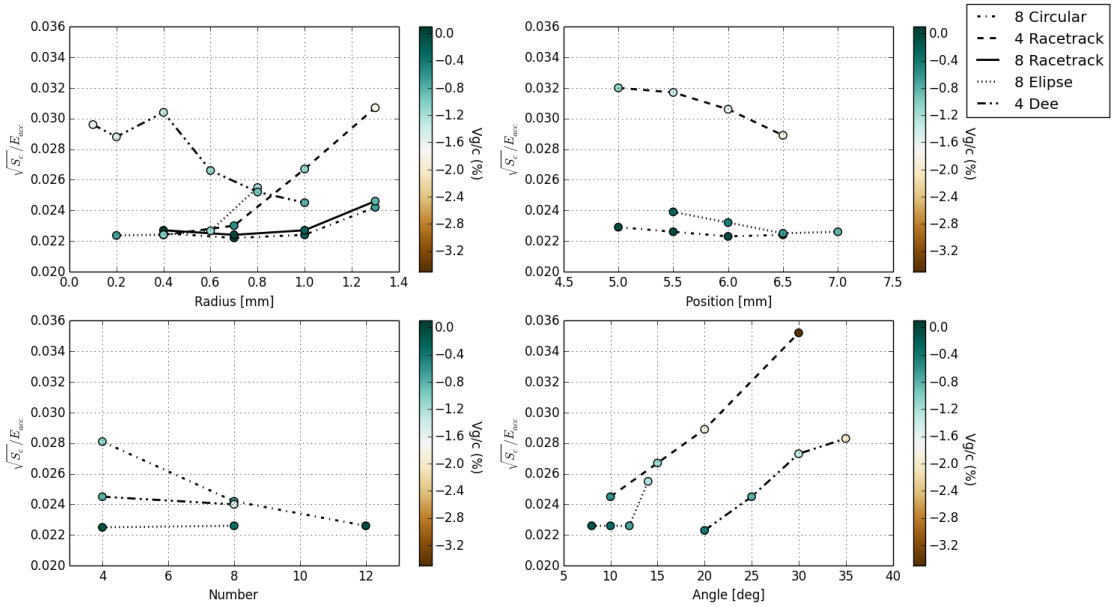

Fig. 3.36 The peak modified Poynting vector field data with group velocity shown on colour bar for $\varphi = \frac{2\pi}{3}$.

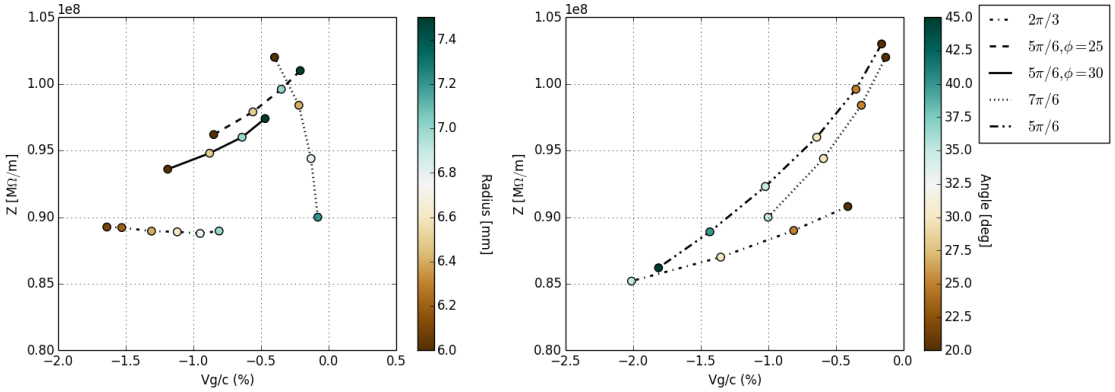

Fig. 3.37 Shunt impedance of structures with varying phase advances. ϕ in this plot represents the slot angle ψ for the only structures with fixed ψ.

In Figure 3.38 the 3 phase advances are split into 3 distinct bands. The lowest normalised E_{peak} is $\varphi = \frac{2\pi}{3}$ followed by $\varphi = \frac{5\pi}{6}$ then by $\varphi = \frac{7\pi}{6}$. The nose cones are in the peak electric field of the cavity; they were identical for all phases with the length of the gap scaled with the length of the cell. The normalised E_{peak} for the $\varphi = \frac{7\pi}{6}$ is realistically too high for high gradient operation.

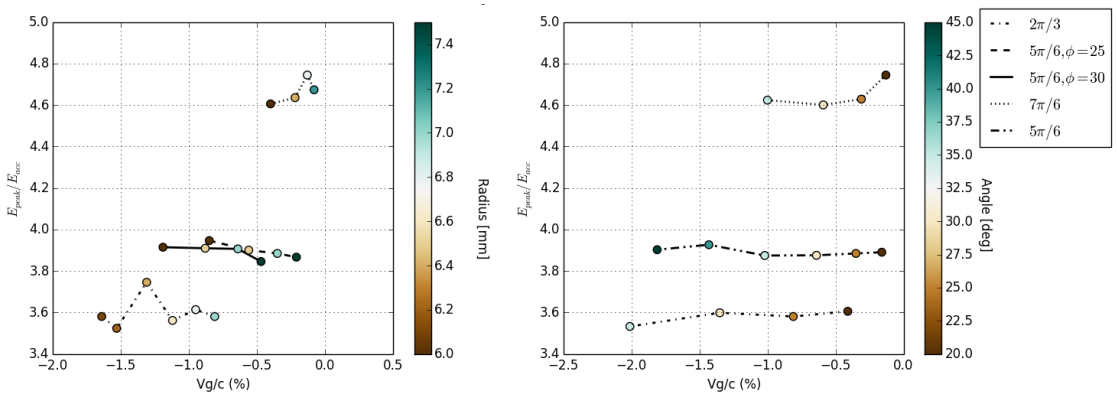

Fig. 3.38 Normalised peak electric field of structures with varying phase advances. ϕ in this plot represents the slot angle ψ for the only structures with fixed ψ.

Figure 3.39 shows the peak surface magnetic field for each structure. The $\varphi = \frac{2\pi}{3}$ had the lowest B_{peak} and the highest v_g which are both advantageous given the structure is being optimised for high inter-cell coupling. The peak surface magnetic field for the $\varphi = \frac{5\pi}{6}$ structure rapidly increases with v_g.

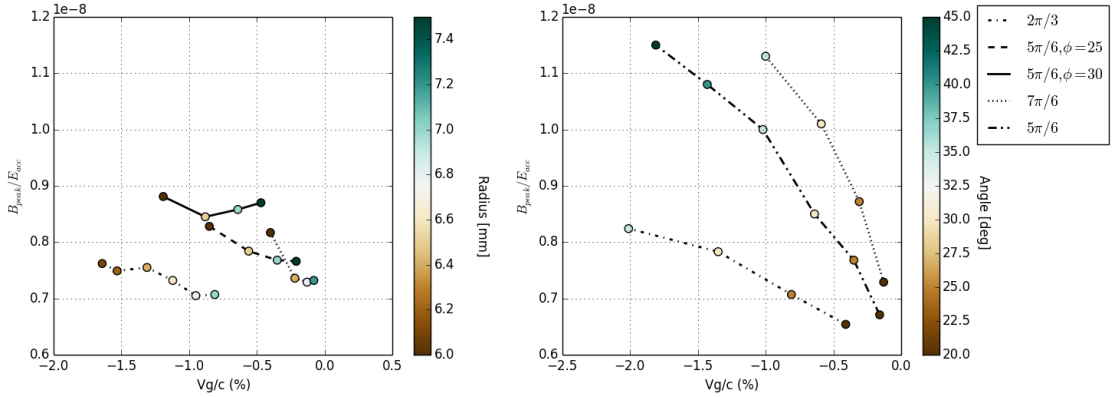

Fig. 3.39 Normalised peak magnetic field of structures with varying phase advances. ϕ in this plot represents the slot angle ψ for the only structures with fixed ψ.

Figure 3.40 unsurprisingly shows that the trends for S_c follow that of the peak surface electric and magnetic fields. The $\varphi = \frac{7\pi}{6}$ structure has the highest S_c for the lowest v_g. The $\varphi = \frac{2\pi}{3}$ structure and the $\varphi = \frac{5\pi}{6}$ are very similar, with $\varphi = \frac{2\pi}{3}$ only slightly lower for some values of v_g.

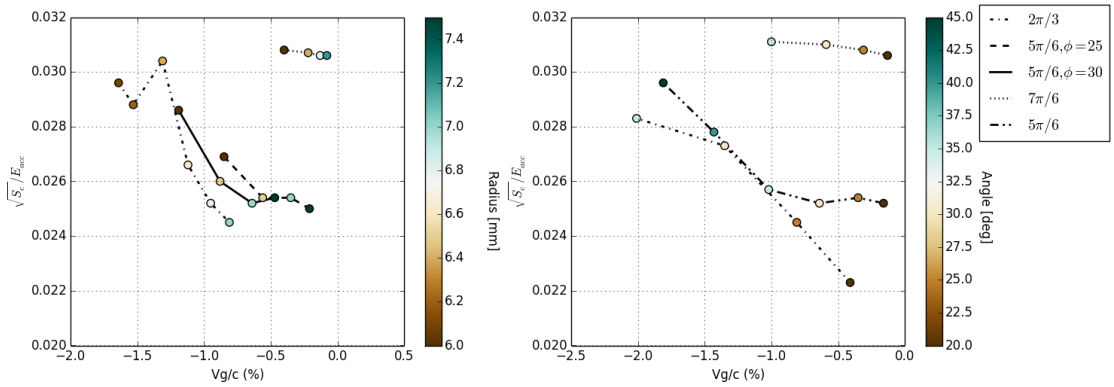

Fig. 3.40 Normalised modified Poynting vector of structures with varying phase advances. ϕ in this plot represents the slot angle ψ for the only structures with fixed ψ.

Having investigated a range of coupling slot styles and phase advances, two structures were selected for further optimisation, using what was learnt in the coupling slot study. One $\varphi = \frac{2\pi}{3}$ structure as it has a greater range of v_g and consistently had lower peak fields than the other phase advances. However the $\varphi = \frac{5\pi}{6}$ structure had the highest shunt impedance per v_g and high gradient operation is the priority for ProBE, so that structure will be further optimised too.

As the coupling slots are in the magnetic peak region of the structure, coupling slots were chosen mainly for their low peak magnetic field. Circular slots were chosen for the $\varphi = \frac{2\pi}{3}$ structure. 8 racetrack slots were chosen for the $\varphi = \frac{5\pi}{6}$ structure because this phase advance had a smaller range of achievable v_gs, and the racetrack slot geometry showed a slightly higher v_g than the circular slots.

3.5.2 Backwards Travelling Wave Structures

A 50 cm travelling wave structure has around 100 cells coupled together at a phase advance of $\frac{2\pi}{3}$. Figure 3.33 shows that only the '4 Racetrack' and '4 Dee' could achieve $> 2\%$ coupling required for a structure of that length. The 8 slot structures simulated had lower peak surface magnetic fields for the same v_g as the 4 slot geometries, thus it was decided to continue optimisation of those rather than the 4 slots and instead use a shorter structure < 30 cm in length. A 30 cm structure at 12 GHz has an optimum group velocity[†] of 0.6% of the speed of light. Some single cell structures with periodic boundaries were simulated to investigate the gradient performance at sufficient group velocities. The nose cone parameters were optimised individually for each structure, informed by the nose cone optimisation study already performed. Single cell simulations are not as informative for travelling wave structures as they are for standing wave structures due to the way the field

[†]Approximate optimum group velocity for a constant impedance structure.

decays throughout the structure. The group velocity, power, attenuation, and gradient in each cell of the entire structure must be considered to get a good indication of how the structure will perform. For every structure in this section, the size of the coupling slots was swept using the Eigenmode solver in CST. The shunt impedance, Q-factor and fields were determined as a function of group velocity to allow for whole structures to be modelled. The same mesh was used as in the rest of this chapter; a tetrahedral mesh with 40 cells per wavelength and third order curvature. The gradient limits and input power also remain the same.

The gradient of the X-band side-coupled standing wave structure investigated earlier was limited by inter-cell coupling. 12 GHz travelling wave structures are investigated in the following section to see if they still have high shunt impedance when cell to cell coupling is included in the simulation. The $\varphi = \frac{7\pi}{6}$ structure had high peak fields and mediocre shunt impedance, so will not be considered as a full structure. However the $\varphi = \frac{2\pi}{3}$ with 8 circular coupling slots will be considered as will the $\varphi = \frac{5\pi}{6}$ with 8 racetrack slots.

Figure 3.29 shows the optimum group velocity for a 30 cm structure length is $\approx 0.6\%^{v_g}/_{c}$. It is assumed 6×30 cm structures would fit in 3 metres allowing 120 cm of beam transport line between structures for matching sections to keep the transverse beam size small through the cavities. With 1.8 m of accelerating length a gradient of 55 MV/m would be necessary for the full 100 MeV acceleration. Accounting for off crest acceleration, for the beam to see 55 MV/m at a synchronous phase of 20° (See Chapter 5) we require the peak gradient to be 60 MV/m. On top of this we include a 5 MV/m safety margin to account for unforeseen losses such as losses in the RF distribution network that is yet to be designed. Thus the gradient we aim for in the small aperture optimisation is 65 MV/m.

12 GHz bTW single cell $\varphi = \frac{2\pi}{3}$

Figure 3.41 shows the modified Poynting vector distribution for a 12 GHz structure with $v_g = 0.65\%^{v_g}/_{c}$; the S_c peak is on the coupling slots. Limited by $S_{c_{max}} = 4$ W/μm^2 alone it is calculated to have a gradient of > 81MV/m, however limited by available power and shunt impedance it is calculated to peak at 58 MV/m.

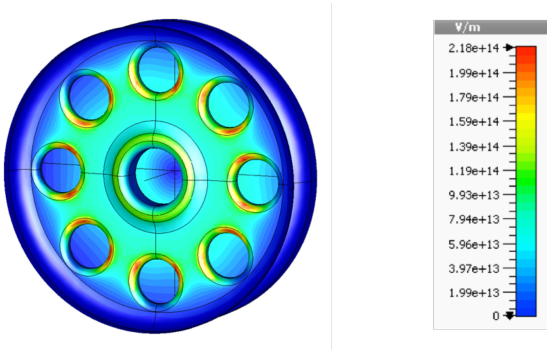

Fig. 3.41 The electric field profile for a 12 GHz single cell cavity $\varphi = \frac{2\pi}{3}$ with 8 circular coupling slots.

Figure 3.42 shows S_c in each cell throughout the structure and the gradient in each cell. The colour bar indicates the changing group velocity through the structure, in this case it is a constant impedance structure so it remains constant. The S_c peak in the first cell is almost 50% over the limit for the acceptable breakdown rate of 1×10^{-6} bpp/m, and the overall average gradient is only calculated to reach 55 MV/m.

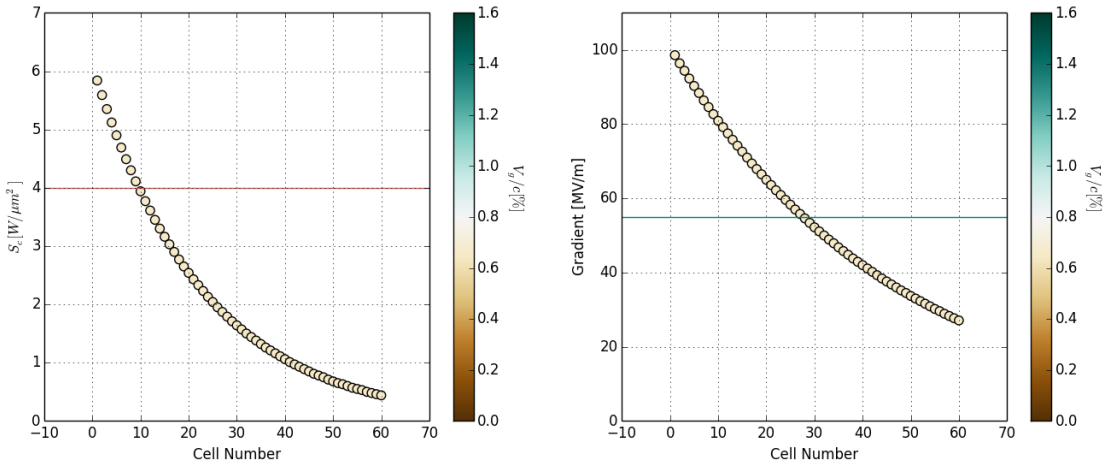

Fig. 3.42 The modified Poynting vector and gradient across a 60 cell 12 GHz $\varphi = \frac{2\pi}{6}$ constant impedance structure. The red bar indicates the maximum allowable S_c and the blue bar indicates the overall structure gradient of 55 MV/m.

Figure 3.43 shows the S_c and gradient variation through a constant gradient structure where the group velocity is decreased throughout the structure by tapering the coupling slots as shown in Figure 3.44, to keep the gradient constant. Attempting the desired 65 MV/m in each cell requires a high group velocity of 1.5% of the speed of light. Although the S_c in this structure remains below the limit of 4 W/μm^2, the field attenuation is too high to fill the final cells towards the output of the cavity.

Thus a 30 cm structure is not adequate using this $\varphi = \frac{2\pi}{3}$ 12 GHz constant gradient structure with 8 circular slots.

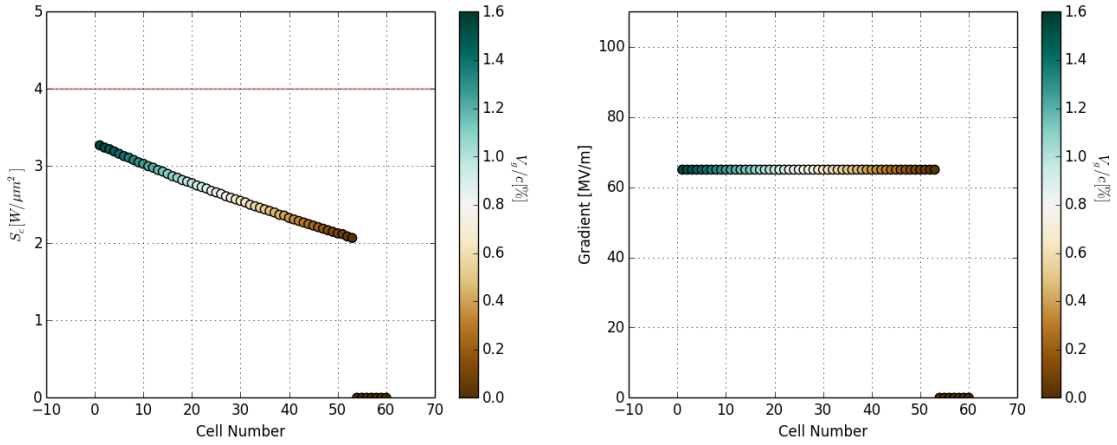

Fig. 3.43 The modified Poynting vector and gradient across the 60 cell 12 GHz $\varphi = \frac{2\pi}{6}$ constant gradient structure. The red line indicates the peak S_c limit.

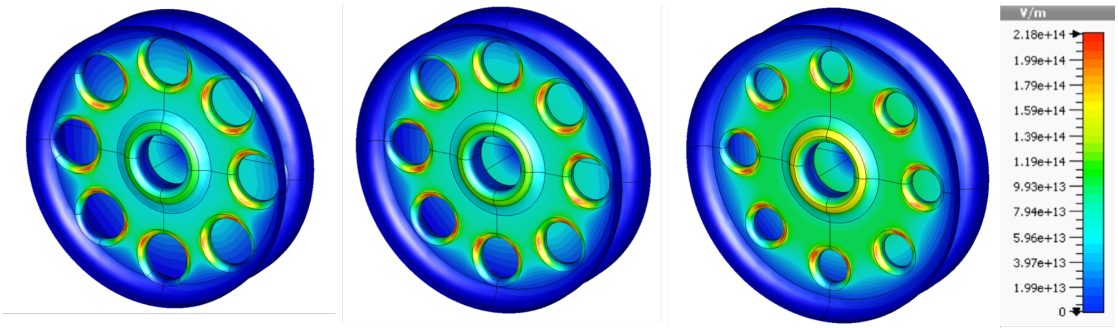

Fig. 3.44 S_c of the first, middle, and last cell of the hybrid $\varphi = \frac{2\pi}{3}$ structure from left to right. The group velocity is decreased through the structure by tapering the coupling slots.

A '*hybrid*' constant impedance/constant gradient structure was investigated to minimise S_c in the first few cells by operating at a higher group velocity and hence lower field than a constant impedance structure, but to then taper the group velocity to keep the gradient as constant as possible while still getting power to the end of the structure. Figure 3.45 shows the structure has an acceptable S_c through all of the cells but the overall gradient of the structure is only 58.9 MV/m. To raise this gradient one could attempt starting at a higher group velocity but this is limited by the how much coupling can be achieved in the first cell. In the case of this structure shown in Figure 3.41, the maximum group velocity achievable was 1.25% of the speed of light which was limited by the distance between the coupling slots. A limit of 2 mm between the coupling slots was imposed, as with a thin 1 mm septum separating adjacent cells, the septum would lose the structural

integrity required to reach the high temperatures necessary in the manufacturing and assembly processes described in Chapter 6.

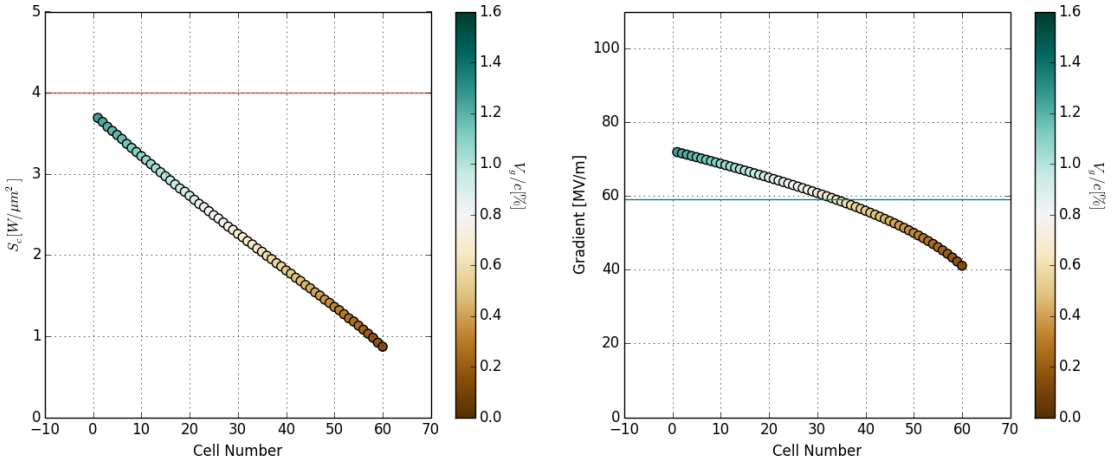

Fig. 3.45 The modified Poynting vector and gradient across the 60 cell 12 GHz $\varphi = \frac{2\pi}{6}$ hybrid constant impedance/constant gradient structure. The red line indicates the maximum allowable S_c and the blue line indicates the overall gradient of the structure: 58.9 MV/m.

12 GHz bTW single cell $\varphi = \frac{5\pi}{6}$

A 12 GHz backwards travelling wave structure was also investigated with a phase advance between cells of $\varphi = \frac{5\pi}{6}$ and 'racetrack' coupling slots. Figure 3.46 shows the modified Poynting vector peak on the coupling slots of a cell with a group velocity of 0.69% of the speed of light. In single cell periodic simulations it indicated a maximum gradient of over 87MV/m limited by S_c alone, however with the available power and R_s this structure would only reach 59.5 MV/m which is 1.5 MV/m higher than the $\varphi = \frac{2\pi}{3}$ structure.

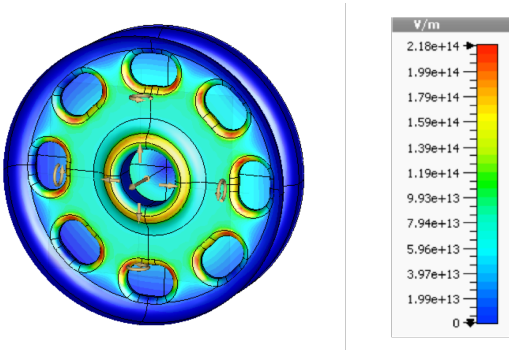

Fig. 3.46 The modified Poynting Vector distribution for 12 GHz single cell cavity $\varphi = \frac{5\pi}{6}$ with 8 racetrack coupling slots.

Like the $\varphi = \frac{2\pi}{3}$ structure the peak S_c was too high for the $\varphi = \frac{5\pi}{6}$ to be used as a constant impedance structure and is shown in Figure 3.47.

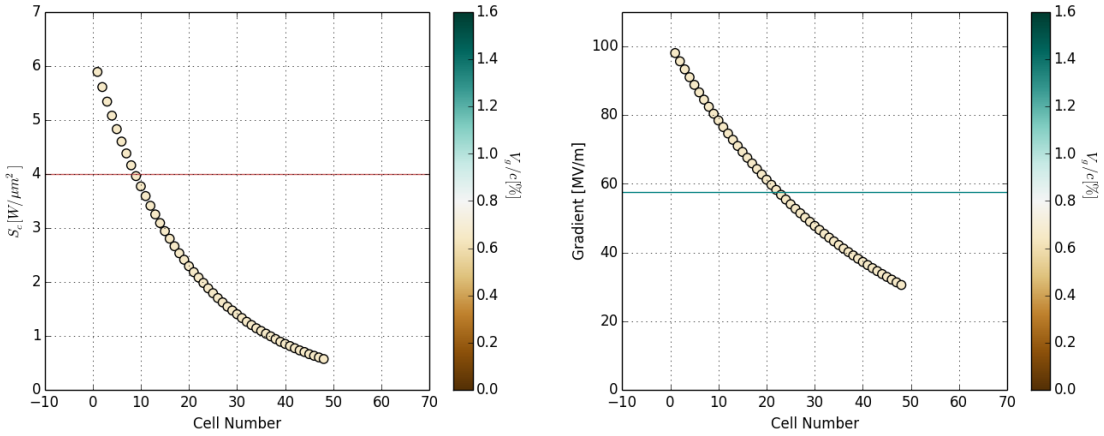

Fig. 3.47 The modified Poynting vector and gradient across the 48 cell 12 GHz $\varphi = \frac{5\pi}{6}$ constant impedance structure.The red line indicates the maximum allowable S_c and the blue line indicates the overall gradient of the structure: 57.6 MV/m.

A constant gradient structure was also investigated and can be seen in Figure 3.48, as before, the field attenuation was too high to maintain adequate gradient throughout the structure, however this was only by one cell which has been removed. A $\varphi = \frac{2\pi}{3}$ cell with $v_g = 0.6v_g/c$ has a Q_0 of approximately 4400 whereas a $\varphi = \frac{5\pi}{6}$ cell with the same group velocity has a Q_0 of 4800 as the cell is slightly longer, thus there is less power attenuation through the structure. However the modified Poynting vector is 20% over the imposed gradient limit, and optimising to reduce it would require further shortening of the structure as the S_c peak is on the coupling slot.

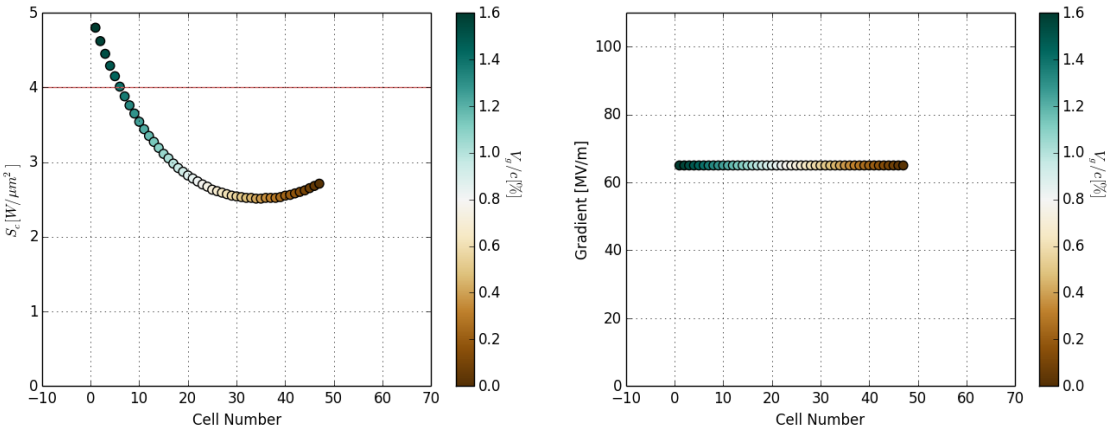

Fig. 3.48 The modified Poynting vector and gradient across the 47 cell 12 GHz $\varphi = \frac{5\pi}{6}$ constant gradient structure.

15 cm Backwards Travelling Wave Structure

A shorter backwards travelling wave structure was investigated to determine if 15 cm long structures could reach a higher gradient than the previous 30 cm structures. As the number of klystrons would remain constant, they would have half the input power of the 30 cm structures. The optimum group velocity of a 15 cm 12 GHz structure is 0.3% of the speed of light for a constant impedance structure (Figure 3.29).

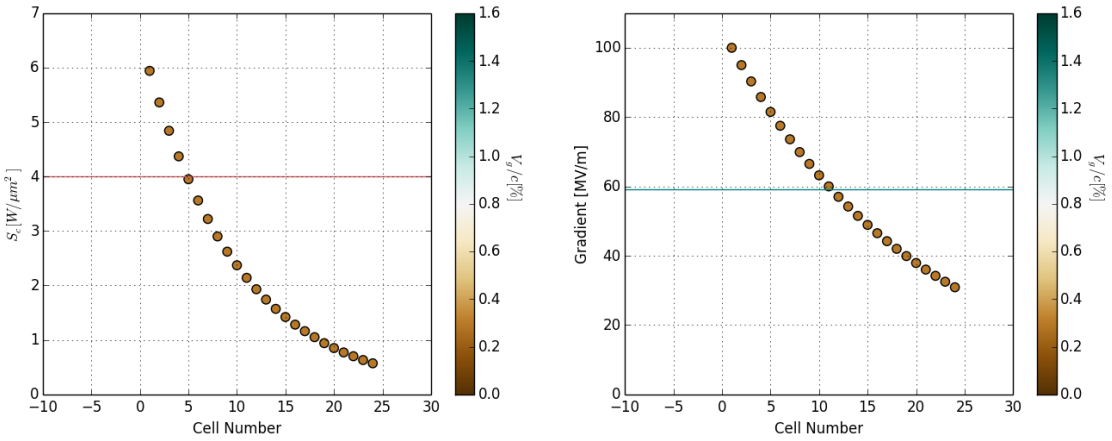

Fig. 3.49 The modified Poynting vector and gradient across the 24 cell 12 GHz $\varphi = \frac{5\pi}{6}$ constant impedance structure. Red line indicates the maximum allowable S_c whilst the blue line indicates the overall structure gradient 59.1 MV/m.

In Figure 3.49 one can observe the peak modified Poynting vector is almost 50% too high in the first cell. The low group velocity through the structure gives rise to high peak fields, enabling an overall structure gradient of 59.1 MV/m which is comparable to the structures twice its length. The peak fields can be optimised but the gradient can only drop as a result. On the other hand, the shorter constant gradient structure shown in Figure 3.50 easily fulfilled the 65 MV/m required gradient within the S_c limit. In order to not lose any active acceleration length two structures would be placed side by side to effectively form a 30 cm cavity. The RF distribution network would feed the two structures from a 3 dB hybrid coupler. This has been demonstrated at the CLIC test facility (CTF3) and is shown in Figure 3.51. This solution is satisfactory as a small aperture ProBE cavity.

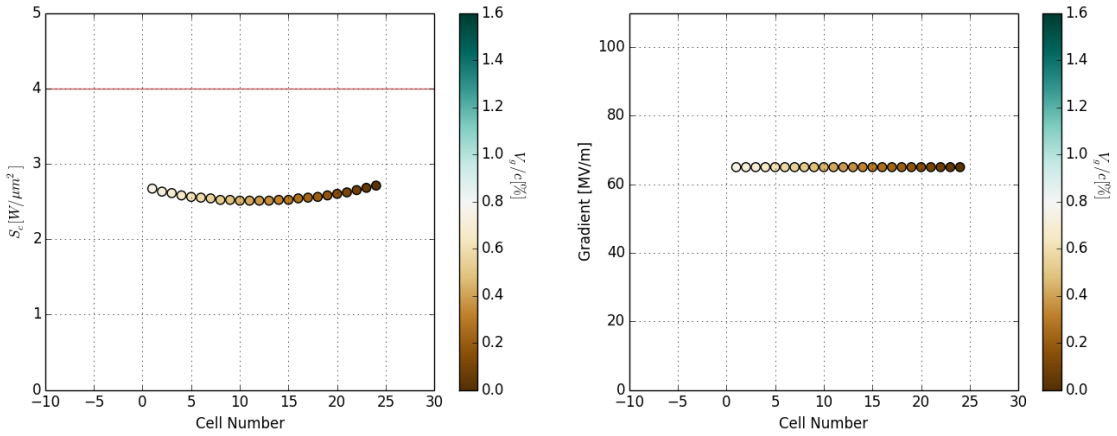

Fig. 3.50 The modified Poynting vector and gradient across the 24 cell 12 GHz $\varphi = \frac{5\pi}{6}$ constant gradient structure. The red line indicates the peak S_c limit. Gradient = 65 MV/m.

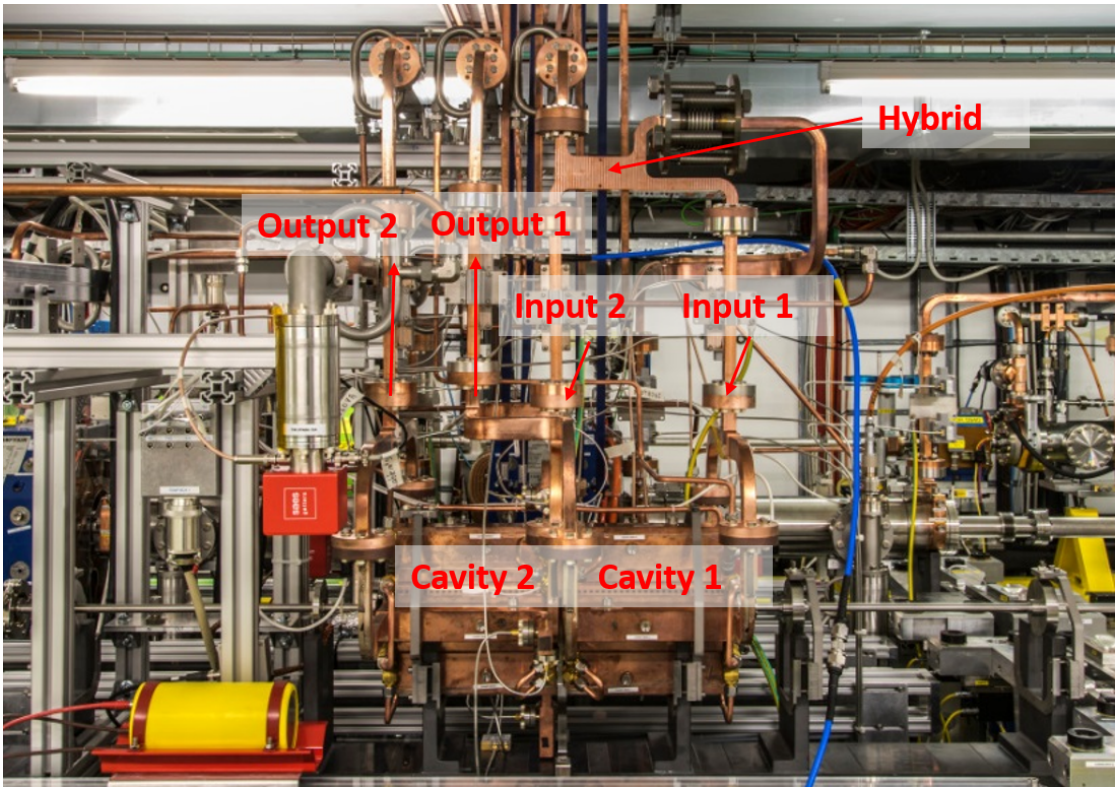

Fig. 3.51 CLIC superstructure installed at CTF3. The structure consists of two cavities side by side. The RF power is distributed to them via a 3dB Hybrid coupler [118].

S-band 1.75 mm aperture TWS

In the case of the standing wave structures from the previous section, it was shown that the high shunt impedance at 12 GHz was undermined by the high coupling

required through so many cells, and the 3 GHz structure was calculated to reach a higher gradient. A 3 GHz bTW structure was also investigated. For a 30 cm structure the approximate optimum group velocity is only 0.06% of the speed of light. A single cell periodic structure was optimised with a phase advance of $\varphi = \frac{2\pi}{3}$ and circular coupling slots. In Figure 3.52 one can observe the S_c is much higher distributed across the whole cell than that of the 12 GHz structures which peak only on the coupling slots. Despite this the peak S_c does not limit the gradient it is calculated to reach 65 MV/m in simulation. However with the available power and shunt impedance it would only reach 57.4 MV/m, thus we can conclude the S-band bTW structure would not reach the required gradient. It is apparent that to utilise the high shunt impedance of X-band at small apertures the cavity lengths must be short.

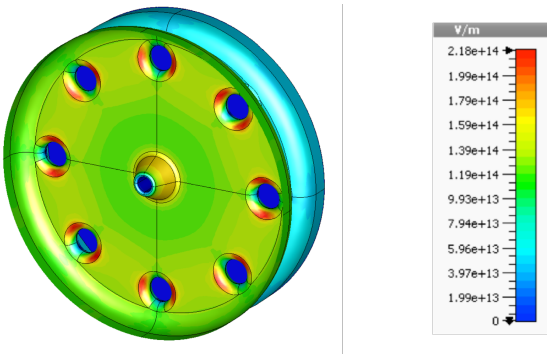

Fig. 3.52 The modified Poynting vector distribution of a 3 GHz $\varphi = \frac{2\pi}{3}$ bTW structure with a v_g/c of 0.07%.

3.5.3 Septum thickness and peak surface electric field

The optimisation of standing wave cavities at the beginning of this chapter has been performed using septum thickness scaled with frequency: 1 mm for 12 GHz through to 4 mm for 3 GHz. Septum thickness does not strictly scale with frequency however because the thickness of the septum is not an RF parameter but a mechanical parameter. The septum thickness should be thick enough that it does not creep when in the furnace for bonding. The mechanical strength of copper, along with the thermal properties do not depend on frequency. Figure 3.53 shows the results of a septum thickness study. The shunt impedance and thus gradient has a strong dependence on septum thickness. 12 GHz travelling wave cavities have been successfully manufactured as part of the CLIC high gradient test program with a 1 mm septum thickness [119–121] but in this case it is feared a standing wave cavity at 12 GHz would need a thicker septum to support the heavier side-coupled cavity. Furthermore the CLIC accelerating structures are coupled through the iris aperture, if coupling slots are added through the septum of the backwards travelling wave

structure might require a thicker septum. A 9.3 GHz cavity has been successfully manufactured with a 1.75 mm septum at the Cockcroft Institute [122], so it is assumed this thickness would also be sufficient for this application. A 2 mm septum thickness has been successfully manufactured in the backwards travelling wave medical linac designed by the TERA collaboration *with* coupling slots through the septum [22]. It is therefore assumed that a 2 mm septum thickness is possible at C-band too due to the smaller transverse size at this frequency than at S-band.

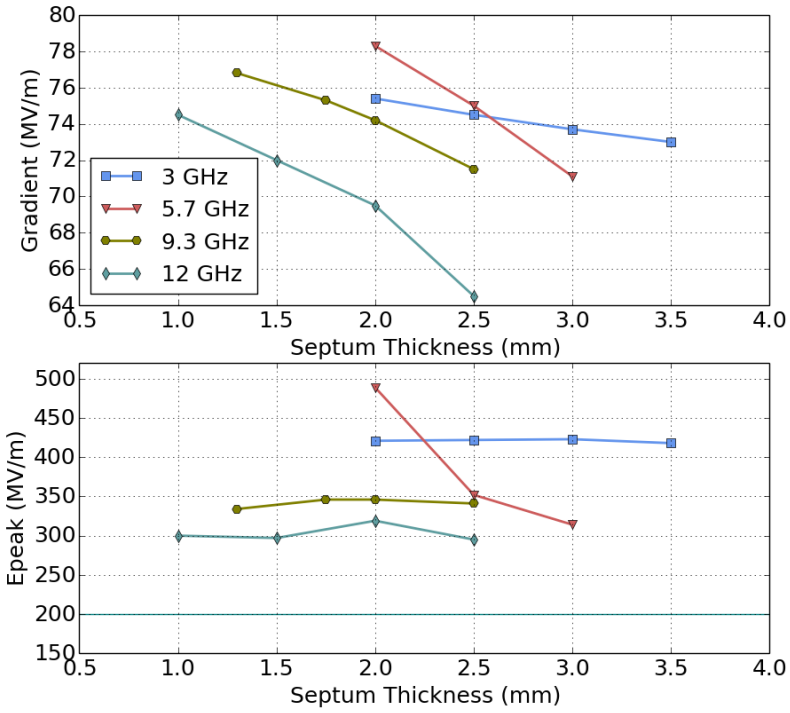

Fig. 3.53 Single cell pillbox cavity with a re-entrant section with a 1.75 mm aperture. Peak fields are limited by S_c alone and which results in high peak surface electric fields. The gradient has been calculated with the available input power and shunt impedance.

The shunt impedance and thus achievable accelerating gradient reduces as the septum thickness increases. In Figure 3.3 at an aperture radius of 1.75 mm the lower frequencies have less shunt impedance than the X-band structures. In Figure 3.53 the septa have not been scaled with frequency and nose cones incorporated. The lower frequency structures now exhibit comparable gradients to the X-band structures. Even with scaled septa the C- and S-band structures were calculated to have higher shunt impedance at larger apertures, thus in the large aperture optimisation C- and S-band cavities will be investigated with 2 mm septa thickness'. The lower plot from Figure 3.53 shows the peak surface electric fields resulting from using only S_c as a limit on peak fields. The figures shown are

very high, even for high gradient operation. Normal conducting structures rarely exceed 200 MV/m within an acceptable breakdown rate. Before S_c was proposed as a single RF breakdown constraint [82], the surface electric field was considered to be the primary gradient limiting quantity due to its direct role in the field emission mechanism [89]. In the next chapter a large aperture structure is considered and a peak surface electric field limit of 200 MV/m shall be introduced alongside the modified Poynting vector. The limit of 200 MV/m was taken from experimental data and is discussed in section 4.1.

3.6 Summary

In this chapter we have seen a simple pillbox cavity evolve into a re-entrant cavity and then into coupled standing wave and travelling wave cavities. The assumption that X-band structures could reach higher gradients at small apertures was made looking at Figure 3.3, that overlooked the effects of re-entrant and coupling on shunt impedance and therefore gradient. Figure 3.54 shows the maximum gradient of cavities with 2 mm aperture radii. The blue bars show plain pillbox cavities without coupling or nose cones and the red bars show the increase in gradient[‡] with nose cones. The green and teal bars then show the gradient calculated for 10 cm and 30 cm standing wave cavities respectively. We can see that once coupling is added, the higher frequency structures' gradients are reduced more than the lower frequency cavities.

[‡]Peak fields limited by S_c and gradient calculated with available power and shunt impedance.

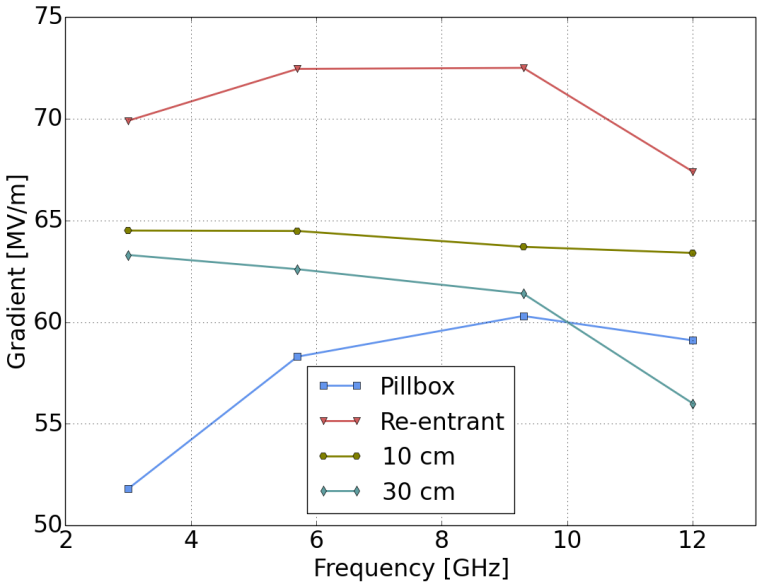

Fig. 3.54 Figure showing maximum gradient with and without re-entrant and coupling. The 10 and 30cm structures are side-coupled standing wave structures.

The reduction in gradient caused by the addition of inter-cell coupling was not seen with backwards travelling wave structures. Only one that was investigated was calculated to reach the required gradient. The 3 GHz travelling wave structure did not perform better than the X-band structures as it was limited by shunt impedance and input power. The only feasible cavity for this application was the 15 cm $\varphi = \frac{5\pi}{6}$ constant gradient backwards travelling wave structure which was calculated to reach 65 MV/m. The 3 GHz side-coupled standing wave cavity was calculated to reach 63.3 MV/m and in Figure 3.3 one can see that the shunt impedance does not reduce much by increasing the aperture radius. For this reason, alongside the beam dynamics study presented in Chapter 5 the possibility of increasing the aperture diameter further will be investigated.

Chapter 4

Large Aperture High Gradient Cavity Optimisation

4.1 Large Aperture Optimisation

At the end of the previous chapter it was decided to optimise multi-cell S- & C-band cavities with 2 mm septum thickness as shunt impedance scales with septum thickness and this is the smallest septum successfully demonstrated in this frequency range. Even with a scaled septum S- & C-band demonstrated the highest shunt impedance for a larger 4 mm aperture radius as is shown in Figure 3.8, where the gradient is calculated with the shunt impedance and input power at 100 MW/m with S_c limited to 4 W/μm^2 . The small aperture optimisation chapter used the modified Poynting vector as a single limit on peak fields. However as was seen in Figure 3.53 this resulted in very high peak surface electric fields. Peak surface electric field is widely regarded as a gradient limiting quantity, thus it is necessary to implement a limit for high gradient optimisation. There is lots of available high gradient data at X-band from the CLIC high gradient test program, however there is very little data available at lower frequencies. The TERA foundation performed single cell high gradient tests of S- and C-band cavities at the CLIC Test Facility (CTF) at CERN [123, 67, 91]. One single cell cavity was tested at both S- and C-band, so although informative, the conclusions that can be drawn from this data are limited.

Results from the TERA 3 GHz high gradient test program are shown in Figure 4.1. The results from winter 2012 are considered to be from an under-conditioned cavity [124], and the value of the peak surface electric field is uncertain as there was no direct probe inside the cavity. These uncertainties are accounted for with

multiple fits to the data. The blue fit indicates a maximum surface electric field of $\approx$ 240 MV/m for a breakdown rate of 10^{-6} bpp/m. The more conservative black fit indicates maximum surface electric field of $\approx 160 - 180$ MV/m. The C-band single cell structure tested yielded slightly higher peak surface electric fields for a given BDR, however the frequency dependence of peak surface electric field is questionable, this is discussed in [125]. For this reason along with the error uncertainties in the data a maximum surface electric field of 200 MV/m for both S- and C-band cavities was decided. This is also the limit used in the CLIC high gradient test program [120].

The peak field limit S_c has also been revised for this study. In the small aperture optimisation $S_{c_{max}}$ =4 W/μm^2 because it was considering 12 GHz power sources which typically have maximum pulse lengths of 1.5 μs. In this optimisation study we are considering lower frequencies of $\leq$5.7 GHz and power sources in this range can typically pulse up to 5 μs. S_c scales with BDR as

$$\text{BDR} \propto S_c^{15} t^5$$

[82] as such the new $S_{c_{max}}$ =2 W/μm^2. The simulations in this chapter have been done using the Eigenmode solver in CST. A tetrahedral mesh was used with 40 cells per wavelength and third order curved elements.

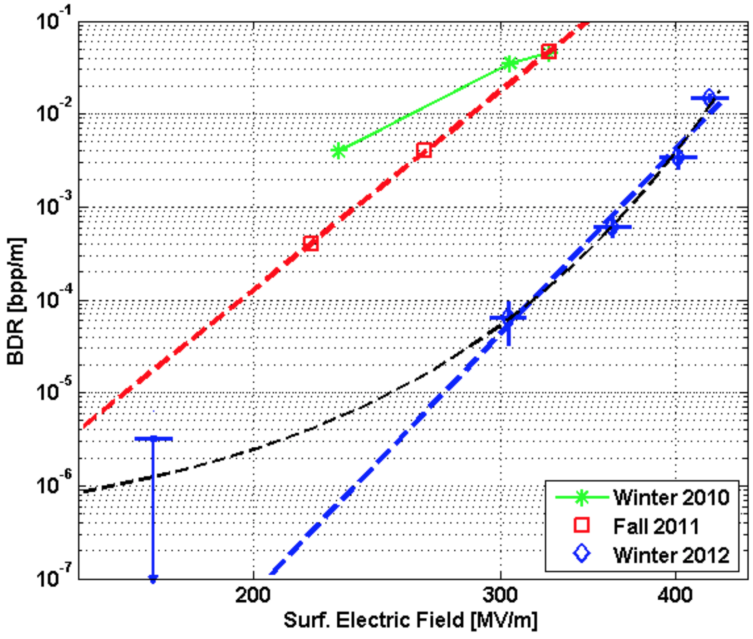

Fig. 4.1 Scaling fits taken from the TERA publication on the 3 GHz single cell high gradient test results [67].

4.2 Travelling Wave

S- and C-band backwards travelling wave structures with an aperture of 4 mm radius and a septum thickness of 2 mm were investigated as single cell structures. As a starting point they were optimised for the optimum v_g for a constant impedance structure as was done in the previous chapter. In the small aperture optimisation chapter the constant gradient structures reached higher gradients than constant impedance but the optimal v_g for a constant impedance structure serves as a good average across the structure. For a 30 cm long S-band structure that is $0.07\%^{v_g}/_{c}$ and $0.16\%^{v_g}/_{c}$ for C-band. Initially 16 circular coupling slots were simulated at a phase advance of $\varphi = \frac{5\pi}{6}$ as that phase advance yielded the highest shunt impedance in the coupling slot study done in the 'small aperture' chapter. It did not have as larger range of v_gs but the lower frequency cavities considered in this structure do not have such a high coupling requirement. Opening the beam aperture will have a negative effect on the shunt impedance, so that is prioritised by choosing $\varphi = \frac{5\pi}{6}$. Figure 4.2 shows the electric field profiles of the single cell structures simulated. S-band is the larger structure on the left. In the centre is the C-band 16 slot structure; the space between the slots was limited to 2 mm minimum and this restricted the maximum v_g to 0.18%. A constant gradient of this length requires a higher group velocity at the start of the structure to adequately fill each cell. Thus the number of coupling slots was reduced to 8, shown on the right, although there are fewer slots, they are free to be larger. From the coupling slot study we learned that fewer larger slots will result in higher peak magnetic fields for the same v_g but the overall coupling requirement is not as high as it was with X-band so it should not be gradient limiting.

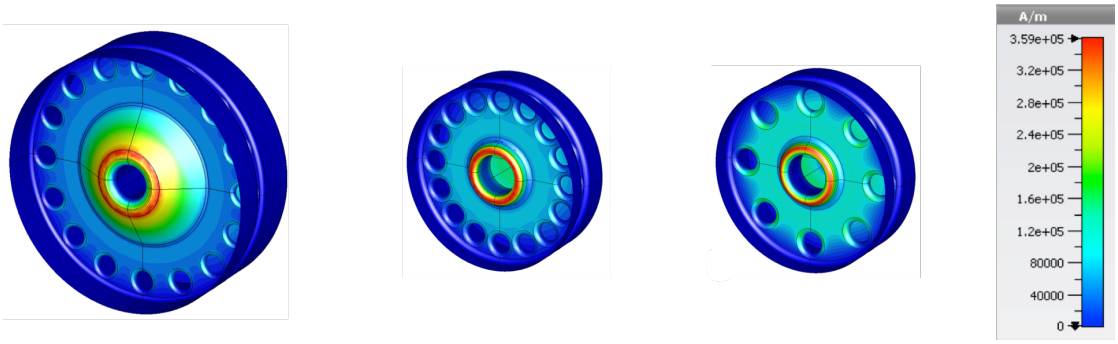

Fig. 4.2 Absolute component of the electric field profiles of S- and C-band travelling wave structures investigated at 4 mm aperture. Initially 16 coupling slots were implemented for the C-band (centre) structure but v_g was limited by space between slots so 8 slots were used (right).

As with each structure mentioned thus far, the nose cones for these single cell structures were individually optimised. The fields were calculated in CST

Parameter	Value
Cone Angle (CA)	25°
Inner Nose Radius (R_{in})	1 mm
Outer Nose Radius (R_{on})	1 mm
Inner Corner Radius (R_{ic})	1 mm
Flat (L_f)	0

Table 4.1 Minimum nose cone parameters considered in the large aperture optimisation.

Microwave Studio [112], and the nose cone parameters altered to bring the fields within acceptable limits while maximising shunt impedance. The optimisation process for the S-band single cell travelling wave structure is shown in Figure 4.3. The parameters are initially set at their minimum values for manufacture [117].

These values produce sharp nose cones which usually enhance the electric field beyond acceptable limits then visualising the location of the peak surface electric field, one can increase blend radii or the nose cone angle to lower the peak fields, utilising the nose cone optimisation study. Firstly the optimum gap between the nose cones is identified as was demonstrated in Figure 3.21. Then the radii and cone angle are optimised. The inner nose cone radius (R_{in}) is closest to the beam axis as was shown in Figure 3.9. It is desirable to keep that radius small as that is the ideal location of the peak field. The nose cone study in the previous chapter showed that R_{on} can be varied with a smaller effect on shunt impedance. Firstly an attempt was made to reduce the peak field by increasing R_{on}. This reduced the peak surface electric field by 59 MV/m. Figure 4.3 shows that start to saturate and an even smaller reduction in E_{peak} would be seen between 3 mm and 4 mm. Next E_{peak} was reduced by a further 25 MV/m by increasing R_{in}. The flat section (L_f) that lies between R_{in} and R_{on} was increased next. The first step from 0 to 0.2 mm reduced E_{peak} by 23 MV/m: however there was no advantage to increasing it further as it reduced E_{peak} by < 1 MV/m. Next the nose cone angle (CA) was swept, and at 55° it brings E_{peak} just over the limit at 204 MV/m. L_f was then revisited to try and reduce the 4 MV/m but the reduction in gradient was substantial so it was left at 204 MV/m. Overall, using solely S_c as a gradient limiting quantity, this structure would have reached 55 MV/m, but using the peak surface electric field as a limiting quantity, the gradient is reduced to 48.8 MV/m.

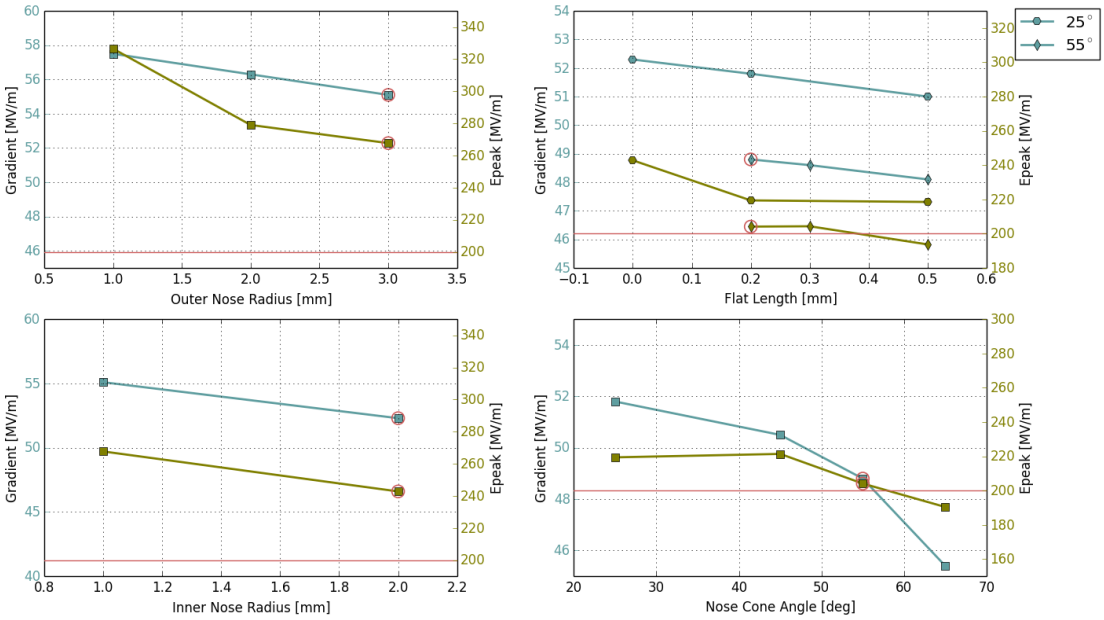

Fig. 4.3 Nose cone optimisation process for S-band $\varphi{=}\frac{5\pi}{6}$ single cell structure. The gradient is calculated with the available shunt impedance and 12.8 MW input power per structure. Legend indicates the nose cone angle.

The main figures of merit for both the S- and C-band single cell structures are shown in Table 4.2. Comparing the two: C-band has a higher shunt impedance and thus gradient than the S-band structure but the group velocity is higher than the optimum and shunt impedance decreases with rising v_g. Furthermore there are fewer S-band cells in 30 cm than C-band cells so even though at first glance the C-band structure outperforms the S-band structure, the whole structure must be considered before drawing any conclusions. The single cell only being calculated to reach 50 MV/m within the gradient limits is a good indication that it will not reach the target 55 MV/m. The peak magnetic field in both cases operating at the gradients they reach is comfortably within the 273 A/kV limit for pulsed magnetic heating to remain $<$ 40K. Both structures very slightly exceeded the 200 MV/m peak surface electric field limit, but were within the $S_c{=}2$ W/μm^2 limit. Next the radius of the coupling slots was swept to vary the v_g for an entire structure.

	Parameter	S-band	C-band	Units
f	Frequency	3	5.7	GHz
r_c	Cell Radius	30.7	18.4	mm
l	Cell Length	24.81	13.06	mm
v_g/c	Group Velocity	-0.09	-0.17	%
t_{fill}	Filling time	1.1	0.6	μs
Q_0	Q-factor	9657	7306	
Z	Shunt Impedance	61.9	65.3	MΩ/m
E_{acc}	Gradient	48.8	50.1	MV/m
E_{peak}/E_{acc}	Normalised Peak Surface E-field	4.2	4	
H_{peak}/E_{acc}	Normalised Peak Surface H-field	4.3	4.8	A/kV
S_c	Modified Poynting Vector	2	1.6	W/μm^2

Table 4.2 Parameters for single cell $\varphi=5\pi/6$ backwards travelling wave structures. Gradient is limited by 12.8 MW input power with available shunt impedance. Both are limited by peak surface electric field.

Figure 4.4 shows the fields, gradient and group velocity throughout the 21 cells of a C-band backwards travelling wave structure with a phase advance of $\varphi=5\pi/6$. Single cell simulations indicated that at the optimum group velocity, the structure would operate at 50 MV/m limited by the peak surface electric field. To operate as a constant gradient structure with the required 55 MV/m the peak surface electric field would have to be 13% over the 200 MV/m limit. Furthermore, the v_g must be relatively slow at the start of the structure and power dissipates before the last cell, so no power is transmitted through the structure. This is why the final cell has been removed leaving only 21 cells instead of 22. The magnetic fields on the couplings slots in the first half of the structure would cause pulsed magnetic heating of over 40 K which could cause cracking and trigger the breakdown mechanism.

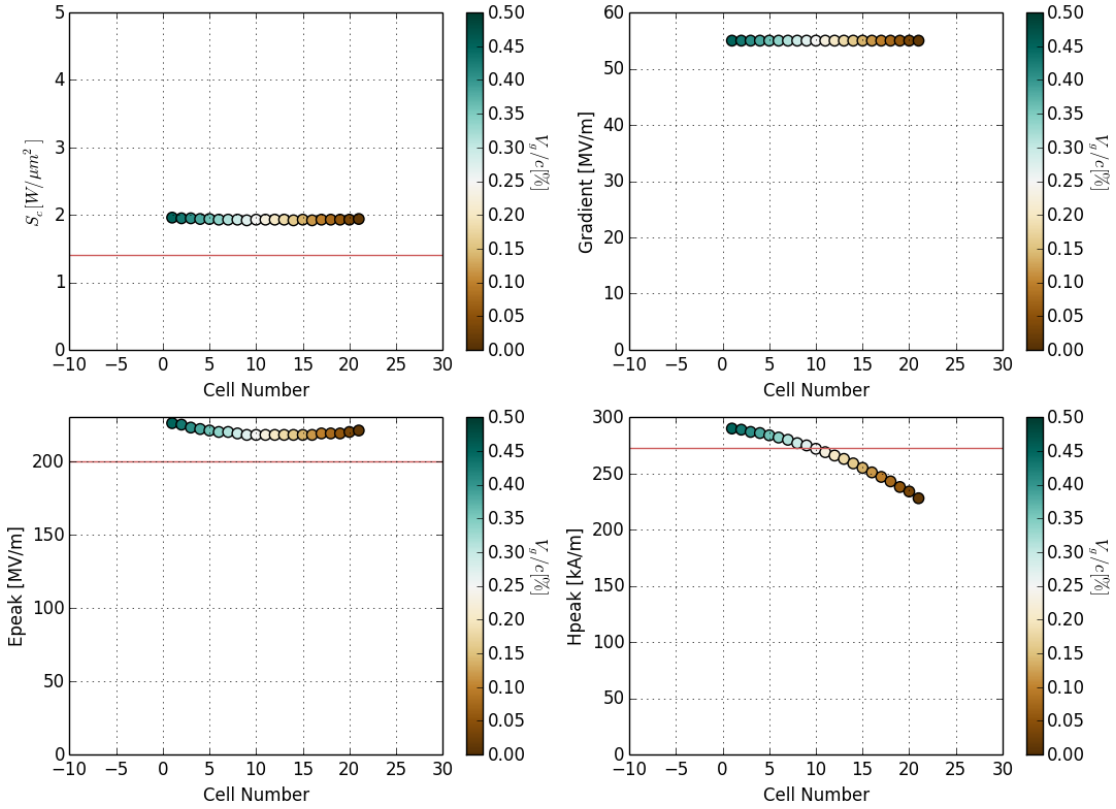

Fig. 4.4 C-band constant gradient backwards travelling wave structure $\varphi=\frac{5\pi}{6}$ peak fields and gradient limited by 12.8 MW input power and available shunt impedance. Red lines indicate maximum allowable values for each respective plot.

Figure 4.5 shows the fields, gradient and group velocity throughout the 15 cells of an S-band backwards travelling wave structure, also with a phase advance of $\varphi=5\pi/6$. Unlike the C-band structure, there are few enough cells for the power to comfortably fill the whole structure with 3 kW transmitted at the output. The relatively low number of cells means the structure does not suffer from high peak magnetic fields as a result of high inter-cell coupling. However, to achieve a constant gradient of 55 MV/m throughout, the peak surface electric field must be exceeded by 16%, and S_c is also over the limit.

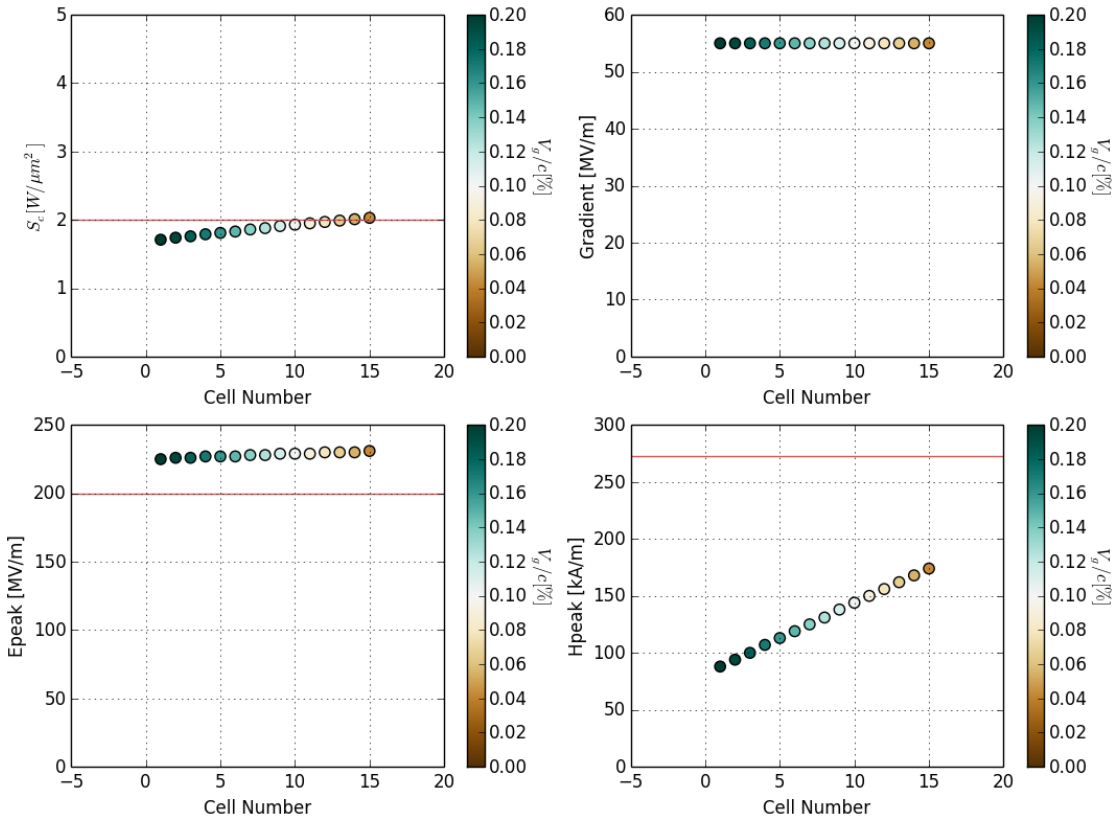

Fig. 4.5 S-band constant gradient backwards travelling wave structure $\varphi{=}\frac{5\pi}{6}$ peak fields and gradient limited by 12.8 MW input power and available shunt impedance. Red lines indicate maximum allowable values for each respective plot.

4.3 Standing Wave

Side-coupled standing wave structures were also investigated at both S- and C-band with a 4 mm aperture radius. The quadruplet simulated in CST is shown in Figure 4.6, with the $\frac{\pi}{2}$ mode excited. Both the S- and C-band cavities had their nose cones individually optimised following the same methodology as mentioned in the previous section. The coupling slots were also individually optimised. The S-band structure shown in Figure 4.6 still only requires 2% coupling so has a regular length side-coupled cavity. The C-band structure shown in Figure 4.7 has had the length of the side-coupled cavity increased to increase the coupling to >4% without lowering the cell further down into the accelerating cavity and reducing the shunt impedance. Table 4.3 shows the main figures of merit for a C-band side-coupled structure. At a gradient of 48.5 MV/m the surface electric field peaks at 212 MV/m on the nose cone. This allows for no further optimisation to increase the gradient as that would increase the peak field further above the limit. Both the peak surface electric field and S_c are limiting the gradient in this case.

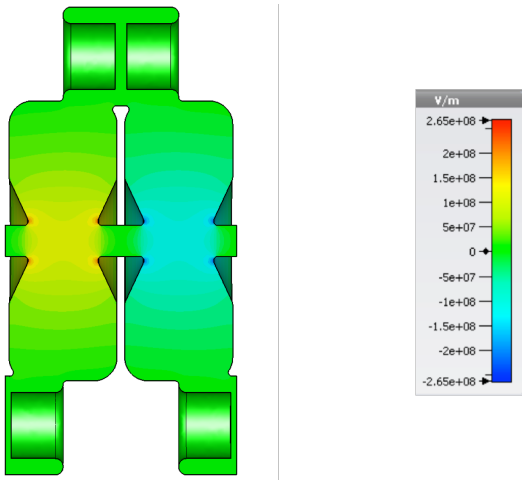

Fig. 4.6 Cross section of S-band side-coupled standing wave structure quadruplet model used in simulation with periodic boundaries. Electric field plot showing the $\frac{\pi}{2}$ mode.

5.7 GHz SCSWS			
	Parameter	Value	Units
f	Frequency	5.7	GHz
S	Septum Thickness	2	mm
r_c	Accelerating Cell Radius	16.9	mm
r_{sc}	Coupling Cell Radius	7.2	mm
l	Accelerating Cell Length	15.7	mm
l_{sc}	Coupling Cell Length	20	mm
N_{cell}	Number of Accelerating Cells	19	
d	Coupling Slot Depth	1.4	mm
k	Coupling factor	4.2	%
Q_0	Q-factor	7804	
t_{fill}	Filling time	220	ns
Z	Shunt Impedance	61.2	MΩ/m
E_{acc}	Gradient	48.5	MV/m
E_{peak}	Peak Surface E-field	212	MV/m
H_{peak}	Peak Surface H-Field	320	kA/m
S_c	Modified Poynting Vector	2	W/μm^2

Table 4.3 Parameter table for the 5.7 GHz side-coupled standing wave cavity. Gradient is limited by 12.8 MW input power, and available shunt impedance.

Figure 4.7 shows the surface magnetic field profile of the C-band side-coupled standing wave quadruplet simulated. This peak field is a result of the amount of

coupling required for the 19-cell cavity. The peak field can be reduced by increasing the length of the side-coupled cell and reducing the slot depth however this is already a 'long cell'. Increasing the length further requires a reduction in cell radius to tune it to the correct operating frequency, and the capacitive region in the side-coupled cell becomes too small. The capacitive gap in the side-coupled cell could be reduced to tune the coupling cell, but it has been limited at 3 mm to keep peak fields small.

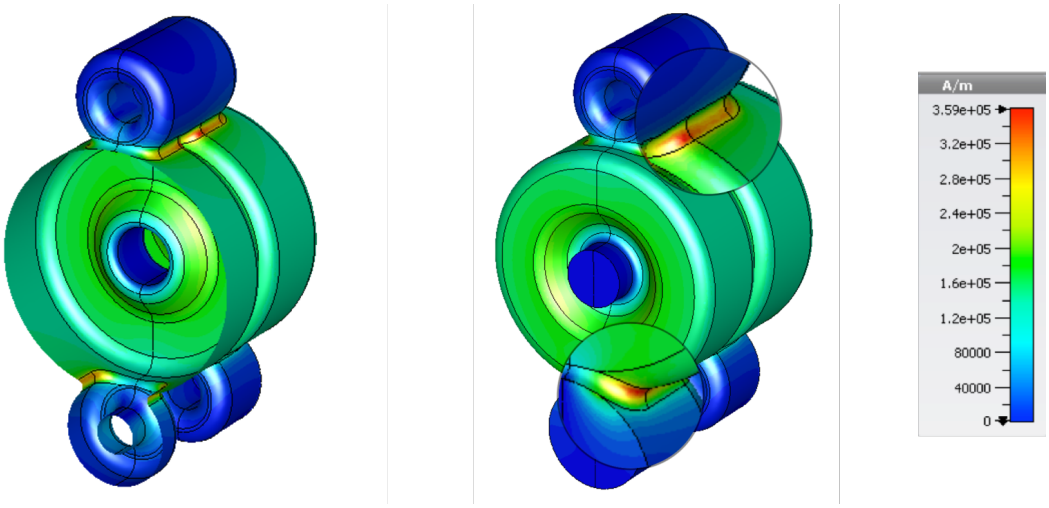

Fig. 4.7 Magnetic field profile of a C-band side-coupled quadruplet.

3 GHz SCSWS			
	Parameter	Value	Units
f	Frequency	3	GHz
S	Septum Thickness	2	mm
r_c	Accelerating Cell Radius	36	mm
r_{sc}	Coupling Cell Radius	12.4	mm
l	Accelerating Cell Length	29.8	mm
l_{sc}	Coupling Cell Length	29.8	mm
N_{cell}	Number of Accelerating Cells	10	
d	Coupling Slot Depth	1.5	mm
k	Coupling factor	2.3	%
Q_0	Q-factor	13260	
t_{fill}	Filling time	700	ns
Z	Shunt Impedance	75.3	MΩ/m
E_{acc}	Gradient	53.8	MV/m
E_{peak}	Peak Surface E-field	210	MV/m
H_{peak}	Peak Surface H-Field	262	kA/m
S_c	Modified Poynting Vector	0.9	W/μm^2

Table 4.4 Parameter table for the 3 GHz side-coupled standing wave quadruplet. Gradient is limited by 12.8 MW input power, and available shunt impedance.

The main parameters and figures of merit for the 3 GHz side-coupled standing wave quadruplet seen in Figure 4.6 are shown in Table 4.4. The coupling requirement for this structure is only 2% so it was unnecessary to use a long coupling cell to reduce the peak surface magnetic field on the coupling slots. The peak surface magnetic field was only 262 kA/m at 2.3%; slightly more coupling than is necessary. The 3 GHz quadruplet was calculated to achieve a gradient of 53.8 MV/m outperforming its C-band counterpart by 5.3 MV/m, with lower peak fields. S_c was much lower than the limit of 2 W/μm^2, but increasing the size of the nose cone to increase gradient further would have also raised E_{peak} which was already over the limit at 210 MV/m.

	Parameter	S-band bTW	C-band bTW	C-band SW	S-band SW	Units
f	Frequency	3	5.7	5.7	3	GHz
l	Cell Length	24.8	13.1	15.7	29.8	mm
N_{cell}	Number of cells	15	22	19	10	
v_g/c	Group Velocity	-0.2	-0.5	4.2	2.3	%
k	k-factor	-0.04	-0.0			
t_{fill}	Filling time	0.8	0.4	1.4	4.4	μS
Z	Shunt Impedance	85.4	65.6	61.2	75.3	$M\Omega/m$
P_{in}	Input Power	10	10	11.4	11.6	MW
E_{acc}	Gradient	48.6	47.5	46.8	51.1	MV/m
E_{peak}	Peak Surface E-field	204	200	200	200	
H_{peak}	Peak Surface H-field	153	256	302	267	kA/m
S_c	Peak Modified Poynting Vector	1.6	1.53	1.74	0.8	$W/\mu m^2$

Table 4.5 parameters for each large aperture structure considered with the input power reduced to bring the peak surface electric field within limits. Group Velocity indicates the values at the start and end of the structures. The C-band bTW did not have enough power to fill the entire structure with 10 MW input power. Values in red exceed target values.

The figures of merit for each full large aperture structure considered in this chapter are summarised in Table 4.5 where the input power, for some structures, has been reduced to operate within the peak surface electric field limit of 200 MV/m. Comparing all of the structures, the S-band structures are calculated to reach higher gradients than the C-band structures for both standing and travelling wave. This could be due to the same limits imposed on both despite the frequency difference. The limit of 2 mm septum thickness was imposed on both structures and shunt impedance strongly varies with septum thickness. Relative to the cell length, the S-band structures have a thinner septum. Additionally, as discussed at the start of the chapter C-band structures are likely to exceed the peak surface electric field of S-band structures at the same breakdown rate, however the data for this frequency is limited and the frequency dependence of the peak surface electric field before breakdown is contested in the literature. The C-band backwards travelling wave structure did not have enough power to fill the end cell when the power was reduced to 10 MW. The nose cones could be reduced to lower E_{peak} instead but this would lower the gradient further. The C-band standing wave structure exceeded the peak

surface magnetic field limit of 273 kA/m. The S-band structures have the highest gradient, but the standing wave structure is slightly higher than the backwards travelling wave structure. It is for those reasons we conclude the S-band standing wave structure is most suitable for our design goals and brings us closest to our target gradient of 55 MV/m. It has the added advantage of a small peak S_c which means we can operate at the 5 μs pulse length where the S_c limit is 1.4 W/μm^2, meaning the linac will produce the necessary beam current as is shown in Chapter 5. A prototype will be built and once the cavity is high power tested we may find it's possible to operate the cavity at a slightly higher peak surface electric field with an acceptable breakdown rate.

4.4 Final Prototype Structure

The S-band quadruplet was further optimised to reduce cavity coupling and to add bead pull access to the side-coupled cells. The details of the final prototype quadruplet are shown in Table 4.6. The optimisation was completed using the Eigenmode solver in CST. A tetrahedral mesh was used with 40 cells per wavelength and third order curvature. This was increased to 70 cells for the final optimised structure for the best possible accuracy. This was the finest mesh the distributed computing network used could successfully simulate.

3 GHz Prototype Structure			
	Parameter	Value	Units
f	Frequency	2.9985	GHz
S	Septum Thickness	2	mm
r_c	Accelerating Cell Radius	36	mm
r_{sc}	Coupling Cell Radius	13.1	mm
l	Accelerating Cell Length	29.8	mm
l_{sc}	Coupling Cell Length	29.8	mm
N_{cell}	Number of Accelerating Cells	11	
d	Coupling Slot Depth	1.2	mm
k	Coupling factor	2	%
Q_0	Q-factor	13279	
t_{fill}	Filling time	4.4	μs
Z	Shunt Impedance	75.5	MΩ/m
E_{acc}	Gradient	53.9	MV/m
E_{peak}	Peak Surface E-field	215	MV/m
H_{peak}	Peak Surface H-Field	261	kA/m
S_c	Modified Poynting Vector	0.9	W/μm^2

Table 4.6 Parameters for the final prototype structure - Gradient limited by 12.8 MW input power and available shunt impedance.

The coupling slot was reduced from 1.5 mm to 1.2 mm reducing coupling from 2.3% to the 2% required. This has a small effect on the shunt impedance and increased the overall gradient by 0.1 MV/m. With the full prototype structure in mind, additional access apertures were added to the side-coupled cells to allow for a bead pull experiment to measure the fields in them during cavity tuning. Subsequently the radius of the side-coupled cells increased slightly. The additional access apertures are shown in Figure 4.8.

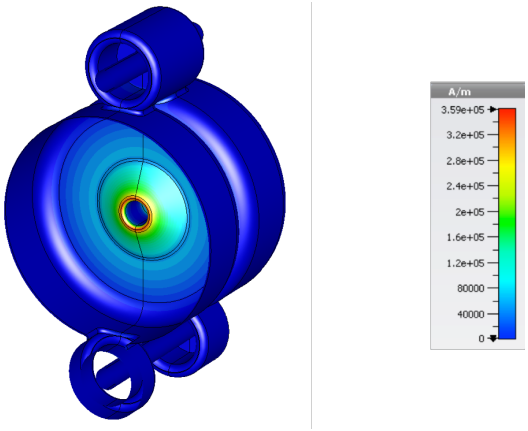

Fig. 4.8 The prototype Quadruplet electric field distribution.

As the final cavity design is a bi-periodic side-coupled structure, it has two $\pi/2$ modes. Figure 4.9 shows the unexcited $\pi/2$ mode in the coupling cells on the left, and the excited accelerating cells on the right. The two modes are within 69 kHz. The coupling factor was calculated for a maximum stopband of 1.5 MHz so it is well within this.

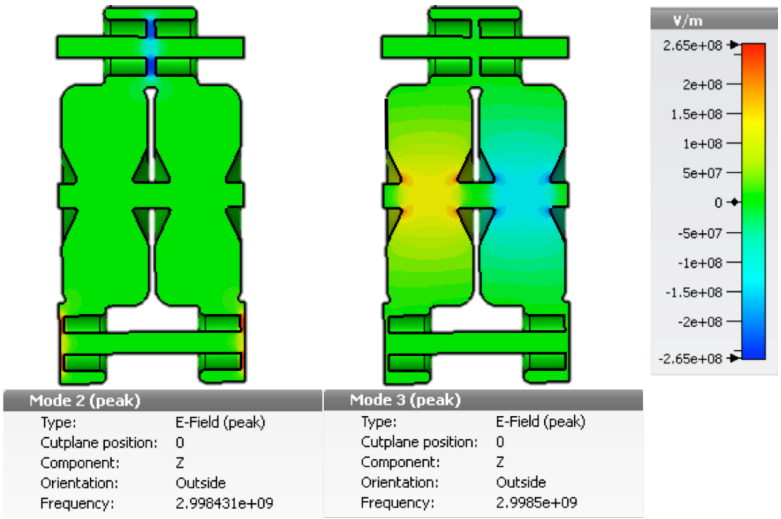

Fig. 4.9 Peak E-field (Z) in the final side-coupled quadruplet. The unexcited $\pi/2$ mode in the coupling cells on the left, and the excited accelerating cells on the right.

4.4.1 Power Coupler

Construction of a full prototype vacuum model begins with the addition of a power coupler. A power coupler is essentially a transition piece between the cavity wall and WR284 S-band waveguide; what the RF power distribution network is made of. Typically power is coupled into side-coupled standing wave structures magnetically through the centre cell. Figure 4.10 shows the vacuum model of a coupling cell added between the two accelerating cells of a quintuplet.

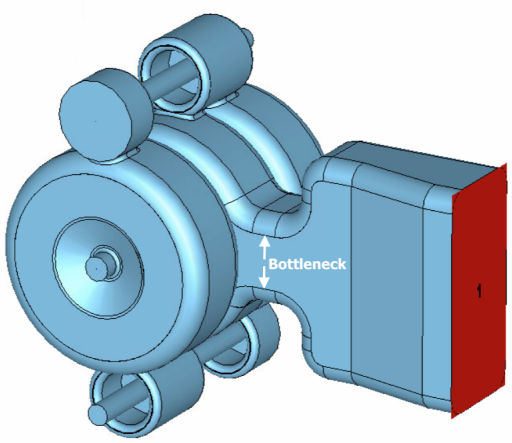

Fig. 4.10 Vacuum model of the power coupler added to a coupling cell in the centre of the optimised quintuplet.

The red rectangular input port is where the flange will be located to connect to WR284 waveguide. The width of WR284 is wider than the length of the cell so the coupler is tapered down to match. Just before the cavity the coupler tapers further to a bottle neck. The width of this bottleneck is adjusted to adjust the amount of coupling between the cavity and the power source. This must be tuned to achieve critical coupling which is when no power is reflected back from the cavity to the power source. The coupling factor was introduced in Chapter 2 as

$$\beta_c = \frac{Q_0}{Q_e} \tag{4.1}$$

and a cavity is critically coupled when β_c=1. Q_e scales with the number of cells so for a three cell model of what will eventually become an 11-cell prototype $\beta_c \approx 3.7$. The Eigenmode solver in CST has result templates for both Q_0 and Q_e. Initially the bottle neck width was adjusted to achieve Q_0=13307 and Q_e=3532 thus β_c=3.76. This result is slightly overcoupled but close enough as the addition of the six additional accelerating cells and two endcells into the full prototype model will require further optimisation. The addition of the power coupler perturbs the field and the frequency must be tuned. Tuning the coupling cell in the centre with its radius like was done with the previous accelerating cells however changes the

cell to cell coupling and detunes the coupling cell. The radius of the coupling cell was kept constant, and instead the cell was tuned with the nose cones. Changing the distance between the nose cones changes the capacitance between them and thus the resonant frequency of the cell. The gap between the nose cones was increased from 18 mm in the accelerating cells to 19.5 mm in the centre coupling cell to achieve field flatness within 10.3% at 2.9985 GHz. Figure 4.11 shows the Z-component of the electric field in the model (coupler not shown) and there is strong field in the side-coupled cells. This is not expected as the side-coupled cells were tuned to 2.9985 GHz as part of the quintuplet previously.

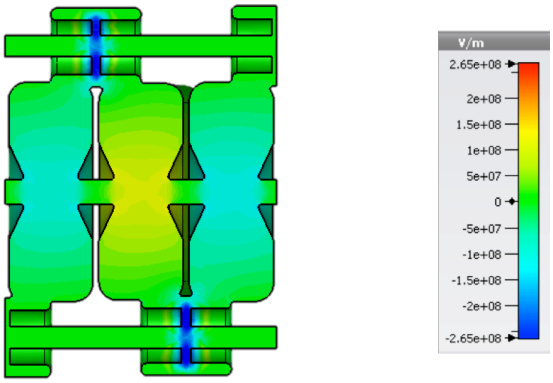

Fig. 4.11 Z-component of the E-field inside the coupling cell with power coupler (not pictured) with two ordinary coupling cells. Unwanted fields are shown in the side-coupled cells.

The radius of the side-coupled cell and the gap were swept in an attempt to re-tune these cells but just moved further away in frequency. As too much field in a neighbouring cell suggests too much coupling between the cells, the length of the side-coupled cell and thus the coupling slot was reduced. As 2% coupling should provide field flatness within 1% it was assumed there was room to reduce the coupling by a small amount. 1% is very tight similar cavities have been tuned within 3% field flatness. The resulting field map is shown in Figure 4.12 and the field is no longer seen in the side-coupled cells.

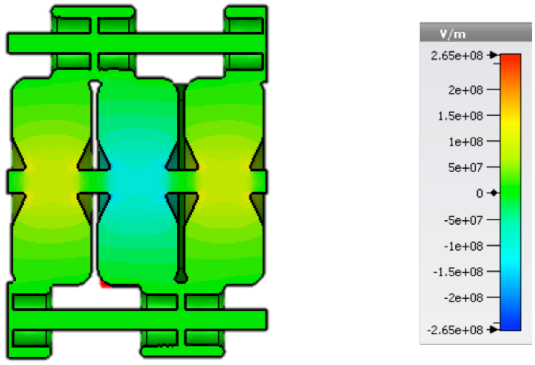

Fig. 4.12 Z-component of the E-field inside the coupling cell with power coupler (not pictured) with two ordinary coupling cells.

The magnitude of the electric field along the beam axis is plotted in Figure 4.13. The green line shows the electric field of the model shown in Figure 4.11 with unwanted field in the side-coupled cells. The red line shows the field in Figure 4.12 where the length of the coupling cell has been reduced by 1 mm. Neither solution are completely field flat within an acceptable margin, but the optimum obviously exists somewhere between those two points.

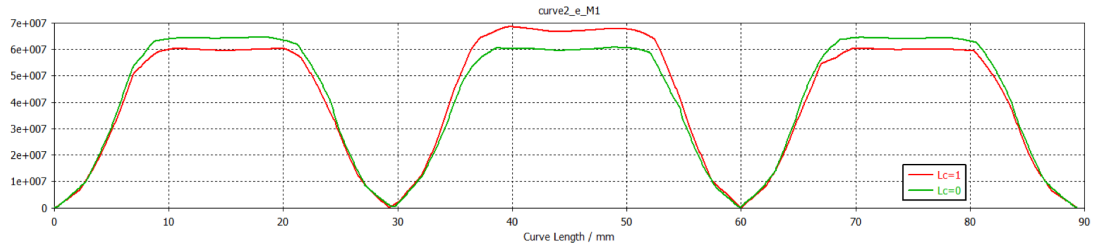

Fig. 4.13 Electric field along the beam axis of the three cell power coupler model. Green line has no reduction in length for the side-coupled cell and the red line has reduced the length by 1 mm.

The reduction in the length of the side-coupled cell was swept between 0-1 mm and the structure was found to be field flat with length reduced by 0.4 mm shown in Figure 4.14. $S_{11} > -5$dB for the 3-cell model and coupler because it has been tuned to $\beta_c = 3.76$. When the other 8 cells are added to the model it will reduce to < -30 dB when $\beta_c = 1$.

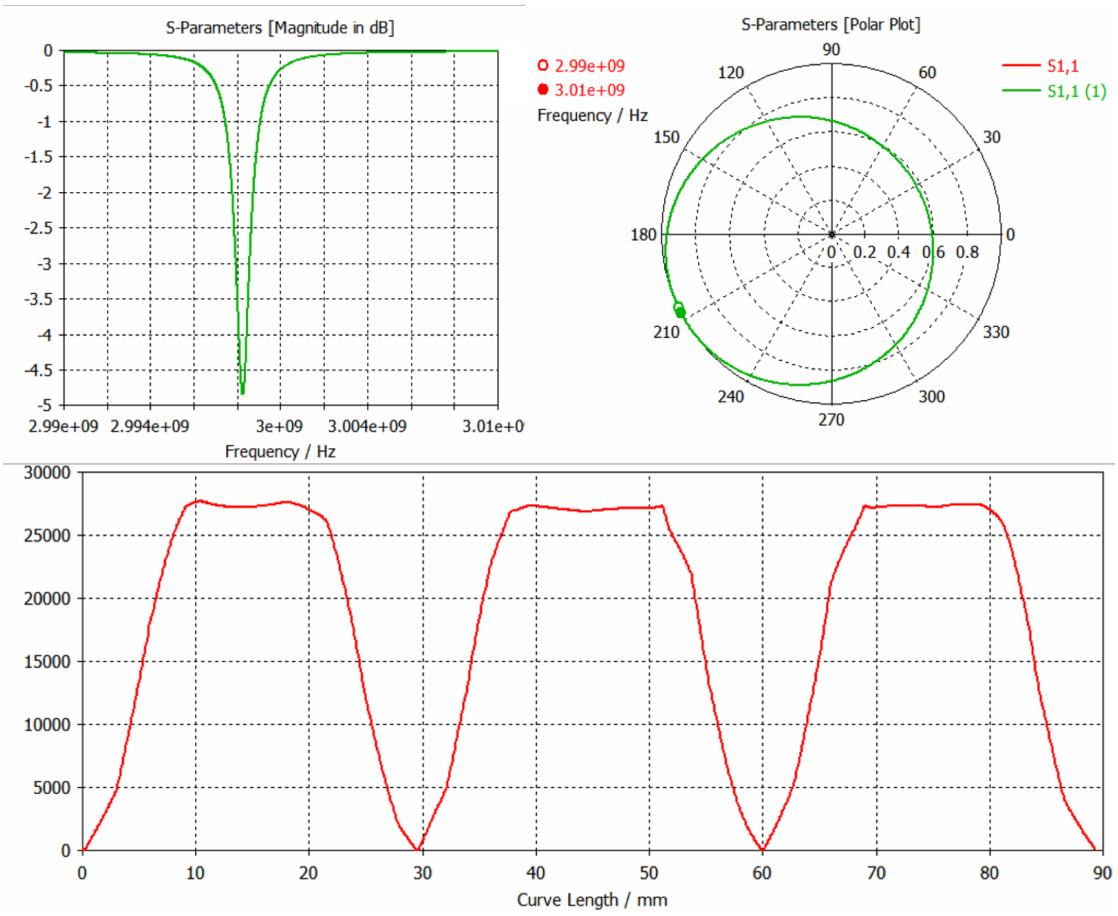

Fig. 4.14 S-parameters of the 3-cell coupler model showing it is overcoupled (Top). Z-component of E-field along the beam axis of the 3-cell coupler model (Bottom).

4.4.2 End cells

The cells on the end of the structure differ to the normal accelerating cells because they couple to a side-coupled cavity on one side, and the beam pipe on the other. This is shown in Figure 4.15.

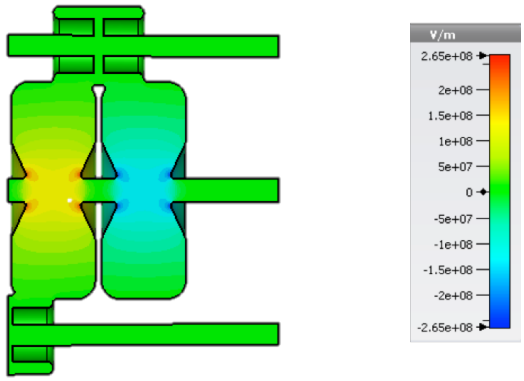

Fig. 4.15 End cell model comprised of beam pipe one end cell, one accelerating cell and 1.5 coupling cells. Z-component of electric field is shown.

The frequency of the two end cells has to be adjusted to account for this perturbation. Adjusting the radius would also alter the coupling slot and perturb the field in the adjoining coupling cell and thus the neighbouring accelerating cell. Thus the end cell nose cone gap was reduced from 18 mm to 17.88 mm like with the coupling cell, this slightly increased the local E_{peak}. Z-component of the electric field on axis is plotted in Figure 4.16

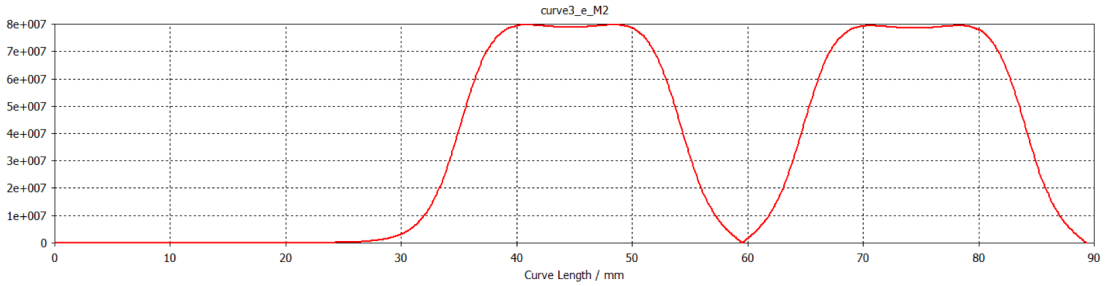

Fig. 4.16 Z-component of E-field along the beam axis of the end cell model.

4.4.3 Full structure

In the previous sections the coupler cell and the end cells have been tuned to 2.9985 GHz by adjusting the length of the gap between the nose cone. The bottleneck of the coupler has been adjusted to achieve roughly critical coupling. In this section the end cells are added to the 3-cell coupler model with normal accelerating and coupling cells between to form an 11-cell prototype structure. The vacuum model is shown in Figure 4.17.

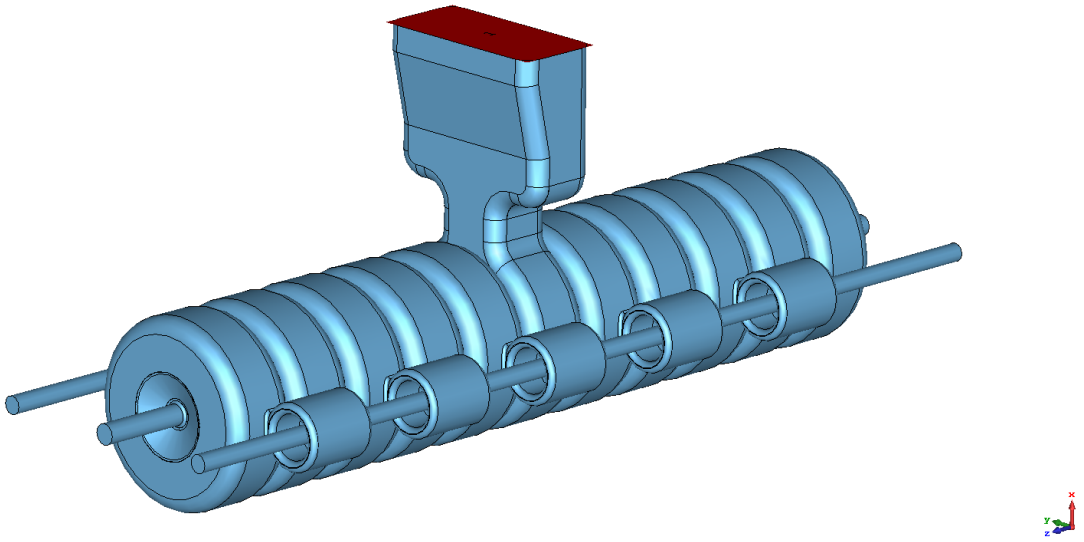

Fig. 4.17 CST vacuum model of the 11-cell prototype structure.

Previously the length of the side-coupled cell was reduced by 0.4 mm to achieve field flatness after the addition of the power coupler. The magnitude of the electric field along axis is plotted in Figure 4.18 and shows the cavity is no longer field flat.

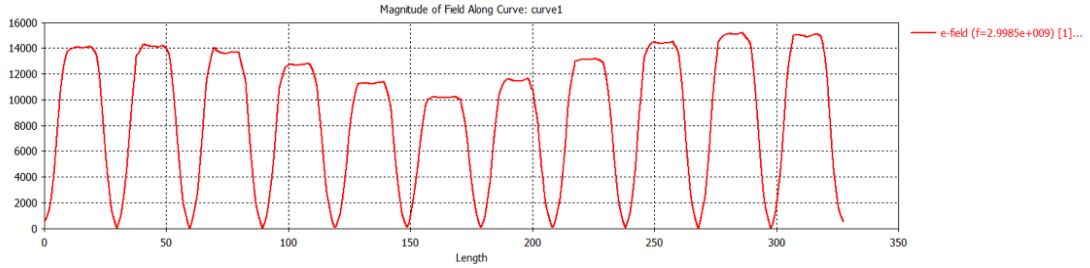

Fig. 4.18 Magnitude of the electric field along axis of the 11-cell prototype structure with a reduction in coupling of 0.4 mm.

Figure 4.19 shows S_{11} for the 11-cell model shown in Figure 4.17. The cavity is no longer well matched reflecting more than half the power at the operating frequency. There is also an unwanted mode near 3 GHz.

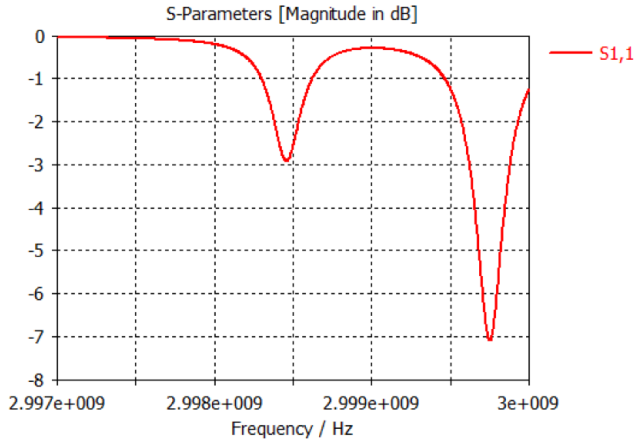

Fig. 4.19 .

The reduction in accelerating cell length was swept again to find the optimum. Reducing the length of the coupling cells by a further 0.05 mm was necessary to achieve the electric field distribution shown in Figure 4.20 and plotted in the top plot of Figure 4.21.

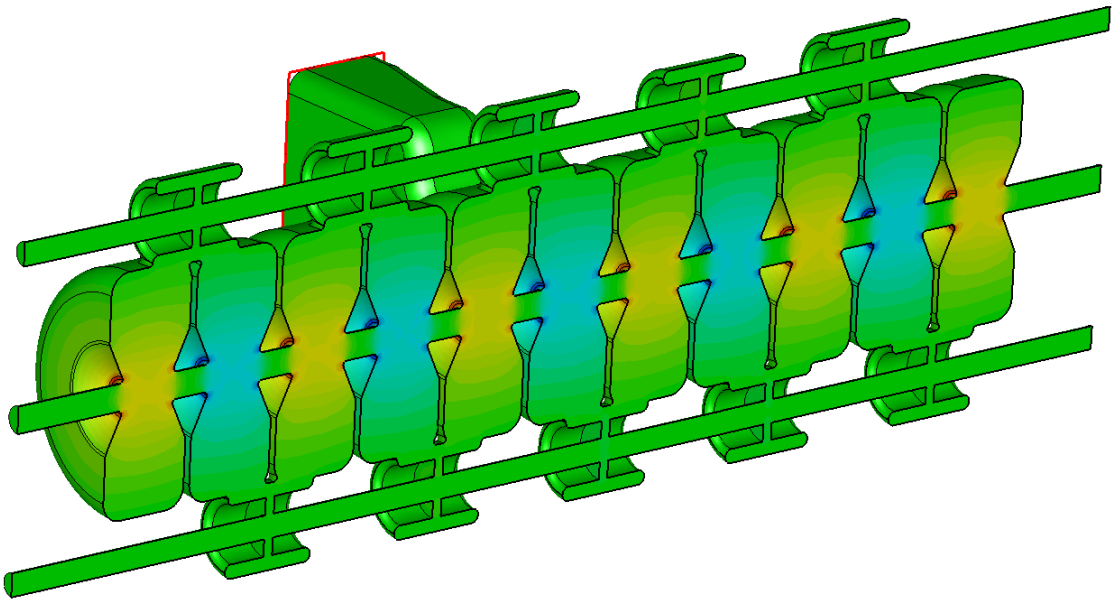

Fig. 4.20 The 11-cell prototype electric field distribution after final optimisation.

The bottleneck of the power coupler was also re-optimised to achieve critical coupling that is shown in Figure 4.21. The final results shown in this figure were obtained running a high mesh simulation (70 cells per wavelength) as this is the final characterisation before manufacturing the structure.

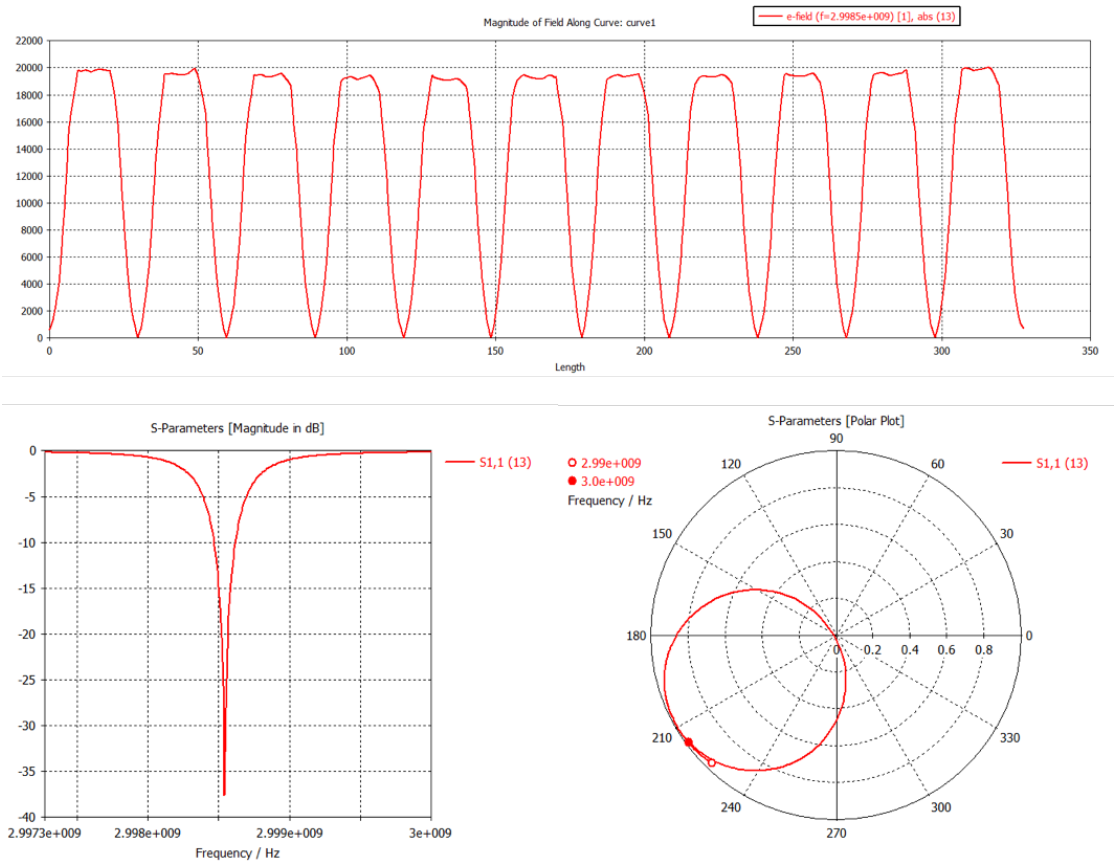

Fig. 4.21 Electric field distribution along the beam axis of the prototype model after final optimisation (Top). S-parameters of prototype structure after final optimisation simulations (Bottom).

The resonance peak in the bottom left plot of Figure 4.21 is slightly off frequency which was initially thought to be acceptable due to the large tuning ability provided by the tuning pins which are added in Chapter 6. After the drawings of this cavity had been completed and sent to the manufacturer an additional simulation was done using the Eigenmode solver to confirm the final dispersion curve of the prototype structure. This is shown in Figure 4.22. Only modes 7-12 appear as one one expect in a typical dispersion curve. Mode 12 is the accelerating $\pi/2$ mode and mode 13 is the side-coupled $\pi/2$ mode. It is clear that the stopband has not closed and thus the accelerating mode lies on a plateau rather than the steepest past of the dispersion curve. The accelerating mode will be unstable due to its proximity to its neighbour mode 11.

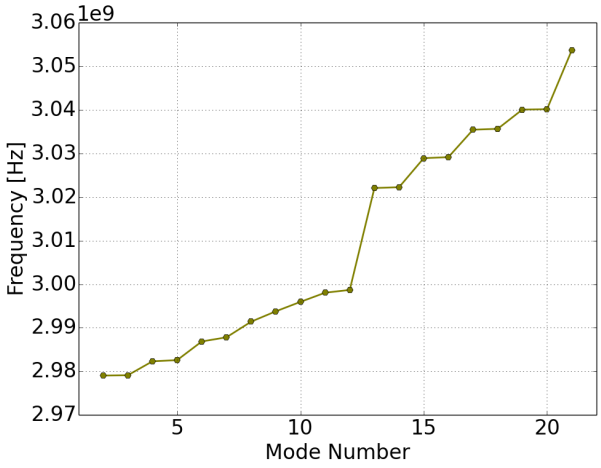

Fig. 4.22 Dispersion curve of the final prototype structure. The stop-band between the two $\pi/2$ modes has not been adequately closed.

The final tuning simulations for the full prototype were performed using the frequency domain in CST, with a field monitor set up at 2.9985 GHz to observe the fields at this frequency. Due to the final structure being completed in great haste to meet a non-negotiable deadline, the widening of the stopband was regrettably overlooked until after the manufacture of the disks. It was assumed that because field flatness had been satisfied the stopband was also closed. Reducing the length of side-coupled cell simply detuned them and took them far away from the resonant accelerating cells. Figure 4.23 shows the accelerating mode of the final prototype structure at 2.998 69 GHz. The mode is only slightly off frequency but unfortunately the field is not completely flat as is shown in Figure 4.24. The mode should be able to be bought to the correct frequency with the tuning pins presented in Chapter 6. This will allow a high power test of the cavity to still be successfully completed. However it is unlikely the large 20 MHz stop-band between the accelerating $\pi/2$ mode and the side-coupled $\pi/2$ mode, can be closed with the tuning pins. It may be possible to send the machined disks for further machining to take a millimetre off of the side-coupled cells before bonding, and bring the structure within the range of the tuning pins.

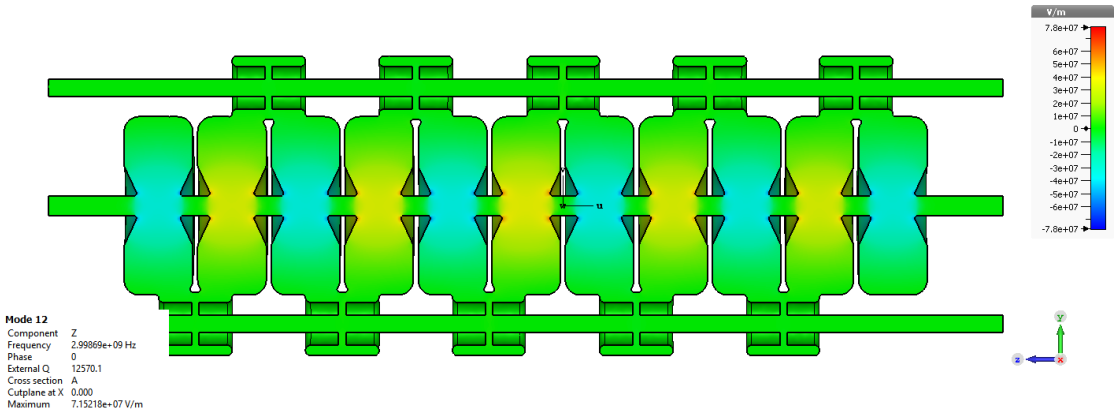

Fig. 4.23 E_z of the accelerating mode of the final prototype structure at 2.99869 GHz.

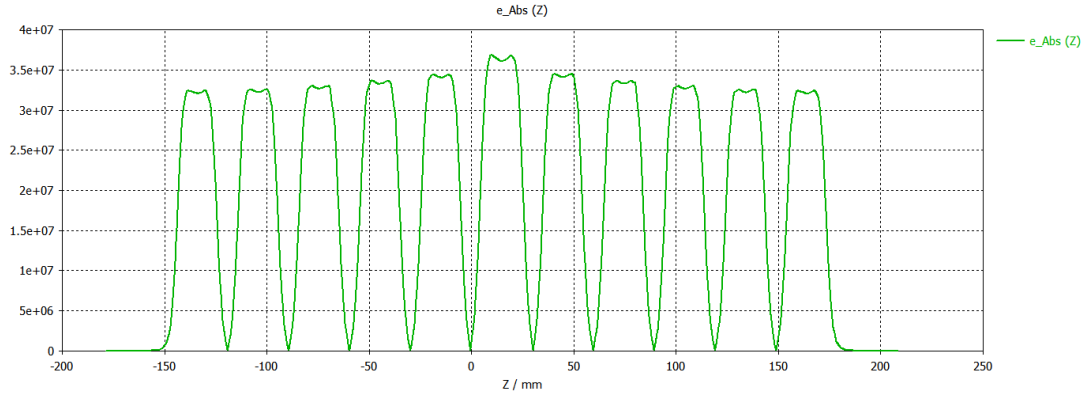

Fig. 4.24 The Z-component of the electric field on axis of the accelerating mode of the final prototype structure.

Chapter 5

Beam Dynamics

Transverse and longitudinal beam dynamics were introduced in Chapter 2 alongside many other concepts necessary for designing an RF cavity. The primary goal of an RF cavity is to accelerate a beam of charged particles to the desired output energy, but it is also important to produce enough output current. Beam dynamics must be considered from the very start of the cavity design process and throughout to ensure the RF design is optimal for that specific application. In the case of the ProBE linac the beam current must be sufficient to ensure imaging of each patient in a clinically acceptable period of time. A significant beam loss of around 90% of particles is inherent in all cyclinac schemes due to the large frequency mismatch between the 72.8 MHz cyclotron and the high frequency (3-12 GHz) linac, a small transverse aperture can contribute more loss considering the relatively large transverse emittance c.10 mm − mrad obtained from therapy cyclotrons. In this chapter the beam dynamics studies that were undertaken alongside, and informed the RF cavity optimisation are presented. Both a small aperture and a large aperture scheme were considered. By minimising the beam aperture radius, one can maximise the shunt impedance and thus accelerating gradient of a cavity. However, a smaller aperture means the transverse beam size must be kept to a minimum requiring more focussing magnets between cavities. More magnets between cavities means less space for accelerating cavities, and shorter cavities require higher gradients to achieve the same acceleration. Therefore a large aperture scheme was also studied to see if the optimal was longer cavities with lower gradient, that require less intense focussing between cavities. Following that the cavity length is investigated to ensure that is also the optimum. In this study the starting energy is 230 MeV and the final energy is 330 MeV.

5.1 Cyclotron Linac Beam Matching

The ProBE booster linac is a normal conducting pulsed machine, the RF power is pulsed to enable higher peak powers to be utilised while the average power is suitably low to prevent excess heating. A typical 50 MW klystron foreseen to power this linac can be pulsed at a maximum repetition rate of 200 Hz with a maximum pulse length 5 μs, corresponding to a maximum duty cycle of 0.1%, meaning the linac is off for the vast majority of the time - 99.9%. At PSI [59] cyclotron beam 'chopping' has been successfully demonstrated, to reduce activation of the linac during 'off time' [126]. This enables the cyclotron beam to be pulsed at 200 Hz to match the klystron repetition rate, with a rise time of 1 μs. Within each 5 μs flat top 'pulse' from the cyclotron are 357, 0.8 ns long pulses, bunched at the cyclotron frequency of 72.8 MHz which corresponds to every 13.7 ns. 1 period of RF at 3 GHz is 0.3 ns long thus each proton bunch from the cyclotron sees just over 2.5 RF periods in the linac. These concepts are visualised in Figure 5.1.

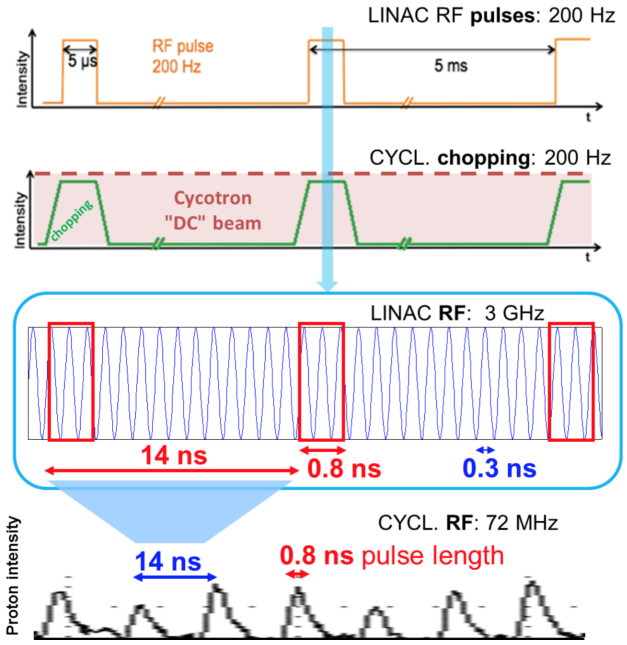

Fig. 5.1 Timing diagram for the cyclinac scheme, showing, from top to bottom, the linac RF pulses, the cyclotron pulses, the linac RF in each pulse and the proton intensity profile [67].

The Christie Varian ProBeam cyclotron [127] has an extraction current at 230 MeV up to 800 nA. Taking into account the duty cycle at 200 Hz from the cyclotron linac frequency mismatch, the average current entering the linac is 0.8 nA. To achieve the required imaging current of 3.2 pA [128] the linac must have a total transmission of only 0.4%. If the structure needs to operate with a lower duty cycle, the transmission required through the structure to deliver the same dose must

increase. The thermal cavity simulations performed in Chapter 6 have estimated the cavity may need to run at a 40 Hz repetition rate to keep the average power low. Lowering the repetition rate to 40 Hz requires 2% total transmission through the linac for the required beam current at 330 MeV.

5.2 Transverse and longitudinal losses

In Chapter 2 it was shown that a synchronous phase should be chosen on the rising edge of the wave for longitudinal bunch stability. Ideally all of the particles will see the same accelerating gradient and have equal energy leaving the linac resulting in 100% *longitudinal* transmission after the energy selection (ES) system. Unfortunately this is not practically possible and many particles will see different acceleration and be removed by the energy selection system at the end of the linac. These losses are referred to as longitudinal losses. Particles can also be lost on the structures iris due to the beam size exceeding the diameter of the aperture and hit the cavity iris or if they are deflected transversely and fail to rejoin the bunch. We refer to these as *transverse losses*. These two loss mechanisms couple together in the case that an off axis particle sees a smaller electric field due to the radial electric field distribution in the aperture. Such a particle may gain less energy than the synchronous particle and consequently fall out of the stable bunch (see Section 2.2.1) it may then be removed by the ES system. Similarly a particle in the bunch may deviate in energy and thus experience a larger kick from a quadrupole, resulting in it colliding with a cavity iris and being lost. In these cases a longitudinal effect results in a transverse loss and vice versa.

5.3 Cavity Aperture Study

5.3.1 Small Aperture Scheme

The small aperture beam dynamics scheme aims to benefit from the fact that pCT requires a smaller beam current than proton therapy linacs, or high energy physics experiments. It is thought that by minimising the beam size throughout the cavities, the aperture radius can also be minimised and higher gradients can be achieved as a result of higher shunt impedances. In the small aperture scheme, higher gradients are also necessary because more space between cavities must be occupied by magnets to keep the beam size small. Figure 5.2 shows a diagram of a beam envelope through an RF cavity, with the 'waist' or smallest point set in the centre of the structure. If the length of the cavity is reduced, so is the maximum beam size that exists within that cavity. This alongside the need for more magnets

between cavities contributes to lower active acceleration length of the linac and increases the gradient requirement.

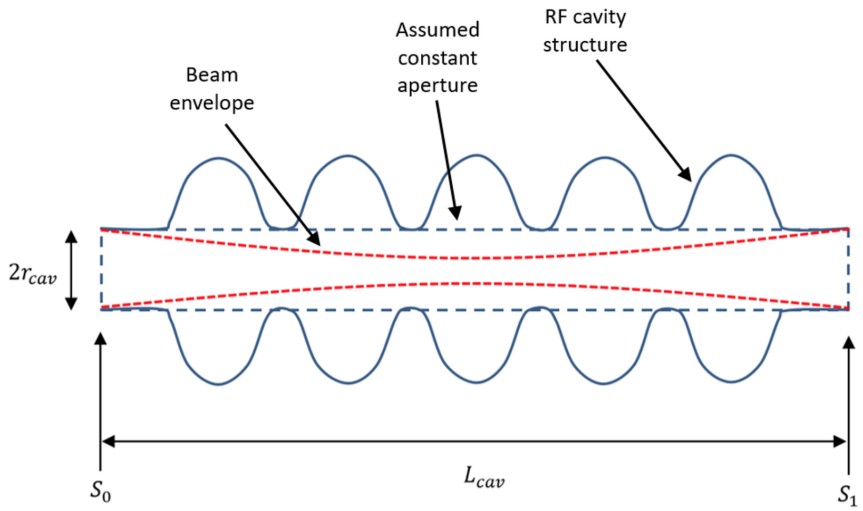

Fig. 5.2 Typical beam envelope through an RF cavity. The beam envelope is shown in red, and the smallest part of the beam or the 'waist' is shown in the centre of the cavity [129].

As the bunch length is long compared to the RF wavelength the beam parameters were optimised to maximise transmission for the entire RF cycle rather than a small range of phases. The cavity was modelled as a drift length as it was assumed the transverse and longitudinal fields over an entire RF cycle would cancel. Thus the transfer matrix for cavity was given as

$$\begin{bmatrix} x_1 \\ x_1' \end{bmatrix} = \begin{bmatrix} 1 & L_{cav} \\ 0 & 1 \end{bmatrix} \begin{bmatrix} x_0 \\ x_0' \end{bmatrix} = \begin{bmatrix} x_0 + L_{cav} x_0' \\ x_0' \end{bmatrix} \tag{5.1}$$

As is shown in Figure 5.2, the beam size is minimised in the central cell to minimise the overall beam size in the cavity. The aperture radius r_{ap} at the beginning and end of the cavity can be projected onto phase space as shown in Figure 5.3. The vertical dashed lines represent the cavity aperture radius (r_{ap}) at the entrance to the cavity and the diagonal dashed lines represent the aperture at the cavity exit. Inside of the parallelogram is the largest ellipse possible at the acceptance of the cavity. From this the acceptance Twiss parameters and the emittance at the start of the cavity were determined.

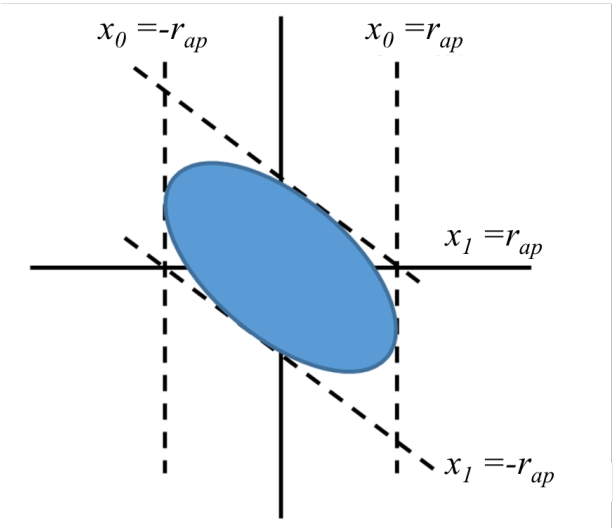

Fig. 5.3 The allowed phase space region through an RF cavity with aperture radius r_{ap} and the largest phase space ellipse possible inside of it [129].

Using Equation 5.1 the aperture limit at the end of the cavity was written as $x_1 = x_0 + L_{cav}x_0' = \pm r_{ap}$ and the limits on phase space were then written as

$$x_0 \leq r_{ap} \tag{5.2}$$

$$x_0 \geq r_{ap} \tag{5.3}$$

$$x_0' \leq \frac{r_{ap} - x_0}{L_{cav}} \tag{5.4}$$

$$x_0' \geq \frac{r_{ap} + x_0}{L_{cav}} \tag{5.5}$$

This describes a parallelogram in phase space but the acceptance will be the largest ellipse that fits inside of this parallelogram. The corners of the parallelogram were next expressed as

$$P_1 : (x, x') = (r_{ap}, 0) \tag{5.6}$$

$$P_2 : (x, x') = (r_{ap}, -\frac{2r_{ap}}{L_{cav}}) \tag{5.7}$$

$$P_3 : (x, x') = (-r_{ap}, 0) \tag{5.8}$$

$$P_4 : (x, x') = (-r_{ap}, \frac{2r_{ap}}{L_{cav}}) \tag{5.9}$$

The midpoints between the corners of the parallelogram are where the ellipse touches it and were then expressed as

$$M_1 : (x, x') = (r_{ap}, -\frac{r_{ap}}{L_{cav}}) \tag{5.10}$$

$$M_2 : (x, x') = (0, -\frac{r_{ap}}{L_{cav}}) \tag{5.11}$$

$$M_3 : (x, x') = (-r_{ap}, \frac{r_{ap}}{L_{cav}}) \tag{5.12}$$

$$M_4 : (x, x') = (0, \frac{r_{ap}}{L_{cav}}) \tag{5.13}$$

The points $M_1 - M_4$ were then equated to the corresponding points on the parametrised phase space ellipse shown in Figure 2.9. From M_4

$$\sqrt{\frac{\varepsilon}{\beta_T}} = \frac{r_{ap}}{L_{cav}} \tag{5.14}$$

From M_1

$$\sqrt{\varepsilon\beta_T} = r_{ap} \tag{5.15}$$

$$-\alpha_T\sqrt{\frac{\varepsilon}{\beta_T}} = -\frac{r_{ap}}{L_{cav}} \tag{5.16}$$

and from these the acceptance Twiss parameters and the geometric emittance for the minimum aperture scheme were determined in terms of the length of the cavity L_{cav} and the radius of the aperture r_{ap}

$$\beta_{T_{acc}} = L_{cav} \tag{5.17}$$

$$\alpha_{T_{acc}} = 1 \tag{5.18}$$

$$\varepsilon_{g_{acc}} = \frac{r_{ap}^2}{L_{cav}} \tag{5.19}$$

and as we require the beam to be be focussing in both the horizontal and vertical planes at the start of the cavity, and defocussing in both planes at the output of the cavity, $\beta_{T_{acc}} = \beta_{T_{out}}$ and $\alpha_{T_{acc}} = \alpha_{T_{out}}$, where $\beta_{T_{out}}$ and $\alpha_{T_{out}}$ are the output Twiss parameters.

The magnets between RF cavities that keep the beam on track are called matching sections. Having determined the optimum beam parameters at the acceptance and output of each cavity, the matching sections were designed. In order to match the four Twiss parameters $\beta_{T_{acc}}, \beta_{T_{out}}, \alpha_{T_{acc}}and\alpha_{T_{out}}$ 4 degrees of freedom were needed, and thus 4 quadrupoles in each matching section. Permanent Magnet Quadrupoles (PMQs) were chosen for this application due to their compact size. The aperture radius of the PMQs was chosen as 6 mm to allow for a large

beam 'blow-up' between cavities, helping to minimise the beam size inside the cavities. The PMQs were assumed to be 3 cm each in length and 2 cm each side of the magnet was left free for practical purposes. This made the minimum length of each matching section L_{match} =22 cm. The total linac length should not exceed 3 m to ensure it can fit in the allocated space in the Christie beam line. If the number of RF cavities in the linac is n and length of the cavity is L_{cav} then the active accelerating length is nL_{cav} assuming no matching section is required after the final cavity there will be $n-1$ matching sections and

$$nL_{cav} + (n-1)L_{match} \leq 3 \tag{5.20}$$

A maximum gradient of 65 MV/m was assumed for the small aperture scheme based on the optimisation studies presented in Chapter 3. This is comparable to what has been demonstrated experimentally for medium-β 3 GHz cavities (see Chapter 7. Using a typical synchronous phase of 20° the accelerating gradient seen by the beam will be lowered to 61 MV/m thus the active accelerating length of the linac must be at least 1.64 m to gain 100 MeV. 6×22 cm matching sections will fit in the remaining 1.36 m non active length thus the minimum aperture scheme can consist of a maximum of 7 × 24 cm cavities.

The acceptance Twiss parameters and emittance derived in Equations 5.17 were used with the values L_{cav}=24 cm and r_{ap}=1.75 mm to design the matching sections for the small aperture scheme. MAD-X [130] is a code developed at CERN to simulate beam dynamics and optimise beam optics, and it was employed to study the matching the sections outside of this work [129]. The study indicated a quadrupole strength of K=367 m^{-2} or a field gradient of 1044 Tm^{-1} was necessary to make the minimum aperture scheme feasible. Neodymium PMQs magnets can produce a pole tip field of up to 1.4 T. In this study the quadrupoles were assumed to be 3 cm in length with a bore radius of 6 mm to allow for a large beam size between cavities.The K-strength of a magnet is calculated as

$$K = \frac{g}{pc} = \frac{cg}{\beta E} \tag{5.21}$$

where $g = B/r_b$ is the quadrupole field gradient which is the pole tip field B divided by the bore radius of the PMQ (r_b). This makes the maximum K-strength at 330 MeV (β= 0.6729) 82 m^{-2}. As the required K-strength of the magnets is over 4 times larger than the feasible K-strength of normal conducting magnets, the small aperture scheme is deemed infeasible for the ProBE project. It could be feasible for a linac with more flexibility over the total length.

5.3.2 Large Aperture Scheme

As the minimum aperture scheme was deemed infeasible for the ProBE linac a large aperture scheme was also investigated. The FODO beam dynamics scheme was introduced in Chapter 2 as single focussing and defocussing quadrupoles placed in alternate drift spaces between RF cavities. Using single quadrupoles between structures minimises the non-accelerating lengths between cavities and thus maximises the accelerating length of the linac because the cavities can be longer. The maximum beam size in the cavity increases with the length of the cavity as was shown in Figure 5.2, which means the aperture radius will have to be larger. The shunt impedance and thus accelerating gradient has been shown to depend strongly on the beam aperture radius so increasing the aperture will lower the maximum achievable gradient but there will be a greater total accelerating length with longer cavities so a lower gradient will be required for the same net acceleration.

Particle Tracking Simulations

Particle tracking simulations were performed in ASTRA (A Space Charge Tracking Algorithm) [131] alongside this work as a case study to both investigate the difference between 'coupled' and 'uncoupled' phase space analysis, and to verify an analytical model that was developed to estimate particle transmission through a linac [129]. 'Uncoupled' phase space analysis describes the case where transverse and longitudinal losses are treated as completely separate loss mechanisms. Two separate simulations are run; one for transverse and one for longitudinal. The longitudinal particle distribution lies on the design axis of the beam which does not allow for the coupling of transverse and longitudinal effects which were defined at the beginning of this Chapter. This 'uncoupled' deign methodology is sometimes adopted to reduce the number of particles necessary for the simulation and thus computational time. In a 'coupled' phase space analysis many particles, on the order of 100%, can be lost transversely on the aperture so $\geq 10^6$ particles have to be used to ensure enough particles remain for the longitudinal analyses. The 'uncoupled' analysis and theoretical model are irrelevant to this work and will be ignored. The results of the 'coupled' simulations are the most accurate and thus the result that informs our choice of aperture for the large aperture scheme.

Using only 1×3 cm quadrupole for each matching section with 2 cm gaps either side for flanges makes each matching section 7 cm assuming 7 cavities like in the small aperture study, 258 cm are free to be occupied by structures. This makes each cavity just under 37 cm each so it was decided to round this up to 40 cm and have one less cavity to save on manufacturing costs. In this arrangement each matching section is 12 cm long. The simulation set up is shown in Figure 5.4.

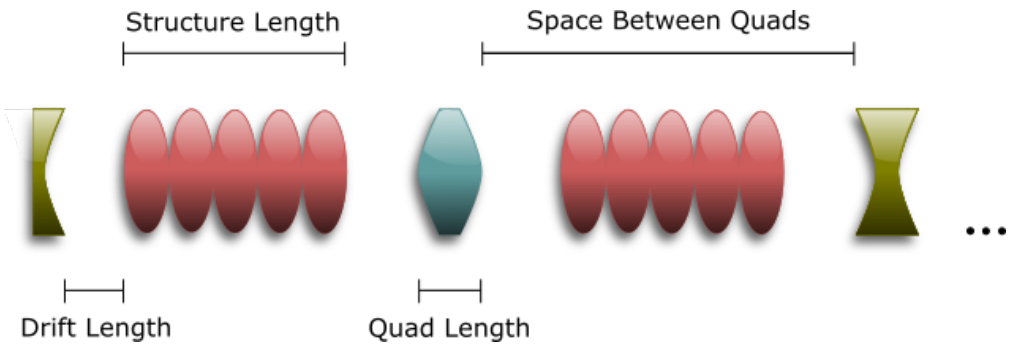

Fig. 5.4 Linac layout as it was set up in ASTRA. Green elements represent defocussing quadrupoles, blue elements represent focussing quadrupoles and the red elements represent RF cavities.

Field maps produced by CST microwave studio were imported into ASTRA to model the fields in the cavity. Only fields from within the beam aperture were used. If a particle exceeds the aperture it experiences no force, including no restorative force thus it will continue to propagate without returning to the beam axis. Rather than design many different cavities with varying apertures and lengths for these particle tracking simulations, one representative field map was taken and manipulated for other parameters. The aperture radius was swept in this study so the transverse dimensions of the field map were scaled. The length of the field map was also manipulated to account for the increasing β in each cavity. Changing the cavity length without changing the field amplitude violates Gauss' law for both the electric and magnetic fields, which states

$$\begin{aligned} \frac{\partial E_x}{\partial x} + \frac{\partial E_y}{\partial y} + \frac{\partial E_z}{\partial z} &= 0 \\ \frac{\partial B_x}{\partial x} + \frac{\partial B_y}{\partial y} + \frac{\partial B_z}{\partial z} &= 0. \end{aligned} \tag{5.22}$$

However, as ASTRA scales the fields inside the cavity to ensure the same average gradient in each cavity, Gauss' law would have been broken in any case. The input field map is essentially arbitrary. Furthermore, transverse forces in the cavity are deemed to have a negligible effect on beam optics for 230-330 MeV protons. The effective quadrupole K-strength for an RF cavity can be expressed as

$$K_{cav} = -\frac{\omega e V_{cav} \sin\phi}{2\gamma^3\beta^4 mc^4} \tag{5.23}$$

which is $0.003 - 0.007\text{m}^{-2}$ for this range of cavity voltages. This is negligible relative to the quadrupole K-strengths in the linac between $1 - 100\text{m}^{-2}$. Only at low energies ($\simeq$ 20 MeV) when the beam rigidity is less will the transverse fields in the cavity have an effect on the beam optics. After the particles were tracked through the linac including accelerating structures and quadrupoles, the

results were post-processed in MATLAB [132]. All of the particles that exceeded the cavity aperture are removed first as they are considered transverse losses and will also have the wrong energy at the end of the simulation but should not be counted as longitudinal losses. After the aperture losses were removed, all particles greater than 1 MeV more or less than 330 MeV were removed replicating the energy selection system. The total transmission remains.

Initial Particle Distribution

An initial particle distribution was created for each individual simulation. The optimum Twiss parameters for each aperture size were tracked back to the centre of the first quadrupole (where the simulation begins) using the thin lens approximation detailed in Chapter 2. The maximum (β_{Tmax}) and minimum (β_{Tmin}) β_T-functions for the centre of the first quadrupole were calculated from Equation 2.32 as

$$\begin{aligned} \beta_{Tmax} &= \frac{L}{\sin\frac{\mu}{2}}\sqrt{\frac{1+\sin\frac{\mu}{2}}{1-\sin\frac{\mu}{2}}} \\ \beta_{Tmin} &= \frac{L}{\sin\frac{\mu}{2}}\sqrt{\frac{1-\sin\frac{\mu}{2}}{1+\sin\frac{\mu}{2}}} \end{aligned} \tag{5.24}$$

where L is the space between the quadrupoles. This minimises β_T and thus the transverse size of the bunch ensures maximum transmission through the linac. Figure 5.5 shows how the maximum β_T-function varies with the betatron phase advance. It has a very broad minimum but the true minimum was at 76° so that was chosen to minimise the beam size.

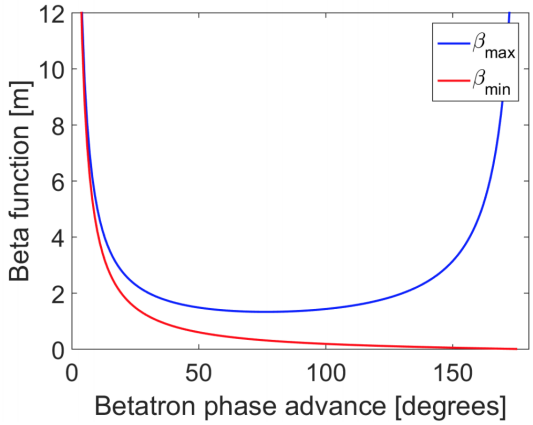

Fig. 5.5 Maximum (blue) and minimum (red) β_T function as a function of the betatron phase advance μ for a 40 cm long cavity [129].

Some generic cyclotron 1σ normalised emittance values were chosen for the initial particle distribution, as the specification of the ProBeam cyclotron [127]

was not public, they are shown in Table 5.1. The transverse normalised emittance $\varepsilon_x = 5 \times 10^{-6}$ m-rad and longitudinal $\varepsilon_y = 8.5 \times 10^{-6}$ m-rad, the transverse distribution was assumed to be Gaussian in both $x, x' \& y, y'$. As was explained in Figure 5.1 the output of the cyclotron appears to the linac CW, as such a beam uniform in z and Gaussian in z' with an energy spread of 2%.

Parameter	Value	Units
Cyclotron Frequency	72.8	MHz
Chopping rep. rate	200	Hz
Bunch length	0.8	ns
Bunch Charge	0.142	c
Beam Current	800	nA
Energy	230	MeV
Energy Spread	2	%
Normalised emittance x	$5 \times 10^{-}6$	m-rad
Normalised emittance y	$8.5 \times 10^{-}6$	m-rad
Geometric emittance x	$6.7 \times 10^{-}6$	m-rad
Geometric emittance y	$1.1 \times 10^{-}6$	m-rad

Table 5.1 Generic cyclotron parameters used to create the initial particle distribution in the cavity length study.

Results

In Section 5.1 the mismatch in frequencies was shown to discard 99.9% of the beam from the cyclotron output, and that the linac would need a transmission of 0.4% to achieve the required imaging current of 3.2 pA at 200 Hz. If a lower repetition rate of $\geq$40 Hz is adopted the required transmission through the linac rises to $\geq$2%. The results of the large aperture particle tracking simulations are shown in Figure 5.6. The blue line represents the coupled phase space analysis described in this section. It is shown that 2% total transmission corresponds to an aperture radius of around 3.7 mm. This was rounded up to 4 mm because more transmission means faster imaging which is desirable for medical applications. It also allows for a safety margin.

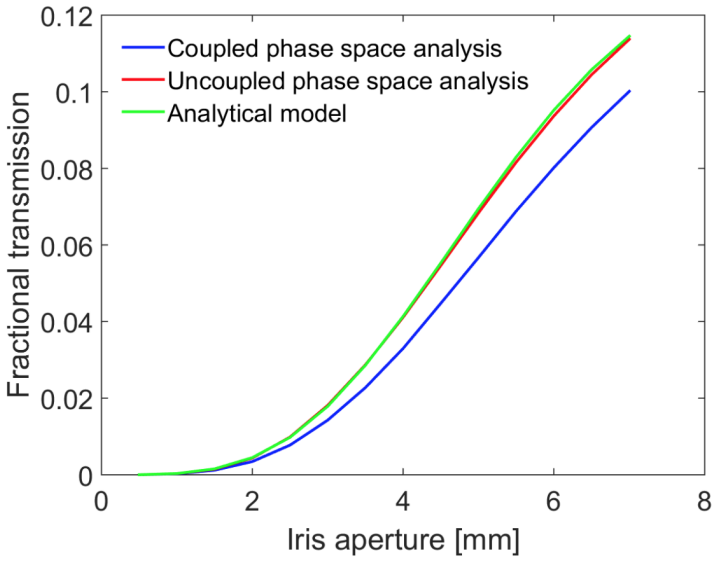

Fig. 5.6 Results of the large aperture particle tracking study [129].

5.4 Cavity Length Study

An aperture radius of 4 mm has been selected with FODO beam optics for the ProBE linac. The previous study fixed the structure length at 40 cm and swept the size of the aperture radius in particle tracking simulation. In this section the aperture radius will be fixed while the cavity length is swept to find the optimum structure length for the ProBE linac.

The same methodology as was presented in the large aperture particle tracking simulations was followed. The same simulation model was used as was presented in Figure 5.4, however the number of cavities was not fixed at 6, but varied depending on the cavity length and thus how many would fit in the three meter space with the matching sections on either side.

An initial particle distribution was created for each different length simulation using the same generic cyclotron parameters as is shown in Table 5.1. The optimum Twiss parameters at the start of the simulation were calculated for the initial particle distribution in the same way as in the large aperture particle tracking. The thin lens approximation was used to define the transfer matrices which were introduced in Chapter 2. The optimum acceptance beam parameters for each cavity length were tracked back to the centre of the first quadrupole where the simulation begins.

The maximum K-strength in this study was calculated to be 82 $m^{-}2$ in the small aperture study. This study was done as part of this thesis work whereas the large aperture tracking study was done in parallel. For that reason slightly different quadrupole lengths were used. In this study the length of the quadrupoles

has been set at 0.035 m. $\sqrt{82} \cdot 0.035 = 0.32$ which is less than 1 and thus valid for use with the thin lens approximation. If the thick lens mathematics was used, element M_{11} of the transfer matrix for the FODO cell would equal 0.95 instead of 1 with the thin lens. Thus we find the approximation valid for this study.

Figure 5.7 shows how the β_T-function varies with the betatron phase advance. The maximum β_T has a rather broad minimum across a range of μ, but it's true minimum is around 70°, and is thus a suitable betatron phase advance for the cavity length study.

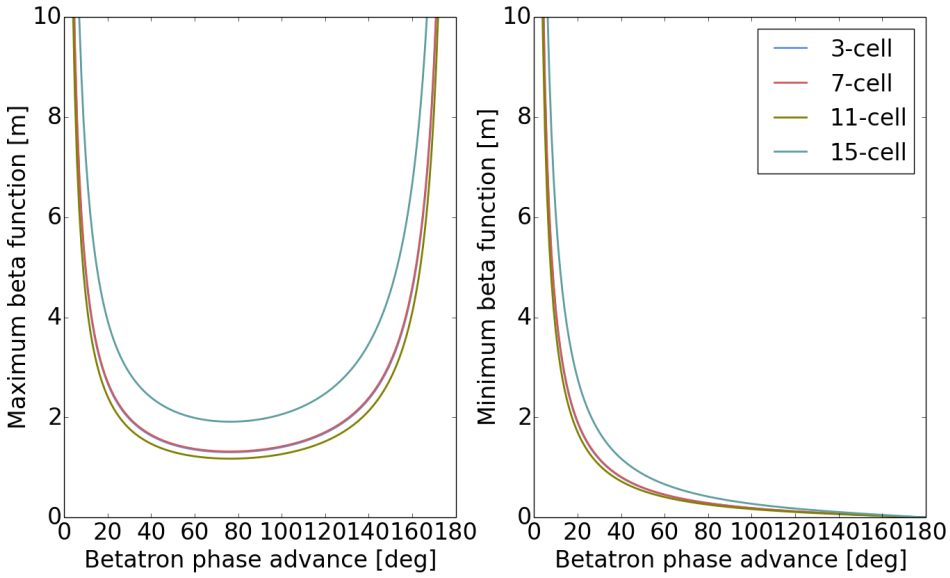

Fig. 5.7 Maximum and minimum β_T-functions with varying number of cells.

Particles were tracked through as many structures as would fit in 3 metres with a quadrupole and two drift spaces between each. The simulation was repeated for four different linacs with 3,7,11, and 15-cell structures. The drift lengths were altered for each cavity length to ensure the quadrupole strength remains what is physically achievable with neodymium (NdFeB) rare-earth permanent magnets.

In each of the Figures 5.9 to 5.12 one can see the initial particle distributions in blue beneath the green final particle distributions plotted in phase space. The reference particle used by ASTRA begins in the centre of the bunch, and each bunch contains 1 million macro particles - each represented by one marker. The particles whose radial position, $\sqrt{x^2 + y^2}$, exceeded the beam aperture were removed first these are what we consider '*aperture losses*'. The remaining particles are considered to be the *transverse* transmission and this is what is presented in the top three plots. The energy selection system at the end of the linac will then remove all particles exceeding ±2% of 330 MeV these are considered '*ESS losses*'. The particles remaining after the energy selection system are considered to be the *longitudinal*

transmission and this is what is shown in the centre three plots. The remaining particles after both transverse and longitudinally lost particles have been removed are shown in their position at the *start* of the linac in the bottom three plots and this is known as the *acceptance* of the linac. If one was to 'tailor' a beam deliberately for the ProBE linac, they should make it identical to (or smaller than) this acceptance. The bottom right plots show that in all cases investigated ideal energy distribution at the start of the linac to maximise transmission, has a slightly higher energy at the tail end of the bunch. This helps to bunch the beam, which keeps it together in the linac,ensuring particles see similar fields and stay together resulting in higher transmission.

Initially the quadrupole parameters were fixed in this study. This meant the drift length had to be adjusted to keep the quadrupole strengths within practically achievable limits. The assumption is that no particles are lost on the quadrupoles as the PMQ design has not been finalised and can be altered to accommodate the maximum β_T, the bore radius of the quadrupole could be increased if necessary in that part of the linac, and the length of the quadrupole could be increased slightly to ensure the K-strength does not exceed practical limits. Initially the drift length was set at 50 mm as a compact solution is a priority and 50 mm is a reasonable distance to allow for interfaces between components.

The smallest structure investigated was a 3-cell structure with a length of approximately 10 cm. With the original drift length of 50 mm, 12 structures could fit in a 3 meter space alongside 11 quadrupoles. However, the k-strength would need to be 155 m^{-2} which is approximately double the achievable maximum of 82 m^{-2} possible with neodymium PMQs with a 6 mm bore radius and 35 mm in length. The bore radius would need to be halved to achieve the required field gradient, and would thus be smaller than the structure aperture which would reduce transmission rather than improve it. Instead, the drift length was increased to 14 cm from 5 cm, which reduces the quad strength but also the number of structures in 3 meters down to 7.

The resulting data from the particle tracking simulations in ASTRA were processed using MATLAB [132] and are presented in Figure 5.8. One can see the effect of increasing the structure length as was shown in Equation 5.24. As the cavity length L_{cav} increases, the beam size increases as $\sqrt{L_{cav}}$, thus more particles are lost on the aperture and transverse transmission decreases. The longitudinal transmission also decreases as the structure length increases. Longer structures have greater phase slippage, so some of the beam slips out of the RF bucket, consequently doesn't reach the required energy and is thus removed by the energy selection system. However in this case, there was an exception. The 3-cell structure has lower longitudinal transmission than the 7-cell structure. Looking at the top right hand plot of Figure 5.9, the beam has not bunched as well as it has in the

longer cavities. This is due to the accelerating length of the linac not being long enough for the beam to form stable bunches. There is thus an optimum total transmission around 7-cells, or 25 cm.

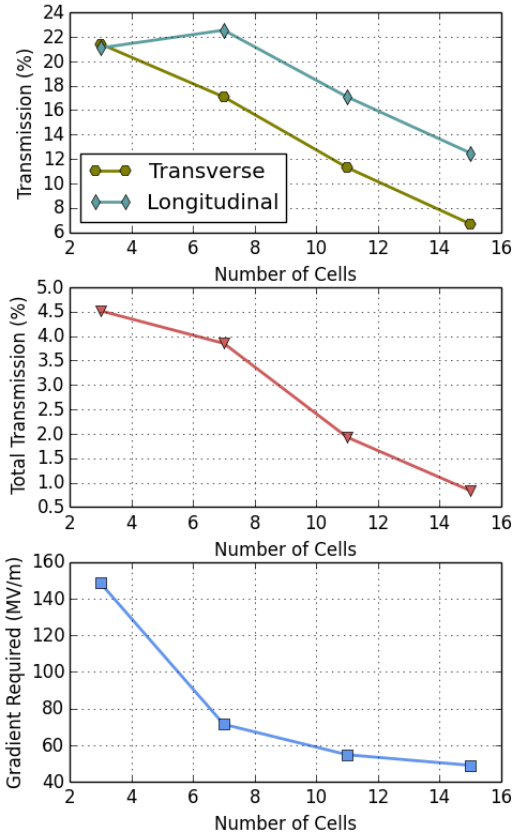

Fig. 5.8 Transverse and longitudinal transmission (top), total transmission (centre) and required gradient (bottom) vs. number of cells per cavity.

3-cell structure

The bottom plot in Figure 5.8 shows that, the longer each structure is, the lower the required gradient is. Although the 3-cell structure has the highest transmission, it also requires an excessively high accelerating gradient. 7×3-cell structures would have an active accelerating length of 82 cm. 100 MeV acceleration in this length would require a gradient of 121 MV/m; the structures in the small aperture section were calculated to reach 60 MV/m, but they were limited by inter-cell coupling so higher gradients would be achievable with a 3-cell structure. 120 MV/m has been demonstrated at KEK as part of the CLIC high gradient test programme with the TD24-KEK-KEK [133], however that was concerning a $\beta = 1$ unloaded structure. Furthermore, one must consider that we accelerate off crest so the beam

will interact with a lower gradient than that. Assuming a synchronous phase of ϕ_s=20°, the gradient requirement rises to 129 MV/m, assuming 15% losses the gradient required increases to 149 MV/m which would be extremely challenging even for a fully relativistic structure, with current technological capabilities, thus the conclusion is that 3-cell structures are infeasible for this application.

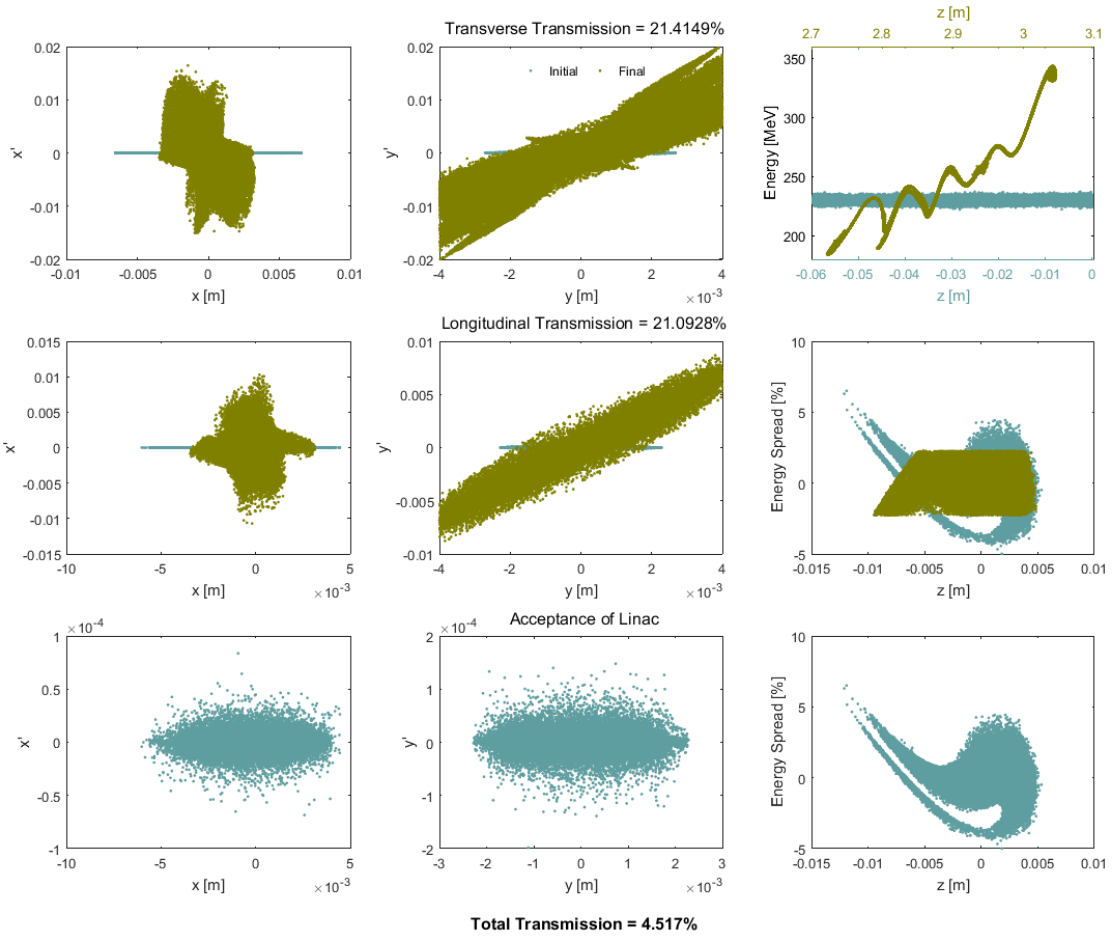

Fig. 5.9 Transmission through 7×3-cell cavities and matching sections between.

7-cell structure

The 7-cell structure is approximately 25 cm long and assuming 50 mm drift lengths 8 structures will fit in 3 m. However, like the 3-cell structure, this would require an unobtainable K-strength of ≈ 99 m^{-2}. For this reason the drifts were increased to 80 mm so that 7 structures are in 3 m. Although in the simulation the quad length was kept as 35 mm, in reality to keep within the maximum K-strength, the length would also need to be increased by around 300 microns. It is assumed such a small change will have little effect on the total transmission. The transmission of the 7-cell structure option is shown in Figure 5.10 and is comfortably over the 2% target at 3.85%. The required gradient however is 71 MV/m which we know from the previous chapter is even challenging with a smaller aperture radius than

4 mm. If one were to instead keep the drift length at 50 mm but increase the quad length to 42 mm, the K-strength would be reduced to a feasible figure and fit in an eighth structure. This would lower the gradient requirement to 62.5 MV/m, which is still challenging for a $\beta = 0.6$ normal conducting RF cavity with a 4 mm aperture radius. In the previous chapter only two structures were calculated to achieve gradients that high with an aperture less than half size, and the cavity would only be 50 mm shorter, so coupling would still influence the shunt impedance.

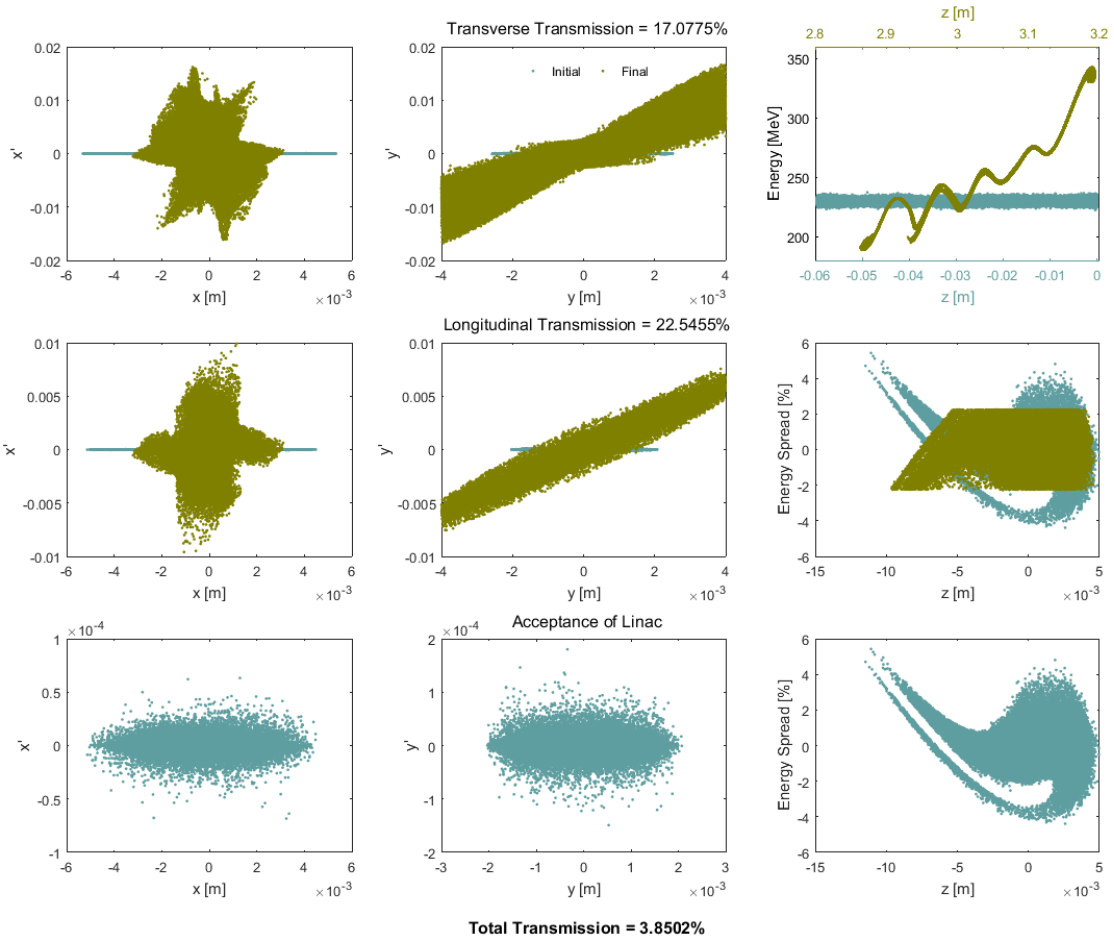

Fig. 5.10 Transmission through 7×7-cell cavities and matching sections between.

11-cell structure

The 11-cell cavity is approximately 35 cm in length and the results for the tracking simulations are shown in Figure 5.12. With 50 mm drift lengths and 35 mm long quadrupoles, 6 structures will fit in 3 m. This makes the required gradient 54.8 MV/m. In Chapter 7 a 3 GHz low-β medical structure is presented that was tested at over 50 MV/m [22], so this is closer to the high gradient performance one can expect for this type of linac.

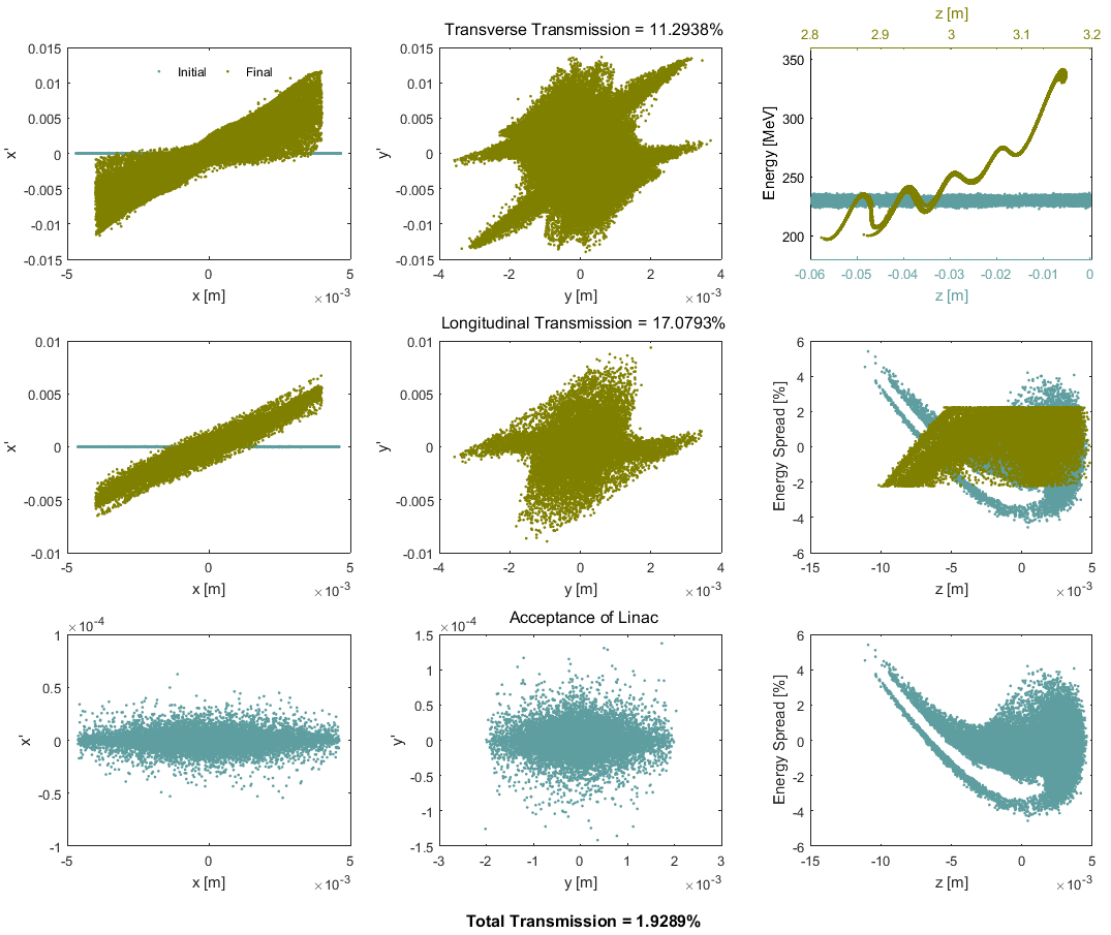

Fig. 5.11 Transmission through 6×11-cell cavities and matching sections between.

15-cell structure

The particle tracking results for the 15-cell structure are shown in Figure 5.12. The structure is approximately 50 cm in length. with 50 mm drift lengths and 35 mm long quadrupoles one can only fit 5 structures in 3 m. The simulation was performed with these parameters and that takes the linac length over the 3 meter limit by 10 cm but the length of the quadrupoles could be reduced to 22 mm within the maximum K-strength and this would reduce the total linac length by 50 mm. Reducing the drift length by 5 mm would bring the linac within 3 m but 50 mm drifts are what we consider the minimum feasible drift. The total transmission through this linac was only 0.8% which would provide adequate transmission for pulse repetition rates down to 104 Hz and the gradient requirement is reduced to 49 MV/m.

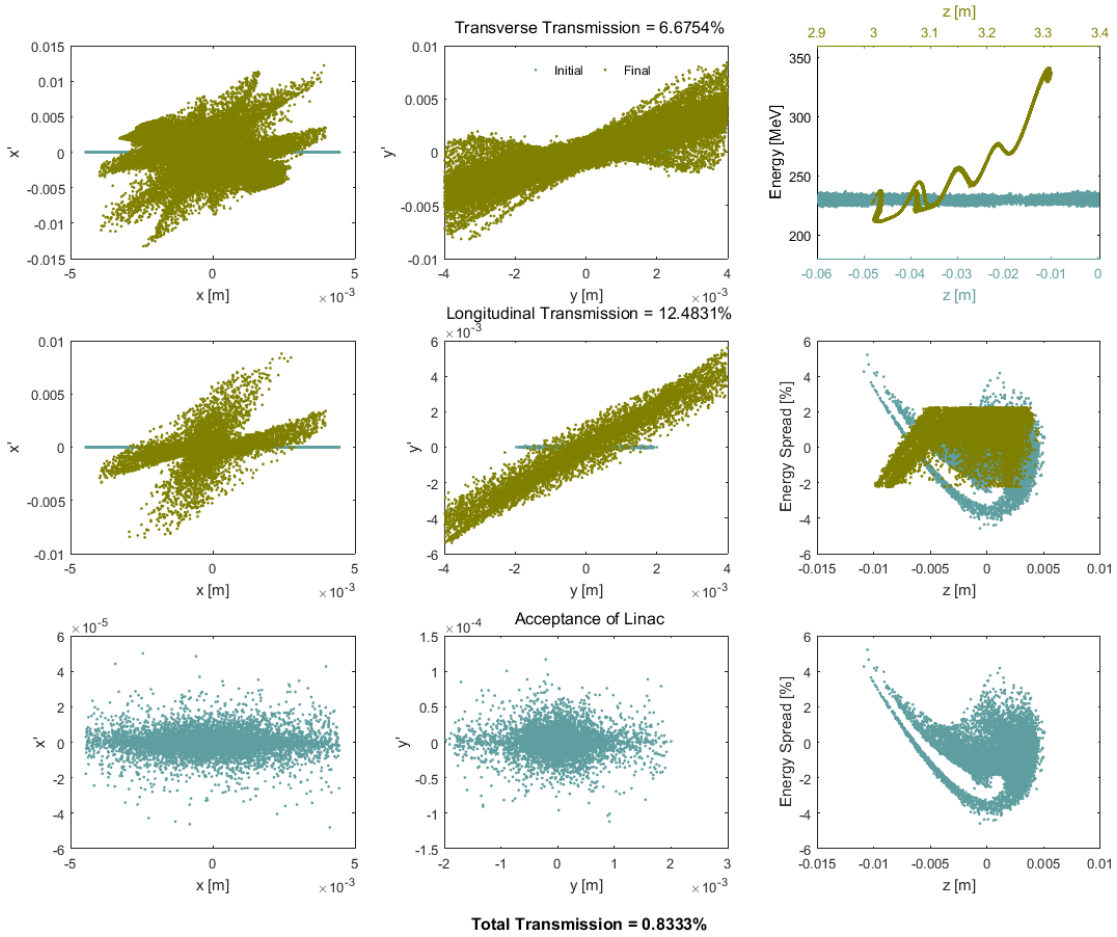

Fig. 5.12 Transmission through 5×15-cell cavities and matching sections between.

Discussion

The gradient required for a 15-cell cavity is only 5 MV/m less than that of the 11-cell cavities so there is not much benefit to increasing the length past 11-cells. The intercell coupling constant would have to be higher for a 15-cell cavity which would reduce the shunt impedance, and with a total transmission of 0.8% it would have to operated at 104 Hz or higher to achieve the desired output current. The 11-cell structure is calculated to provide enough output current down to 42 Hz. The 7-cell cavity requires a slightly higher gradient but the transmission allows more flexibility with the repetition rate. It can fit one more cavity in 3 m than the 11-cell structure which would result in higher manufacturing costs. Previously no medium-β cavity has been shown to achieve 71 MV/m. For these reasons we conclude the ProBE linac will consist of 6×11-cell structures, which provides just under 2% total transmission to the patient. It provides flexibility over the repetition rate, only has 6 cavities, and the gradient target in the range of demonstrated cavities. The key parameters are summarised in Table 5.2.

Parameter	Value	Units
Structure length	≈35	cm
Number of cells	11	
Aperture Radius	4	mm
Minimum rep. rate	40	Hz
PMQ Length	3.5	cm
PMQ Strength	72.4	$m^{-}2$
Number of PMQs	6	
Number of cavities	6	
Required gradient	54.8	MV/m
Total transmission	1.92	%

Table 5.2 Summary of the final linac design parameter after the cavity length study.

Chapter 6

Mechanical Engineering of ProBE Cavity

6.1 Tolerance Sensitivity

Once the RF design of any cavity is complete, one must complete a tolerance study to investigate the sensitivity of the parameters in the cavity to machining tolerances. Errors made during machining and cavity bonding can detune the cells. Tuning studs have been added to the ProBE prototype structure to enable cavity tuning post manufacture. In 2014 the TERA foundation with CLIC conducted an experiment to test varying tuning hole dimensions for their S-band high gradient structure [134]. That structure was subsequently manufactured and successfully tuned employing tuning holes with a 10.5 mm diameter hole and 1.6 mm of copper between the tuning stud and the cavity. The tuning studs to be brazed to the surface of the cavity have a diameter of 6 mm. On average tuning studs of this geometry perforated the cavity wall at 3.5 mm of deformation. The smallest deformation that damaged the cavity wall was 2.5 mm [134], thus we consider 2 mm to be the absolute maximum deformation possible. A single cell cavity with the same dimensions as the accelerating cell of the ProBE design was simulated with both 'push' and 'pull' type tuning deformations. The nominal frequency was 3.008 65 GHz which is slightly higher than the 2.9985 GHz design frequency due to the loss of the coupling cell. The simulation models and results are shown in Figures 6.1 and 6.2. The tuning deformations were designed to closely mimic the actual deformation caused by a tuning stud. The inner circle visible on the simulation model is the diameter of the tuning stud, and the blend around it is the radius of the tuning stud hole which would stretch around the tuning stud in a similar fashion. The tuning depth shown on the x-axis corresponds to the highest or lowest point of the deformation with respect to the outer wall for pull and push respectively. The 'push' studs resulted in a frequency shift Δf of 2.1 MHz at a 1 mm insertion depth and 6.3 MHz

at the very maximum 2 mm insertion depth. The resulting peak surface magnetic field was $< 1\%$ higher than that caused by the coupling slots, and is still within the peak surface magnetic field design limit. Similarly the 'pull' studs resulted in a frequency shift Δf of -1.87 MHz at a 1 mm retraction height which is slightly less than the 'push' stud. At the maximum height of 2 mm Δf was -4.1 MHz. The resulting peak surface magnetic field was $< 6\%$ higher than that caused by the coupling slots, which is larger than in the case of the 'push' stud but is still below 200 kA/m, well within the limit of 273 kA/m.

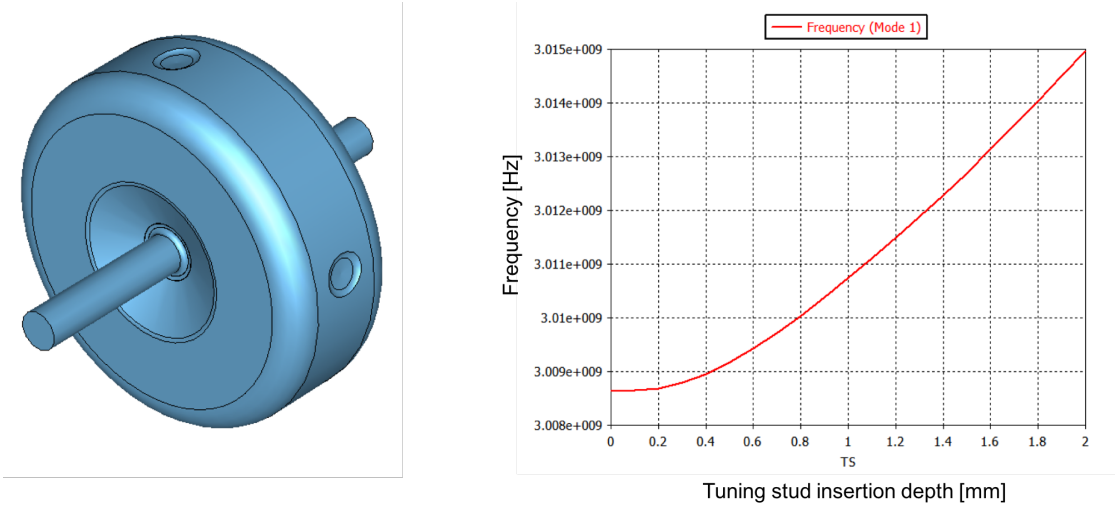

Fig. 6.1 The simulation model for the 'push' tuning studs and a plot showing the resulting frequency shift in Hz. The x-axis is how many mm the tuning stud has been inserted into the cavity wall.

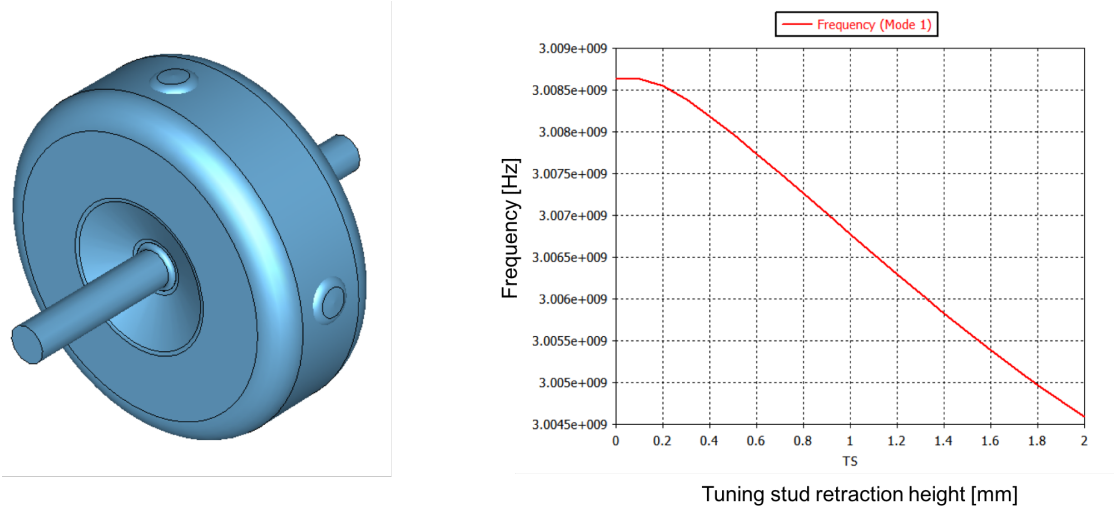

Fig. 6.2 The simulation model for the 'pull' tuning studs and a plot showing the resulting frequency shift in Hz. The x-axis is how many mm the tuning stud has been pulled from the cavity wall.

Tuning studs are brazed onto the cavity wall, then a slide hammer which is shown in Figure 6.4 is used to push and pull the stud gently deforming the cavity surface. The cylindrical weight is thrown to either side of the handle to push or pull the tuning stud. If the cavity wall is deformed too much, the stud can perforate the cavity wall. Ceramic installation pins have been designed using CATIA [135] to hold the tuning studs in position while they are brazed. This assembly is shown in Figure 6.3 where the top right magnification shows grooves in the tops of the installation pins. Wire is wrapped around the structure and holds the pins in place during brazing.

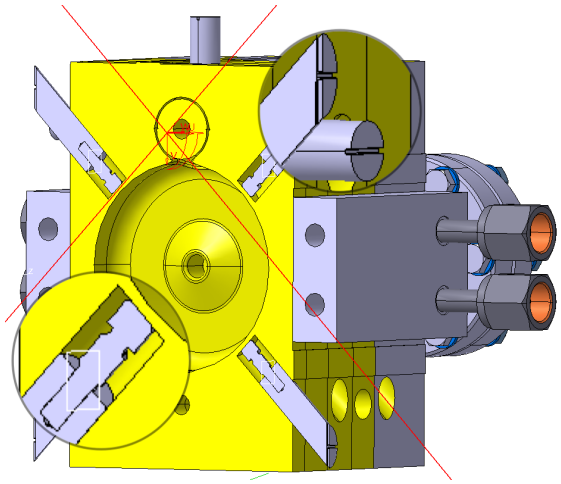

Fig. 6.3 Tuning studs in assembly with the ceramic pins used to hold studs in position during brazing.

Fig. 6.4 Slide-hammer used to push and pull the tuning studs. The weight is thrown to either end of the shaft to deform the cavity wall [134].

How much tuning capability we have in either direction is now known. Next the sensitivity of each feature or parameter of the cavity must be determined to ensure the manufacturing tolerances are within the tuning range. Each parameter was independently increased by 1μm and simulated to obtain the frequency shift $\frac{df}{d\mu m}$ in the excited accelerating mode. Simulations were done in the Eigenmode solver using a tetrahedral mesh with 60 cells per wavelength. Third order curvature was used and so was adaptive mesh refinement. Parameters were altered by 1μm

because that is the accuracy possible in modern precision machining. The results of these simulations are displayed in Table 6.1. The cavity was also simulated with 10μm added to each parameter in case the frequency shift has non-linear behaviour in some of the sensitive regions of the cavity i.e capacitive region between the nose cone. The columns headed '10-40μm Δf (kHz)' contain a worst case analysis, where it is assumed all of the parameters will have that machining error, and each will result in a positive frequency shift; the totals are the sum of those errors. This analysis suggests the structure should be machined to 10μm accuracy to guarantee the structure can be tuned with the range of the tuning pins in Figures 6.1 and 6.2.

It is highly unlikely that each parameter in the cavity would have the maximum machining error specified in the specification, and with the same frequency shift direction. Mechanical engineers will often use a Root Sum Squared (RSS) analysis which is commonly used to reduce manufacturing costs under the fair assumption that some of the machining errors will cancel out the frequency shift from others. Table 6.1 contains a total RSS frequency shift for 20-40μm. Using this analysis we could still tune the cavity with a machining accuracy of 40μm. The technical specification in Appendix A was sent with the drawings and desired manufacturing tolerances to multiple precision machining companies. VDL [136] from the Netherlands won the contract. After discussion with VDL, the cost of manufacture dominated the choice of machining accuracy. The final column of Table 6.1 shows the tolerances that were agreed with VDL, to save costs they were able to guarantee 60% of the parts would be manufactured within 20μm tolerance which is shown in green. 20% of the parts would be within 30μm tolerance shown in yellow; and the final 20% of the parts would be within 40 μm tolerance shown in red. The reader should note the most sensitive parameters were assumed to have the largest error in this study, then a RSS analysis was performed. The blue row is the blend on the coupling slot. This is a complex geometry and an important RF parameter with peak fields and determines cell to cell coupling. VDL have guaranteed it within 100 μm tolerance due its complex geometry.

The machining tolerances were calculated using only the accelerating mode, however the parameters located in the side coupled cavity should have bee calculated using the mode in the coupling cells. The capacitive gap in the side-coupled cell was calculated to have a sensitivity of 1 kHz/μm using the accelerating mode. If the same calculation was done using the mode in the coupling cell it would have yielded 69 kHz/μm. As the manufacturing had already been completed when this was realised the sensitivity of the other parameters in the side coupled cell will not be calculated in this work.

Parameter	**Para**	**Frequency**	**df/dz**	**Frequency**	**10μm Δf**	**20μm Δf**	**30μm Δf**	**40μm Δf**	**RSS 20**	**RSS 30**	**RSS 40**	**RSS VDL**
		(Hz)	**(kHz/μm)**	**(Hz)**	**(kHz)**	**(kHz)**	**(kHz)**	**(kHz)**	**(μm)**	**(μm)**	**(μm)**	
Nominal	Orig.	2998494888	N/A	2998494888								
Septum Thickness	S	2998532244	37	2998843294	348	697	1045	1394	4.86E+05	1.09E+06	1.94E+06	1.94E+06
Nose Cone Gap	G_c	2998538072	43	2998913949	419	838	1257	1676	7.02E+05	1.58E+06	2.81E+06	2.81E+06
SC Cell Length	l_{sc}	2998496756	2	2998492234	3	5	8	11	2.82E+01	6.34E+01	1.13E+02	2.82E+01
Acc Cell Length	l	2998460978	-34	2998155034	340	680	1020	1359	4.62E+05	1.04E+06	1.85E+06	1.04E+06
Accelerating Radius	r_c	2998421795	-37	2997737908	378	757	1135	1514	5.73E+05	1.29E+06	2.29E+06	2.29E+06
Side Coupled Radius	r_{sc}	2998495130	0	2998485478	5	9	14	19	8.86E+01	1.99E+02	3.54E+02	8.86E+01
Outer Corner Radius	R_{oc}	2998512491	18	2998644796	150	300	450	600	8.99E+04	2.02E+05	3.60E+05	2.02E+05
SC Outer Corner Radius	R_{oc}SC	2998494510	0	2998499216	4	9	13	17	7.49E+01	1.69E+02	3.00E+02	7.49E+01
Inner Corner Radius	R_{ic}	2998496070	1	2998495105	0	0	1	1	1.88E-01	4.23E-01	7.52E-01	4.23E-01
Inner Nose Radius	R_{in}	2998472027	-23	2998260610	234	469	703	937	2.20E+05	4.94E+05	8.78E+05	4.94E+05
Outer Nose Radius	R_{on}	2998491354	-4	2998437369	58	115	173	230	1.32E+04	2.98E+04	5.29E+04	1.32E+04
Aperture Radius	A	2998476243	-9	2998301907	96	193	289	386	3.72E+04	8.38E+04	1.49E+05	3.72E+04
Side Coupled Aperture	S_cA	2998496429	1	2998497530	1	3	4	5	6.98E+00	1.57E+01	2.79E+01	6.98E+00
Slot Blend	B_{sc}	2998491976	-3	2998440076	55	110	164	219	1.20E+04	2.70E+04	4.81E+04	3.00E+05
Capacitive Radius	R_{scc}	2998497536	1	2998500694	3	6	9	12	3.37E+01	7.58E+01	1.35E+02	3.37E+05
Capacitive Gap	L_{scc}	2998496130	1	2998496240	1	3	4	5	7.31E+00	1.65E+01	2.92E+01	7.31E+00
				Total kHz	**2096**	**4193**	**6289**	**8385**	**1611**	**2416**	**3222**	**3022**

Table 6.1 Table containing the tolerance sensitivity of the ProBE prototype cavity.

6.2 Thermal Analysis

During operation, the pulsed RF power inside the cavity will dissipate heat into the cavity walls. As the copper heats the structure it will thermally expand. This expansion can alter the frequency of the cells, and not always in a uniform way. This is referred to as operational detuning. The operational detuning must remain within the bandwidth of the structure which will not be known for certain until the structure is built and has been tuned. It can be estimated from Figure 4.21 as 230 kHz and the operational detuning must not exceed this bandwidth. This is not to be confused with the sensitivity analysis performed in the previous section to determine machining tolerances. Tuning pins cannot be used to correct for operational detuning. To a certain extent cooling water can be used to tune during operation, but ideally the structure should remain within bandwidth at steady state. In addition, we must consider the temperature gradient across the structure. If some cells heat up more than others, they will expand more and have a slightly different frequency. This will result in poor field flatness and a phase shift across the structure.

6.2.1 CST Thermal Simulations

The thermal losses in steady state were calculated using CST Microwave Studio. An initial electromagnetic solver computed the surface loss distribution, then this field is coupled to a multi-physics simulation. The loss distributions from the first simulation are scaled to the correct average power, and imported as a field to the thermal solver, which then calculates the resulting temperature gradient across the structure.

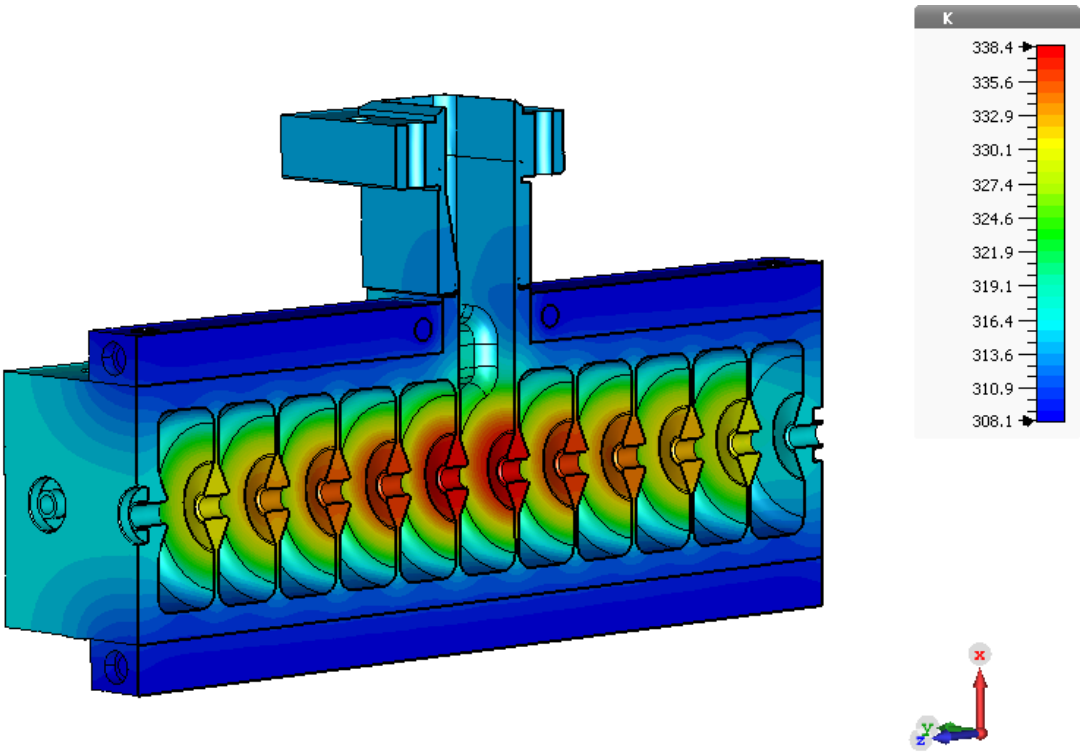

Fig. 6.5 Temperature distribution of the cavity at steady state with 4 kW average power.

One of the most significant features contributing to the high gradient of this cavity is the thin septum (2 mm). However this limits the thermal conductivity between the cooling blocks brazed to the surface of the cavity and the central nose cone region. The resulting 30K temperature difference from 4 kW average input power can be seen in Figure 6.5. The maximum operational temperature inside the cavity for a range of average powers is presented in Figure 6.6. The cavity was modelled as lossy copper with a heat capacity of 0.39 kJ/K/m and an electrical conductivity of 5.8×10^7 S/m. The cooling channels contained distilled water at an ambient temperature of 35°C that was not flowing and fixed at that temperature. It is assumed we will have the ability to keep the water in the cooling circuit at a constant temperature during operation and this is calculated in section 6.2.2. At the start of the simulation the structure is entirely 35°C.

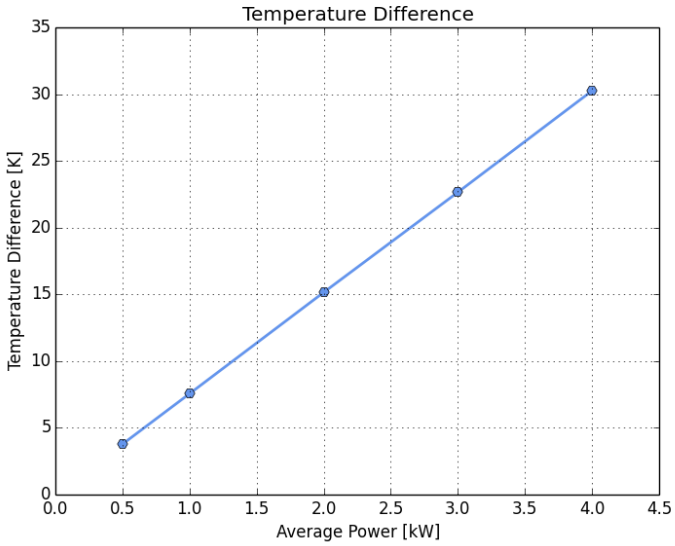

Fig. 6.6 Maximum temperature difference across the cavity from 0.5-4 kW average power.

For each input power, the temperature distribution field was imported into CST multi-physics studio and served as a field source for the mechanical solver. The input port was set as the only 0 displacement boundary and the copper had a thermal expansion coefficient of 17E-6/K. The resulting displacement field is presented in Figure 6.7. CST also allows the user to select deformation in the X, Y and Z directions independently. Figure 6.8 shows the maximum absolute displacement for 0.5, 1, 3 & 4 kW of average power with a fit shown in red.

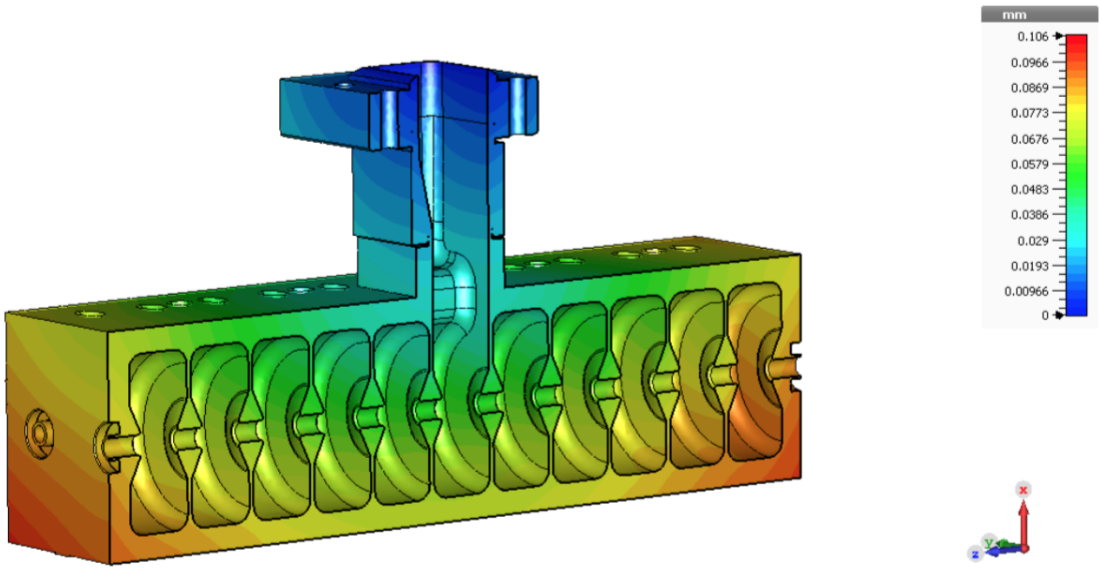

Fig. 6.7 The absolute displacement field consequent of the 4 kW average RF heating the structure. Displacement is with respect to the fixed knife edge of the flange on the input coupler.

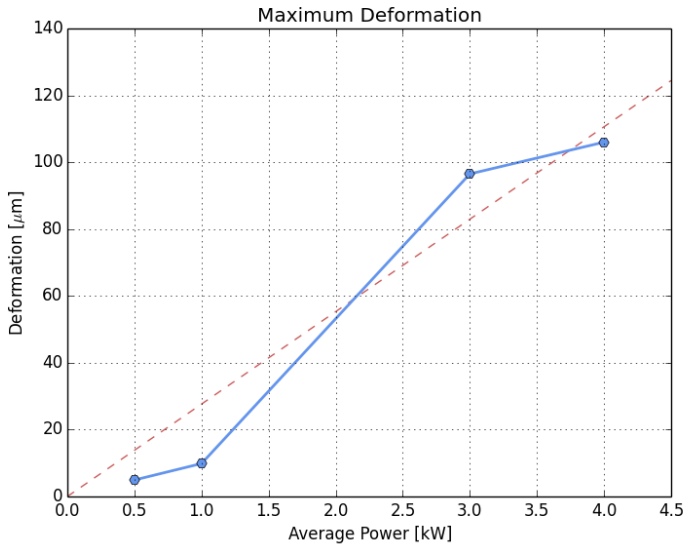

Fig. 6.8 Maximum displacement from thermal expansion. Red dashed line is a fit.

In order to estimate the shift in frequency as a result of this thermal deformation, values from the displacement field were gathered for certain key parameters. We have already established the rate of change of the frequency with machining errors, these values were used to estimate the frequency shift due to thermal expansion.

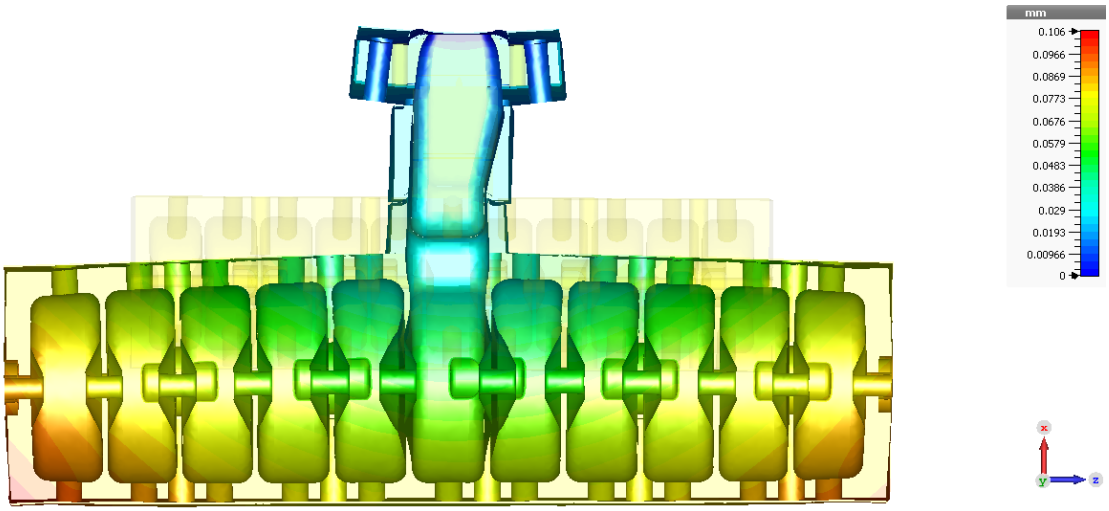

Fig. 6.9 Simulated deformation of the cavity at steady state with an average power of 4kW magnified by 1000×.

In Figure 6.9 one can visualise an exaggerated version of the thermal expansion of the structure. The deformation is magnified by 1000× as it is difficult to visualise such a small deformation by eye. From this plot we can conclude the middle cell with the power coupled into it experiences the maximum deformation. When comparing the displacement to the machining sensitivities we will use values from the centre of the structure to make a conservative estimate.

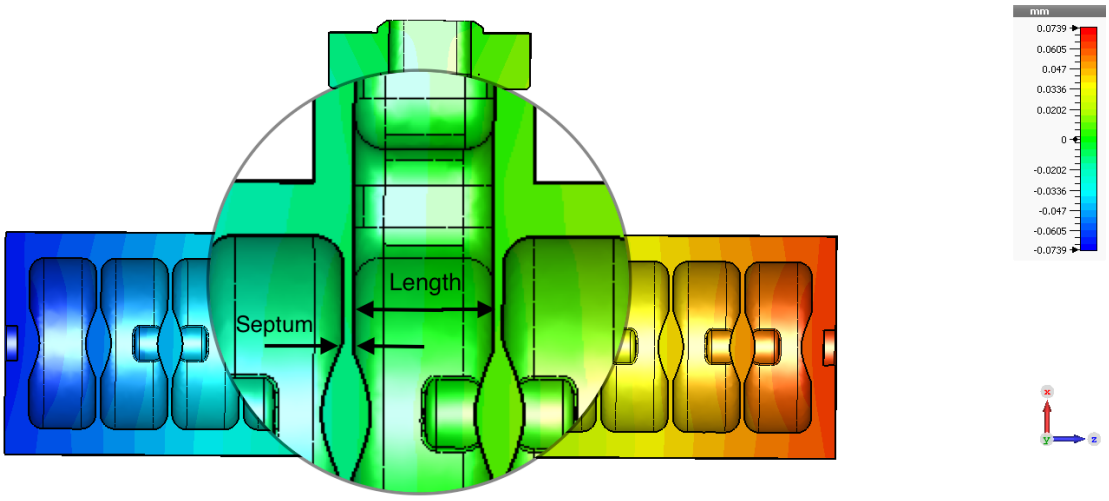

Fig. 6.10 Displacement field map in the Z direction. Parameters 'Septum' and 'Length' are also shown.

The deformation values were taken from the field plot in CST. Some parameters are exclusively in one plane. Figure 6.10 shows the parameters Septum and Length, which can be measured using only the deformation in the 'Z' direction. For other more complex parameters like the coupling slot blend, the absolute deformation plot was used.

Table 6.2.1 displays the $\frac{df}{d\mu m}$ values obtained in simulation. The values were calculated by increasing each parameter by 1μm in CST then confirmed by increasing each parameter by 10μm. There is a slight discrepancy between the values despite a fine mesh being used. The mesh edges were as small as 1.5μm in sensitive areas, which is larger than some of the displacement values. This level of accuracy is considered appropriate given the accuracy of the approximation technique. The largest difference is seen for the accelerating radius. This results in a slightly larger frequency shift seen using the 10μm $\frac{df}{d\mu m}$ values, thus they will be used to gain a conservative estimate.

Parameter	**Para**	**Frequency (Hz)**	**df/dz (kHz/μm)**	**disp. (μm)**	**f-shift (kHz)**	**Frequency (Hz)**	**10μm Δf (kHz)**	**disp. (μm)**	**f-shift (kHz)**	**Δ**
Nominal	Orig.	2998494888	N/A			2998494888				
Septum Thickness	S	2998532244	37	0.992	37	2998843294	348	0.992	35	-2
Nose Cone Gap	G_c	2998538072	43	4.577	198	2998913949	419	4.577	192	-6
SC Cell Length	l_{sc}	2998496756	2	3.0281	6	2998492234	-3	3.0281	-1	-6
Acc Cell Length	l	2998460978	-34	5.126	-174	2998155034	-340	5.126	-174	0
Accelerating Radius	r_c	2998421795	-37	7.59	-277	2997737908	-378	7.59	-287	-10
Side Coupled Radius	r_{sc}	2998495130	0	5.27	1	2998485478	-5	5.27	-2	-3
Outer Corner Radius	R_{oc}	2998512491	18	2.67	47	2998644796	150	2.67	40	-7
SC Outer Corner Radius	R_{oc}SC	2998494510	0	1.1552	0	2998499216	4	1.1552	0	1
Inner Corner Radius	R_{ic}	2998496070	1	0.14	0	2998495105	0	0.14	0	0
Inner Nose Radius	R_{in}	2998472027	-23	0.55	-13	2998260610	-234	0.55	-13	0
Outer Nose Radius	R_{on}	2998491354	-4	0.31	-1	2998437369	-58	0.31	-2	-1
Aperture Radius	A	2998476243	-9	2.38	-22	2998301907	-96	2.38	-23	-1
Side Coupled Aperture	A_{sc}	2998496429	1	1.39	1	2998497530	1	1.39	0	-1
Slot Blend	B_{sc}	2998491976	-3	5.00E-02	0	2998440076	-55	5.00E-02	0	0
Capacitive Radius	R_{scc}	2998497536	1	2.67	4	2998500694	3	2.67	1	-3
Capacitive Gap	L_{scc}	2998496130	1	1.1922	1	2998496240	1	1.1922	0	-1
			Total kHz		-199				-236	-36

Table 6.2 Estimated frequency shift due to 3 kW average input power. df/dz are the frequency shifts calculated in Table 6.1 for 1μm shift and the second set of frequency values are from 10μm deformation. Disp. is the displacement in μm taken from CST field maps as shown in Figure 6.7.

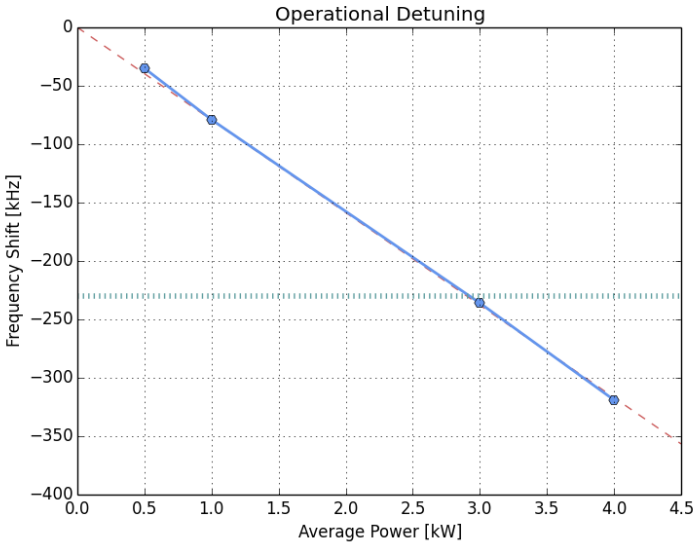

Fig. 6.11 Estimated operational detuning for a range of input powers. Maximum allowable shift shown at 230 kHz.

The estimated maximum operational detuning for a range of average powers is presented in Figure 6.11. The behaviour is fairly linear as one would expect. It shows that any average power above 3 kW will detune outside of the bandwidth of the cavity. We want to operate well within the bandwidth of the cavity, and with adequate field flatness. With 12.8 MW input power per structure we can operate with a rep rate of 40 Hz and pulse length of 4.5μs yielding average power of 2.3 kW. This should keep the structure adequately within bandwidth and still have sufficient transmission through the structure. This is just an estimate; during testing further analysis will be performed with thermocouples on the structure and monitoring the reflected and transmitted signals out of the structure to monitor performance.

6.2.2 Heat Transfer Calculations

In this section it will be assumed that cooling blocks on the prototype structure must effectively dissipate 2.3 kW of average power from the structure to the cooling water. The previous section indicates the structure may still be within bandwidth and field flatness at 2.3 kW average power so that case will be calculated. Firstly one can determine how much water must flow through the cooling circuit per minute to dissipate that average power. Then a chiller with suitable pump capacity can be chosen. Assuming only 2K temperature rise between the output and return ports of the chiller, the necessary mass flow rate $\dot{m}$ can be calculated as

$$\dot{m} = \frac{\dot{Q}}{\Delta T \cdot C_p} = \frac{2300}{2 \cdot 4180} = 0.275 \text{ kg/s} \tag{6.1}$$

where $\dot{Q}$ is the heat transfer rate ΔT is the change in temperature and is the specific heat capacity at constant pressure. It is assumed to be at constant pressure as the pressure drop is small. The specific heat capacity of water is C_p=4180 J Kg^{-1} K^{-1} at 35°C. Dividing the mass flow rate by the density of water at 35°C ($\rho = 994.1$ kg m^{-3}) gives a flow rate in m^3s^{-1} of $2.77\times10^{-}4$. This is equal to 16.6 litres per minute (LPM), so a 20 LPM chiller will be needed to dissipate 2.3 kW average power.

The prototype structure will be tested at S-box, the S-band high gradient test facility at CERN. The chillers available at this facility are SMC HRS024-W-20, and the cooling capacity curves are shown in Figure 6.12. Depending on the season, the ambient temperature in the bunker is around 10-30°C so one chiller may be sufficient to cool the entire structure assuming a circulating fluid temperature of around 35°. The following section will look at the cooling circuit in depth to determine if that will be the case.

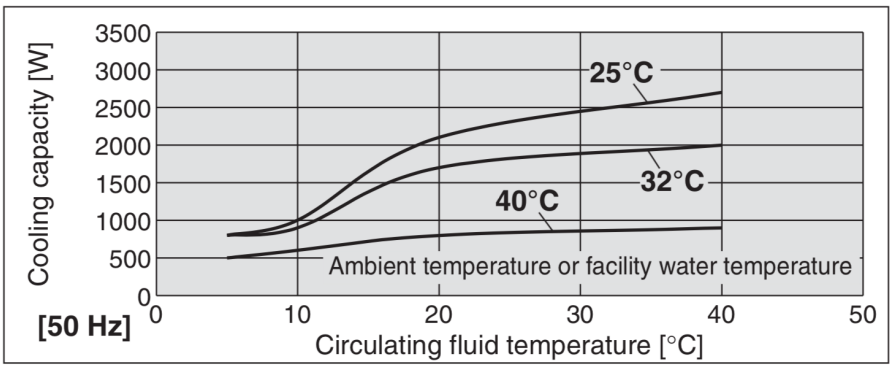

Fig. 6.12 Cooling capacity of the chiller anticipated for testing [137].

The ProBE structure has four cooling channels with an 8 mm diameter it is assumed they shall be connected in series to the chillers single output port and that the water shall return to the single return port. There are two $\approx$ 30 cm cooling pipes on the underside of the structure, and two $\approx$ 30 cm cooling pipes on the top making $\approx$ 120 cm in total. This length is necessary to estimate the pressure drop in the cooling circuit. The pipes connecting the cooling circuit in series with the chiller are not included in this length as they can be large and thus do not contribute to the pressure drop.

To calculate the pressure drop in the cooling circuit one must first determine the Reynold's number (LPM). The Reynold's number is a non-dimensional formula that characterises the magnitude of the action of the viscous forces with respect to inertial forces [138]. It is calculated as

$$\mathrm{Re} = \frac{\rho v D}{\eta} = \frac{994.1 \cdot 5.5 \cdot 0.008}{7.2 \times 10^{-4}} = 60832 \tag{6.2}$$

where the velocity v is the flow rate divided by the cross sectional area of the pipe, and $\eta = 0.7191 \times 10^{-3}$ is the dynamic viscosity of water at 35°C. Turbulent flow in a pipe will yield a Reynold's number > 4000 and in this case it is fully turbulent at 60832. The Reynold's number can then be used to calculate the Darcy friction factor f_D [139] which is a dimensionless quantity that describes the friction losses in pipe flow. It is estimated for turbulent flow by

$$f_D = [0.79ln(Re) - 1.64]^{-2} = [0.79ln(60937) - 1.64]^{-2} = 0.02 \tag{6.3}$$

The friction factor can then be used to calculate the pressure drop in the circuit using equation 6.4 [139].

$$\Delta P = \frac{f_D \rho v^2 L}{2D} = \frac{0.02 \cdot 994.1 \cdot 5.5^2 \cdot 1.2}{2 \cdot 0.008} = 45 \text{ kPa} \tag{6.4}$$

The pressure drop through the 1.2 m circuit was calculated as 45 kPa. Figure 6.13 is the pump capacity of the chiller taken from its specification [137]. With the circulating fluid flowing at 16.6 LPM and the chiller operating at 50 Hz the chiller can cope with a pressure drop of up to ≈120 kPa, which is comfortably over the pressure drop of this particular cooling circuit.

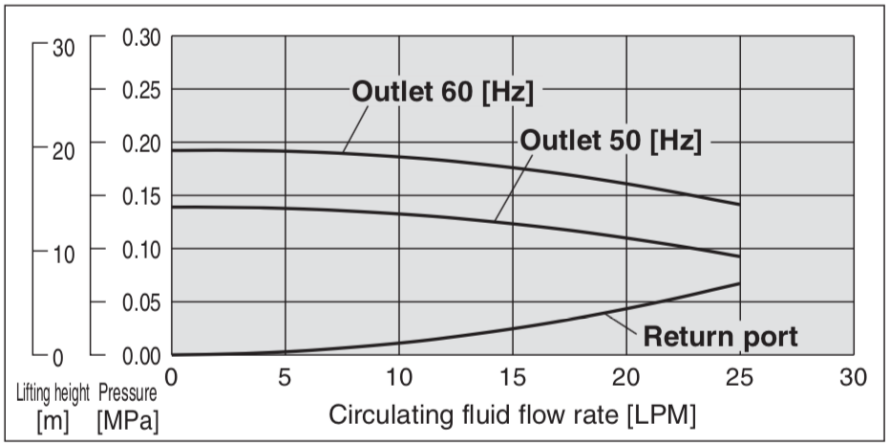

Fig. 6.13 Pump capacity of the chiller anticipated for testing [137].

The chiller is confirmed to have a large enough pump to provide the necessary flow rate to remove 2.3 kW of average power while only heating the cooling water by 2K. Next one must calculate if the surface area of the pipes is sufficient to transfer heat between the copper and the cooling water, and what the resulting temperature difference between the two will be. The Prandtl number Pr is a ratio of the viscosity η to thermal diffusivity (κ/C_p) and is given as

$$\text{Pr} = \frac{\eta \cdot C_p}{\kappa} = \frac{7.2 \times 10^{-4} \cdot 4180}{0.62} = 4.85 \tag{6.5}$$

where κ is the thermal conductivity of water at 35°C. This can then be used along with the previously computed Reynold's number and friction factor to calculate the ratio of the heat flow that actually occurs to the heat that would conduct through a characteristic length of fluid. This is expressed as the dimensionless Nusselt number Nu [139]

$$Nu = \frac{(f/8)(Re - 1000)Pr}{1 + 12.7(f/8)^{\frac{1}{2}}(Pr^{\frac{2}{3}} - 1)} = \frac{(0.02/8)(60832 - 1000)4.85}{1 + 12.7(0.02/8)^{\frac{1}{2}}(4.85^{\frac{2}{3}} - 1)} = 333 \tag{6.6}$$

The heat transfer coefficient (h) between the copper pipe wall and the fully turbulent cooling water can now be calculated as

$$h = 0.023 \times \frac{\kappa}{D}\mathrm{Re}^{0.8}\mathrm{Pr}^{n} = 0.023 \times \frac{0.62}{0.008}60832^{0.8}4.85^{0.4} = 22523\mathrm{W/K} \tag{6.7}$$

Where D is the pipe diameter, and $n = 0.3$ if the fluid is cooling and $n = 0.4$ if it is heating. The temperature rise of the cooling water in the cooling circuit can thus be calculated as

$$\Delta T = \frac{\dot{Q}}{hL\pi D} = \frac{2300}{22523 \cdot 1.2 \cdot \pi \cdot 0.008} = 3.4\mathrm{K} \tag{6.8}$$

Thus, to maintain a temperature of 35°C on the cooling blocks as was simulated in CST, the chiller's water temperature must be set to 31.6°C.

6.3 Design of Manufacturing Disks

The RF design of the prototype linac was done using a vacuum model, which was then encased in copper for the thermal analysis. In this section we consider the manufacture of the structure. Side-coupled cavities have been manufactured before, but never for such high power/gradient. The complex geometries inside the cavity result from peak field limiting blends in crucial RF areas. Figure 6.14 shows some of the ways existing side-coupled cavities have been machined in the past. The structure on the left is the 805 MHz side-coupled cavity for the Fermilab [63] linac upgrade. It has had the accelerating and side-coupled cells machined separately. Each cell is machined in two halves then brazed together as a first step, then the side-coupled cells are brazed to the accelerating cell as a second step [140]. This leaves a sharp knife edge around the coupling slot, which will enhance the magnetic field in that area. At lower power this may be tolerable, but the high gradient ProBE cavity has a large magnetic peak field in this region which is shown in Figure 6.17. The slots must be rounded to reduce field enhancement.
Side-coupled cavities can also be manufactured with the side-coupled cavity and

the accelerating cavity in one disk as is shown in the centre and right images of Figure 6.14. The cells are bonded together at the septum. The centre structure has also incorporated water cooling into the septum of the cavity eliminating some of the temperature gradient problems discussed in the previous section [141]. The ProBE structure only has a 2 mm septum thickness, too thin to cut through the septum and withstand the forces of milling and machining, followed by the high temperatures and pressures required for bonding and brazing without deforming; it will have to be machined such that the thin septum is kept whole.

Fig. 6.14 Previous manufacturing techniques for side-coupled cavities.Fermilab 805 MHz coupled cavity linac (left) [140], SNS coupled cavity linac (centre) [101], LIBO coupled cavity linac (right) [18]

.

6.3.1 1-disk design

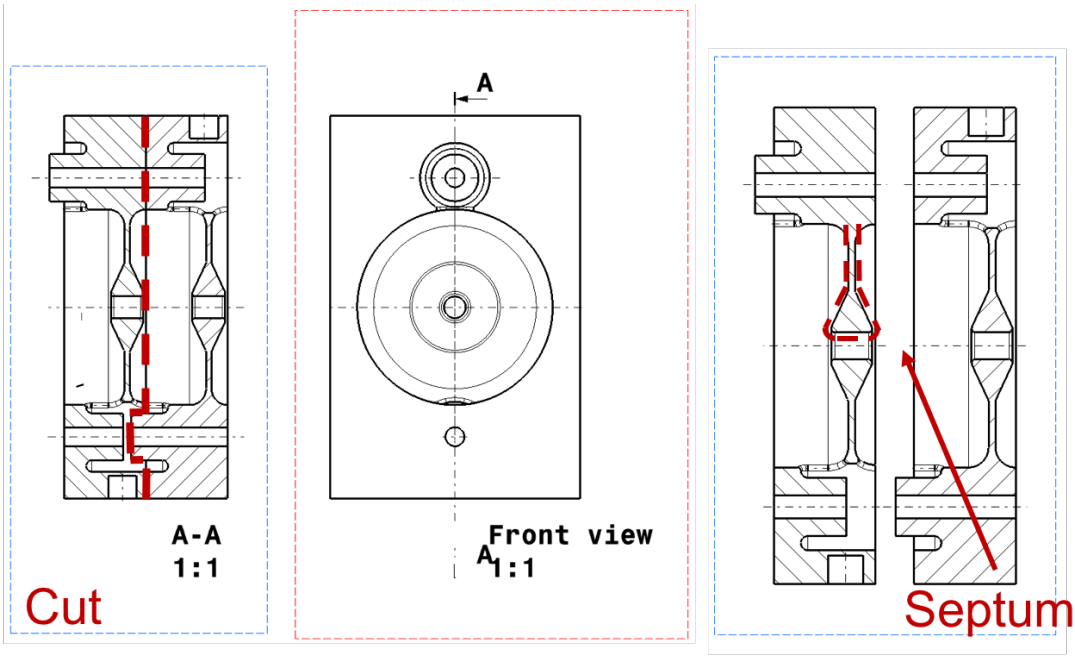

Fig. 6.15 One disk per cell cut.

The first of two disk designs in shown in Figure 6.15. Each accelerating cell is machined from one rectangular disk, separated just after the blend on the outer corner of the cell. The capacitive region of the side-coupled cell extends beyond the outer edge of the disk. The disks are slotted together after machining and hydrogen bonded together. Interlocking grooves were added to allow precise alignment, and are shown in Figure 6.16.

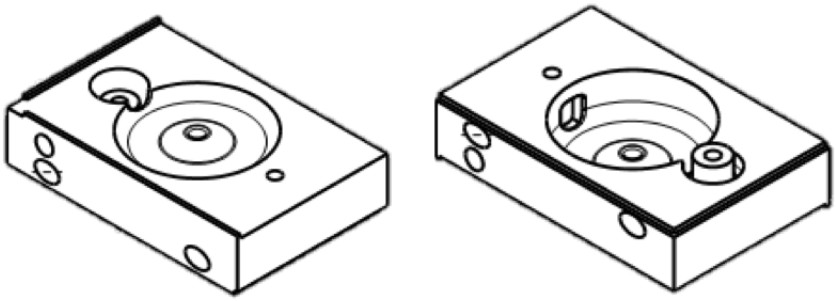

Fig. 6.16 Interlocking alignment technique.

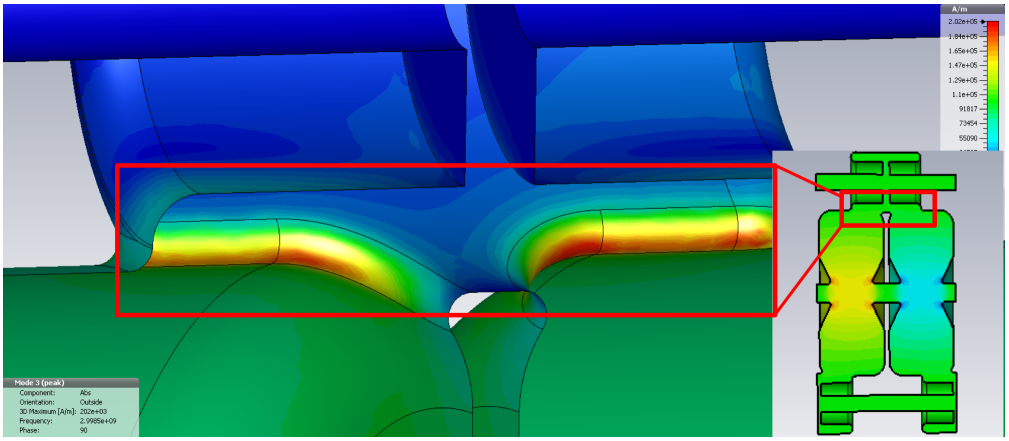

Fig. 6.17 Magnetic peak field on the coupling slot.

The peak surface magnetic field on the coupling slot is shown in Figure 6.17. Pulsed magnetic heating can result in this expanding and contracting repetitively, which can lead to cracking in the copper. Micro-cracks then further enhance the field and it is thought this can lead to RF breakdown. As was discussed in the optimisation chapters, the size of this slot dictates the cell to cell coupling. For both of these reasons it is a fairly critical area requiring high accuracy and surface finish. An isometric view of the 1-disk design is shown in Figure 6.18 and one can see the coupling slot is rather difficult to access with machining tools. The capacitive section on one side completely blocks access to the region. It would be very difficult to achieve the desired 100μm tolerance with this design.

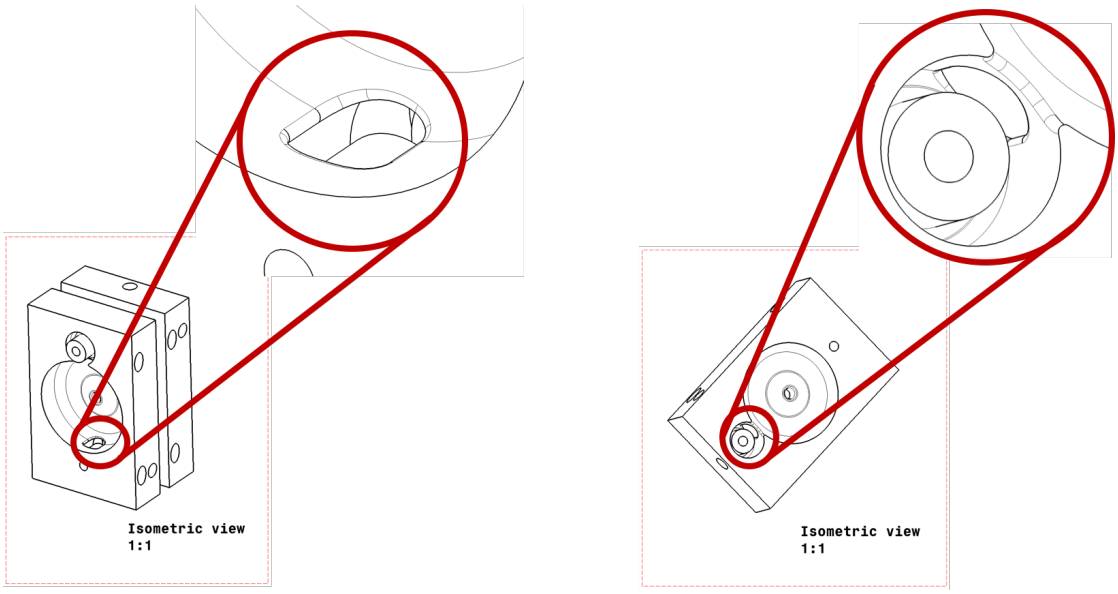

Fig. 6.18 The difficult to access coupling slot.

6.3.2 2-disk design

The original 1-disk design was altered to allow for better access to the coupling slot. By cutting the disk again on the other side of the septum, the septum can remain intact while opening up access to the coupling slot. The revised cut is shown in Figure 6.19.

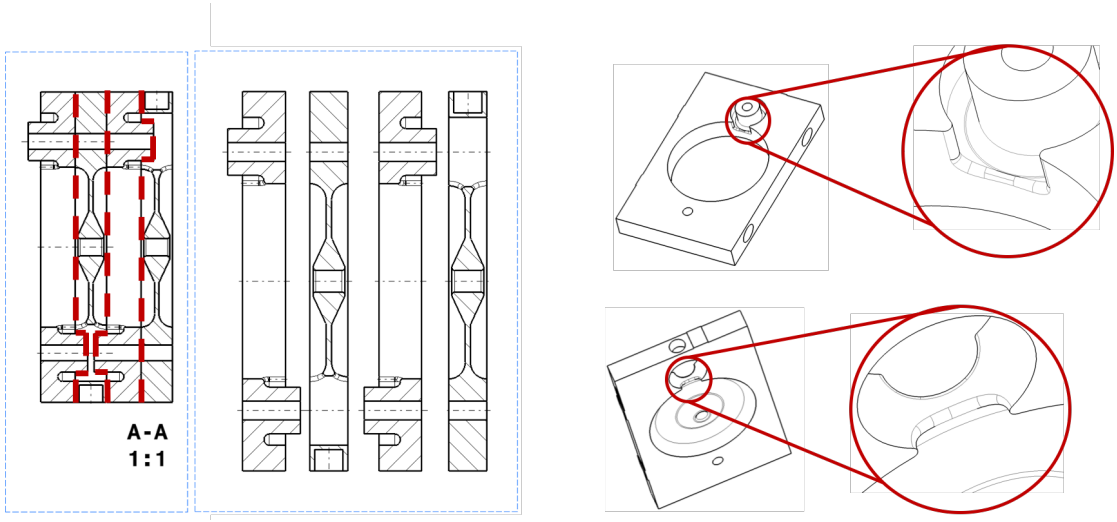

Fig. 6.19 Alternative cut with 2 disks per cell.

The previous disk design had used an interlocking groove system to ensure proper alignment during assembly. That was replaced in this design by 3 precision surfaces, two on the long edge of the rectangle and one on the short edge. The tabs extend by 0.5 mm and are shown in Figure 6.20, and are machined to 5μm flatness

with respect to the other dimensions of the cavity. Before the disks are bonded they shall be assembled in a V-block as shown in Figure 6.24. The only part of the structure to touch the precision flat V-block is the precision flat surfaces, ensuring perfect alignment of the internal cavity features.

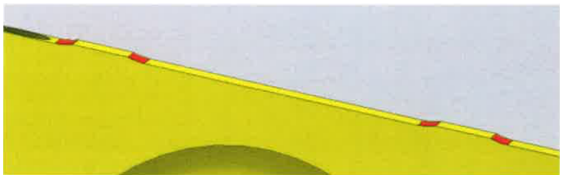

Fig. 6.20 Precision surfaces were added to the disks for alignment.

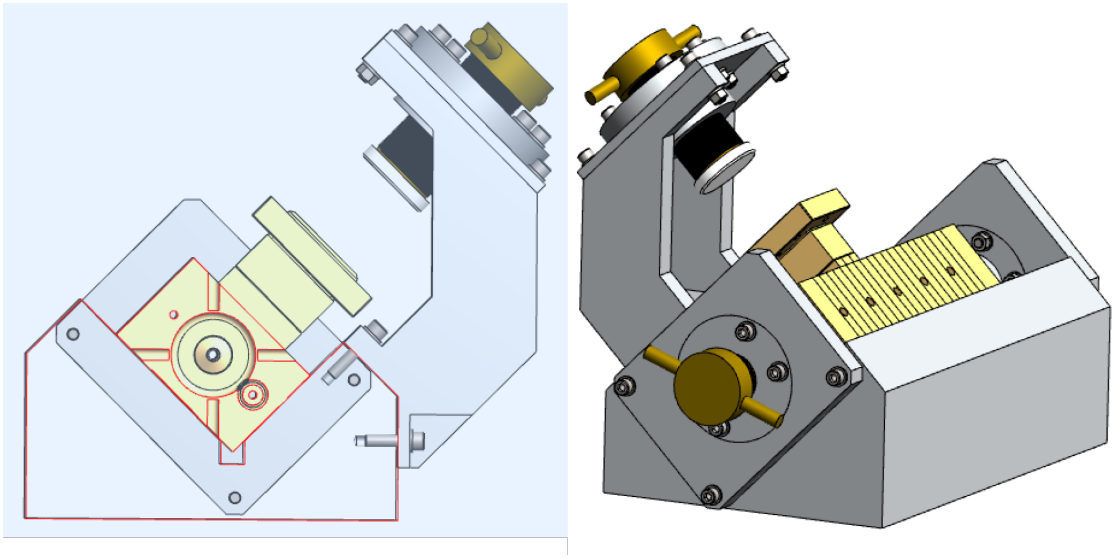

Fig. 6.21 Tooling to clamp the machined disks together to do an initial RF measurement before bonding. (image courtesy of Lancaster University)

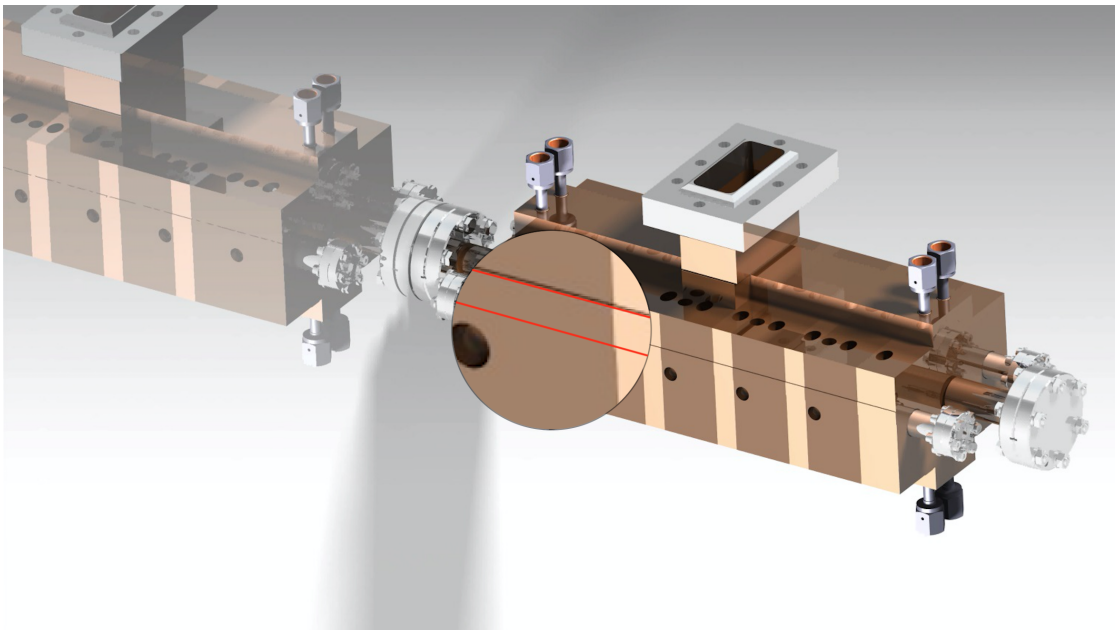

Fig. 6.22 Final rendered image of ProBE cavity. Magnification of the alignment surface highlighted in red.

6.4 Manufacture

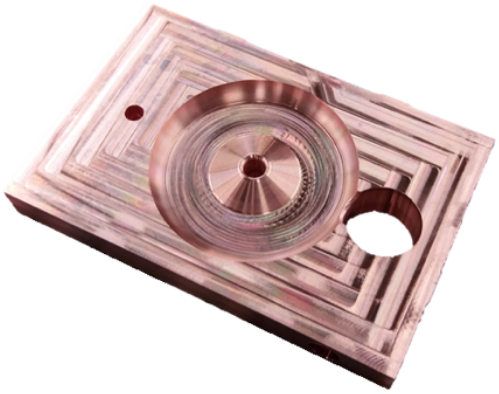

Fig. 6.23 Disk after pre-machining stage of manufacture.

The contract for the ProBE disks has been placed with VDL Enabling Technologies Group. The technical specification sent for quotes is attached as Appendix A. The raw material for the disks was Oxygen-free Electronic copper as per the CERN technical specification N° 2000 - Ed. 8 EDMS No: 790780. The disks will be heat treated to relieve stress after machining; the technical specification recommends 245°C for 2 hours in vacuum but VDL will use 240° for 4 hours. The quality of the surfaces to be bonded is one of the most critical factors affecting a successful process. The surfaces must be as smooth and flat as possible to ensure

good contact between disks. A surface roughness of Ra=0.025 μm was requested on the bonding surfaces in the technical specification, however to reduce costs this was amended to Ra=0.04 μm for the final structure. In the high power zones of the RF-area (the iris and the coupling slot) the surface finish will be 0.1 μm for all other areas it will be 0.2 μm. The requested surface flatness was 3 μm but again, to save costs this was increased to 5 μm.
The positional accuracy requested in the technical specification was 20 μm, to reduce costs this was extended to a guaranteed positional accuracy of 40 μm. However, 20μm accuracy will remain the goal for end machining and VDL have assured us 60% of the parts will achieve this accuracy, 20% will be 30 μm and the remaining 20% will be within 40 μm. These tolerances were considered earlier in the chapter when calculating the tolerance sensitivity.
A positional tolerance of 3 μm to reference A on the drawings was requested on all drawings, however this was increased to further save costs. VDL have guaranteed a thickness tolerance of 5 μm and a parallelism of 5 μm.
8 witness disks have also been produced to accompany the ProBE disks in each stage of the bonding/brazing procedures. The can be used post testing to determine where the copper may have been contaminated in the worst case. The cooling blocks are being machined elsewhere as they are not precision pieces, along with the tuning studs, installation pins and the RF flange.

Figure 6.24 shows the planned bonding and brazing steps that will complete the construction of the ProBE prototype cavity. Firstly, the machined disks will be stacked up in a graphite V-block for alignment. The precision alignment surfaces shown in Figures 6.20 & 6.22 will be the only part that comes into contact with the V-block. Straightness value, profile & tilt measurements are performed using a special measurement column at the bonding laboratory. Once it is aligned to the 5-7μm straightness specification the graphite V-block is carefully removed. Next 60 kg of weight is applied to the structure to ensure 0.1 MPa applied pressure on the top disk.

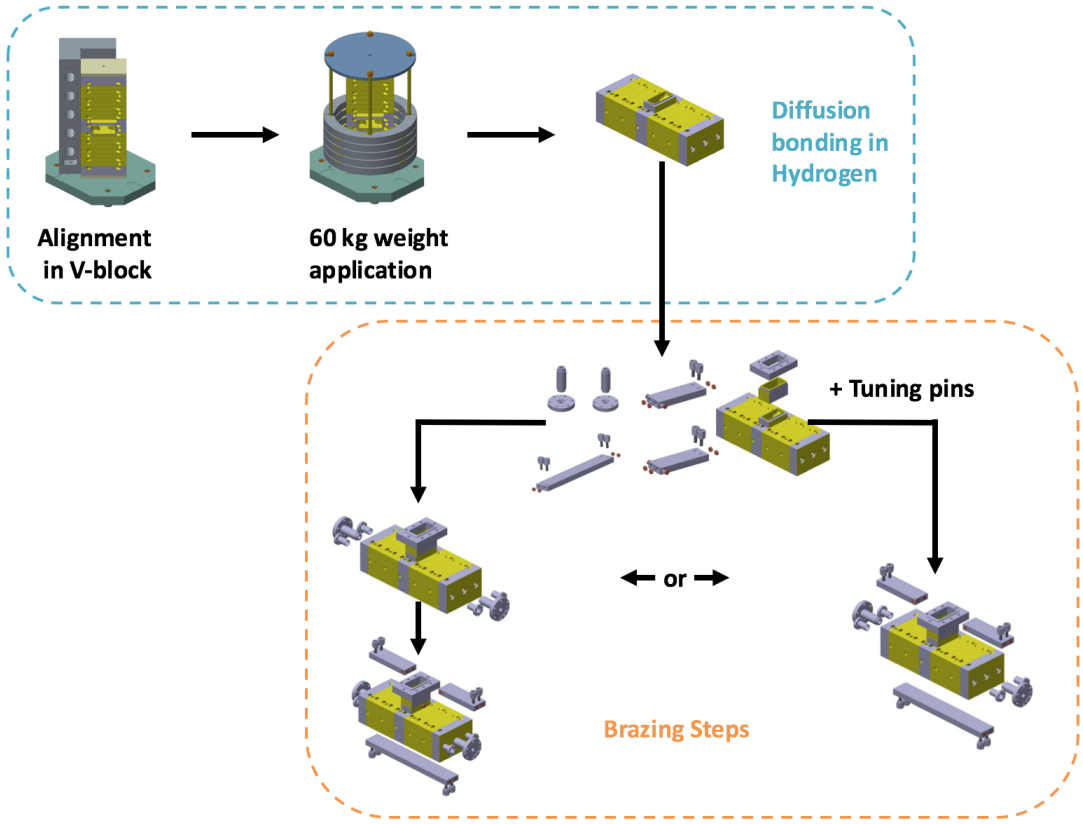

Fig. 6.24 Figure shows the alignment, and weight tools for hydrogen bonding of the disks. After the disks have been bonded together the remaining pieces are brazed on in various steps of decreasing temperature. (Design and images courtesy of Niklas Templeton at Daresbury Laboratory, UK.

The entire structure is then baked at 1030° for 1.5 hours, in high vacuum ($10^{-5} - 10^{-6}$ mbar), and a hydrogen partial pressure of 20 mbar. The temperature profile for the process is presented in Figure 6.25. The heat and pressure cause a diffusion reaction between the grains at the boundaries between disks. The temperature causes increased thermal movement and increased diffusion of atoms in the lattice. The atoms in the joint region become so close together that they begin to share electrons creating covalent bonds. This causes some grains to grow across the border at the expense of others, and thus the separate disks become one solid copper block.

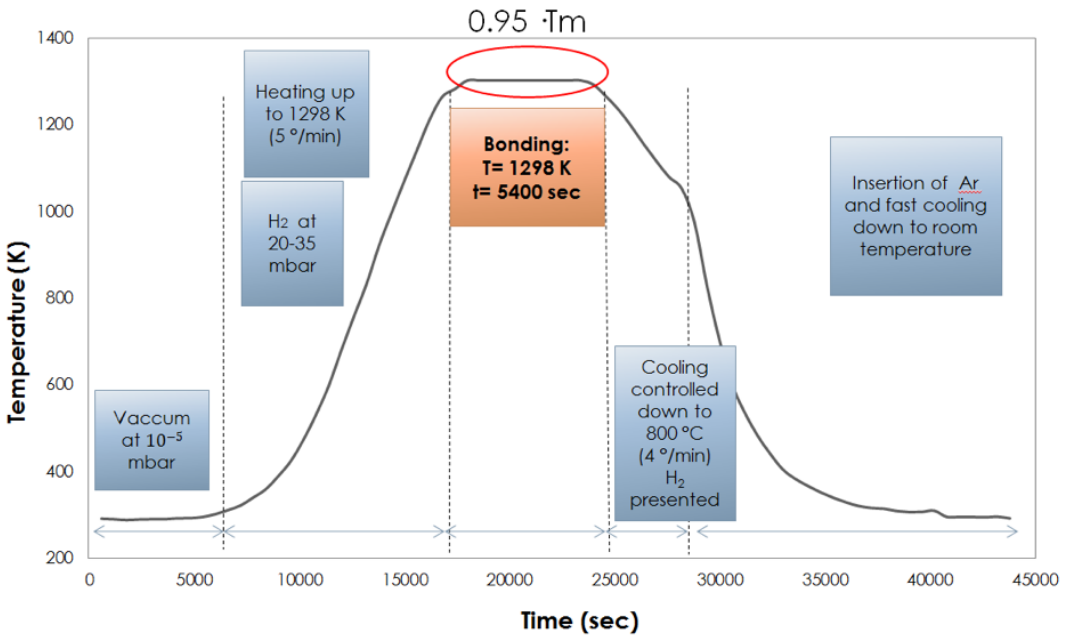

Fig. 6.25 Temperature profile for bonding process under H_2 partial pressure [142].

After baking the structure is measured again by the measurement column to confirm it meets the straightness specification. Next the flanges are brazed to the beam pipes at the same time as the water circuit plugs are brazed into the cooling blocks along with the Swagelocks, although not shown in Figure 6.24 the tuning pins are also brazed in this step. The cooling blocks and beam pipes are then brazed to the structure at a lower temperature in either one or two steps. The silver/copper brazing material changes its ratio of silver to copper to accommodate for the lower temperature of subsequent steps.

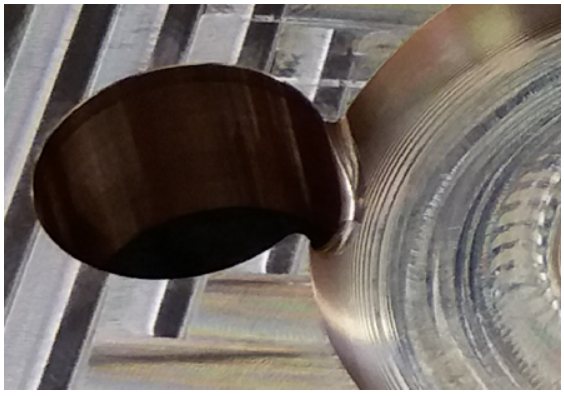

Fig. 6.26 Disk after pre-machining stage of manufacture.

Chapter 7

S-Box High Gradient Tests

7.1 S-Box High Power Test Bench

The CLIC X-band high gradient test facility, fondly referred to as '*The X-boxes*', was established to support the development of high gradient structures and the testing of high power components in the 50-100 MW range for the CLIC project. There is increasing interest in high gradient operation of S-band structures especially for medical and security linacs. Along with that interest comes an interest in verifying the S_c model [82] and existing scaling laws at 3 GHz as current experimental data is only single cell and limited as was described in section 4.1. A collaboration between the TERA foundation and CERN developing high gradient S-band medical cavities has led to a 3 GHz test stand now referred to as *S-box*. The test bench is shown in Figure 7.1.

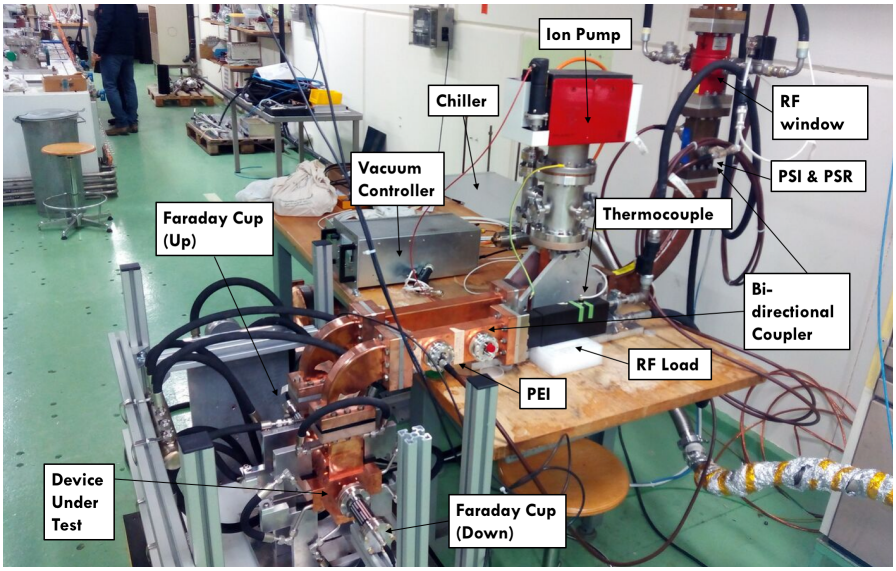

Fig. 7.1 The S-band high gradient test bench installed in CTF2 at CERN as part of the CLIC high power test program.

The operation is based exactly on that of the X-Boxes; a stand-alone high power test stand. The X-box facility is operated by a collaboration of PhD students, post-docs and fellows, each with a vested interest in a specific part of the experiments. The author participated in commissioning and operation of the S-band high gradient experiment presented in this chapter as the ProBE structure will need to be tested in an S-band high power test facility and results of this test are of interest to the ProBE project as it is the first high power test of an entire 3 GHz high gradient cavity.

The practical experience gained in S-box gave the author insight into the requirements of the prototype RF structure. In Chapter 6.1 the author was able to design the cooling circuit based on the exact chillers available at the facility. Having taken part in the installation of accelerating structures the author ensured enough space remained between the flanges and the structure to fit hands and tools necessary for tightening bolts. The author's contribution to this experiment was in the commissioning and daily operation of S-box. The author installed the necessary RF cables for reading the signals, and calibrated them when necessary. Tested and installed the down-mixing crate and the interlock crate which are described in more detail in this chapter. Following the commissioning of S-box the author participated in the daily operation of the test bench. This consisted of maintenance and repairs of equipment, ensuring the data was being collected accurately for later analysis, and communicating results to the X-box team and the wider high gradient community. Typical problems that could arise were breakdowns in the modulator causing interlocks and needing to be reset. Tuning of the input pulse if it became deformed, changing the pulse length and rise time. Identifying from the RF signals on the graphical user interface (GUI) if the phase locked loop (PLL) in the down-mixing crate was locked to the reference clock. As with all new software there were bugs in the code initially that had to be firstly identified and then solved. In this chapter the S-box experimental set up is described and the preliminary results are discussed in the context of ProBE.

7.2 Cavity Conditioning

When accelerating structures are first manufactured, they are not able to reach the high field levels that they have been calculated to operate at. They first have to undergo high power conditioning to prepare the RF surfaces for stable operation at the highest powers. Experiments show that probability of RF breakdown reduces for a certain field level after some number of RF pulses have been applied. Cavity conditioning consists of starting at very low power ($<$1 MW) and short pulse length (50 ns) and gradually ramping the power up step by step to the maximum power. Once the maximum power is reached, the power is reduced and the pulse

length increased. This process continues until the nominal parameters are met then the cavity is operated at that power level until the BDR reduces to a stable level. This is when the cavity is deemed to be conditioned. This process can be observed in Figure 7.2. The BDR is kept fairly constant by a conditioning algorithm implemented on LabVIEW. Only during the flat run at the end of the conditioning process is the BDR seen to drop below 10⁻6. The vacuum levels and breakdowns are monitored throughout this process to keep the BDR low and prevent any irreversible damage. Initially a process of out-gassing occurs when the surfaces first see RF, surface contaminants and an oxide layer are removed by the RF. Breakdowns are thought to remove small field emitters from the surface of the cavity walls, which is why the dark current is shown to start relatively high, but decrease with further conditioning. It is thought that it is not the number of breakdowns that enhances the structures performance but the number of pulses. This is discussed in more depth in [133].

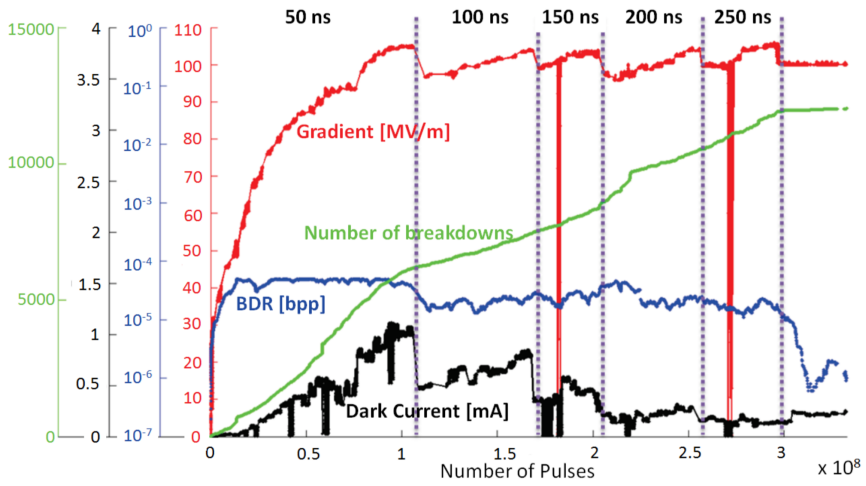

Fig. 7.2 Conditioning history of a TD26CC prototype tested at X-box 1 (CERN). The accelerating gradient is shown in red. The number of pulses is shown on the x-axis and the pulse lengths are given at the top. The BDR in breakdowns per pulse is shown is blue. The cumulative number of breakdowns is shown in green and the dark current is shown in black [133].

7.3 Experimental Set Up

Figure 7.3 shows the functional diagram for the S-box experiment. The low level RF (LLRF) 2.9985 GHz signal is generated in an RF generator card in a PXI crate [143] shown in Figure 7.5, and is IQ modulated to preserve both amplitude and phase information. It is then sent to a Microwave Amplifiers [144] solid state power amplifier (SSPA) to be amplified to up to 400 W. The 400 W signal is then sent to the CERN-built modulator and klystron unit and amplified to up to 43 MW

at a maximum repetition rate of 50 Hz. The klystron is a MKS14 from the former CTF3 linac shown in Figure 7.4. A circulator protects it from reflections and a directional coupler is installed on the output to measure transmitted and reflected signals. The RF power is distributed through a WR284 copper waveguide network under SF6 up to a ceramic window (Figure 7.1) just before a bi-directional coupler before the device under test (DUT). A −60 dB bi-directional coupler attenuates the incident (PSI) and reflected (PSR) signals so they can be sampled by the LLRF system. After the structure another directional coupler attenuates the transmitted (PEI) power signal for the LLRF system and sends the remaining power to a water cooled RF load. The directional couplers and RF load are shown labelled in Figure 7.1. Two Faraday cups upstream and downstream of the DUT, which are used to measure field emitted electrons and detect RF breakdown, are also shown. Also visible in Figure 7.1 is the chiller attached to the water channel cooling the DUT, and the vacuum controller and ion pump keeping the system after the ceramic window under ultra high vacuum (UHV) which is pressure levels below 10^{-7} mbar. The current DUT is the backwards travelling wave (bTW) or 'KT*' medical structure designed by a collaboration between TERA and CERN [134]. It was designed as a constant gradient structure with a high gradient of 50 MV/m, and powered by 2.5 μs pulses of 20 MW at a repetition rate of 30 Hz. The aims of this experiment are to verify the structure's gradient within a maximum breakdown rate of 10^{-6} breakdowns per pulse per metre (bpp/m), and to see if the modified Poynting vector model and scaling laws extend to high gradient S-band structures.

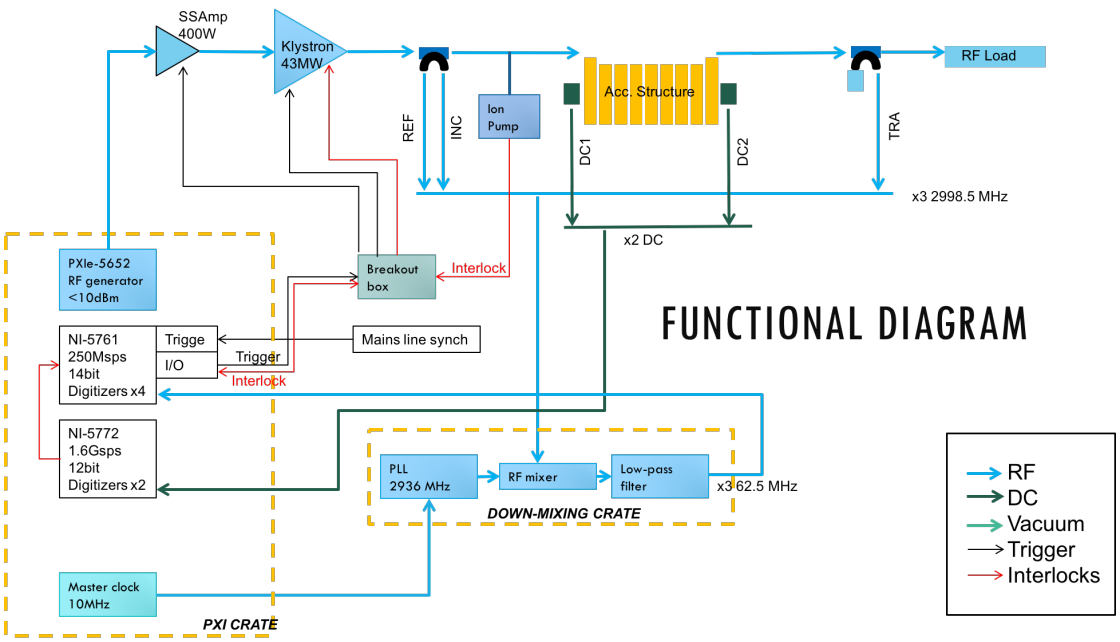

Fig. 7.3 Functional diagram of the S-box experiment at CERN.

*funded by the CERN knowledge transfer fund.

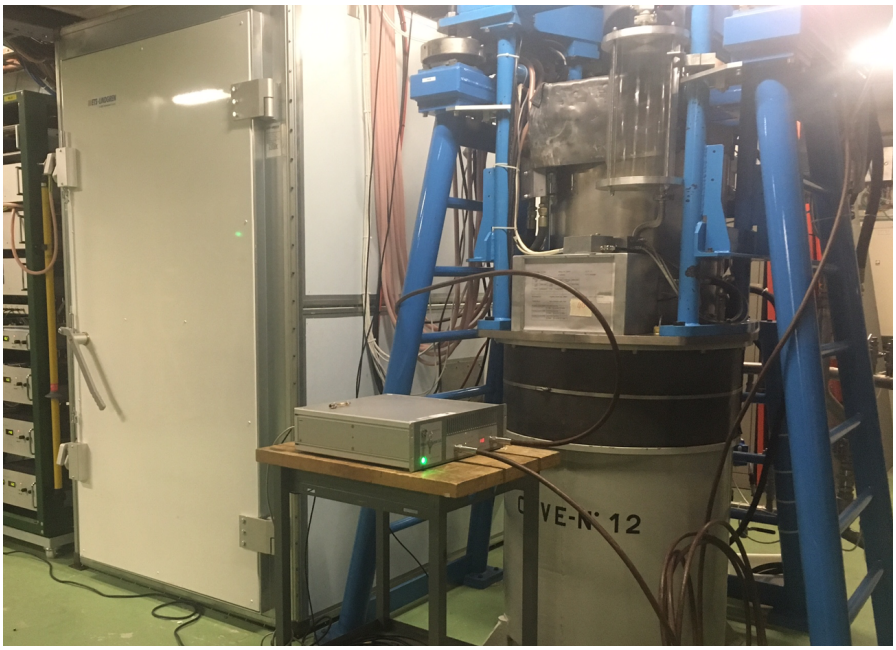

Fig. 7.4 The high power set up of the S-box experiment. Featuring modulator 43 MW klystron and 400 W solid state power amplifier.

7.4 Electronics

A National Instruments PXI crate is at the heart of the S-box experiment. A LabVIEW code based on the X-Box 2 experiment was simplified to control S-box and acquire the data. Figure 7.5 shows the main electronics rack for the 3 GHz test bench. Here the LLRF and interlocks come together in the PXI system to ensure accurate data acquisition, protection of the equipment and DUT, and safety of users.

The RF signals are attenuated −60 dB through bi-directional waveguide couplers before being sent to the electronics rack from the bunker via 50 Ω coaxial cables. They are then attenuated by further −20 dB through coaxial directional couplers before entering the down-mixing stage. There is additional attenuation of approximately −13 dB in the cables between the DUT and the electronics rack in the klystron gallery above the CTF2 bunker. It is important to log accurately the attenuation between the klystron and the PXI to reduce uncertainty of the power at which breakdowns occur. The entire RF network is carefully calibrated to be sure of the RF measurements. This done by sending a known RF power from a 3 GHz signal generator, then taking measurements with a power meter and noting the attenuation. LabVIEW is calibrated by sending a known power, then noting the response of the digitisers which can be visualised on the GUI in mV. The power level is swept from zero to the maximum power, polynomials are fitted to the results and the coefficients are entered into the GUI for each channel. Calibrations are vital and are performed regularly to ensure reliable and accurate results.

7.4.1 Interlocks

Interlocks are used in the system to prevent RF being pulsed when it may damage the structure or become unsafe for the operators. The PXI controller monitors the RF signals in real time and will immediately stop the RF pulsing in the event of any of the signals exceeding the set thresholds. A sharp rise in the reflected power (PSR), dark current signals from the Faraday cups, and the vacuum pressure, are all notifiers of an RF breakdown and thresholds are set by the operator. Once a threshold is exceeded the PXI stops the RF, logs a breakdown and the pulse shape is saved for later analysis. The RF is stopped to prevent the breakdown mechanism being sustained and damaging the structure. There are several other interlocks that may cause the PXI to stop the RF for safety reasons. Flow meters both on the cooling circuit connected to the chiller and the structure, and the internal CTF2 cooling circuit dedicated to the RF load, will stop the RF in the event of a cooling water failure. There is an additional RTD sensor on the RF load to ensure it doesn't exceed a safe operating temperature. The CERN control centre (CCC) oversees the experiments at CERN and an enable signal is only sent to the modulator once a patrol has been done of the bunker and access is completely restricted to humans. Removal of the key from the control room to the bunker will result in a safety interlock and stop the RF to prevent any person being accidentally irradiated. Finally there is an 'Authorisation RF' signal between a PLC above the modulator and the PXI which will stop the RF if the modulator or klystron itself interlocks. A klystron can interlock it's own safety system if it's internal vacuum is compromised or it has a breakdown in one of it's cavities for example.

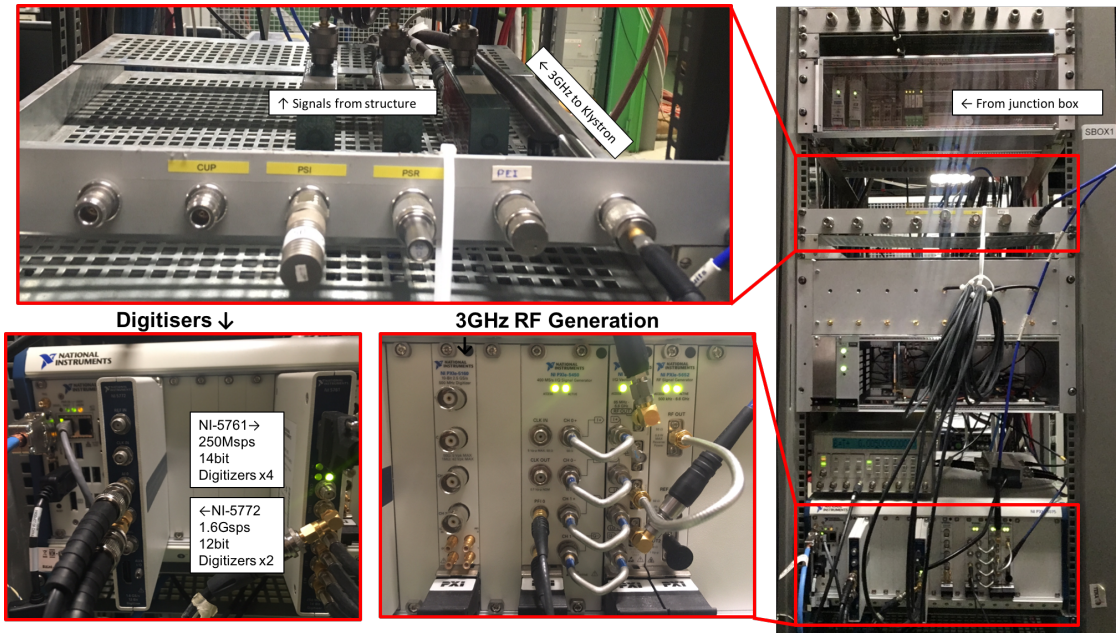

Fig. 7.5 The S-box electronics rack in the CTF3 klystron gallery.

7.4.2 Data Acquisition

The incident, reflected, and transmitted RF signals are acquired by a NI-5761 digitiser card shown in Figure 7.5. This has a high 14-bit resolution, limited to 250 mega samples per second (Msps) but there are 3000 million periods RF periods per second which would only sample once per every 12 RF periods. The Nyquist theorem states that to reconstruct a sine wave the sampling rate must be at least twice that of the signal frequency. Ideally however, we want 4 samples per every RF period to avoid amplitude errors or aliasing. With 4 samples per RF period the signal can be completely reconstructed. 250 Msps divided by 4 is 62.5 Msps therefore to sample 4 times in every RF period we must down-mix the signal to 62.5 MHz intermediate frequency (IF).

The NI-5772 has two channels with a faster sampling rate of 1.6 Gsps but a lower 12 bit resolution. Thus this card is used to sample the Faraday cup signals. During a normal pulse there is a stable dark current of field emitted electrons at that given power level captured by the backwards travelling wave, and detected by the Faraday cups. During a breakdown pulse, the Faraday cup signal will saturate thus high resolution is not vital, but the high sample rate ensures speedy detection of the breakdown and a prompt response from the PXI to stop the RF.

7.4.3 Down-mixer

The schematic of the down-mixer used for the S-box experiment is shown in Figure 7.6. In the first stage a phase locked loop (PLL) locks a 2.9365 GHz voltage controlled oscillator (VCO) to the 10 MHz PXI reference clock to ensure accurate synchronism and phase acquisition. The signal is attenuated to bring it within the stable range of a bandpass filter placed to remove any harmonics before the signal is split into two by a 3 dB splitter. The two signals are then attenuated further to bring them comfortably below the 1 dB compression point of the 17 dB amplifier. This large amplification facilitates the splitting of the signal into 8 separate channels for down-mixing. Before the 2.9365 GHz signal is mixed with the 2.9985 GHz signals from the structure, a circulator is placed to prevent any power travelling back through the 8-way splitter and combining which could destroy the amplifier before it. After the circulator the RF signals are input having already been attenuated (-20 dB) by coaxial couplers in the electronics rack (Figure 7.5). The resulting intermediate frequency (IF) signal is then amplified and filtered again to remove any higher order harmonics created in the mixer. Finally the resulting 62.5 MHz IF signals are attenuated to bring them down to 13 dBm for input to the PXI digitisers.

The down-mixer was tested to ensure the only frequency present at the ADC's was 62.5 MHz. As expected there were small peaks for the harmonics at 125.5 MHz,

2.6 GHz, 2.8 GHz, 2.937 GHz, and 2.9985 GHz but these are filtered in the down-mixer and are all <50 dBm. Figure 7.7 shows the Fourier transform of the frequencies on one of the output channels†. There are unwanted peaks at 65.8 MHz and 59.2 MHz. They are only −42 dBm so are not of any concern. These higher order harmonics are not successfully filtered out by the filters in the down-mixer due to their proximity to the fundamental.

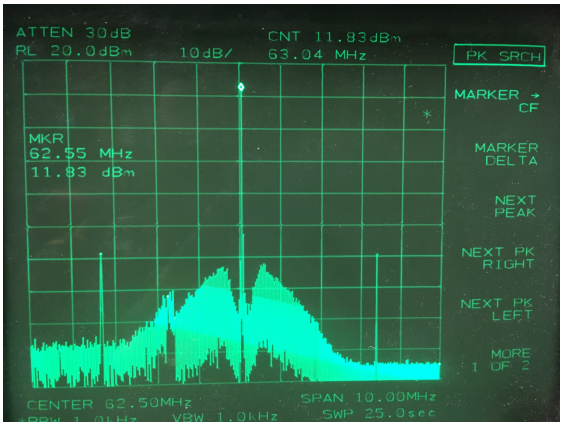

Fig. 7.7 Fourier transform of frequencies out of the original down-mixer.

A replacement down-mixing crate was designed to replace the original down-mixer which would eventually return to the IFIC high-gradient test bench. In an attempt to improve the output signal the maximum splitter used was 1:4, reducing the available channels to 8 which is still plenty for S-Box's current needs. The revised design can be seen in Figure 7.8. Care was taken to ensure each power level prior to amplification was ≈ 10 dBm below the saturation point to avoid harmonics and an additional low pass filter was implemented before the 4 way splitters. Unfortunately this down-mixer has not been constructed as it was more convenient for IFIC to re-build their original design in Valencia than to delay the KT structure testing by removing the down-mixer to send back.

†All channels were tested and this figure is representative of them all

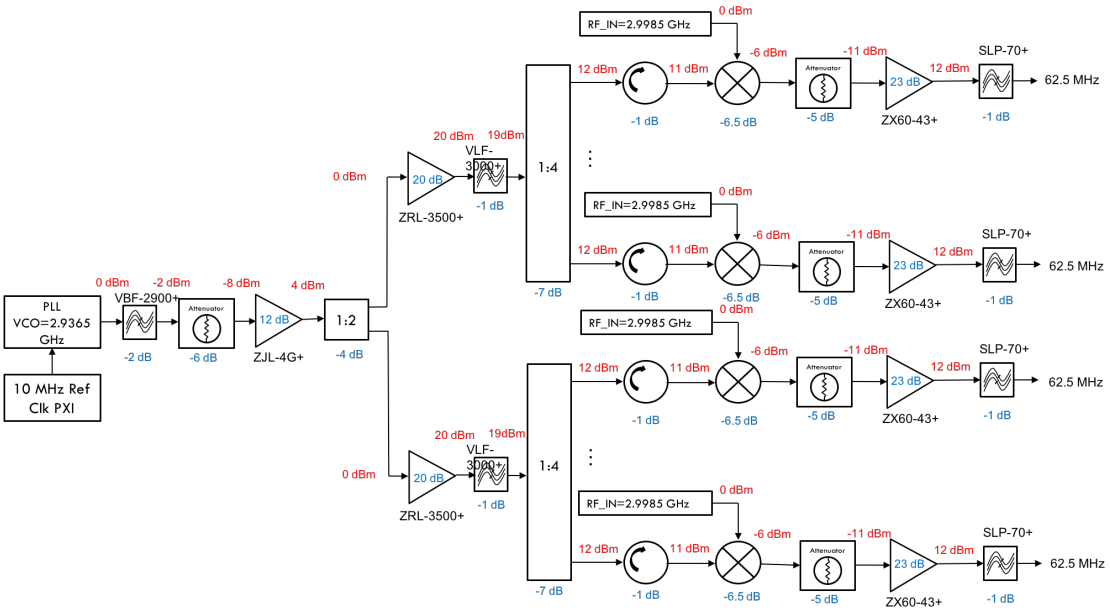

Fig. 7.8 The revised down-mixer schematic

7.5 Breakdown Detection

The 'real-time operating system' on the PXI controller allows us to visualise the structure's response to each pulse in real time. The LabVIEW GUI enables us to view the ADC's response to a known power level in mV and we can calibrate by sweeping the input power level from a signal generator, then fit the ADC's response to a polynomial and enter the coefficients in the configuration file. Once it has been calibrated the LabVIEW GUI shows us the incident, reflected and transmitted powers. LabVIEW programs are comprised of lots of subroutines called virtual instruments (VIs). The main VI in the S-box control program is shown in Figure 7.9 and it shows a typical pulse with no breakdown. The green trace shows the 350 ns square pulse input to the structure. The pink trace shows the power reflected by the structure. The two distinct peaks are a result of the high frequency components that create the square pulse being outside of the structure's bandwidth. The red trace shows the transmitted power at the end of the structure to be absorbed by the load. There is a short delay between the start of the incident pulse and the start of the transmitted pulse due to the structure filling and as the filling time of this structure is approximately 200 ns and the pulse length is 350 ns there is no stable flat top on the transmitted pulse. The blue trace shows the current in the Faraday cup upstream of the structure. It is larger than the current in the downstream Faraday cup (red dashed line) because it is a backwards travelling wave structure and the dark current gets captured by the wave travelling *upstream*. This is a normal pulse, but the traces deviate from this in the case of an

RF breakdown and we set thresholds on the LabVIEW GUI to both stop the RF to avoid damaging the cavity and save the relevant data for later analysis.

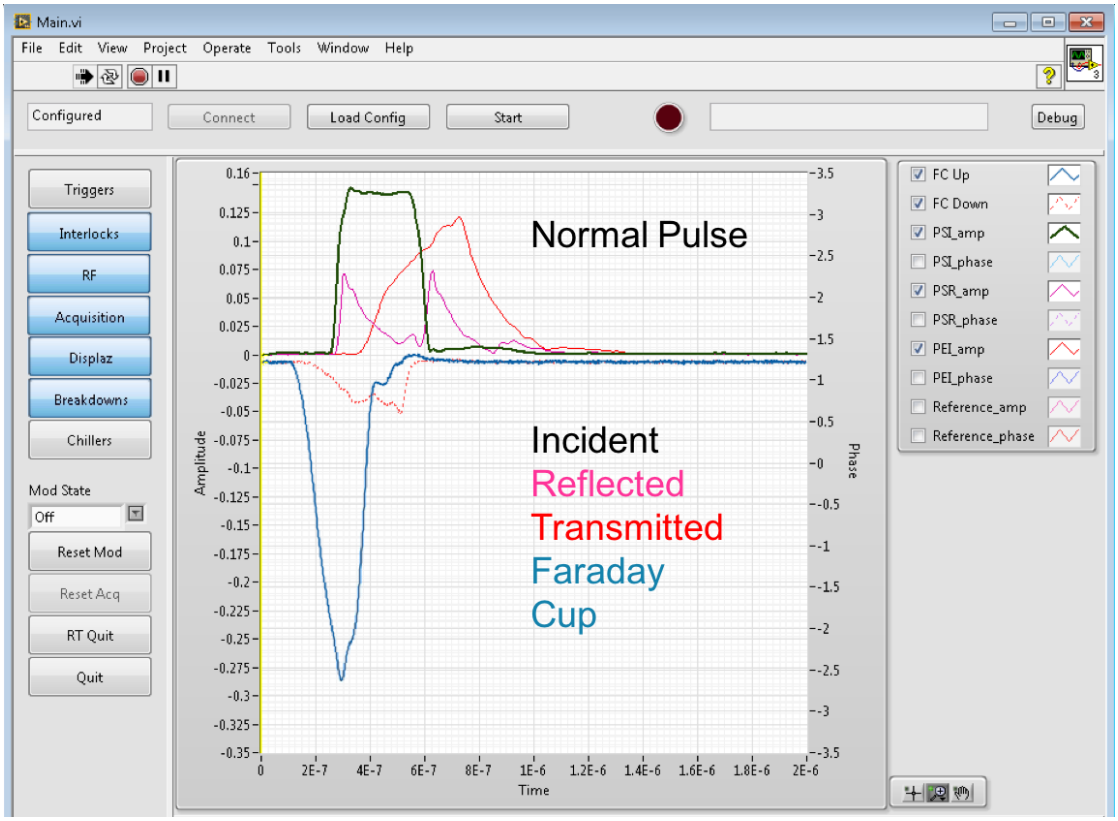

Fig. 7.9 A normal pulse including incident power, reflected power, transmitted power and Faraday cup signals.

When a breakdown occurs in the iris of a structure that iris is obstructed and there is a subsequent rise in the reflected signal, and a reduction in the transmitted signal. An RF breakdown appears like a short circuit would. Typical high gradient travelling wave structures, like the CLIC structures, will couple power from one cell to the next through the iris. The KT structure however is magnetically coupled through coupling slots in the cell walls. Peak S_c fields exist on both the nose cones around the iris and the coupling slots, thus one could say it is just as likely to breakdown there. It is also likely to change the reflected and transmitted signals in ways that have not seen before in the CLIC high gradient test program. Figure 7.10 shows the simulated total structure reflection as a function of the breakdown positioning along the structure for different breakdown scenarios. The black dashed line separates two distinct regimes; breakdowns in the beam aperture (above) and breakdowns in the coupling slots (below). As a general trend the reflection decreases the further down the structure it occurs, this is due to the reflected signal attenuating through the structure on it's way back to the directional coupler. From this it was thought that the transverse breakdown position could be estimated as

well as the longitudinal position. However, the measured results did not show such a well defined separation between the two. These results are discussed in more detail in [134].

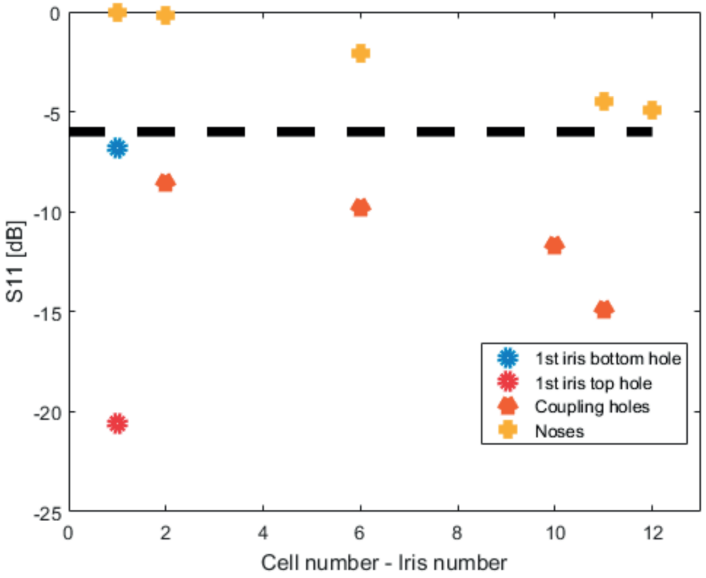

Fig. 7.10 Simulated total structure reflection as a function of the breakdown positioning along the structure [134].

Another way of detecting a breakdown in the structure during conditioning is observing the Faraday cup signals. They will typically saturate in the event of a breakdown and the thresholds set on the GUI will be exceeded. An example of a typical breakdown pulse is shown in Figure 7.11, and it is quite easy to conclude that a breakdown has occurred when comparing it to the normal pulse in Figure 7.9. Both of the Faraday cup currents have saturated (red & blue), the reflected signal has risen to the same level as the input pulse and there is barely any transmitted power after the incident pulse.

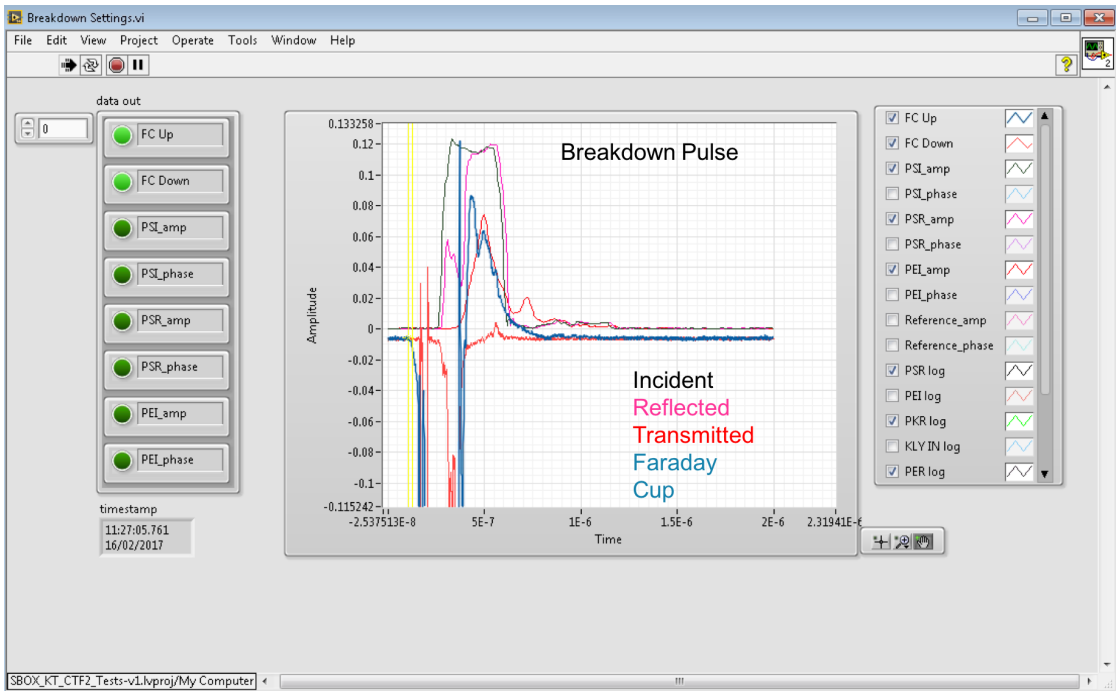

Fig. 7.11 A breakdown pulse detected by the Faraday cup signals. The red and blue traces below zero are the Faraday cups signals. The incident (green), reflected (pink) and transmitted (red) signals are above zero.

It is not always so easy to distinguish a breakdown pulse from a normal pulse however. Figure 7.12 shows a pulse that was saved by the PXI crate because it triggered a breakdown threshold. In a typical pulse like the one shown in Figure 7.9 the reflected signal has 2 peaks approximately half the amplitude of the incident pulse but in this pulse the second peak is almost the same amplitude. Visually, there is no distinctive change in the transmitted pulse in comparison to the normal pulse, and the Faraday cup signals have barely changed at all with the exception of a peak in the middle of the pulse. This demonstrates that breakdown pulses are not all alike and the threshold settings are important for accurate breakdown rate calculation. The pulse in question may have broken down on the tail end of the pulse which would explain why the transmitted signal is not too different from a normal pulse. The breakdown could have been located somewhere between the directional coupler and the structure itself, this would explain why there was not a large field emission current detected by the Faraday cups.

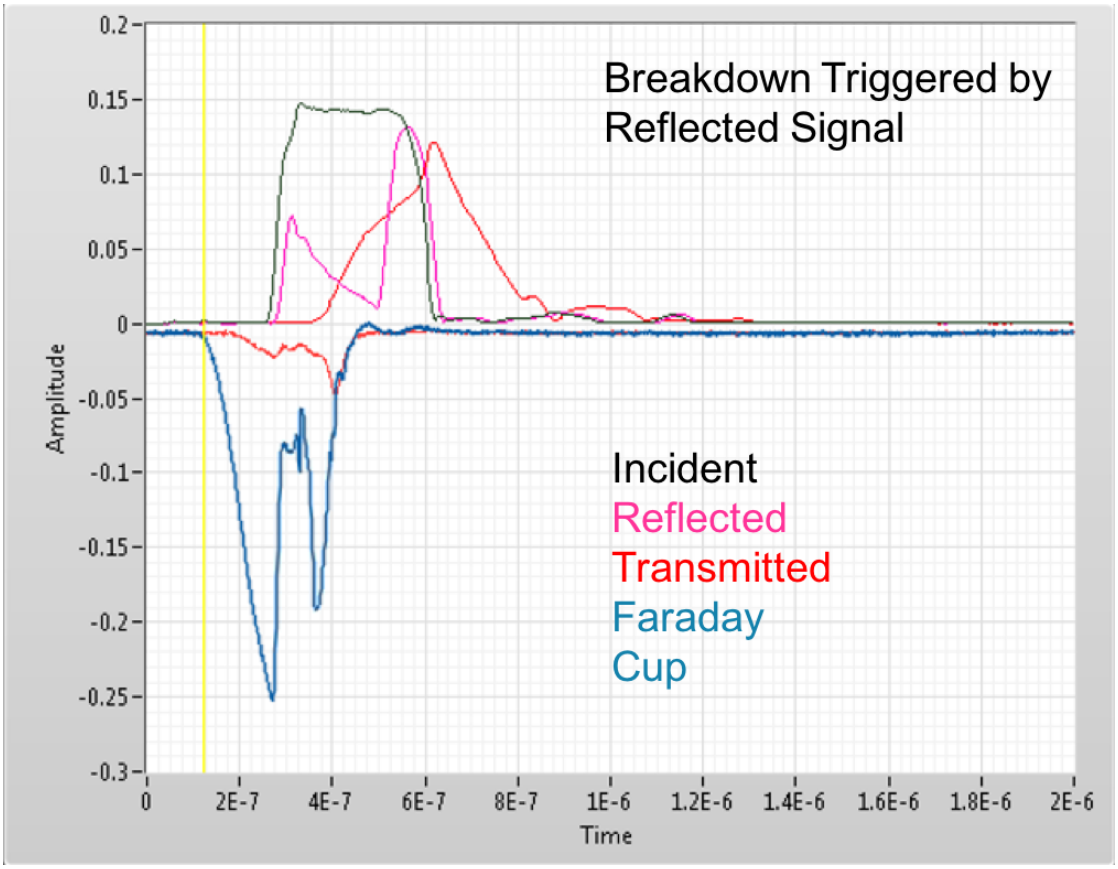

Fig. 7.12 A breakdown pulse detected by the reflected signal. The red and blue traces below zero are the Faraday cups signals. The incident (green), reflected (pink) and transmitted (red) signals are above zero.

7.6 Conditioning Algorithm

During daily operation of the high gradient test bench operators can visualise the conditioning of the DUT on the GUI as shown in Figure 7.13. The top left displays the real time RF signals and the dark current. The top right displays the current incident power level in Watts, and one can see the power level frequently drop to zero because of a breakdown event. The bottom right displays the vacuum level inside the DUT in mbar, the peaks correspond to breakdown events increasing the pressure in the structure. The bottom right hand window shows the RF control VI where the operator can manually control the power entering the structure or leave it for the conditioning algorithm to control.

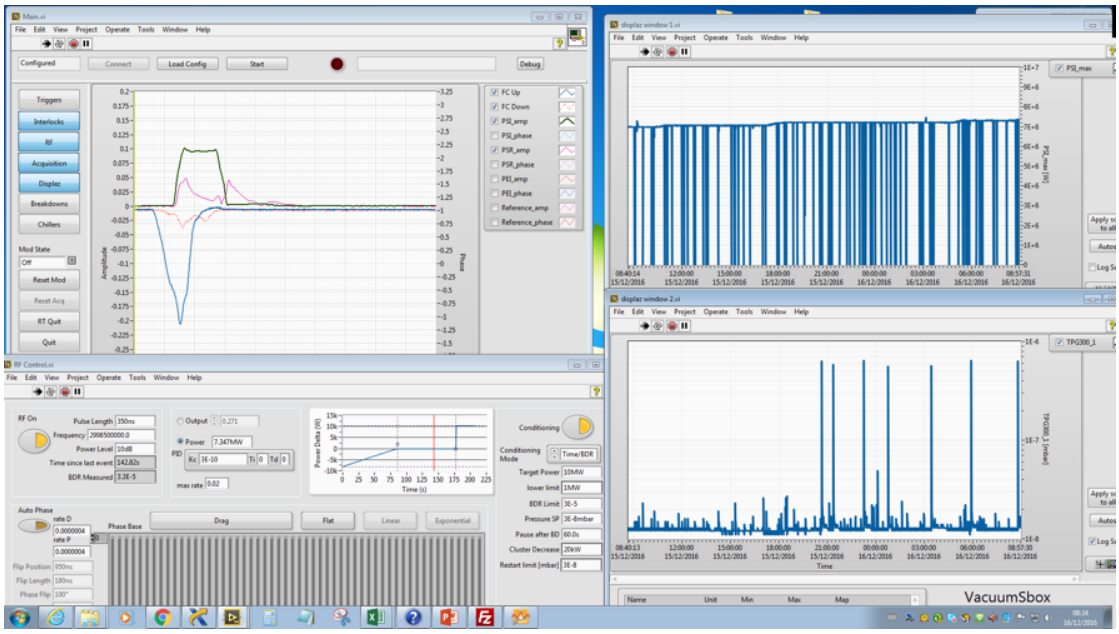

Fig. 7.13 S-box operational screenshot.

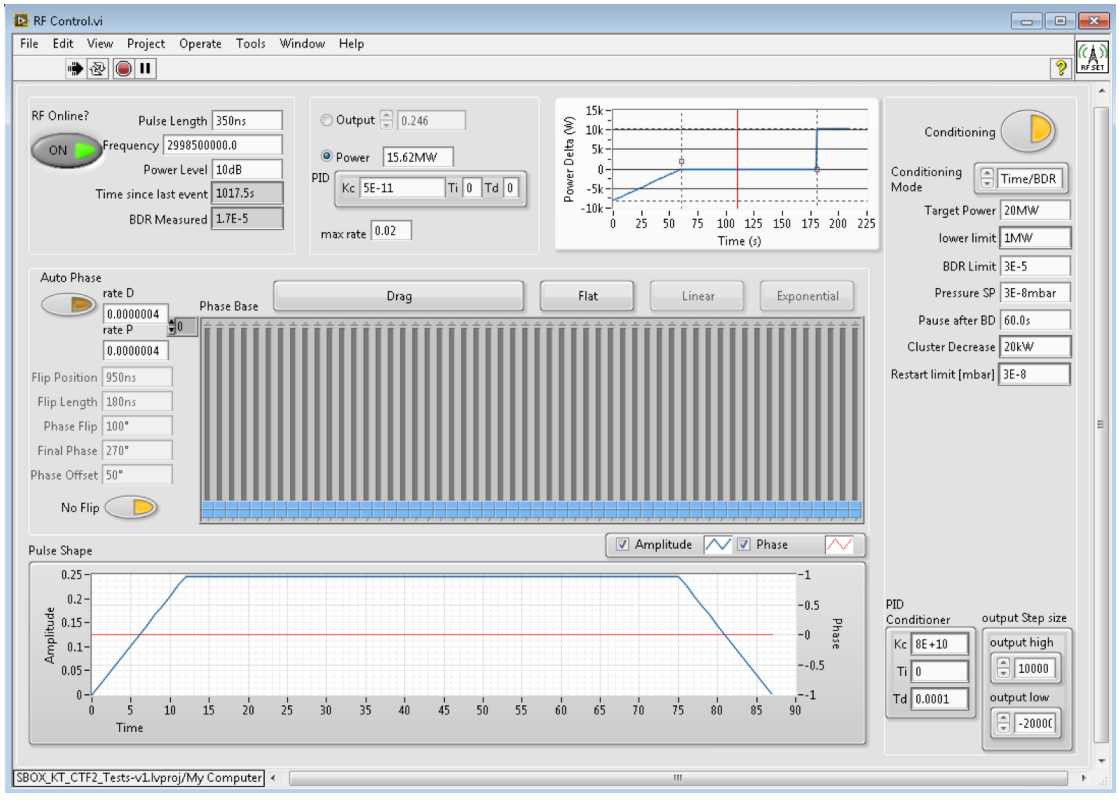

Fig. 7.14 Screenshot of the 'RF Control' VI including the conditioning algorithm (top left).

A close up of the RF control VI is shown in Figure 7.14. Here the operator can choose to control the power level manually or leave it to the control algorithm. In

the top right the operator can send an 'RF ON' signal to the modulator, and set the pulse length. It is here that the GUI displays the time since the last breakdown event in seconds, and the current breakdown rate measured over the previous two hours. To the right of this box the operator can set the power level, and also the K_c constant of the proportional-integral-derivative (PID) controller that increases the power from zero to the power level set in the box above. The rate of change of power resulting from the K_c controller is not intuitive. To avoid setting it too high[‡] the operator can also set a maximum rate of change to avoid excessively aggressive conditioning. The control panel for the conditioning algorithm is found on the far right of the VI, when activated the algorithm controls the cavity conditioning with the power level while monitoring the breakdown rate. Here one can set the target power for the DUT and also set a lower power limit, and crucially a breakdown rate limit. There is also a pressure set point here and the operator can decide how long the RF should be stopped for following a breakdown event, however the power will not be restarted until the vacuum has recovered to the restart limit. The PXI will check the vacuum level every 5 s during an interlock. The control algorithm will also reduce the power if a breakdown cluster is detected and the amount to reduce the power level is also set here. The PID conditioner can be fine tuned within this window, but the specifics of the algorithm can also be more intuitively tuned with the graphical representation shown at the top of the VI. The axes show 'Power Delta (W)' vs. 'Time (s)', and the blue line can be dragged and dropped by the operator. During operation the red bar scrolls across the x-axis with time and if it reaches 175 s[§] without any breakdown event occurring it will increase the power by 10 kW, and will continue at that power until a breakdown occurs. When a breakdown occurs the red bar starts again at zero seconds. If a breakdown occurs within the first 60 s the power will be reduced accordingly and the red bar will begin again at zero. If a breakdown occurs within the flat section the red bar will start again but the power level will remain the same. It has been shown that its the number of pulses that condition a structure rather than the number of breakdowns [133]. We want to avoid ramping the power too fast and causing excessive breakdowns that can damage the cavity permanently. Instead we want to gradually increase the power level and gently condition the structure maintaining a fairly constant breakdown rate, which is what the algorithm attempts to do.

7.7 Preliminary Results

The conditioning history of the KT structure is shown in Figure 7.15. The structure was designed to operate at 50 MV/m with a pulse length of 2.5 μs with an expected

[‡]The higher the value the faster the ramp in power.

[§]this is the current shown settings but can be changed my the operator.

breakdown rate of 10^{-6} [134]. The conditioning was started at a pulse length of 350 ns, and the structure exceeded its design gradient at around 130 million pulses. The pulse length was increased to 900 ns and quickly reached 50 MV/m which is typical of accelerating structures when the pulse length is increased but still below nominal values. The pulse length was increased again to 1.2 μs at which point the modulator and klystron started to have technical problems so the blue curve flattening out is not a limit placed by the structure but a limit on the high power capability of the experiment.

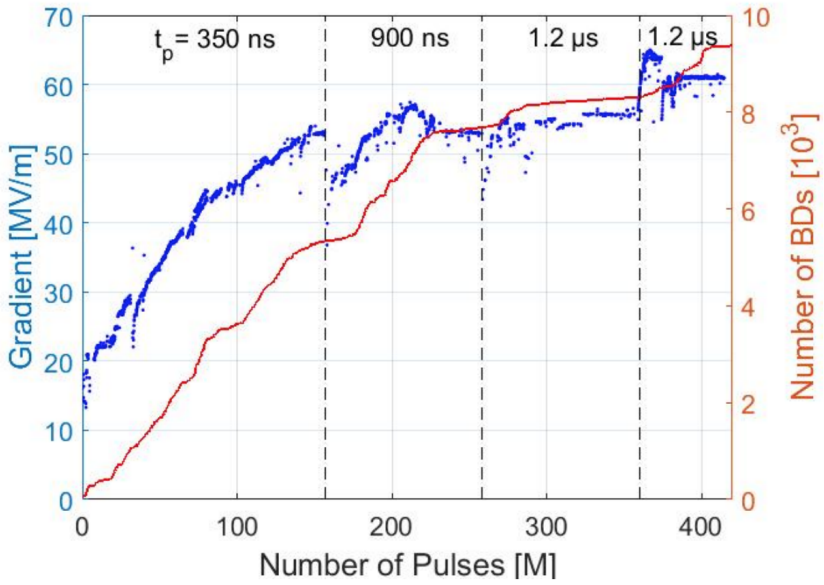

Fig. 7.15 The conditioning history of the KT structure. The gradient is shown in blue and the cumulative number of breakdowns (BDs) is shown in red [145].

After the installation of a new modulator and klystron a flat run was conducted where the power is kept constant and the BDR is allowed to decay to a stable rate at which time the cavity is deemed to be conditioned. Figure 7.16 shows the BDR decaying during the 60 MV/m flat run where the BDR dropped to 4×10^{-6} break downs per pulse (bpp). This corresponds to 2.1×10^{-5} bpp/m.

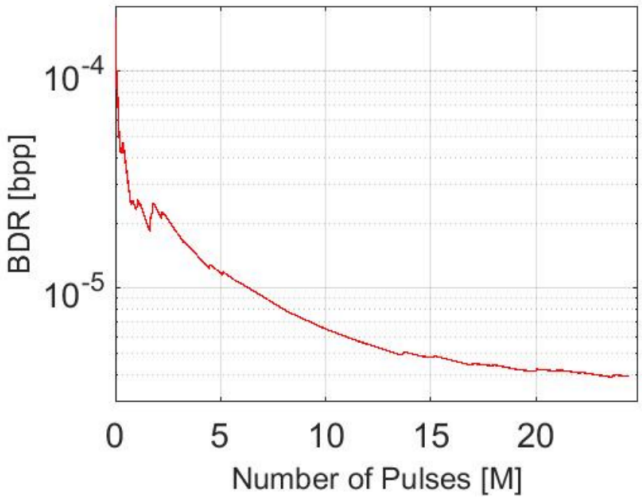

Fig. 7.16 BDR with respect to the accumulated number of pulses during conditioning at constant power. Gradient = 60 MV/m [145].

At the time of writing the experiment is ongoing to test the structure at the design pulse length of 2.5 μs flat top. Assuming the cavity is conditioned at 60 MV/m we can estimate the BDR at the nominal gradient of 50 MV/m and pulse length of 2.5 μs using

$$\frac{E_{acc}^{30} \cdot t_p^5}{BDR} = const. \tag{7.1}$$

as 3.4×10⁻6. This is still slightly higher than the target BDR of 1×10⁻6 but it is promising that it will continue to condition at the longer pulse length and drop to or even below the target BDR.

Table 7.1 shows the main parameters for both the KT bTW structure and the ProBE structure. The ProBE structure has a much longer filling time than the bTW structure because it is standing wave. Travelling wave cavities are known to have faster filling times than standing wave structures which has an advantage in a pCT application because it means the cavity is ready to accelerate beam in a shorter time, increasing patient throughput.

ProBE has higher peak fields than the bTW structure. Initially the limit set on the peak surface electric field was 200 MV/m like the bTW and CLIC structures. After the final optimisation the peak surface electric field of ProBE rose to 215 MV/m but as there is no definitive model limiting this value it was accepted. Only a high power test will answer if this will increase the BDR above acceptable limits.

S_c and the pulse length are both also higher for the ProBE cavity than the bTW structure. Using the scaling law

$$\frac{Sc_{acc}^{15} \cdot t_p^5}{BDR} = const. \tag{7.2}$$

and scaling from the CLIC nominal parameters of S_c=5 W/μm^2, t_p=200 ns and BDR=10^{-6} the ProBE cavity is predicted to operate at a BDR of 3.89×10^{-}11. Despite the relatively long pulse length this is still extremely low due to the low S_c peak in the ProBE cavity. There is no expectation that the ProBE cavity will perform at this BDR in a high power test. The design of the cavity was more focussed on aggressively maximising the shunt impedance with sharp nose cones around the beam axis. This is where the 215 MV/m peak surface electric field is located and is expected to dominate the BDR. If the assumption is made that the bTW structure is conditioned after the high power test presented in this chapter then Equation 7.2 can be used to predict the BDR of the ProBE cavity to be 5.9×10^{-4}. This would not be considered an acceptable breakdown rate for pCT however the high power test of the bTW is ongoing and may condition further. The high power test of the ProBE structure in S-box will yield some interesting results for the applicability of the scaling laws to lower frequencies.

bTWS vs ProBE Comparison				
	Parameter	ProBE	bTW	Units
L_{cav}	Cavity Length	32.8	18.9	cm
t_{fill}	Filling time	4.4	0.22	μs
t_p	Pulse length	4.5	2.5	μs
E_{acc}	Gradient	53.9	50	MV/m
E_{peak}	Peak Surface E-field	215	200	MV/m
S_c	Modified Poynting Vector	0.9	0.75	W/μm^2

Table 7.1 Comparison between the main design parameters of the KT bTW structure and ProBE.

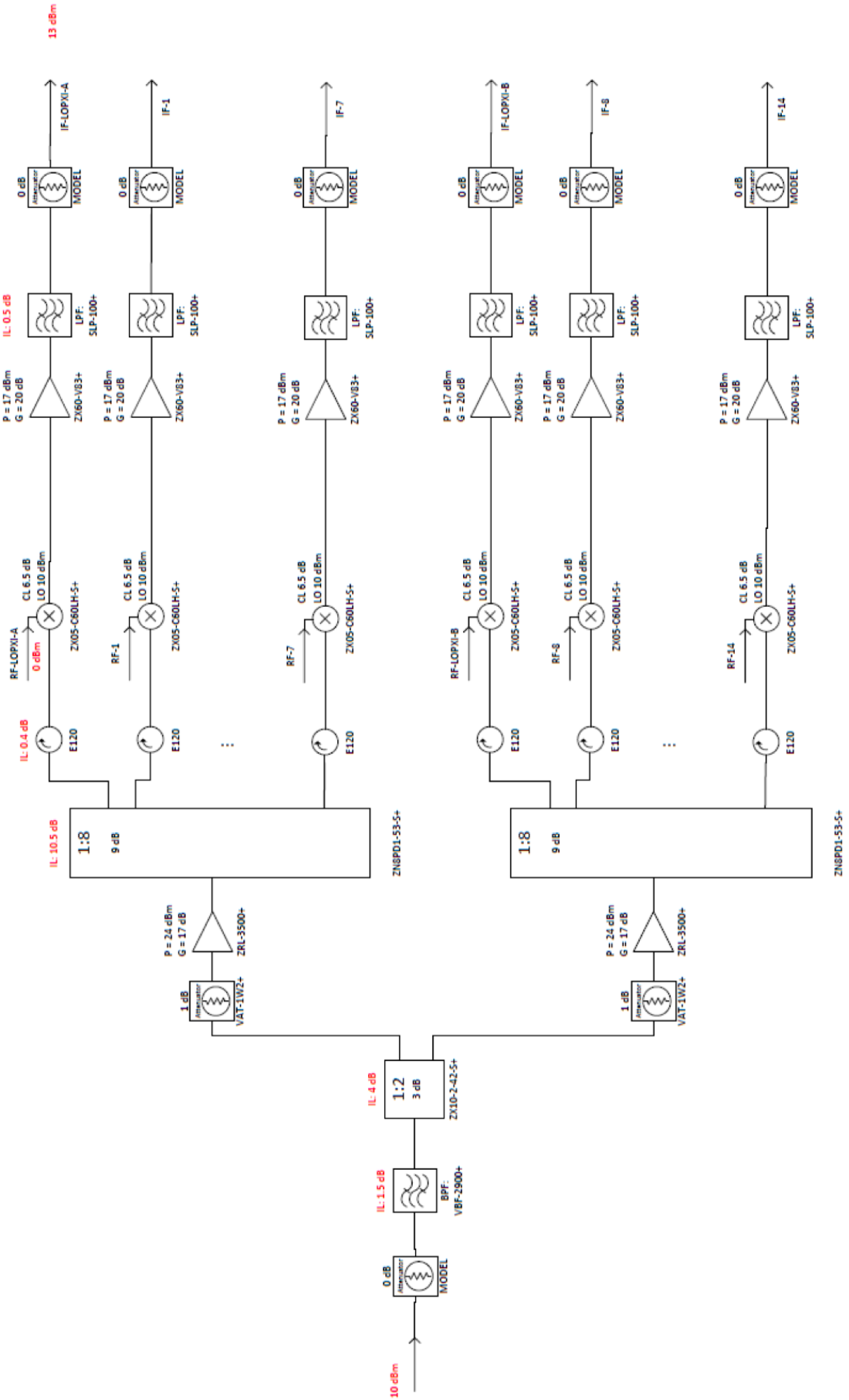

Fig. 7.6 The original down-mixer design for the S-box experiment

Chapter 8

Discussion and Conclusion

The main goal of this work was to design a high gradient proton boosting linac suitable to upgrade existing proton therapy centres that have 250 MeV cyclotrons, to provide 350 MeV protons to be used for proton imaging. In Chapter 1 the literature around proton imaging was reviewed and the demand for improved imaging techniques within the proton therapy community was presented alongside multiple ongoing research efforts to make proton imaging a reality. In this work the techniques used in the CLIC high gradient test program were employed to design a cavity with a gradient twice that of the typical proton accelerator. The relevant accelerator physics required to complete the work presented in this thesis was introduced in Chapter 2. The RF optimisation of both a small aperture and large aperture scheme were presented in Chapters 3 & 4.1 respectively. In these chapters both travelling wave and standing wave cavities were considered as potential structures for the ProBE linac. A beam dynamics and particle tracking study was presented in Chapter 5 where both small and large aperture solutions were considered. The optimum length of the cavity at an aperture radius of 4 mm was determined. Chapter 6 presented the mechanical engineering considerations surrounding the manufacture of the ProBE prototype cavity, where many of the techniques from the CLIC high gradient test program were employed. Finally in Chapter 7 the author contributed to the commissioning and operation of the S-box high gradient test bench at CERN, where a high gradient medical linac was being high power tested and where the ProBE prototype cavity is foreseen to be tested when it is complete. At the time of writing the cavity disks have been delivered by VDL and are shown in Figure 8.1.

Fig. 8.1 Final machined disks after delivery by VDL.

8.1 ProBE Conclusions

The RF optimisation for ProBE began with single cell pill box cavity simulations. Plotting shunt impedance against aperture for 4 different frequencies showed that, for very small aperture radii, 12 GHz had the highest shunt impedance per unit length due to the ratio between the aperture radius and the wavelength. Recognising that the final proton imaging application of this booster linac could cope with very low transmission, a small aperture at 12 GHz was adopted to utilise the high shunt impedance. Standing wave and backwards travelling wave structures were designed at both 3 GHz and 12 GHz. It then became apparent that the effects of cell to cell coupling on the shunt impedance overrides any advantage hoped to be gained from using the higher frequency. The wavelength being smaller at higher frequencies means there are more accelerating cells or 'gaps' in a fixed length structure, and thus more cell to cell coupling is required for suitable phase and amplitude drop across the structure. Shorter structures were also investigated, and although the effect of cell to cell coupling was reduced, the 3 GHz structure still outperformed the 12 GHz structure.

The entire small aperture optimisation was done using the modified Poynting vector (S_c) as the sole peak field limit. However due to large nose cones around

the beam axis, the peak surface electric fields were far higher than acceptable. The high gradient community have typically believed that the peak surface electric field achievable before RF breakdown occurs scales with frequency as per the Kilpatrick criterion. The CLIC high gradient test program has published lots of high power test data at 12 GHz, but at the time of optimisation the only high gradient data available at 3 GHz was the single cell tests done by TERA [124]. Unfortunately they were not sure the cavities had finished the conditioning process. A conservative 200 MV/m peak surface electric field limit was imposed, and was exceeded by 15 MV/m in the final structure. Since then the first high gradient test at 3 GHz has begun, and the structure has exceeded the 200 MV/m limit at 1.2μs pulse length. It is yet to reach its design pulse length but even at its maximum pulse length of 2.5μs it is still below the maximum S_c proposed in [82]. This structure is likely to be limited by E_{peak} before it reaches the maximum S_c. As the maximum S_c of ProBE is also far from the maximum, it will also likely be limited by E_{peak}. It could be the case that a scaling factor must be applied to S_c to apply it to 3 GHz cavities as a peak field limit. It could also be the case that magnetically coupled cavities are not limited by S_c in the same way that electrically coupled cavities are. Further analysis into the data obtained in the current and future high power tests of S-band cavities in S-box and other facilities may answer these questions.

A novel method to manufacture side-coupled cells from two disks was presented in Chapter 6. Cutting the cells this way allows for a radius to be machined around the previously difficult to access coupling slot. This reduced peak magnetic fields around the coupling slot and means the structure can be fed with higher power, have higher inter-cell coupling, and still maintain a high shunt impedance.

In the large aperture optimisation presented in Chapter 4.1, only S- and C-band cavities were investigated as they showed the highest shunt impedance for a 4 mm aperture radius. The maximum S_c was reduced from 4 to 2 W/μm^2 because S- and C-band high power klystrons usually have longer maximum pulse lengths. Backwards travelling wave and standing wave structures were designed and both S_c and the peak surface electric field limited the gradient achievable. The highest gradient calculated was the S-band side-coupled standing wave structure, which was limited by the peak surface electric field as S_c was only 0.9 W/μm^2.

In Chapter 5 both small and large aperture optics schemes were investigated. It was initially thought that the aperture could be minimised to achieve very high shunt impedances at X-band. This however required four impractically strong magnets between each cavity to focus the beam and achieve an acceptable current at the linac output. A large aperture FODO scheme was instead adopted and particles were also tracked through varying length structures using ASTRA to determine the optimum structure length. The conclusion was that although there is an advantage to having shorter structures with less cells due to inter-cell coupling,

more structures can't necessarily fit in the allocated space for the linac. For example the 3-cell and 7-cell structures could both only fit 7 structures in 3 meters with associated matching sections. The 3-cell structures require a higher gradient as there are less accelerating gaps. For smaller structures to be advantageous, the gradient improvement due to the reduction in inter-cell coupling has to be large enough to give the beam more energy than the same number of larger structures would have. However there is an upper limit to this due to gradient limits such as peak surface electric field and S_c so it is not always advantageous to have shorter structures. Additionally the 3-cell structures were not long enough for the beam to bunch adequately and this resulted in higher losses in the energy selection system. In this case the optimum was to have 6×11-cell structures given the 3 m space constraint at the Christie hospital, and current high gradient capabilities.

Ultimately this work was a feasibility study, and the conclusion is that a linac upgrade to existing proton therapy centres is feasible. This thesis focused on a specific case study of the Christie hospital which has a 250 MeV cyclotron as a proton source for treatment and a 3 m space in the beam line for a booster linac. Naturally this is the case for many proton therapy centres, and in the future when proton imaging technology is more advanced they may not be able financially to upgrade to a higher energy cyclotron or an FFAG solution. The pulsed linac upgrade is a flexible and versatile solution able to adapt to the needs of any facility desires 350 MeV protons. In this work we demonstrated in simulation the ability to reach the gradients necessary for a project such as this while maintaining sufficient current for imaging, and in the S-box experiment we have seen a similar cavity designed under the same gradient limits and manufacturing processes reach upwards of its design gradient albeit at a less than nominal pulse length.

Also in this work the 3 GHz test bench '*S-box*' was commissioned at CERN, for the purpose of testing S-band cavities as part of the CLIC high-gradient test programme. There is increasing interest in high gradient behaviour at 3 GHz. High gradient test benches are being constructed in IFIC and INFN as well as S-box at CERN. The experiment, despite setbacks such as broken modulators and klystrons, is conditioning the bTW structure well, and useful high gradient data at 3 GHz is being collected for future analysis. At the time of writing the bTW structure has exceeded it's design gradient up to 1.2 μs and is expected to continue rising. It has reached higher surface electric fields during conditioning than the typical CLIC structures. After this structure is conditioned a second identical structure will be high gradient tested either at S-box or at the IFIC facility. The ProBE structure is also foreseen to be tested at S-box, which will contribute 3 GHz standing wave high gradient data to that of the backwards travelling wave structures, and all of the existing X-band data. In Chapter 7 the performance of the bTW structure was scaled to the ProBE prototype parameters. It was predicted to operate at a

breakdown rate of $5.9\times10^{-}4$ which would not be a suitable breakdown rate for a medical linac. However, the bTW has not finished conditioning at the time of writing, and as such the parameter used for the scaling will likely improve.

8.2 ProBE Final Parameters

Table 8.1 and 8.2 contain the final design parameters for the ProBE prototype linac. At the start of the optimisation process it was decided to use 2×50 MW klystrons to power the linac via WR284 waveguide. This means each 50 MW klystron will be feeding 3 structures. This will require the design and manufacture of a 3-way high power splitter at 3 GHz. Alternatively 3×30 MW klystrons could be used with hybrids to split the power between 2 structures each. A travelling wave structure would have been desirable due to the shorter filling times associated with travelling wave structures. Table 4.5 showed the S-band SWS to have a filling time over 5 times longer than the S-band TWS. Ultimately it was decided to build the SWS prototype as it demonstrated a higher gradient than the alternatives in simulation.

3 GHz Prototype Structure			
	Parameter	Value	Units
f	Frequency	2.9985	GHz
S	Septum Thickness	2	mm
r_c	Accelerating Cell Radius	36	mm
r_{sc}	Coupling Cell Radius	13.1	mm
l	Accelerating Cell Length	29.8	mm
l_{sc}	Coupling Cell Length	29.8	mm
R_{oc}	Outer Corner Radius	6	mm
R_{ic}	Inner Corner Radius	2	mm
R_{on}	Outer Nose Radius	2	mm
R_{in}	Inner Nose Radius	2	mm
CA	Nose-cone Angle	65	Deg
N_{cell}	Number of Accelerating Cells	11	
d	Coupling Slot Depth	1.2	mm
k	Coupling factor	2	%
Q_0	Q-factor	13279	
Q_l	Loaded Q-factor	6444	
Z	Shunt Impedance	75.5	MΩ/m
E_{acc}	Gradient	53.9	MV/m
E_{peak}	Peak Surface E-field	215	MV/m
H_{peak}	Peak Surface H-Field	261	kA/m
S_c	Modified Poynting Vector	0.9	W/μm^2

Table 8.1 The parameters for the final prototype structure. Gradient is limited by 12.8 MW input power and available shunt impedance.

Parameter	Value	Units
Structure length	≈35	cm
Number of cells	11	
Aperture Radius	4	mm
Repetition rate	40	Hz
Pulse Length	5	μs
PMQ Length	3.5	cm
PMQ Strength	72.4	m^-2
Number of PMQs	6	
Number of cavities	6	
Required gradient	54.8	MV/m
Total transmission	1.92	%

Table 8.2 Summary of the final linac optics design parameters.

8.3 Future work

The work described in this thesis is only the very beginning of the ProBE project. At the time of writing the precision machined disks that make up the cavity itself have been delivered and visually inspected for scratches and imperfections. One of the rejected disks in shown in Figure 8.2. The next step is to align and clamp the disks together, and measure the S-parameters of the cavity with a VNA (vector network analyser). This should highlight any discrepancies from the metrology reports, and also provide an opportunity to re-machine any faulty disks before they are all bonded together. In Figure 4.22 it was shown that confluence between the accelerating cells and coupling cells was not successfully met. Increasing the size of the side-coupled cavity radius should bring this within the tuning range of the tuning pins. This step however is not necessary for a high power test of the prototype to take place using the accelerating mode. The nearest mode is only 650 kHz away from the accelerating mode so may also be excited which is not ideal but for a high power test without beam it should suffice.

Fig. 8.2 One of the final disks provided by VDL. This particular cell was rejected as it was out of tolerance. However, it represents the final machined disks. This disk has a counterpart which contains the re-entrant section.

The disks will need to be hydrogen bonded together at 1035°C under vacuum (10^{-5} mbar) with a H_2 partial pressure (20 mbar) [142]. Witness disks have been manufactured and will accompany the structure through each step of bonding/brazing for further pollution analysis. After the main disk stack has been bonded the beam pipes, cooling blocks, tuning studs, and flanges will be brazed on in steps of decreasing temperature. Once the structure is built the fields will be measured via bead pull experiment and if necessary each cell will be tuned to ensure minimal reflections at the operating frequency, and the same field amplitude and phase advance throughout the structure.

It has been mentioned throughout this work that the ProBE structure will then need to be high power tested at one of the 3 GHz high gradient test facilities, likely S-box. The data collected during this conditioning and test can then be compared to the 2 bTW structures at 3 GHz, and also to the CLIC X-band structures to shed more light on how the breakdown rate varies with frequency, and which scaling laws should be applied when. Things to look out for during the ProBE tests would be multipacting in the side-coupled cells, breakdowns on the coupling slots, and breakdowns on the iris. Once the testing is complete one may wish to cut the cavity open to investigate damage caused by breakdown. The equation for the maximum voltage at which multipacting can occur between parallel plates is

$$V_{max} = \frac{m\omega^2 x_0^2}{2e} = 2993 \text{ V}. \tag{8.1}$$

The field in the simulation model for the prototype cavity is not flat in the side-coupled cells so each cell has a different field amplitude. Only one cell is at risk of multipacting with a voltage of 2673 V. However, the side-coupled cells in

addition to the accelerating cells have tuning studs brazed to the surface, so one could avoid possible multipacting by adjusting the field level in the cell.

Once the analysis from the high power tests is complete, one has the opportunity to further improve upon the design if it is necessary. If tests show the cavity can reach higher peak fields than 215 MV/m while operating at an acceptable breakdown rate one may wish to reduce the gap between the nose cones and increase the gradient of the structure. If there are many breakdowns on the coupling slots during testing, one might wish to adopt the side-coupled cavity design shown in Figure 3.18 to eliminate them, which would also simplify the machining. There are other changes that could be made to the mechanical design that would reduce the cost of manufacture and make it more accessible to proton imaging centres. For example the cooling channels could be incorporated into the cavity disks for better heat dissipation during operation, and to reduce the copper requirement for separate cooling blocks. The push-pull tuning studs could also be replaced with one-directional tuning, where the cavity is deliberately manufactured at slightly lower frequency and rather than braze studs to the surface, ball bearings deform the cell wall through threaded holes in the cavity disks. The RF design could also be re-optimised for another application or facility with different space requirements, or with a different proton source. Linac-only proton therapy centres have a much smaller transverse beam emittance and could reduce the cavity aperture size to increase the gradient further.

The long term future plans for the ProBE project are to test multiple cavities at the Christie hospital with a clinical beam. It is foreseen that there will be two prototype cavities and a matching section of permanent magnet quadrupoles between them to also test the linac optics. As beam rigidity increases with energy, stronger magnets are required to bend the beam towards the patient at 350 MeV than 250 MeV so the existing gantry design for the Christie would not be suitable should the ProBE linac be installed. A superconducting gantry design is currently being researched at Manchester University along with the entire beam delivery system. It is hoped that in the not so distant future, there will be a commercially viable option for cyclotron based proton therapy centres to upgrade their facilities with a compact high gradient linac. It is believed this will improve the effectiveness of proton therapy as a cancer treatment, thus improving not only cancer survival rates, but patients' quality of life during and after treatment.

Bibliography

[1] Freddie Bray, Jacques Ferlay, Isabelle Soerjomataram, Rebecca L. Siegel, Lindsey A. Torre, and Ahmedin Jemal. Global cancer statistics 2018: GLOBOCAN estimates of incidence and mortality worldwide for 36 cancers in 185 countries. *CA: A Cancer Journal for Clinicians*, 2018.

[2] Anna Wysocka-Rabin. *Advances in Conformal Radiotherapy using Monte Carlo Code to Design New IMRT and IORT Acclerators and Interpret CT Numbers*. EuCARD Editorial Series on Accelertor Science, 2013.

[3] D. K. Bewley. The 8 mev linear accelerator at the mrc cyclotron unit hammersmith hospital, london. *The British Journal of Radiology*, 58(687):213–217, Mar 1985.

[4] Wieslaw Maciszewski and Waldemar Scharf. Particle accelerators for radiotherapy: present status and future. In *Astroparticle, Particle and Space Physics, Detectors and Medical Physics Applications*, volume Volume 2, pages 402–410. World Scientific, July 2004.

[5] Robert R. Wilson. Radiological Use of Fast Protons. *Radiology*, 47(5):487–491, November 1946.

[6] R.W. Schulte, V. Bashkirov, M. C. Loss Klock, T. Li, A. J. Wroe, I. Evseev, D. C. Williams, and T. Satogata. Density resolution of proton computed tomography. *Medical Physics*, 32:1035–1046, 2005.

[7] K. M. Hanson, J. N. Bradbury, T. M. Cannon, R. L. Hutson, D. B. Laubacher, R. J. Macek, M. A. Paciotti, and C. A. Taylor. Computed tomography using proton energy loss. *Physics in Medicine & Biology*, 26(6):965, 1981.

[8] R. Schulte, V. Bashkirov, Tianfang Li, Zhengrong Liang, K. Mueller, J. Heimann, L. R. Johnson, B. Keeney, H. F. W. Sadrozinski, A. Seiden, D. C. Williams, Lan Zhang, Zhang Li, S. Peggs, T. Satogata, and C. Woody. Conceptual design of a proton computed tomography system for applications in proton radiation therapy. *IEEE Transactions on Nuclear Science*, 51(3):866–872, June 2004.

[9] Wilhelm Conrad Röntgen. Hand mit Ringen: Radiographic print, January 1896.

[10] Freund,L. Ein mit Röntgenstrahlen behandelter Fall von Naevus pigmentosus piliferus. *Wiener Medizinische Wochenschrift*, 47:428–434, 1897.

[11] Milford D. Schulz. The supervoltage story. *American Journal of Roentgenology*, 124(4):540–559, August 1975.

[12] R. J. Van de Graaff, K. T. Compton, and L. C. Van Atta. The Electrostatic Production of High Voltage for Nuclear Investigations. *Physical Review*, 43(3):149–157, February 1933.

[13] W. F. Hanson. The Changing Role of Accelerators in Radiation Therapy. *IEEE Transactions on Nuclear Science*, 30(2):1781–1783, April 1983.

[14] D. W. Kerst. The Betatron. *Radiology*, 40(2):115–119, February 1943.

[15] Betatron. `https://en.wikipedia.org/w/index.php?title=Betatron&oldid=879946413`, 2019. Accessed 29.01.2019.

[16] Rolf Wideröe. Über ein neues Prinzip zur Herstellung hoher Spannungen. *Archiv für Elektrotechnik*, 21(4):387–406, July 1928.

[17] Theresa Johnston. A Cannon for Oncologists. *Stanford Magazine*, May 2011.

[18] U. Amaldi, P. Berra, K. Crandall, D. Toet, M. Weiss, R. Zennaro, E. Rosso, B. Szeless, M. Vretenar, C. Cicardi, C. De Martinis, D. Giove, D. Davino, M. R. Masullo, and V. Vaccaro. LIBO—a linac-booster for protontherapy: construction and tests of a prototype. *Nuclear Instruments and Methods in Physics Research Section A: Accelerators, Spectrometers, Detectors and Associated Equipment*, 521(2):512–529, April 2004.

[19] C. Ronsivalle, M. Carpanese, C. Marino, G. Messina, L. Picardi, S. Sandri, E. Basile, B. Caccia, D. M. Castelluccio, E. Cisbani, S. Frullani, F. Ghio, V. Macellari, M. Benassi, M. D'Andrea, and L. Strigari. The TOP-IMPLART project. *The European Physical Journal Plus*, 126(7), July 2011.

[20] Silvia Verdú-Andrés, Ugo Amaldi, and Ángeles Faus-Golfe. Literature review on linacs and ffags for hadron therapy. *International Journal of Modern Physics A*, 26(10n11):1659–1689, April 2011.

[21] Amaldi, U. and Larsson, B. *Hadron Therapy in Oncology.* Elsevier, Amsterdam, 1994.

[22] S. Benedetti, A. Grudiev, and A. Latina. High gradient linac for proton therapy. *Physical Review Accelerators and Beams*, 20(4):040101, April 2017.

[23] S. Webb. *Intensity-Modulated Radiation Therapy.* CRC Press, May 2015.

[24] S. Webb, G. Hartmann, G. Echner, and W. Schlegel. Intensity-modulated radiation therapy using a variable-aperture collimator. *Physics in Medicine & Biology*, 48(9):1223, 2003.

[25] F. Colombo, A. Benedetti, F. Pozza, A. Zanardo, R. C. Avanzo, G. Chierego, and C. Marchetti. Stereotactic radiosurgery utilizing a linear accelerator. *Applied Neurophysiology*, 48(1-6):133–145, 1985.

[26] W. Lutz, K. R. Winston, and N. Maleki. A system for stereotactic radiosurgery with a linear accelerator. *International Journal of Radiation Oncology, Biology, Physics*, 14(2):373–381, February 1988.

[27] Zahra Taheri-Kadkhoda, Thomas Björk-Eriksson, Simeon Nill, Jan J. Wilkens, Uwe Oelfke, Karl-Axel Johansson, Peter E. Huber, and Marc W. Münter. Intensity-modulated radiotherapy of nasopharyngeal carcinoma: a comparative treatment planning study of photons and protons. *Radiation Oncology*, 3:4, January 2008.

[28] T. Bortfeld, H. Paganetti, and H. Kooy. MO-A-T-6b-01: Proton Beam Radiotherapy — The State of the Art. *Medical Physics*, 32(6-13):2048–2049, June 2005.

[29] Ute Linz. *Ion Beam Therapy - Fundamentals, Technology, Clinical Applications*. Springer.

[30] K. Peach, P. Wilson, and B. Jones. Accelerator science in medical physics. *The British Journal of Radiology*, 84:S4–10, December 2011.

[31] J. Beringer, J. F. Arguin, R. M. Barnett, K. Copic, O. Dahl, D. E Groom, C. J. Lin, J. Lys, H. Murayama, C. G. Wohl, W. M. Yao, and P. A. Zyla. Review of Particle Physics. *Physical Review D*, 86(1), July 2012.

[32] Hywel Owen, Ranald MacKay, Ken Peach, and Susan Smith. Hadron accelerators for radiotherapy. *Contemporary Physics*, March 2014.

[33] Matthew M. Ladra and Torunn I. Yock. Proton Radiotherapy for Pediatric Sarcoma. *Cancers*, 6(1):112–127, January 2014.

[34] Antje-Christin Knopf and Antony Lomax. In vivo proton range verification: a review. *Physics in Medicine & Biology*, 58(15):R131, 2013.

[35] Simon J. Thomas. Margins for treatment planning of proton therapy. *Physics in Medicine and Biology*, 51(6):1491–1501, March 2006.

[36] Robert P. Johnson. Review of medical radiography and tomography with proton beams. *Reports on Progress in Physics*, 81(1):016701, 2018.

[37] P. J. Doolan, M. Testa, G. Sharp, E. H. Bentefour, G. Royle, and H.-M. Lu. Patient-specific stopping power calibration for proton therapy planning based on single-detector proton radiography. *Physics in Medicine and Biology*, 60(5):1901–1917, March 2015.

[38] Wayne Newhauser, Jonas Fontenot, Nicholas Koch, Lei Dong, Andrew Lee, Yuanshui Zheng, Laurie Waters, and Radhe Mohan. Monte Carlo simulations of the dosimetric impact of radiopaque fiducial markers for proton radiotherapy of the prostate. *Physics in Medicine and Biology*, 52(11):2937–2952, June 2007.

[39] Oliver Jäkel and Petra Reiss. The influence of metal artefacts on the range of ion beams. *Physics in Medicine and Biology*, 52(3):635–644, February 2007.

[40] Ming Yang, X. Ronald Zhu, Peter C. Park, Uwe Titt, Radhe Mohan, Gary Virshup, James E. Clayton, and Lei Dong. Comprehensive analysis of proton range uncertainties related to patient stopping-power-ratio estimation using the stoichiometric calibration. *Physics in Medicine & Biology*, 57(13):4095, 2012.

[41] H. Q. Woodard and D. R. White. The composition of body tissues. *The British Journal of Radiology*, 59(708):1209–1218, December 1986.

[42] D. R. White, H. Q. Woodard, and S. M. Hammond. Average soft-tissue and bone models for use in radiation dosimetry. *The British Journal of Radiology*, 60(717):907–913, September 1987.

[43] D. R. White, J. Booz, R. V. Griffith, J. J. Spokas, and I. J. Wilson. ICRU Reports. *Journal of the International Commission on Radiation Units and Measurements*, os23(1):184–186, January 1989.

[44] M. Yang, G. Virshup, J. Clayton, X. R. Zhu, R. Mohan, and L. Dong. Theoretical variance analysis of single- and dual-energy computed tomography methods for calculating proton stopping power ratios of biological tissues. *Physics in Medicine & Biology*, 55(5):1343, 2010.

[45] M. van Herk, P. Remeijer, C. Rasch, and J. V. Lebesque. The probability of correct target dosage: dose-population histograms for deriving treatment margins in radiotherapy. *International Journal of Radiation Oncology, Biology, Physics*, 47(4):1121–1135, July 2000.

[46] A. J. Lomax, T. Boehringer, A. Coray, E. Egger, G. Goitein, M. Grossmann, P. Juelke, S. Lin, E. Pedroni, B. Rohrer, W. Roser, B. Rossi, B. Siegenthaler, O. Stadelmann, H. Stauble, C. Vetter, and L. Wisser. Intensity modulated proton therapy: a clinical example. *Medical Physics*, 28(3):317–324, March 2001.

[47] Jan Unkelbach, Thomas Bortfeld, Benjamin C. Martin, and Martin Soukup. Reducing the sensitivity of IMPT treatment plans to setup errors and range uncertainties via probabilistic treatment planning. *Medical Physics*, 36(1):149–163, January 2009.

[48] Jan Unkelbach, Timothy C. Y. Chan, and Thomas Bortfeld. Accounting for range uncertainties in the optimization of intensity modulated proton therapy. *Physics in Medicine & Biology*, 52(10):2755, 2007.

[49] Chul-Hee Min, Chan Hyeong Kim, Min-Young Youn, and Jong-Won Kim. Prompt gamma measurements for locating the dose falloff region in the proton therapy. *Applied Physics Letters*, 89(18):183517, Oct 2006.

[50] Thirolf, P.G. A compton camera prototype for prompt gamma imaging, June 2015. Nucleus-Nucleus.

[51] Cho Jongmin, Wang Min, Gonzalez-Lepera Carlos, Mawlawi Osama, and Cho Sang Hyun. Development of bimetallic (Zn@Au) nanoparticles as potential PET-imageable radiosensitizers. *Medical Physics*, 43:4775–4788, July 2016.

[52] Michael F. Gensheimer, Torunn I. Yock, Norbert J. Liebsch, Gregory C. Sharp, Harald Paganetti, Neel Madan, P. Ellen Grant, and Thomas Bortfeld. In Vivo Proton Beam Range Verification Using Spine MRI Changes. *International Journal of Radiation Oncology*, 78(1):268–275, September 2010.

[53] S. N. Penfold, A. B. Rosenfeld, R. W. Schulte, and K. E. Schubert. A more accurate reconstruction system matrix for quantitative proton computed tomography. *Medical Physics*, 36(10):4511–4518, October 2009.

[54] J. T. Taylor, C. Waltham, T. Price, N. M. Allinson, P. P. Allport, G. L. Casse, A. Kacperek, S. Manger, N. A. Smith, and I. Tsurin. A new silicon tracker for proton imaging and dosimetry. *Nuclear Instruments and Methods in Physics Research Section A: Accelerators, Spectrometers, Detectors and Associated Equipment*, 831:362–366, September 2016.

[55] Uwe Schneider, Jürgen Besserer, Peter Pemler, Matthias Dellert, Martin Moosburger, Eros Pedroni, and Barbara Kaser-Hotz. First proton radiography of an animal patient. *Medical Physics*, 31(5):1046–1051, May 2004.

[56] A. M. Cormack. Representation of a Function by Its Line Integrals, with Some Radiological Applications. *Journal of Applied Physics*, 34(9):2722–2727, September 1963.

[57] Leaders in Proton Therapy Technology and Treatment. `https://www.protominternational.com/`. Accessed 08.01.2018.

[58] F. Wang, J. Flanz, and R. Hamm. Injection study of the Radiance 330 synchrotron with a 1.6 MeV RFQ linac. In *AIP Conference Proceedings*, pages 649–651, 2012.

[59] Paul Scherrer Institut (PSI). `https://www.psi.ch/`. Accessed 25.09.2017.

[60] N. J. Pogue, L. Stingelin, and A. Adelmann. Analysis and suppression of RF radiation from the PSI 590 mev cyclotron Flat Top Cavity. *Nuclear Instruments and Methods in Physics Research Section A: Accelerators, Spectrometers, Detectors and Associated Equipment*, 828(Supplement C):156–162, August 2016.

[61] Cockcroft Web. `https://www.cockcroft.ac.uk/`. Accessed 08.01.2018.

[62] About the John Adams Institute | John Adams Institute for Accelerator Science. `https://www.adams-institute.ac.uk/`.

[63] Fermilab | About Fermilab. `http://www.fnal.gov/pub/about/`. Accessed 08.01.2018.

[64] C. Johnstone and S. Koscielniak. New nonscaling FFAG for medical applications. In *Particle Accelerator Conference, 2007. PAC. IEEE*, pages 2951–2953. IEEE, 2007.

[65] K. J. Peach, J. H. Cobb, S. L. Sheehy, H. Witte, T. Yokoi, M. Aslaninejad, M. J. Easton, J. Pasternak, Roger Barlow, and H. L. Owen. PAMELA: Overview and status. In *First International Particle Accelerator Conference*, Kyoto, Japan, 2010. JACoW.

[66] S. Tygier, K. B. Marinov, R. B. Appleby, J. A. Clarke, J. M. Garland, H. L. Owen, and B. J. A. Shepherd. Medical therapy and imaging fixed-field alternating-gradient accelerator with realistic magnets. *Physical Review Accelerators and Beams*, 20(10), October 2017.

[67] Alberto Degiovanni. *High Gradient Proton Linacs for Medical Applications*. PhD thesis, Ecole Polytechnique Federale de Lausanne, March 2014.

[68] HKS Architects - Christie NHS Foundation Trust Proton Beam Therapy Centre. `http://www.hksinc.com/places/christie-nhs-foundation-trust-proton-beam-therapy-centre/`. Accessed 11.11.2018.

[69] ProBeam® Multi-Room Proton Therapy Solution | Varian Medical Systems. `https://www.varian.com/oncology/products/treatment-delivery/probeam-multi-room-proton-therapy-solution`. Accessed 11.11.2018.

[70] Katie Butler. Incredible pictures show proton beam machine arriving at The Christie. `http://www.manchestereveningnews.co.uk/news/greater-manchester-news/christie-hospital-proton-beam-machine-13226585`, June 2017. Accessed 11.11.2018.

[71] H. F. W. Sadrozinski, V. Bashkirov, B. Colby, G. Coutrakon, B. Erdelyi, D. Fusi, F. Hurley, R. P. Johnson, S. Kashiguine, S. McAllister, F. Martinez-McKinney, J. Missaghian, M. Scaringella, S. Penfold, V. Rykalin, R. Schulte, K. Schubert, D. Steinberg, and A. Zatserklaniy. Detector development for Proton Computed Tomography (pCT). In *2011 IEEE Nuclear Science Symposium Conference Record*, pages 4457–4461, October 2011.

[72] The Christie Charity. `http://www.christie.nhs.uk/the-christie-charity`. Accessed 15.01.2018.

[73] Hywel Owen. Private Communication, 2015.

[74] Ewa Oponowicz and Hywel Owen. Superconducting Gantry Design for Proton Tomography. In *8th International Particle Accelerator Conference*, pages 4795–4797, Copenhagen, Denmark, May 2017. JACOW.

[75] James Clerk Maxwell. VIII. A dynamical theory of the electromagnetic field. *Philosophical Transactions of the Royal Society of London*, 155:459–512, January 1865.

[76] John David Jackson. *Classical Electrodynamics*. John Wiley & Sons, 1962.

[77] Thomas P. Wangler. *RF linear accelerators*. Wiley-VCH ; John Wiley, distributor, Chichester, 2nd rev. and enlarged ed. edition, 2008.

[78] Sarah Cousineau, Jeff Holmes, and Yan Zhang. Lecture 3 - RF Acceleration in Linacs. Part 1. United States Particle Accelerator School Lecture, January 2011.

[79] Benjamin Cheymol. *Development of beam transverse profile and emittance monitors for the CERN LINAC4*. PhD thesis, Université Blaise Pascal, 2011.

[80] R.H.Fowler and L.Nordheim. Electron emission in intense electric fields, May 1928.

[81] Graeme Burt. RF Linear Accelerators: Gradient limits. The Cockcroft Institute Post-Graduate Lectures, 2015.

[82] A. Grudiev, S. Calatroni, and W. Wuensch. New local field quantity describing the high gradient limit of accelerating structures. *Physical Review Special Topics - Accelerators and Beams*, 12(10), October 2009.

[83] François Rohrbach. *Sur les mécanismes qui conduisent à la formation de l'étincelle électrique à très haute tension et sous ultra-vide par la mesure des temps de retard à la disruption*. PhD thesis, CERN, Geneva, 1971.

[84] K. Nordlund and F. Djurabekova. Defect model for the dependence of breakdown rate on external electric fields. *Physical Review Special Topics - Accelerators and Beams*, 15(7), July 2012.

[85] Eliyahu Zvi Engelberg, Yinon Ashkenazy, and Michael Assaf. Stochastic Model of Breakdown Nucleation under Intense Electric Fields. *Physical Review Letters*, 120(12), March 2018. arXiv: 1803.09360.

[86] Jan Wilhelm Kovermann. *Comparative Studies of high-gradient RF and DC breakdowns*. PhD thesis, CERN, December 2010.

[87] A Kyritsakis, M Veske, K Eimre, V Zadin, and F Djurabekova. Thermal runaway of metal nano-tips during intense electron emission. *Journal of Physics D: Applied Physics*, 51(22):225203, June 2018.

[88] T.J. Boyd. Kilpatrick's criterion. Group AT-1 Technical Report: AT-1:82-28, Los Alamos, December 1982.

[89] W. D. Kilpatrick. Criterion for Vacuum Sparking Designed to Include Both rf and dc. *Review of Scientific Instruments*, 28(10):824–826, October 1957.

[90] W Wuensch. Clic-note-649 - the Scaling of the Traveling-Wave RF Breakdown Limit.

[91] Silvia Verdu-Andres. *High-Gradient Accelerating Structures Studies and their Application in Hadrontherapy.* PhD thesis, Universitat de Valencia, December 2012.

[92] I Wilson. CLIC-note-52 - Surface Heating of the CLIC Linac Structure, October 1987.

[93] Erk Jensen. RF Cavity Design. CERN Accelerator School Lecture, 2009.

[94] William Barletta. RF-accelerators: Standing wave linacs. United States Particle Accelerator School Lecture, June 2012.

[95] A. Robson, P. N. Burrows, N. Catalan Lasheras, L. Linssen, M. Petric, D. Schulte, E. Sicking, S. Stapnes, and W. Wuensch. The Compact Linear Collider (CLIC): Accelerator and Detector, December 2018. arXiv: 1812.07987.

[96] Graeme Burt. Low-Beta Acceleration. Cockcroft Institute Postgraduate Lecture, 2018.

[97] Frank Gerigk. Review on trends in normal conducting linacs for protons, ions and electrons, with emphasis on new technologies and applications. In *28th Linear Accelerator Conference*, number TU1A01, East Lansing, Michigan, May 2017.

[98] F Gerigk and R Wegner. Design of the Pi-Mode Structure (PIMS) for Linac4. In *Particle Accelerator Conference*, page 3, Vancouver, BC, Canada, 2009.

[99] The Very Model of a Modern PI-Mode Structure - CERN Document Server. `https://cds.cern.ch/record/1664309/files/`. Accessed 14.01.2019.

[100] N. Holtkamp. Status of the SNS project. In *Proceedings of the 2003 Bipolar/BiCMOS Circuits and Technology Meeting*, number 03CH37440, pages 11–15, Portland, OR, USA, 2003. IEEE.

[101] Mechanical design of the SNS coupled cavity accelerator. In *Proceedings*, volume 3.

[102] H Ao, K Hasegawa, and K Hirano. First High-Power ACS Module for J-PARC Linac. In *Proceedings of the Linear Accelerator Conference, LINAC'2006*, page 3, Knoxville, Tennessee, USA, 2006.

[103] G Devanz, P Bosland, M Desmons, P Hardy, F Leseigneur, M Luong, F Peauger, J Plouin, and D Roudier. ESS Elliptical Cavities and Cryomodules. page 5, 2013.

[104] A Facco and di Legnaro. Low and medium beta SC cavities. In *Proceedings of EPAC 2004*, page 5, Lucerne, Switzerland, 2004.

[105] RadiaBeam Technologies. `http://www.radiabeam.com/`. Accessed 28.01.2019.

[106] Sergey V. Kutsaev, Ronald Agustsson, Salime Boucher, Richard Fischer, Alex Murokh, Brahim Mustapha, Alireza Nassiri, Peter N. Ostroumov, Alexander Plastun, Evgeny Savin, and Alexander Yu. Smirnov. High-gradient low- β accelerating structure using the first negative spatial harmonic of the fundamental mode. *Physical Review Accelerators and Beams*, 20(12), December 2017.

[107] Alberto Degiovanni, Walter Wuensch, and Jorge Giner Navarro. Comparison of the conditioning of high gradient accelerating structures. *Physical Review Accelerators and Beams*, 19(3):032001, March 2016.

[108] Hasan Padamsee. *RF Superconductivity: Science, Technology, and Applications*. John Wiley & Sons, April 2009.

[109] S.M. Hanna. Applications of X-band technology in medical accelerators. In *Proceedings of the 1999 Particle Accelerator Conference*, volume 4, pages 2516–2518, New York, NY, USA, 1999.

[110] F Löhl, J Alex, H Blumer, and M Bopp. Status of the SwissFEL C-band Linac. In *Proceedings of FEL2013*, page 5, New York, NY, USA, 2014.

[111] Walter Wuensch. High-gradient X-band technology: from TeV colliders to light sources and more. *CERN Courier*, March 2018.

[112] CST MICROWAVE STUDIO® - 3d EM Simulation Software. `http://www.cst.com/products/cstmws`. Accessed 14.03.2018.

[113] Welcome to the Compact Linear Collider Website. `http://clic-study.web.cern.ch/`. Accessed 04.03.2018.

[114] ADAM | A Research Company Inspired By CERN. `http://www.adam-geneva.com/`. Accessed 05.03.2018.

[115] AVO | Who We Are. `http://www.advancedoncotherapy.com/About/Who-we-are`. Accessed 05.03.2018.

[116] AVO | Linac Image Guided Hadron Technology LIGHT. `http://www.advancedoncotherapy.com/Our-LIGHT-system/Product-overview`. Accessed 05.03.2018.

[117] Marco Garlasche. Private communication, 2015.

[118] New module installed in CLIC test facility - CERN Document Server. `https://cds.cern.ch/record/1982610?ln=de`. Accessed 17.03.2018.

[119] A. Grudiev and W. Wuensch. Clic-note-773 – design of an X-Band Accelerating Structure for the CLIC Main Linac, 2008.

[120] Design of the CLIC main linac accelerating structure for CLIC conceptual design report. In *Proceedings of Linear Accelerator Conference, LINAC2010*, Tsukuba, Japan, 2010.

[121] M. Aicheler and CERN, editors. *A Multi-TeV linear collider based on CLIC technology: CLIC Conceptual Design Report*. CERN, Geneva, 2012.

[122] Graeme Burt, Thomas Abram, Praveen Kumar Ambattu, Christopher Lingwood, Ian Burrows, Trevor Hartnett, J. Hindley, Christopher White, Peter Corlett, Andrew Goulden, Peter McIntosh, Keith Middleman, Yuri Saveliev, and Robert Smith. Design and Operation of a Compact 1 MeV X-band Linac. In *Linear Accelerator Conference 2012, LINAC2012*, Tel-Aviv, Israel, April 2013.

[123] A. Degiovanni, U. Amaldi, R. Bonomi, M. Garlasché, A. Garonna, S. Verdú-Andrés, and R. Wegner. TERA high gradient test program of RF cavities for medical linear accelerators. *Nuclear Instruments and Methods in Physics Research Section A: Accelerators, Spectrometers, Detectors and Associated Equipment*, 657(1):55–58, November 2011.

[124] Silvia Verdú-Andrés, Ugo Amaldi, Rossana Bonomi, Alberto Degiovanni, Marco Garlaschè, Adriano Garonna, Claudio Mellace, Peter Pearce, and Rolf Wegner. High-Gradient Test of a 3 GHz Single-Cell Cavity. In *Linear Accelerator Conference 2010, LINAC2010*, Tsukuba, Japan, April 2011.

[125] Steffen Döbert. Status of very high-gradient cavity tests. In *Linear Accelerator Conference 2002, LINAC2002*, Gyeongju, Korea, 2002.

[126] C Van Herwaarden. Improvements for the inner region of the COMET cyclotron. Techincal Report, Internal Note, PSI, 2012.

[127] Superconducting Cyclotron | Varian Medical Systems. `https://www.varian.com/oncology/products/treatment-delivery/superconducting-cyclotron`. Accessed 06.03.2018.

[128] Javier Bilbao de Mendizabal. *3 GHz linac booster design from 250 MeV to 350 MeV for medical application at PSI*. PhD thesis, Universite de Geneve, PSI, Villigen, February 2012.

[129] Robert Apsimon. Private communication, June 2018.

[130] MAD - Methodical Accelerator Design. `http://mad.web.cern.ch/mad/`. Accessed 20.02.2019.

[131] Using ASTRA at DESY-Hamburg. `http://www.desy.de/~mpyflo/`. Accessed 25.09.2017.

[132] MATLAB - MathWorks. `https://uk.mathworks.com/products/matlab.html`. Accessed 25.09.2017.

[133] Jorge Giner Navarro. *Breakdown studies for high gradient RF warm technology in: CLIC and hadrontherapy linacs*. PhD thesis, Universitat de Valencia, December 2016.

[134] Stefano Benedetti. *High-gradient and high-efficiency linear accelerators for hadron therapy*. PhD thesis, EPFL - École polytechnique fédérale de Lausanne, 2018.

[135] CATIA™ 3dexperience® - Dassault Systèmes® 3d Software. `https://www.3ds.com/products-services/catia/`. Accessed 18.03.2019.

[136] About VDL. `https://www.vdlgroep.com/en/vdl-groep/about-vdl`. Accessed 18.03.2019.

[137] SMC. Thermo-chiller Series HRS specification document, 2018.

[138] G. F. C. Rogers and Yon Mayhew. *Engineering Thermodynamics: Work and Heat Transfer*. Prentice Hall, Harlow, 4 edition edition, August 1996.

[139] Theodore L. Bergman, Adrienne S. Lavine, Frank P. Incropera, and David P. DeWitt. *Fundamentals of Heat and Mass Transfer*. Wiley, Chichester, May 2011.

[140] M. P. May, J. R. Fritz, T. G. Jurgens, H. W. Miller, J. Olson, and D. Snee. Mechanical construction of the 805 MHz side couple cavities for the Fermilab linac upgrade. In *Linear Accelerator Conference 1990*, Alberquerque, New Mexico, USA, 1991.

[141] John D Bernardin, Curtt Ammerman, and Steve Hopkins. The Design and Performance of a Water Cooling System for a Prototype Coupled Cavity Linear Particle Accelerator for the Spallation Neutron Source. In *The 6th ASME-JSME Thermal Engineering Joint Conference*, 2003.

[142] A. Solodko. Procedure for bonding of copper discs for x-band accelerating structures. Procedure EDMS: 1237642, CERN, Geneva, August 2015.

[143] PXI Platform - National Instruments. `http://www.ni.com/pxi/`. Accessed 26.03.2018.

[144] Microwave amplifiers ltd. `https://microwaveamps.co.uk/`. Accessed 26.03.2018.

[145] A. Vnuchenko, D. Esperante Pereira, S. Benedetti, N. Catalan Lasheras, A. Grudiev, B. Koubek, S. Pitman, I. Syratchev, B. Woolley, W. Wuensch, T. Lucas, M. Volpi, A. Faus Golfe. High-Gradient Performance of an S-Band Backward Travelling Wave Accelerating Structure for Medical Hadron Therapy Accelerators. In *International Particle Accelerator Conference 2018 - IPAC18*, Vancouver, BC, Canada, 2018.

Appendix A

Technical Specification

Engineering | Lancaster University

Price Enquiry

Technical Specification

ProBE structure MELACCL30013

Abstract

This technical specification concerns the machining, dimensional control, packing and delivery of the mechanical components for the ProBE Prototype structure

MELACCL30013

Deliveries are forseen within 10 weeks from reception of order

A.1 INTRODUCTION

A.1.1 Introduction to ProBE: Proton Boosting Extension for Imaging and Therapy

Lancaster Univerity (LU) in collaboration with Manchester University, CERN and the Chrisitie Hosptial are designing a proton boosting linac for medical applications. Proton beam therapy is an alternative to traditional x-ray radiotherapy utilised especially for paediatric malignancies and radio-resistant tumours; it allows a precise tumour irradiation, but is currently limited by knowledge of the patient density and thus the particle range. Typically X-ray computed tomography (CT) is used for treatment planning but CT scans require conversion from Hounsfield units to estimate the proton stopping power (PSP), which has limited accuracy. Proton CT measures PSP directly and can improve imaging and treatment accuracy. The Christie Hospital will use a 250 MeV cyclotron for proton therapy, and ProBE is a pulsed linac upgrade, to provide 350 MeV protons for proton CT within the facility. This technical specificaition is associated with the first 11 cell prototype RF-cavity. The cavity is a normal conducting, 3 GHz side coupled standing wave structure.

A.1.2

The cavity must operate at high pulsed power. It will be operable at a known frequency and have the ability to be tuned by plastic deformation of the walls via tuning pins. Cooling will be applied using chilled waters on the cavity side walls. The RF operating frequency is 2.9985 GHz, and the required input is up to 14 MW peak (2 kW average).

A.2 SCOPE OF THE SUPPLY

The successful bidder (hereinafter referred to as the “contractor”) shall supply the parts for the protoype structure (hereinafter referred to, in whole or in part, as the “supply”) as defined in this technical specification and the documents and drawings attached to it.

A.2.1 Deliverables Included in the Supply

The supply shall include:

- The manufacturing of the parts for the ProBE protoype structure with several geometries (32 parts in total). The parts to be manufactured are described in section A.3.1 (table A.1).
- The dimensional control report.
- The packaging.

A.2.2 Items not included in the supply

Flanges, and cooling blocks are not included in the supply and will be manufactured at CERN.
Assembly of joining of the parts (diffusion bonding / brazing) are not included in the supply and will be carried out afterwards by another company.

A.3 TECHNICAL REQUIREMENTS

A.3.1 General description

The drawings (filenames correspond to the respective file in the CERN Drawing Directory) of the parts to be manufactured are given here below. The 3D version of the drawings are available on request in .catpart (CATIA V5), .step or .igs CAD format. The parts are listed in a sequence corresponding to the order of assembly.

* Drawings for price enquiry purpose only.

The dimensional tolerances and roughness to be achieved for the parts are specified in the drawing should be respected as they are and are and are measured in free-state. The required roughness should be achieved directly by mechnical machining (turning/milling/drilling) and is evaluated according to ISO1302.

Polishing is not allowed.
During manufacturing, only cutting fluids which are halogen free and sulphur free should be used. Blowing the parts with wet air is not allowed. All cleaning procedures must be submitted to LU approval prior to the execution.

Table A.1 List and quantity of parts o be manufactured

Drawing number*	**Description of Drawing**	**Quantity to be Manufactured**	**Material**
MELACCL30013	Full Assembly	-	
MELACCL30009	Endcell 1	1	OFE copper
MELACCL30003	Midcell 1.A	4	OFE copper
MELACCL30001	Midcell 1.B	4	OFE copper
MELACCL30002	Midcell 2.A	4	OFE copper
MELACCL30004	Midcell 2.B	4	OFE copper
MELACCL30008	Coupler Disk 1	1	OFE copper
MELACCL30007	Coupler Disk 2	1	OFE copper
MELACCL30005	Coupler Disk 3	1	OFE copper
MELACCL30010	Endcell 2	1	OFE copper
MELACCL30006	Coupler Waveguide	1	OFE copper
MELACCL30012	Witness Disk	8	OFE copper
MELACCL30011	Beam Pipe	2	OFE copper

Scratches and marks of any nature are not allowed.
The direction of final machining passes of the disks has to be performed in order to avoid the creation of burrs.

The successful bidder must have demonstrated the manufacturing of similar parts at a suitable accuracy.

A.3.2 Dimensional control report

Dimensional control report is required for each machined piece. The contractor must provide LU these dimensional control reports **before shipping the parts for LU approval.** The real numerical values of all tolerated dimensions are required.

Important Dimensions

The most important dimensions are:

- For the case of the midcell disks ***MELACCL30001, MELACCL30003***:

  - The outside diameter of the accelerating cell ⌀72.025±0.001
  - The outside diameter of the coupling cell ⌀25.714±0.001
  - The distance between the nose cones (11.769 mm), and the nose cone angle (50°).
  - Radius R1 shown in view F
  - Flatness of both sides as they will later be joined by diffusion bonding
  - Diameter of Iris (8 mm) and localisation w.r.t. A,B,C
  - Localisations of reference planes B and C
  - Thickness of the parts (13.997 mm)
  - Complete shape accuracy of zone A

- For the case of the midcell disks ***MELACCL30002, MELACCL30004***:
  - The outside diameter of the accelerating cell ⌀72.025±0.001
  - The outside diameter of the coupling cell ⌀25.714±0.001
  - The outside diameter of the re-entrant section ⌀17.316±0.001
  - Radius R1 shown in views B&F respectively
  - Flatness of both sides as they will later be joined by diffusion bonding
  - Diameter of Iris (8 mm) and localisation w.r.t. A,B,C
  - Localisations of reference planes B and C
  - Thickness of the parts (15.769 mm)
  - Complete shape accuracy of zone A

- For the case of the coupler disks 1&3 ***MELACCL30005, MELACCL30008***:
  - The outside diameter of the accelerating cell ⌀72.025±0.001
  - The outside diameter of the coupling cell ⌀25.714±0.001
  - The distance between the nose cones (11.769 mm), and the nose cone angle (50°).
  - The bottleneck width 29.493 mm
  - The sharp edge shown in views G&I respectively
  - Radius R1 shown in view H
  - Flatness of both sides as they will later be joined by diffusion bonding
  - Diameter of Iris (8 mm) and localisation w.r.t. A,B,C
  - Localisations of reference planes B and C

  - Thickness of the parts (13.997 mm)
  - Complete shape accuracy of zone A

- For the case of coupler disk 2 ***MELACCL30007***:
  - The outside diameter of the accelerating cell ⊘72.025±0.001
  - The outside diameter of the coupling cell ⊘25.714±0.001
  - The outside diameter of the re-entrant section ⊘17.316±0.001
  - The width of the bottleneck 29.493 mm
  - The sharp edge shown in view G
  - Radius R1 shown in view H
  - Flatness of both sides as they will later be joined by diffusion bonding
  - Diameter of Iris (8 mm) and localisation w.r.t. A,B,C
  - Localisations of reference planes B and C
  - Thickness of the parts (15.769 mm)
  - Complete shape accuracy of zone A

- For the case of the endcell disks ***MELACCL30009, MELACCL30010***:
  - The outside diameter of the accelerating cell ⊘72.025±0.001
  - The outside diameter of the coupling cell ⊘25.714±0.001
  - The outside diameter of the re-entrant section ⊘17.316±0.001
  - The nose cone angle 65
  - The distance between the cavity wall and the tip of the nose cone 4.944 mm
  - Radius R1 shown in view E
  - Flatness of both sides as they will later be joined by diffusion bonding
  - Diameter of Iris (8 mm) and localisation w.r.t. A,B,C
  - Localisations of reference planes B and C
  - Thickness of the parts (31.765 mm)
  - Complete shape accuracy of zone A

- For the case of the coupler waveguide piece ***MELACCL30006***:
  - Lengths 72.118 mm, 27.766 mm, and 34.028mm
  - Sharp edges shown in views B & C
  - Localisations of reference planes A, B, and C
  - Complete shape accuracy of zone A

A.3.3 Raw material

Raw material for the parts is Oxygen Free Copper (OFE) UNS C10100, and will be delivered by LU. There are two possible options of raw material: Rectangular bar 160mm x 100mm cross section & Round bar ⌀180mm. The contractor should indicate with the draft manufacturing programme (see section A.4.3) what quantity of each bar is required.

Delivery of materials or components to be supplied by LU or CERN on contract loan will be according to an agreed schedule determined on acceptance of the manufacturing schedule. The contractor is required to inspect the materials or components on delivery and agree in writing within 7 days of receipt of the material that it is suitable for the purpose of the contract. A list of all components to be supplied on contract loan will be supplied with the contract.

Any remaining useable copper after manufacture is complete should be returned to CERN.

A.3.4 Identification

The following parts must be identified according to the following model:

Endcell Disk 1:	EC1-01	MELACCL30009
Midcell Disks:	1B1-02	MELACCL30001
	2B1-03	MELACCL30004
	1A1-04	MELACCL30003
	2A1-05	MELACCL30002
	1B2-06	MELACCL30001
	2B2-07	MELACCL30004
	1A2-08	MELACCL30003
	2A2-09	MELACCL30002
	2A3-13	MELACCL30002
	1B3-14	MELACCL30001
	2B3-15	MELACCL30004
	1A3-16	MELACCL30003
	2A4-17	MELACCL30002
	1B4-18	MELACCL30001
	2B4-19	MELACCL30004
	1A4-20	MELACCL30003
Coupler Disk 1:	CD1-10	MELACCL30008
Coupler Disk 2:	CD2-11	MELACCL30007
Coupler Disk 3:	CD3-12	MELACCL30005
Endcell Disk 2:	EC2-21	MELACCL30010
Beam Pipe 1 & 2:	BP-01 & BP-02	MELACCL30011
Witness Disk 1-8:	WD-01...WD-08	MELACCL30012
Coupler Waveguide:	CPLR-01	MELACCL30006

Disks must be marked on the external face as specified on the drawing.

A.3.5 Heat treatment

The recommended stress relieving temperature is 245 °Cduring at least 2 hours in vacuum. LU should be informed about any heat treatment (stress relief) applied on the parts.

A.3.6 Vacuum Cleanliness

For the vacuum components to be completely compatible with the ultra high vacuum environment of the RF cavity a high degree of cleanliness will be necessary at all stages of production to guarantee an acceptably low outgassing rate and weld integrity.

All mechanical cold working operations must exclude the use of heavy organic lubricants since these can be retained to some extent in the surface after the process.

The plate material is to be cleaned before any cutting or forming operation commences. It will be sufficient to swab with acetone, isopropyl alcohol or similar solvent. If a guillotine or press is to be used the blades should be cleaned. Care must be taken that any particulates are removed from the surface of the metal sheet before such operations to ensure that they are not pressed ito the surface during cutting or forming.

When the plate material or any other component forming part of or within the vacuum envelope has been cut, formed and finally machined, the vacuum surface must never be in contact with oily or greasy objects (including bare hands leaving finger prints) unless a thorough cleaning operation is schduled to follow immediately after.

A.4 Performance of the contract

A.4.1 General Conditions

Contracts will be awarded by Lancaster University, throughout this specification the contracting agent is referred to as 'Lancaster Univsersity', 'The University' or 'LU'. All contractual issues will be managed by the university contracts office. The contractor will be required to co-operate closely with Lancaster University and its authorised representative at all stages of the contract. Technical issues will be resolved after adequate discussion with an authorised representative of the Engineering Department of Lancaster University.

This specification will be an integral part of any subsequent contract. The company must indicate acceptance of all applicable clauses, but may wish to comment on a

clause even if it is fully accepted. In the event that any clause is not acceptable either in whole or in part this fact must be clearly recorded together with a full written explanation, where a clause is not applicable the clause number must be recorded with the comment 'Not applicable.'

Where alternative design features or manufacturnig procedures are proposed by the company this must always be in addtion to a bid that fully meets the existing specification.

Unless specifically mentioned otherwise, the contractor shall apply the most restrictive clause in case of ambiguity between the clauses of the contract, including its annexes. All deliverables and activities that are not explicitly mentioned in the technical specification but are essential for the execution of the contract shall be considered an integral part of the technical specification.

The manufacturer will be responsible for any departure from anticipated performance due to the failure of the manufacturer to adhere to any part of this specification.

No change to the specified designs is permitted without the written permission of Lancaster University. However if at any stage of the contract it is clear that advantage could be gained by such modification then the manufacturer is encouraged to bring it to the attention of LU.

Except as agreed under A.4.1, no departure from the drawings may be made without the express permission in writing of The University.

A.4.2 Sub-Contracts

Full details of all sub-contracts must be available to LU, and written permission shall be obtained from LU before placement of such sub-contracts.

LU will require written evidence of a formal contract between the manufacturer and any sub-contractor, together with the legal and contractual obligations that have been established. Information on delivery time scales will be essential.

LU shall have the right of access to the premises of any such sub-contractor for inspection purposes, including witnessing of tests.

A.4.3 Timescales and Delivery

The deadline for this price enquiry is ***16/01/2017***. If you wish to make a bid please e-mail addressed to Graeme Burt and Sam Pitman, details found in section A.6.

LU requires that the supply is delivered by ***03/04/2017*** assuming that the purchase order is sent no later than ***24/01/2017***. Please feel free to comment on this timescale with the quote. Timescales for the project are very important, Earlier delivery of the cavity disks would be considered desirable.

A draft manufacturing programme is required with the quote and a detailed programme including all necessary acceptance tests shall be issued by the contractor within one week of contract placement and must be approved by LU. This programme must contain sufficient detail to enable progress on the contract to be monitored accurately, and shall include preliminary dates for inspections and tests.

LU and its representatives shall have free access during normal working hours to the manufacturing or assembly sites, including any subcontractor's premises, during the contract period. The place of manufacture may only be changed after written approval by LU.

Written progress reports must be submitted to LU at intervals of one month during the contract by e-mail addressed to Graeme Burt and Sam Pitman, copied to Anastasiya Solodko. Contact details can be found in section A.6.

No change may be made to the agreed programme without the written approval of LU. LU must be contacted immediately of any circumstances which might prevent the contract delivery date from being met.

A.4.4 Packing and transport to CERN

The contractor is responsible for the packing and transport to CERN. They shall ensure that the equipment is delivered to CERN without damage and any possible deterioration in performance due to transport conditions.
The discs shall be packaged individually in plastic boxes with high elastic protective film. Fragile label on shipping package is necessary.

A.4.5 Acceptance and guarantee

LU wishes to visit the company in order to perform a visual inspection of the parts before their shipping. However, the acceptance of the supply will be given by LU only after all items have been delivered in accordance with the conditions of the contract in this technical specification and in particular including dimensional tolerances as specified in the drawings. Metrological re-control will be performed at CERN after delivery.

A.4.6 Inspection and Testing

LU or its authorised representative shall have reasonable access to the manufacturer's works and the premises of any sub-contractors for the purposes of inspection and the witnessing of tests.

All tests must be undertaken with equipment and procedures approved by LU.

All tests shall be properly recorded on test certificates and results submitted to LU.

With the components suitably supported, check all relevant dimensions and record the actual measurements. If any of the specified dimensions are not achieved, no rectification is to be made without the prior approval of LU.

A.5 List of Contract Loan Items

A.5.1 1 x Rectangular OFE Copper Block 160 x 100

A.5.2 1 x Round OFE Copper Bar ⌀180 mm

Quantity to be confirmed.

A.6 Contact Persons

A.6.1 Persons to be contacted for technical matters:

Sam Pitman (CERN, BE-RF-LRF)
Tel: +41 22 76 76870
Mob: +44 77 122 69890
Email: Sam.Pitman@cern.ch

In case of absence:

Graeme Burt (Lancaster University Engineering)
Tel: +44 1524 592177
Email: G.Burt1@lancaster.ac.uk

Anastasiya Solodko (CERN, BE-RF-MK)
Tel: +41 22 76 76912
Email: Anastasiya.Solodko@cern.ch

A.6.2 Persons to be contacted for commercial matters:

Graeme Burt (Lancaster University Engineering)
Tel: +44 1524 592177
Email: G.Burt1@Lancaster.ac.uk

In case of absence:

Amanda Fryers (Lancaster University Procurement)
Tel: +44 1524 594499
Email: A.Fryers@lancaster.ac.uk

A.7 Annexes

- Drawings file
- Models file